Manufacturing of Refractory Multi-Principal Element Alloys and Understanding their Micro- and Nanomechanical Behaviour

A thesis

submitted by

K Deekshith Goud

in partial fulfilment of the requirements for the award of the degree of

Doctor of Philosophy

in

Nanoscience and Technology



School of Engineering Sciences and Technology

University of Hyderabad, India

December 2023

Declaration

I, K Deekshith Goud hereby declare that this thesis work entitled "Manufacturing of Refractory Multi-Principal Element Alloys and Understanding their Micro- and Nanomechanical Behaviour" submitted in partial fulfilment of the requirements for the award of Doctor of Philosophy (in Nanoscience and Technology) in the School of Engineering Sciences and Technology (SEST), University of Hyderabad is a bonafide record of the work which was carried out by me under the supervision of Prof. Koteswararao V. Rajulapati. I also declare that the content of this thesis has not been submitted earlier, as a whole or in part, to this University or any other University/Institution for the award of any degree or equivalent.

K beekshith Goud

Reg. No.: 19ENPH01

Nanoscience and Technology

School of Engineering Sciences and Technology

University of Hyderabad

CERTIFICATE

This is to certify that the thesis work entitled "Manufacturing of Refractory Multi-Principal Element Alloys and Understanding their Micro- and Nanomechanical Behaviour", submitted by K Deekshith Goud bearing Reg. No. 19ENPH01 in partial fulfillment of the requirements for the award of the degree of Doctor of Philosophy in Nanoscience and Technology is a bonafide record of research work that has been carried out by him under my guidance and supervision. The content of this thesis has not been submitted earlier, as a whole or in part, to this or any other University/Institution for the award of any degree or equivalent.

Thesis Supervisor

Prof. Koteswararao V. Rajulapati

Dr. KOTESWARARAO V. RAJULAPATI

Professor

School of Engineering Sciences and Technology, University of Hyderabad, Prof. C. R. Rao Road, Gachibowli, Hyderabad - 500 046, INDIA.

University of Hyderabad

Approved by,

जय प्रकाश गौतम Prof. Jai Prakash Gautam Prof. Jai Prakash Gautam

न /DEAN एस.ई.एस.टी / School of Engineering Sciences & Technology

हैदराबाद विश्वविद्यालय UNIVERISTY OF HYDERABAD Dean

School of Engineering Sciences and Technology0046

University of Hyderabad



CERTIFICATE

This is to certify that the thesis entitled "Manufacturing of Refractory Multi-Principal Element Alloys and Understanding their Micro- and Nanomechanical Behaviour" submitted by K Deekshith Goud bearing registration number 19ENPH01 in partial fulfillment of the requirements for the award of Doctor of Philosophy (in Nanoscience and Technology) in the School of Engineering Sciences and Technology (SEST) is a bonafide work carried out by him under my supervision and guidance.

This thesis is free from plagiarism and has not been submitted previously in part or in full to this or any other University or Institution for the award of any degree or diploma. The major part of this thesis has been published in the following publications:

- D.G. Kalali, S. Antharam, M. Hasan, P.S. Karthik, P.S. Phani, K. Bhanu Sankara Rao, K. V. Rajulapati, On the origins of ultra-high hardness and strain gradient plasticity in multi-phase nanocrystalline MoNbTaTiW based refractory high-entropy alloy, Materials Science and Engineering: A. 812 (2021) 141098.
- D.G. Kalali, P.S. Karthik, K.B. Sankara, K. V Rajulapati, Ultra-hard, multi-phase nanocrystalline MoTa and MoTaTi based concentrated refractory alloys, Materials Letters. 324 (2022) 132768.
- D.G. Kalali, Harita Seekala, P.S. Phani, K.B. Sankara, K. V Rajulapati, High speed nanoindentation aided correlative study between local mechanical properties and chemical segregation in equiatomic MoNb and MoNbTi alloys, Journal of Materials Research. 38 (2023) 2919-2929.
- D.G. Kalali, Anjali Kanchi, P.S. Phani, K.B. Sankara, S.V.S. Narayana Murty, K. V Rajulapati, Role of Ti on the microstructure and mechanical properties of MoNbTi medium-entropy alloy. International Journal of Refractory Metals and Hard Materials. 118 (2024) 106487.

K Deekshith Goud completed following courses as part of pre-Ph.D. coursework.

Course No.	Title	Credits	Pass/ Fail
PD 801	Research Methodology	4	Pass
PD 802	Advanced Materials Processing and Characterization	4	Pass
PD 803	Advanced Engineering Mathematics	2	Pass
PD 805	Materials Characterization- I	4	Pass
PD 807	Research and Publication Ethics	2	Pass

Dr. KOTESWARARAO V. RAJULAPATI Supervisor Professor

School of Engineering Sciences and Technology, University of Hyderabad, Prof. C. R. Rao Road, Gachibowli, Hyderabad - 500 046, INDIA. प्रकार प्राप्त गीतम् Prof. Jai Prakash Gautam डीन /DEAN एस.ई.एस.टी / School of Engineering Sciences & Technology हैदराबाद विश्वविद्यालय UNIVERISTY OF HYDERABAD हैदराबाद / Hyderabad - 500046

Acknowledgements

If you feel good, you will do good. University of Hyderabad is a perfect example of this. I have always felt good with the flora and fauna of the university. Especially the stakeholders of the School of Engineering Sciences and Technology provided ample help in every situation during these four years of my stay here.

"Eat and work" is the line from my supervisor *Prof. Koteswararao V. Rajulapati*, which gives me enough encouragement personally and professionally. Due to his continuous support, I never regretted resigning from my job at MRF Tyres Ltd. to pursue my Ph.D. I always remember his dedication to research while working on the manuscripts for submission until 4:00 AM. I can proudly say I am the Prof. Koteswararao V. Rajulapati student for the rest of my life.

I am sincerely thankful to *Prof. Ing- V. V. S. S. Srikanth* and *Dr. Venkata Girish Kotnur*, my RAC committee members, who provided enough encouragement and guidance to carry out my research work without any hindrances.

I sincerely thank the Dean of the School of Engineering Sciences and Technology, *Prof. Jai Prakash Gautam*, and all other faculties in the school for providing me with the facilities and guidance to perform encouraging experiments.

I feel honoured for the continuous guidance of *Prof. K. Bhanu Sankara Rao*, who continuously works towards the advancement of metallurgy. His insights into my work always helped me in learning something new.

I sincerely thank *Dr. Sudharshan Phani Pardhasaradhi*, Scientist F, ARCI, who gave his time from his busy schedule for the necessary guidance whenever required.

I sincerely thank *Dr. K. Guruvidyathri*, School of Engineering Sciences and Technology, University of Hyderabad, for providing the Thermo-Calc software facility.

My sincere thanks to *Dr. S V S Narayana Murty*, General Manager, Materials Development and Production Group, Materials and Mechanical Entity, Liquid Propulsion Systems Center, Trivandrum, for his technical guidance.

This work was supported by the UGC Non-NET BBL fellowship, DST-FIST, DST-PURSE, and the University of Hyderabad - Institute of Eminence program.

Thanks to my fellow lab mates, *Dr. Johny Varghese*, *Madhu Babu*, *Hasan*, *Nanda*, *Nagalakshmi*, *Anil*, *Pranay*, *Sanath*, and my classmates.

I am happy to say I am in a safe loop of these special friends who mentored me professionally and personally, *Shiva Lingam, Medishetty Girish, Gunti Shiva, Kanchi Anjali, G. Vineeth Chary, Bharath and Seenu.*

A very special thanks to my beloved parents and family members, *Nagarathnam Goud*, *Anjali Devi*, *Veera Malla Goud*, *Jayasree*, *Trilok Chandan*, *Tejaswini*, *Giridhar*, *Swetha*, *Ujas*, *Diwith*, *Udvi*, *and Drithi*.

I thank my beloved life partner *Deepthy Kalali*, who is always with me in difficult times. Finally, lots of love to my son *Hanith Sai*.

Deekshith Kalali

Abstract

It is desired to improve the thermal efficiency of gas turbine engines to decrease the global problem of CO₂ emissions, thus reducing global warming. To improve the thermal efficiency of the gas turbine engine, it is essential to increase the operating temperature of the gas turbine engines. This induces high thermal stresses on the turbine engine components. To overcome this problem, an alternative material is required to sustain the high thermal loads during the service. Refractory multi-principal element alloys (RMPEAs) represent a dynamic class of alloys with considerable potential for high-temperature gas turbine engine applications. Notably, the MoNbTaW alloy has expanded the realm of high-temperature applications, surpassing Ni-based superalloys. Despite its impressive compressive strength at 1000 °C (548 MPa), its high density of 13.62 g/cc hinders its applicability for aerospace applications, which demand materials with high strength and low weight.

In a bid to enhance strength and reduce overall density, the current work introduced Ti to the MoNbTaW alloy. The MoNbTaTiW alloy is manufactured via ball milling and spark plasma sintering. It appears that Ti and Fe (from processing media) are responsible for the multi-phase structure realized as well as the extraordinarily high absolute hardness of 13.89 GPa at 500 g load. These values are the highest reported so far in the family of MoNbTaW alloys. A comprehensive analysis on strengthening mechanisms responsible for the extraordinarily high hardness observed in this alloy indicates that solid solution strengthening and grain boundary (Hall-Petch) strengthening are the dominant factors while lattice frictional stress and Taylor hardening also contribute to some extent. The hardness data of this alloy was observed to follow the Meyer hardening power law with an index of 1.82 suggesting the presence of indentation size effect. The strain gradient plasticity of this multi-phase RHEA was explained based on the considerations of GNDs that exists owing to the multi-phase structure with different crystal structures (BCC, FCC1, FCC2), by using the Nix-Gao model. The depth independent hardness of 11.80 GPa and a characteristic length scale of 1.07 µm were realized from the analysis.

Further, to understand the phase transformations and their stabilities, binary (MoTa and MoNb) and ternary (MoTaTi and MoNbTi) RMPEAs were also manufactured. Binary (MoTa) and ternary (MoTaTi) based concentrated refractory alloys are synthesized using ball milling and spark plasma sintering. A single BCC phase which was observed after high energy ball milling has transformed to multiple phases after sintering. An extremely high hardness in the range 16

-10 GPa was measured in the load range 25 g - 500 g and with a very distinct indentation size effect. The indentation size effect observed in the MoTa and MoTaTi alloys is explained using the classic Nix-Gao model and validated using the Meyer power law. Depth-independent hardness is evaluated from the Nix-Gao plot for MoTa alloy is 9.32 GPa with a characteristic length scale of 1.03 μ m. For MoTaTi alloy, depth-independent hardness is 9.92 GPa with a characteristic length scale of 1.20 μ m.

Binary (MoNb) and ternary (MoNbTi) based concentrated refractory alloys are also synthesized using ball milling and spark plasma sintering. Multiple phases are observed after sintering the single-phase MoNb (Fe) and MoNbTi (Fe) milled powders. Ti and Fe (from milling media) are involved in the phase transformations in both MoNb (Fe) and MoNbTi (Fe) alloys. The density of the MoNbTi (Fe) alloy (7.67 g/cc) is very low compared to the various commercial Niobium alloys like C-103 (8.85 g/cc), C-129Y (9.5 g/cc), and C3009 (10.1 g/cc). Extremely high hardness was observed in both the MoNb (Fe) and MoNbTi (Fe) alloys. Hardness at 500 g load for the MoNb (Fe) alloy is 11.08 ± 0.23 GPa and MoNbTi (Fe) alloy is 11.13 ± 0.23 GPa.

Equiatomic MoNb and MoNbTi alloys are synthesized by arc melting to understand the length scale effects on the microstructure and mechanical properties. Exposure to high temperature for considerably longer duration (24 h at 1673 K) did not alter the beneficial effect of grain refinement imparted by Ti addition. Ti addition resulted in a significant grain refinement (from 115 μ m to 34 μ m) of MoNb alloy. The addition of Ti significantly reduces the overall density without effecting the hardness of MoNbTi alloy (MoNb - 4.06 \pm 0.01 GPa, MoNbTi - 4.10 \pm 0.01 GPa). MoNbTi also showed an exceptionally high "density-normalized" hardness when compared to various high-entropy alloys of similar family.

The MoNb and MoNbTi alloy systems manufactured via arc melting have indicated a propensity for chemical segregation that in turn influences the mechanical properties. In this regard, recent advances in high speed nanoindentation mapping have demonstrated the ability to accurately measure mechanical properties at the micrometer length scale. Here a quantitative link between the local chemistry measured via energy dispersive spectroscopy (EDS) and nanoindentation mapping for as-cast and heat treated equiatomic MoNb and MoNbTi alloys. An excellent correlation between chemical composition and hardness is observed. This correlation provides a simple framework to study the effect of chemical segregation on the local mechanical properties of multi-principal element alloys, which can be gainfully used to tailor the microstructure and properties of these alloys.

Analyzing flow stress across binary, ternary, quaternary, and quinary alloys revealed that ternary alloys surpassed several quaternary and quinary counterparts. Importantly, this approach not only improves alloy performance but also reduces manufacturing costs by involving fewer elements, rendering the alloys cost-effective. Thus, the current investigations have introduced novel refractory alloy systems for gas turbine engine applications.

Table of contents

Abstract	vi
List of figures	xiii
List of tables	xviii
Nomenclature	xix
Chapter 1	1
1. Introduction	1
1.1. Background	1
1.2. Objectives and scope	3
1.3. Thesis outline	3
References	5
Chapter 2	8
2. Literature review	8
2.1. History of high-entropy alloys	8
2.2. Definition of high-entropy alloys	8
2.3. Four core effects	10
2.3.1. High-entropy effect	11
2.3.2. Sluggish diffusion effect	11
2.3.3. Lattice distortion effect	12
2.3.4. Cocktail effect	13
2.4. Phase prediction of HEAs	13
2.4.1. Semi empirical parameters	14
2.4.2. CALPHAD methods	15
2.5. Taxonomy of high-entropy alloys	16
2.6. Expansion of high-entropy alloys field	17
2.7. Refractory multi-principal element alloys	18

2.7.1.	Fundamental properties of refractory elements	18
2.7.2.	Applications of refractory multi-principal element alloys	19
2.7.3.	Mechanical properties of refractory multi-principal element alloys	20
2.8. Inc	lentation size effect in refractory multi-principal element alloys	22
2.9. Str	rengthening mechanisms in refractory multi-principal element alloys	25
2.9.1.	Frictional stress	25
2.9.2.	Hall-Petch strengthening	26
2.9.3.	Taylor hardening	28
2.9.4.	Solid solution strengthening	29
2.9.5.	Twin boundary strengthening	31
2.9.6.	Precipitation strengthening	31
2.9.7.	Dispersion strengthening	32
Reference	es	33
Chapter 3		44
3. Experi	mental details	44
3.1. Ma	aterials used	44
3.2. Pro	ocessing of refractory multi-principal element alloys with finer micro	structural
features		45
3.2.1.	Mechanical alloying	46
3.2.2.	Spark plasma sintering	47
3.3. Pro	ocessing of refractory multi-principal element alloys with coarser micro	ostructural
features		49
3.3.1.	Vacuum arc melting	49
3.4. Str	ructural and mechanical characterization	50
3.4.1.	X-ray diffraction	51
3.4.2.	Field emission scanning electron microscopy	53
3.4.3.	Vickers indentation	54
3 4 4	Nanoindentation	55

3.5. He	at treatment	57
Reference	es	58
Chapter 4		61
4. Result	s and Discussion	61
4.1. Ul	tra high hardness and strain gradient plasticity in multi-phase	nanocrystalline
MoNbTa	TiW based refractory high-entropy alloy	61
4.1.1.	Introduction	61
4.1.2.	Experimental procedure	62
4.1.3.	Results and discussion	63
4.1.4.	Summary	81
Refere	nces	82
4.2. Ul	tra-hard, multi-phase nanocrystalline MoTa and MoTaTi based	1 multi-principal
element a	alloys	86
4.2.1.	Introduction	86
4.2.2.	Experimental procedure	86
4.2.3.	Results and discussion	87
4.2.4.	Summary	90
Refere	nces	91
4.3. Lo	w-dense, multi-phase nanocrystalline MoNb (Fe) and MoNbTi ((Fe) based multi-
principal	element alloys	92
4.3.1.	Introduction	92
4.3.2.	Experimental procedure	92
4.3.3.	Results and discussion	93
4.3.4.	Summary	96
Refere	nces	96
4.4. Ro	ole of Ti on the microstructure and mechanical properties of	MoNbTi multi-
principal	element alloy: Performance of the multi-principal element alloy	ys98
111	Introduction	00

4.4.2.	Experimental procedure	.99
4.4.3.	Results	100
4.4.4.	Discussion	109
4.4.5.	Summary1	111
Refere	nces1	112
4.5. Le	ngth scale effects in the MoNb and MoNbTi multi-principal element allo	ys:
Understa	nding their local chemical and mechanical behaviour1	115
4.5.1.	Introduction1	115
4.5.2.	Results	116
4.5.3.	Discussion	122
4.5.4.	Summary	126
4.5.5.	Experimental procedure	127
Refere	nces	129
Chapter 5		134
5. Conclu	sions and Future Scope1	134
5.1. Co	onclusions1	134
5.2. Sc	ope of future work1	138
Annendix	1	139

List of figures

Fig. 1.1 TS and PV plots of the ideal Brayton cycle [1]
Fig. 2.1 Entropy of mixing for equiatomic alloys for different numbers of elements9
Fig. 2.2 Schematic representation showing the material's performance depends on the crystal
structure, microstructure, properties, and processing route
Fig. 2.3 Comparison of (a) pure metal lattice structure (b) severe distorted lattice structure of
HEA
Fig. 2.4 Classification of HEAs based on composition, phase type, and elements used16
Fig. 2.5 Schematic showing the size of compositional space of different high-entropy alloys
field
Fig. 2.6 Compressive strength of the equiatomic MoNbTaW alloy (a) room temperature and
(b) elevated temperatures [39]
Fig. 2.7 Compressive yield strength of the MoNbTaW and MoNbTaVW at different
temperatures compared with Haynes 230 and Inconel 718 superalloys [39]21
Fig. 2.8 High-angle annular dark-field scanning transmission electron microscopy micrograph
of $Al_{0.5}NbTa_{0.8}Ti_{1.5}V_{0.2}Zr$ alloy showing the BCC + B2 checkered pattern similar to Ni-based
superalloy [57]
Fig. 2.9 Schematic showing (a) Variation of hardness with the increase in indentation depth
(Normal ISE, Conventional plasticity, and Reverse ISE) (b) Hardness is the ratio of indentation
load and projected area (c) Berkovich indenter with a half angle of 65.3°23
Fig. 2.10 Schematic showing (a) coarse grain size and (b) finer grain size. In fig 2.9 (b) it is
clear that at finer grain size the number of obstacles in the form of grain boundaries will be
more for the mobile dislocations that leads to strength enhancement
Fig. 2.11 Schematic representation of yield strength of the alloy as a function of grain size. 27
Fig. 2.12 Atoms in the multi-principal element alloy are distributed randomly, increasing the
lattice distortion and hindering the movement of the dislocations, thereby enhancing the solid
solution strengthening of the alloy
Fig. 2.13 Schematic to show how dislocations are hindered at twin boundaries31
Fig. 2.14 Schematic of precipitation hardening mechanism [114]32
Fig. 3.1 Flow chart of the experimental procedures adapted in the current investigation44

Fig. 3.2 Schematic of the milling process in the high-energy ball mill. (a) Metal powder and
metal balls in the milling vial (b) metal powder is fracturing in between the two metal balls
hitting with high velocity47
Fig. 3.3 Schematic of the spark plasma sintering equipment used in this work
Fig. 3.4 Schematic of the Vacuum arc melting system used in this work50
Fig. 3.5 Principle of the X-ray diffraction.
Fig. 3.6 Schematic of the electron beam interaction volume with the sample in the FESEM
investigation53
Fig. 3.7 Schematic of the Vickers indentation using a diamond indenter55
Fig. 3.8 Schematic showing the indents on the sample after high-speed nanoindentation57
Fig. 3.9 Schematic of the tubular furnace used for the heat treatments in this work57
Fig. 4.1 X-ray diffractograms of 1 h milled, 30 h milled and sintered MoNbTaTiW alloy.
Milling for 30 h resulted in a single phase BCC phase complex solid solution; upon sintering
at 1473 K, this BCC has decomposed into a new BCC phase and two different FCC phases
(FCC1, FCC2). A minor presence of TiO ₂ is also noticed
Fig. 4.2 BSE image of sintered sample showing the contrast from three different phases (Grey,
dark and bright). By considering the phase fractions from both X-ray analysis and BSE-SEM
analysis, Grey phase, dark phase and bright phase are confirmed as BCC, FCC1 and FCC2
respectively
Fig. 4.3 BSE-SEM image of the alloy showing the presence of three different phases in
different contrasts (grey, dark and bright) (a); location of grey phase (BCC) shown in red color
in (b); location of dark phase (FCC1) shown in yellow color in (c); location of bright phase
(FCC2) shown in pink color (d). It is clear that the microstructural length scale (particle size)
of the individual phases is within the sub-micron range
Fig. 4.4 Bar chart showing the elemental composition (at. %) in various phases observed in this
alloy. This data was obtained using spot analysis in SEM-EDS. Nominal compositions was
also shown for comparison purposes
Fig. 4.5 Variation of microhardness at different indentation loads in multi-phase MoNbTaTiW-
Fe alloy. A high hardness of 18.87 GPa was observed at 25 g load and a pronounced indentation
size effect can be seen as the load is increased to 500 g
Fig. 4.6 Compilation of hardness data of similar alloys (processed by melting + casting, Powder
metallurgy) from the literature [13-21]; hardness values are normalized with the densities of
corresponding alloys. It is clear that the present alloy shows an exceptional absolute hardness
(Fig. 4.5) and "density-normalized" hardness (indicated with an arrow) 70

Fig. 4.7 Summary of various strengthening mechanisms operating among the various phases
of the present alloy system
Fig. 4.8 Validation of the Vickers hardness data of the present alloy by Meyer power law. Here
P is indentation load, y is average diagonal length. The analysis yields a Meyer index of 1.82
suggesting the presence of indentation size effect
Fig. 4.9 Validation of the experimentally measured hardness data with the Nix-Gao model on
strain gradient plasticity during indentation using self-symmetrical indenters [12]. In this case
Vickers square based diamond pyramid indenter was used
Fig. 4.10 (a) SEM topography image of the residual indent performed at 500 g load, which
shows that deformation volume includes all the three different phases (BCC, FCC1, FCC2) of
the alloy. (b) Schematic illustration of the probable processes that occur beneath the indenter
in this multi-phase RHEA80
Fig. 4.11 (a) X-ray diffractograms of MoTa alloy at 1 h, 30 h of ball milling and after SPS (b)
X-ray diffractograms of MoTaTi alloy at 1 h, 30 h and after SPS
Fig. 4.12 (a) FESEM-BSE microstructure of MoTa (Fe) alloy; (b) Colour contrast
microstructure of MoTa (Fe) alloy, obtained from (a) using ImageJ, that shows three different
phases (red, blue, green) formed after sintering; (c) FESEM-BSE microstructure of MoTaTi
(Fe) alloy; (d) Colour contrast microstructure of MoTaTi (Fe) alloy, obtained from (c) using
ImageJ, that shows two different phases (green, blue)
Fig. 4.13 (a) Variation microhardness in MoTa (Fe) and MoTaTi (Fe) alloys with load upto
9.81 N. A pronounced indentation size effect (ISE) was observed for both the alloys. (b)
Observed ISE clearly follows the Nix-Gao model proposed considering the geometrically
necessary dislocations and multi-phase structure [2]. (c) "Density-normalized" hardness of
various tantalum containing alloys manufactured using the powder metallurgy route compared
with the values obtained in the present work (shown with upward arrows)89
Fig.4.14(a)X-raydiffractogramsofMoNb(Fe)alloyand(b)X-raydiffractogramsofMoNbTi(Fe)alloyand(b)X-raydiffractogramsofMoNbTi(Fe)alloyand(b)X-raydiffractogramsofMoNbTi(Fe)alloyand(b)X-raydiffractogramsofMoNbTi(Fe)alloyand(b)X-raydiffractogramsofMoNbTi(Fe)alloyand(b)X-raydiffractogramsofMoNbTi(Fe)alloyand(b)X-raydiffractogramsofMoNbTi(Fe)alloyand(b)X-raydiffractogramsofMoNbTi(Fe)alloyand(b)X-raydiffractogramsofMoNbTi(Fe)alloyand(b)X-raydiffractogramsofMoNbTi(Fe)alloyand(b)X-raydiffractogramsofMoNbTi(Fe)alloyand(b)X-raydiffractogramsofMoNbTi(Fe)alloyand(b)X-raydiffractogramsofMoNbTi(Fe)alloyand(b)X-raydiffractogramsofMoNbTi(Fe)alloyand(b)X-raydiffractogramsofMoNbTi(Fe)alloyand(b)X-raydiffractogramsofMoNbTi(Fe)alloyand(b)X-raydiffractogramsofMoNbTi(Fe)alloyand(b)X-raydiffractogramsofMoNbTi(Fe)alloyand(b)X-raydiffractogram
(Fe) alloy at different processing conditions
Fig. 4.15 (a) FESEM-BSE microstructure of MoNb (Fe) alloy; (b) Colour contrast
microstructure of MoNb (Fe) alloy that shows three different phases (red, blue, green); (c)
FESEM-BSE microstructure of MoNbTi (Fe) alloy; (d) Colour contrast microstructure of
MoNbTi (Fe) alloy that shows two different phases (green, blue). All the microstructures are
of the sintered condition94
Fig. 4.16 (a) Microhardness details of the MoNb (Fe) and MoNbTi (Fe) alloys at different
loads (b) "Density-normalized" hardness of various Niobium-containing alloys processed via

powder metallurgy route. Further, some Niobium-based commercial alloys are also compared
with the values obtained in the present work [4,6–11]
Fig. 4.17 Equilibrium phase diagram of MoNb alloy (a), vertical section of the (MoNb) _{1-x} Ti _x
phase diagram (c), Phase fraction plots of MoNb (b) and MoNbTi (d) alloys with temperature
scale from 2500 °C to 2600 °C
Fig. 4.18 X-ray diffractograms of equiatomic MoNb and MoNbTi alloys in as-cast and
homogenized conditions (from bottom to top). In all the cases a single BCC phase was observed
[19]102
Fig. 4.19 (a) BSE micrograph of MoNb as-cast alloy, (b) elemental distribution of Mo in as-
cast MoNb alloy, (c) elemental distribution of Nb in as-cast MoNb alloy and (d) overlay image
of the elemental distribution indicating all the elements are homogeneously distributed with
some Nb rich regions in MoNb as-cast alloy. (e) BSE micrograph of the MoNb homogenized
alloy, (f) elemental distribution of Mo in homogenized MoNb alloy, (g) elemental distribution
of Nb in homogenized MoNb alloy and (h) overlay image of the elemental distribution
indicating all the elements are homogeneously distributed with some Nb rich regions in MoNb
homogenized alloy103
Fig. 4.20 (a) BSE micrograph of the MoNbTi as-cast alloy, (b) elemental distribution of Mo in
as-cast MoNbTi alloy, (c) elemental distribution of Nb in as-cast MoNbTi alloy and (d)
elemental distribution of Ti in as-cast MoNbTi alloy. (e) BSE micrograph of MoNbTi
homogenized alloy, (f) elemental distribution of Mo in homogenized MoNbTi alloy, (g)
elemental distribution of Nb in homogenized MoNbTi alloy and (h) elemental distribution of
Ti in homogenized MoNbTi alloy
Fig. 4.21 Inverse pole figure maps of the (a) as-cast MoNb alloy, (b) as-cast MoNbTi alloy, (c)
homogenized MoNb alloy and (d) homogenized MoNbTi alloy. as-cast condition shows an
equiaxed grain morphology, whereas homogenization results in elongated grains in these
alloys106
Fig. 4.22 (a) Hardness measurements at various loads (2000-10000 gf) on MoNb (as-cast and
homogenized) and MoNbTi (as-cast and homogenized). BSE micrograph with indent residual
impression at 10000 gf load on (b) homogenized MoNb alloy and (c) homogenized MoNbTi
alloy108
Fig. 4.23 "Density-normalized" hardness of MoNbTaW family [20–23] of alloys from the
literature including the homogenized MoNb and MoNbTi alloys from the present work
(indicated with an arrow).

Fig. 4.24 "Density-normalized" flow stress of binary, ternary, quaternary and quinary
refractory multi-principal element alloys consisting of Mo, Nb, Ta, W and Ti as a function of
(a) number of elements; red color data points show the maximum value that can be obtained in
these refractory multi-principal element alloys, blue color data point is for CoCrNi multi-
principal element alloy, included for comparison purposes and (b) influence of Ti on refractory
multi-principal element alloys . It suggests that addition of more number of alloying elements,
beyond three in equiatomic proportion, may not offer major advantage in deriving high
hardness (strength) in single phase multi-principal element alloys
Fig. 4.25 X-ray diffractograms of equiatomic MoNb and MoNbTi CCAs in as-cast and
homogenized conditions (from bottom to top). In all the cases, a single BCC phase was
observed
Fig. 4.26 FE-SEM, BSE micrograph with the indent overlay for (a) MoNb in as-cast condition,
(b) MoNb in heat treated condition, (c) MoNbTi in as-cast condition and (d) MoNbTi in heat
treated condition
Fig. 4.27 EDS maps of (a) Nb fraction in as-cast MoNb, (b) Nb fraction in heat treated MoNb,
(c) Ti fraction in as-cast MoNbTi and (d) Ti fraction in heat treated MoNbTi120
Fig. 4.28 Hardness maps from high-speed nanoindentation for (a) MoNb as-cast alloy, (b)
$MoNb\ heat\text{-treated alloy, (c)}\ MoNbTi\ as\text{-}cast\ alloy\ and\ (d)\ MoNbTi\ heat\text{-}treated\ alloy122$
Fig. 4.29 (a) FE-SEM BSE micrograph (b) EDS map (c) hardness map and (d) deconvoluted
hardness map of as-cast MoNbTi alloy
Fig. 4.30 (a) hardness and (c) elastic modulus variation with Nb fraction in MoNb alloys; (b)
hardness and (d) elastic modulus variation with Ti fraction in MoNbTi alloys, showing the
correlation between Nb or Ti fraction and the local hardness and elastic modulus in the as-cast
and heat-treated conditions

List of tables

Table 2.1 Physical properties of the most used refractory elements in the development of
RMPEAs18
Table 3.1 Physical properties of elements used in this work to fabricate various RMPEAs45
Table 3.2 Parameters used during mechanical alloying in the high-energy ball mill46
Table 3.3 Parameters used during spark plasma sintering to sinter the milled powders in this
work
Table 3.4 Parameters used during vacuum arc melting in this work
Table 3.5 Parameters used for the XRD analysis
Table 4.1 Amount of different phases estimated from X-ray diffractograms and BSE-SEM
images 66
images
Table 4.2 Grain size and Hall-Petch strengthening contributions of various phases69
Table 4.2 Grain size and Hall-Petch strengthening contributions of various phases69
Table 4.2 Grain size and Hall-Petch strengthening contributions of various phases69 Table 4.3 Lattice parameter, lattice microstrain, Burgers vector, dislocation density and strain
Table 4.2 Grain size and Hall-Petch strengthening contributions of various phases
Table 4.2 Grain size and Hall-Petch strengthening contributions of various phases
Table 4.2 Grain size and Hall-Petch strengthening contributions of various phases

Nomenclature

Abbrevations

B Bulk Modulus

BCC Body Centered Cubic

BM Ball Milling

BSE Back Scattered Electron

CCAs Complex Concentrated Alloys

CS Compressive Strength

E Elastic Modulus

EBSD Electron Backscatter Diffraction

EDS Energy Dispersive Spectroscopy

FCC Face Centered Cubic

FE-SEM Field Emission Scanning Electron Microscopy

G Shear Modulus

HCP Hexagonal Closed Packed

HEAs High Entropy Alloys

HPT High Pressure Torsion

IPF Inverse Pole Figure

ISE Indentation Size Effect

LEAs Low Entropy Alloys

MA Mechanical Alloying

MEAs Medium Entropy Alloys

MPEAs Multi Principal Element Alloys

RCCAs Refractory Complex Concentrated Alloys

Reverse ISE Reverse Indentation Size Effect

RHEAs Refractory High Entropy Alloys

RMPEAs Refractory Multi Principal Element Alloys

SE Secondary Electron

SEM Scanning Electron Microscopy

SPS Spark Plasma Sintering

SS Solid Solution

SSS Solid Solution Strengthening

VAM Vacuum Arc Melting

VEC Valence Electron Concentration

XRD X-ray Diffraction

Symbols

 $\Delta H_{mix} \hspace{1.5cm} Enthalpy \ of \ Mixing$

 $\Delta S_{mix} \hspace{1.5cm} Entropy \ of \ Mixing$

Ω Omega Parameter

δ Atomic Size Difference

Chapter 1

Introduction

1.1.Background

Gas turbine engine works on the principle of the Brayton cycle [1]. The ideal Brayton cycle undergoes four reversible processes, as shown in the TS (Temperature- Entropy) and PV (Pressure-Volume) plots of Fig. 1.1:

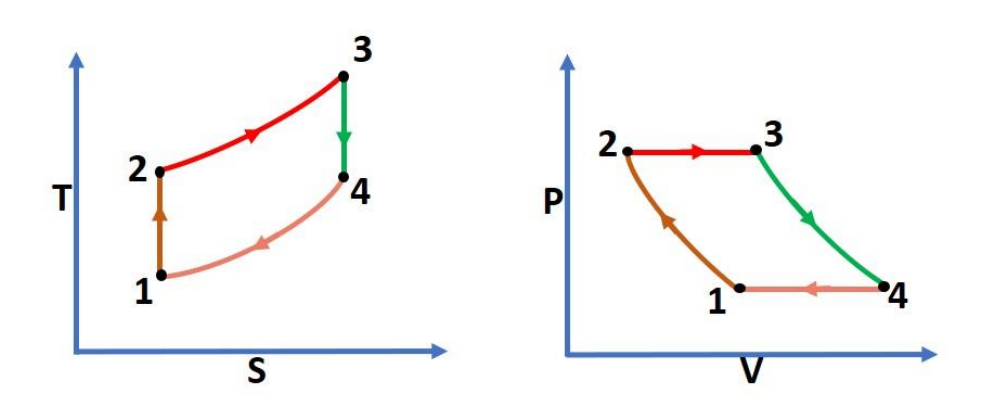


Fig. 1.1 TS and PV plots of the ideal Brayton cycle [1]

From 1-2, adiabatic compression of the air

From 2-3, Constant pressure fuel combustion

From 3-4, Adiabatic expansion of the air

From 4-1, Constant pressure cooling of the air

The thermal efficiency of the ideal Brayton cycle is as shown in equation (1.1)

$$\eta_{thermal} = 1 - \frac{T_1}{T_2}....(1.1)$$

Equation (1.1) states that if the T_2 temperature of the cycle, i.e., if the exit temperature of the compressor increases, the thermal efficiency of the gas turbine engine increases. This increase in T_2 temperature increases the T_3 temperature, which is the inlet temperature of the turbine. This increment of T_3 temperature leads to high thermal stresses on the turbine components. Therefore, the materials used should have high-temperature strength. As a result, the journey of material development started from pure metal to 6^{th} -generation nickel-based superalloys [2–4]. The present-day commercially available turbine engine components are made up of Ni-based superalloys, which are, in general, single crystalline [2]. The primary strength of the Ni-

based superalloys is achieved by the solid solution strengthening of the γ matrix phase and precipitation strengthening of the ordered γ' particles [5]. As on today, Ni-base superalloys (IN718) are used in gas turbine engines at operating temperatures close to 800 °C. Material development w. r. t. Ni-base superalloys, for use in gas turbines, has been hitting the theoretical limit in terms of operating temperatures as they melt around 1200-1300 °C [4]. Therefore new alloys with high melting points, enhanced mechanical properties (both at room temperature and elevated temperatures), good high temperature oxidation properties have to be looked for by the scientific community.

In 2004, a new class of alloy systems was introduced called high-entropy alloys (HEAs) / multiprincipal element alloys (CCAs) / complex concentrated alloys (CCAs) [6]. These HEAs showed extraordinary properties like good corrosion resistance, high strength, and high fracture toughness with single phases, which was not initially expected [7–11]. Initially, it is desired to achieve a single-phase (Body Centered Cubic (BCC), Face Centered Cubic (FCC), and Hexagonal Close-Packed (HCP)) alloy with high strength [7,12–17]. Recently, the concept of HEAs has been extended to multi-phase and non-equiatomic concentrations with excellent mechanical properties [13,15–24]. This showed an opportunity to move away from the center of the compositional space to design various alloys with excellent mechanical properties [19,20,25–28].

Refractory metals in the concept of HEAs expand the application potential of HEAs to aerospace applications such as turbine engine components. This class of alloys is named refractory high-entropy alloys (RHEAs). The most significant and first alloy developed in this class of RHEAs is MoNbTaW RHEA [14]. This has a high room temperature compressive strength of 1211 MPa and high density [14]. Although it has good compressive strength, its high density is not beneficial for aerospace applications.

Therefore, the materials proposed for high-temperature aerospace applications need to have both high strength and low density (i.e., high specific strength). This background of necessity for high specific strength high-temperature materials motivated to manufacture refractory multi-principal element alloys (RMPEAs) for high-temperature aerospace applications. Different manufacturing routes are adopted to understand the effect of microstructure on the strength of the alloy.

1.2. Objectives and scope

Based on the above introduction, it is evident that the RHEA (MoNbTaW) developed by Senkov et al. has good strength, but its density is very high. To improve the strength of the alloy further and to reduce the density, in this work, Ti is added to the MoNbTaW alloy. Further, different binaries and ternaries are chosen from the base alloy (MoNbTaTiW) to understand the phase transformations and their stabilities. Based on this motivation, the objectives of this Ph.D. thesis are as follows:

- (i) To manufacture RMPEAs with high "density-normalized" hardness.
- (ii) To understand the micro- and nanomechanical behaviour of RMPEAs.
- (iii) To understand the length scale effects on the microstructure and mechanical properties.
- (iv) Correlation of local mechanical properties and local chemical segregation using high-speed nanoindentation.
- (v) Estimation of "density-normalized" flow stress of various RMPEAs.

The tasks followed to achieve the objectives are as follows:

- Design and development of MoNbTaTiW, MoTa, MoNb, MoTaTi, and MoNbTi RMPEAs using the MA+SPS route.
- Understanding of strengthening mechanisms for the MoNbTaTiW RMPEA.
- Study on indentation size effect using classic Nix-Gao model for various alloys.
- Development of MoNb and MoNbTi MPEAs via melting and casting route and their structural and nanomechanical characterization.
- Understanding the origins of strengthening mechanisms in these alloys.

1.3. Thesis outline

The outline of the thesis is as follows:

Chapter 1: Introduction discusses the background of the various class of HEAs/MPEAs/CCAs, the necessity of high strength to weight alloys for aerospace applications, different types of processing routes used in this work, and the objectives and scope of this work.

Chapter 2: Literature review discusses the history of HEAs, the definition of HEAs, the core effects of the HEAs, phase prediction of HEAs, mechanical properties, indentation size effect, and strengthening mechanisms of HEAs.

Chapter 3: Experimental procedure discusses materials used, different processing routes, structural and mechanical characterization techniques like XRD, FESEM, Vickers indentation, nanoindentation, and heat treatments.

- Chapter 4: Results and Discussion has sub-sections from 4.1 to 4.5
- 4.1 Presents the work that is already published with the following details: **Deekshith G. Kalali**, Sairam Antharam, Mohsin Hasan, P. Sai Karthik, P. Sudharshan Phani, K. Bhanu Sankara Rao, Koteswararao V. Rajulapati, "On the origins of ultra-high hardness and strain gradient plasticity in multi-phase nanocrystalline MoNbTaTiW based refractory high-entropy alloy," Materials Science and Engineering: A. 812 (2021) 141098.
- 4.2 Presents the work that is already published with the following details: **Deekshith G.** Kalali, P. Sai Karthik, K. Bhanu Sankara Rao, Koteswararao V. Rajulapati, "Ultrahard, multi-phase nanocrystalline MoTa and MoTaTi based concentrated refractory alloys," Materials Letters. 324 (2022) 132768.
- 4.3 Discuss the results and discussion on the "Low-dense, multi-phase nanocrystalline MoNb (Fe) and MoNbTi (Fe) based multi-principal element alloys" processed via ball milling and spark plasma sintering. This work will be submitted for journal publication soon.
- 4.4 Presents the work that is already published with the following details: **Deekshith G.** Kalali, Harita Seekala, P. Sudharshan Phani, K. Bhanu Sankara Rao, Koteswararao V. Rajulapati, "High speed nanoindentation aided correlative study between local mechanical properties and chemical segregation in equiatomic MoNb and MoNbTi alloys," Journal of Materials Research. 38 (2023) 2919-2929.
- 4.5 Presents the work that is already published with the following details: **Deekshith G. Kalali**, Anjali Kanchi, P. Sudharshan Phani, K. Bhanu Sankara Rao, S.V.S. Narayana Murty, Koteswararao V. Rajulapati, "Role of Ti on the microstructure and mechanical properties of MoNbTi medium-entropy alloy," International Journal of Refractory Metals and Hard Materials. 118 (2024) 106487.
- Chapter 5: This chapter discusses the conclusions and future scope of the work.

Appendix: This section shows the Vertical sections of phase diagrams and phase fraction plots drawn using the ThermoCalc TCHEA6 database with respect to various alloys developed in this work.

References

- [1] P.K. Nag, Engineering Thermodynamics, Tata McGraw Hill, 2005.
- [2] D. Jithin, S.K. Selvaraj, K.E. Vijay Vishaal, G. Sundaramali, Comparative Analysis between 5th and 6th Generation Superalloys and Previous Generation Superalloys, Adv. Mater. Sci. Eng. (2022). https://doi.org/10.1155/2022/3530689.
- [3] A. Sato, H. Harada, A.-C. Yeh, K. Kawagishi, T. Kobayashi, Y. Koizumi, T. Yokokawa, J.-X. Zhang, A 5th Generation Sc Superalloy With Balanced High Temperature Properties And Processability, Superalloys. (2008) 131–138.
- [4] H. Harada, N. Rene, High Temperature Materials for Gas Turbines: The Present and Future, Proc. Int. Gas Turbine Congr. 2003. (2003) 1–9.
- [5] J.H. Weber, M.K. Banerjee, Nickel-Based Superalloys: Alloying, Ref. Modul. Mater. Sci. Mater. Eng. (2016) 1–6. https://doi.org/10.1016/b978-0-12-803581-8.02573-x.
- [6] S. Gorsse, J.-P. Couzinié, D.B. Miracle, From high-entropy alloys to complex concentrated alloys [Des alliages à haute entropie aux alliages concentrés complexes], Comptes Rendus Phys. 19 (2018) 721–736.
- [7] B.S. Murty, J.W. Yeh, S. Ranganathan, P.P. Bhattacharjee, High-entropy alloys: basic concepts, High-Entropy Alloy. (2019) 13–30. https://doi.org/10.1016/b978-0-12-816067-1.00002-3.
- [8] E.P. George, D. Raabe, R.O. Ritchie, High-entropy alloys. Nat Rev Mater 4 (2019)515–534 . https://doi.org/10.1038/s41578-019-0121-4.
- [9] P.K. Huang, J.W. Yeh, T.T. Shun, S.K. Chen, Multi-principal-element alloys with improved oxidation and wear resistance for thermal spray coating, Adv. Eng. Mater. 6 (2004) 74–78. https://doi.org/10.1002/adem.200300507.
- [10] D.B. Miracle, O.N. Senkov, A critical review of high entropy alloys and related concepts, Acta Mater. 122 (2017) 448–511. https://doi.org/10.1016/j.actamat.2016.08.081.
- [11] B. Cantor, Multicomponent high-entropy Cantor alloys, Prog. Mater. Sci. 120 (2021) 100754. https://doi.org/10.1016/j.pmatsci.2020.100754.
- [12] N.D. Stepanov, N.Y. Yurchenko, V.S. Sokolovsky, M.A. Tikhonovsky, G.A.

- Salishchev, An AlNbTiVZr0.5 high-entropy alloy combining high specific strength and good ductility, Mater. Lett. 161 (2015) 136–139. https://doi.org/10.1016/j.matlet.2015.08.099.
- [13] N.D. Stepanov, D.G. Shaysultanov, G.A. Salishchev, M.A. Tikhonovsky, Structure and mechanical properties of a light-weight AlNbTiV high entropy alloy, Mater. Lett. 142 (2015) 153–155. https://doi.org/10.1016/j.matlet.2014.11.162.
- [14] O.N. Senkov, G.B. Wilks, J.M. Scott, D.B. Miracle, Mechanical properties of Nb25Mo25Ta 25W25 and V20Nb20Mo 20Ta20W20 refractory high entropy alloys, Intermetallics. 19 (2011) 698–706. https://doi.org/10.1016/j.intermet.2011.01.004.
- [15] O.N. Senkov, C.F. Woodward, Microstructure and properties of a refractory NbCrMo0.5Ta0.5TiZr alloy, Mater. Sci. Eng. A. 529 (2011) 311–320. https://doi.org/10.1016/j.msea.2011.09.033.
- [16] C.L. Tracy, S. Park, D.R. Rittman, S.J. Zinkle, H. Bei, M. Lang, R.C. Ewing, W.L. Mao, High pressure synthesis of a hexagonal close-packed phase of the high-entropy alloy CrMnFeCoNi, Nat. Commun. 8 (2017) 1–6. https://doi.org/10.1038/ncomms15634.
- [17] M.C. Gao, B. Zhang, S.M. Guo, J.W. Qiao, J.A. Hawk, High-Entropy Alloys in Hexagonal Close-Packed Structure, Metall. Mater. Trans. A Phys. Metall. Mater. Sci. 47 (2016) 3322–3332. https://doi.org/10.1007/s11661-015-3091-1.
- [18] Z. Li, F. Körmann, B. Grabowski, J. Neugebauer, D. Raabe, Ab initio assisted design of quinary dual-phase high-entropy alloys with transformation-induced plasticity, Acta Mater. 136 (2017) 262–270. https://doi.org/10.1016/j.actamat.2017.07.023.
- [19] L. Zhang, K. Qian, B. W. Schuller, Y. Shibuta, Prediction on Mechanical Properties of Non-Equiatomic High-Entropy Alloy by Atomistic Simulation and Machine Learning, Metals. 11(6) (2021) 922. https://doi.org/10.3390/met11060922.
- [20] V.K. Soni, S. Sanyal, S.K. Sinha, Microstructure and mechanical properties of non equiatomic FeCoNiCuMo high entropy systems, Adv. Mater. Process. Technol. 8 (2022) 147–160. https://doi.org/10.1080/2374068X.2020.1796166.
- [21] Y.H. Jo, K.Y. Doh, D.G. Kim, K. Lee, D.W. Kim, H. Sung, S.S. Sohn, D. Lee, H.S. Kim, B.J. Lee, S. Lee, Cryogenic-temperature fracture toughness analysis of non-equiatomic V10Cr10Fe45Co20Ni15 high-entropy alloy, J. Alloys Compd. 809 (2019) 151864. https://doi.org/10.1016/j.jallcom.2019.151864.
- [22] M.J. Yao, K.G. Pradeep, C.C. Tasan, D. Raabe, A novel, single phase, non-equiatomic FeMnNiCoCr high-entropy alloy with exceptional phase stability and tensile ductility, Scr. Mater. 72–73 (2014) 5–8. https://doi.org/10.1016/j.scriptamat.2013.09.030.

[23] W. Guo, J. Su, W. Lu, C.H. Liebscher, C. Kirchlechner, Y. Ikeda, F. Körmann, X. Liu, Y. Xue, G. Dehm, Dislocation-induced breakthrough of strength and ductility trade-off in a non-equiatomic high-entropy alloy, Acta Mater. 185 (2020) 45–54. https://doi.org/10.1016/j.actamat.2019.11.055.

- [24] S.S. Nene, K. Liu, M. Frank, R.S. Mishra, R.E. Brennan, K.C. Cho, Z. Li, D. Raabe, Enhanced strength and ductility in a friction stir processing engineered dual phase high entropy alloy, Sci. Rep. 7 (2017) 1–7. https://doi.org/10.1038/s41598-017-16509-9.
- [25] B. Yin, W.A. Curtin, Origin of high strength in the CoCrFeNiPd high-entropy alloy, Mater. Res. Lett. 8 (2020) 209–215. https://doi.org/10.1080/21663831.2020.1739156.
- [26] Y.F. Ye, Q. Wang, J. Lu, C.T. Liu, Y. Yang, High-entropy alloy: challenges and prospects, Mater. Today. 19 (2016) 349–362. https://doi.org/10.1016/j.mattod.2015.11.026.
- [27] F. Maresca, W.A. Curtin, Mechanistic origin of high strength in refractory BCC high entropy alloys up to 1900K, Acta Mater. 182 (2020) 235–249. https://doi.org/10.1016/j.actamat.2019.10.015.
- [28] Y. Xing, C.J. Li, Y.K. Mu, Y.D. Jia, K.K. Song, J. Tan, G. Wang, Z.Q. Zhang, J.H. Yi, J. Eckert, Strengthening and deformation mechanism of high-strength CrMnFeCoNi high entropy alloy prepared by powder metallurgy, J. Mater. Sci. Technol. 132 (2023) 119–131. https://doi.org/10.1016/j.jmst.2022.06.009.

Chapter 2

Literature review

2.1. History of high-entropy alloys

The name High-entropy alloys (HEAs) was coined by Prof. Jien Wei Yeh in 2004 [1]. Later these HEAs are also named as multi-principal element alloys (MPEAs) / Complex concentrated alloys (CCAs) [2]. In 2004, Prof. Brian Cantor published a similar work but named the studied material system as multi-component alloys [3]. It is expected that any invention will have some ancient roots; similarly, for this new class of alloys in the 18th century, German scientist Franz Karl Achard synthesized alloys with 11 elements (Fe, Cu, Pb, Bi, Sb, Zn, Ag, Co, Sn, As and Pt) in different combinations [4]. Efforts of Achard were not recognized as his complete results were in French. Later in 1966, Prof. C.S. Smith published a book mentioning the efforts of Achard [4].

2.2. Definition of high-entropy alloys

Since its inception, there has been a debate on the basic definition of HEAs. One set of researchers believed that entropy should be considered in defining the alloys, whereas another set of researchers said that composition should be considered while defining HEAs. Still, most of the research community believes that achieving a single phase instead of secondary phases/compounds is the primary criterion for obtaining high-strength HEAs. Three definitions are primarily in the discussion of the HEA community.

Prof. Jien Wei Yeh suggested a definition based on the composition chosen to fabricate the alloy. HEAs are those alloys designed with no bias between the five or more principal elements with an atomic percent ranging from 5 to 35 % [1]. In this primary definition of HEAs, there is no importance for entropy such that there is vast space to design these HEAs in the phase diagrams [5].

It is evident that based on equation (2.1) if the Gibbs energy of the alloy system is minimized, a thermodynamic equilibrium alloy system can be achieved. As a result, HEAs can also be defined based on the entropy value [5].

$$G = H - TS$$
(2.1)

Changes in Gibbs free energy of mixing can be written as:

$$\Delta G_{\text{mix}} = \Delta H_{\text{mix}} - T\Delta S_{\text{mix}}....(2.2)$$

 ΔG_{mix} : Enthalpy of mixing

 ΔS_{mix} : Entropy of mixing

The configurational entropy of an equiatomic alloy with n-elements can be derived as equation (2.3) based on the Boltzmann hypothesis.

$$\Delta S_{mix} = Rln(n) \dots (2.3)$$

R (gas constant): 8.314 J/mol K

n: number of elements

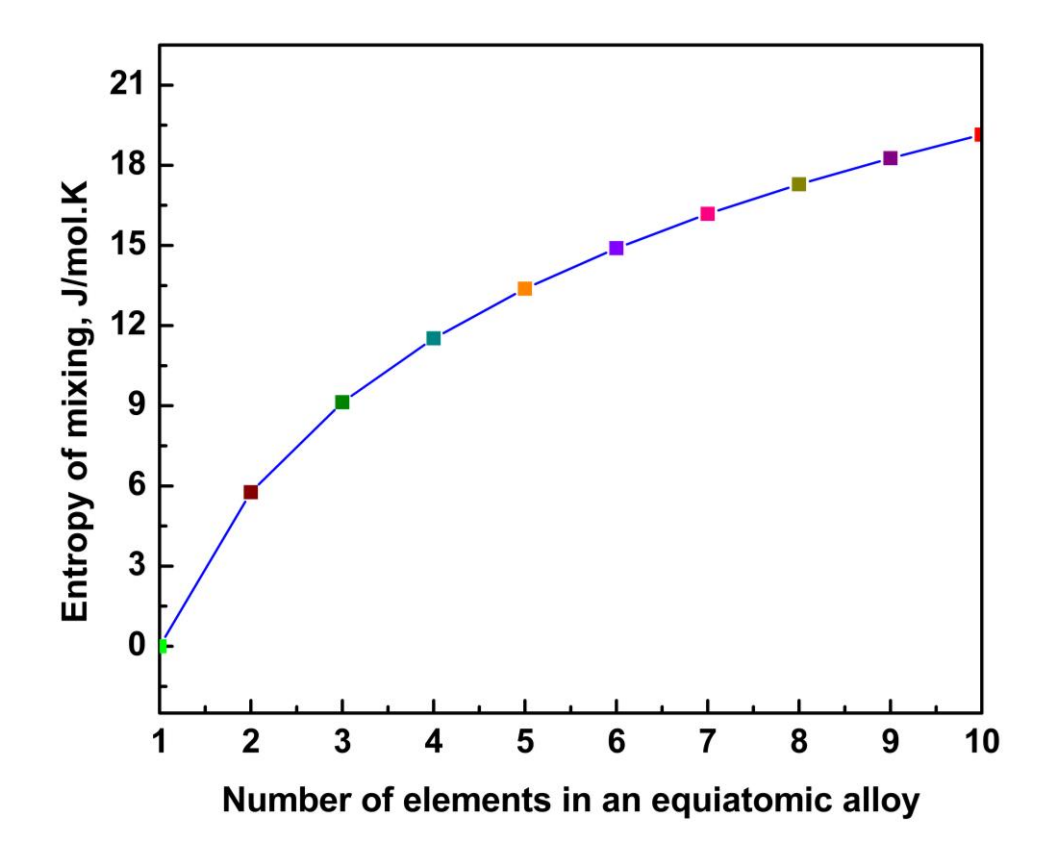


Fig. 2.1 Entropy of mixing for equiatomic alloys for different numbers of elements

In Fig. 2.1, it is shown that the entropy of mixing increases with the number of elements in equiatomic alloys which helps form a solid solution. The entropy of mixing value at 5 elements is considered a lower limit where the enthalpy of mixing will be counterbalanced, and Gibbs free energy will be minimized.

Equation 2.3 is used to classify the alloys based on the entropy of the equiatomic alloys, and it is as follows [6]:

Low Entropy Alloys: $\Delta S_{conf} \leq 0.69R$

Medium Entropy Alloys: $0.69R \le \Delta S_{conf} \le 1.61R$

High Entropy Alloys:
$$\Delta S_{conf} \ge 1.61R$$

Although the above classification is for alloys with equiatomic proportions, various non-equiatomic alloys also show extraordinary mechanical properties. Yeh suggested an equation to evaluate the configurational entropy for non-equiatomic systems, as shown in equation (2.4) [7].

$$\Delta S_{conf} = -R \sum_{i=1}^{n} c_i ln c_i....(2.4)$$

c_i: Atomic percent of the ith element

R: Gas constant

For an equiatomic alloy, the lower limit value for the entropy of mixing is 1.61R, where the enthalpy of the mixing counterbalances. As a result, for the non-equiatomic alloys, 1.5R (higher than the 1.39R corresponding to equiatomic quaternary alloy) was chosen as the lower limit nearer to 1.61R. Now the classification for the non-equiatomic alloys is as follows:

Low Entropy Alloys: $\Delta S_{conf} \leq 1R$

Medium Entropy Alloys: $1R \le \Delta S_{conf} \le 1.5R$

High Entropy Alloys: $\Delta S_{conf} \ge 1.5R$

Now from the above classifications, it is evident that alloys with 5 or more elements are considered High-entropy alloys, alloys with 3 or 4 elements are considered Medium Entropy Alloys, and alloys with 1 or 2 elements are considered Low Entropy Alloys.

2.3. Four core effects

In physical metallurgy, performance of any material will depend on the crystal structure, microstructure, processing route, and its properties, as illustrated in Fig. 2.2. Crystal structure and microstructure mainly depends on the composition of the material and processing route. Crystal structure and microstructure will decide the properties and influences the material's performance. Specifically to HEAs, the properties will be decided based on its four core effects in the below sections [5,8].

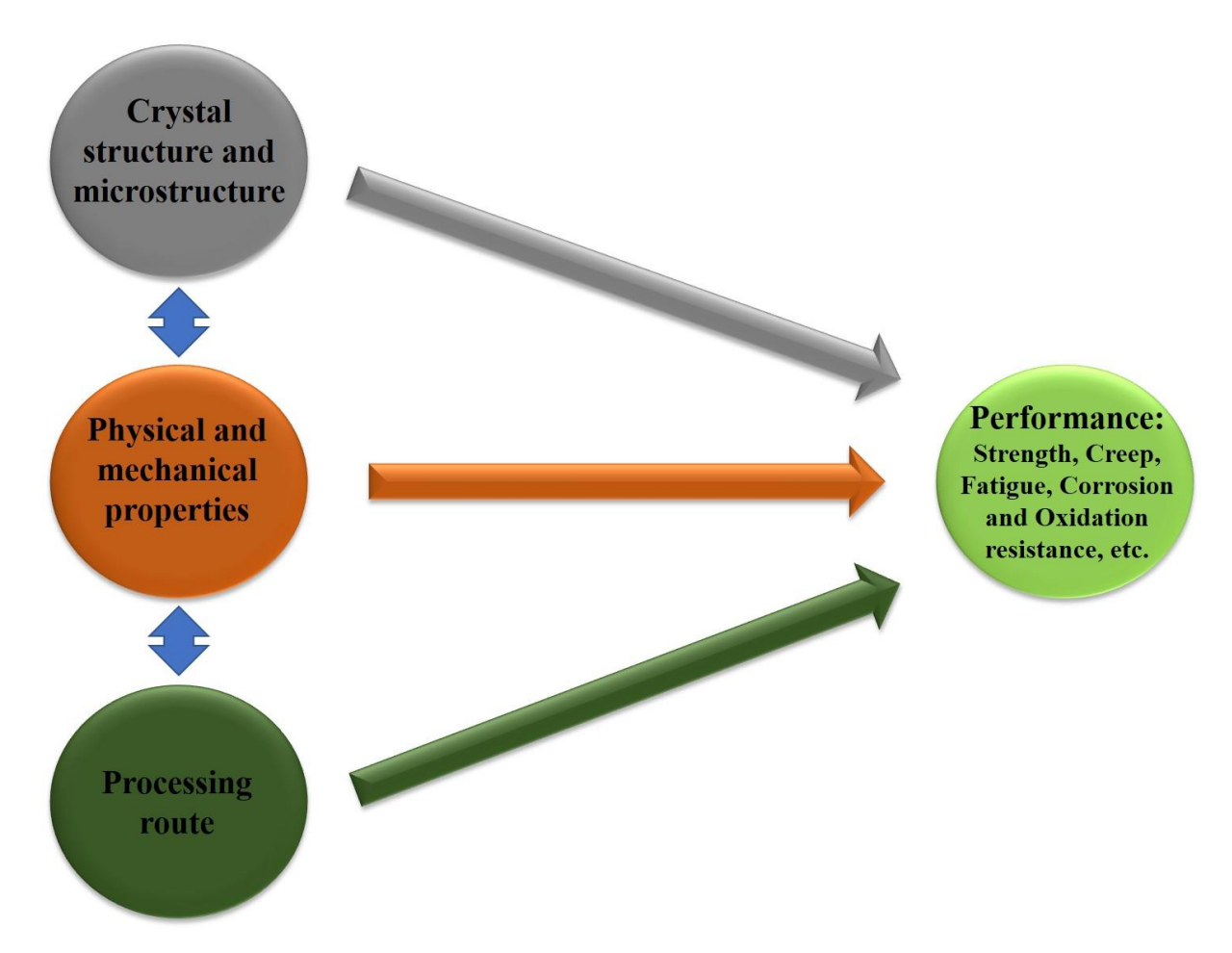


Fig. 2.2 Schematic representation showing the material's performance depends on the crystal structure, microstructure, properties, and processing route.

2.3.1. High-entropy effect

A higher configurational entropy with 5 or more elements may favour solid-solution phases instead of intermetallic phases, and this is known as a high-entropy effect [9]. It was expected earlier, before 2004, that more number of elements in an alloy might result in multi-phase structure and intermetallic phases; But surprisingly, these alloys mainly resulted in a single-phase due to high configurational entropy and minimized the Gibbs free energy [5].

2.3.2. Sluggish diffusion effect

Most of the HEAs research community believes that the diffusion process in the HEAs is slower than the various conventional alloys [8,10–12]. In HEAs, different sites have different local energies due to elements with different physical properties being located. This results in different types of bonding in the local sites. In conventional alloys, when the atoms jump from the high-energy site to the lower-energy site, there will be no variation in local atomic

configuration. The local atomic configuration will vary in the HEAs, and the atoms diffusivity is expected to be slower. It is also not a surprise in the HEAs that if atoms jump from a high-energy site to a lower-energy site, there is a chance of atoms rebounding to their original higher-energy site [8]. High concentrations and rebounding phenomenon may make the diffusion process sluggish in these HEAs. This sluggish diffusion also helps to hinder phase transformations.

Sluggish diffusion helps in the improvement of high-temperature mechanical properties like high temperature strength and creep resistance [8]. Hindrances in the diffusion of atoms are increased due to undulations of lattice potential energy. This results in the increment of activation energy in HEAs, which is why there is sluggish diffusion in HEAs [11]. However, the recent experimental investigations using tracer diffusion suggest that diffusion is not as sluggish as expected [13].

2.3.3. Lattice distortion effect

HEAs are prone to lattice distortion due to elements present of different atomic radii, which was explained in the schematic shown in Fig. 2.3. Specifically, BCC HEAs are more severely distorted [14–19]. In traditional alloys, the lattice sites will be occupied by principal elements, whereas in HEAs, elements with different atomic radii will occupy different sizes randomly. This random distribution of different size elements in different sites increases the lattice distortion in the alloy. This lattice distortion increment hinders the dislocation movement, thereby increasing the contribution of solid solution strengthening [14–19]. Single FCC phase HEAs show low strength compared to the BCC HEAs, but the strength of FCC HEAs will be higher than the conventional alloys with a single FCC phase due to severe lattice distortion [16,20]. In general, the intensity of XRD peaks in HEAs has a reduction, which was explained by Yeh et al. that lattice distortion and thermal effect are the reasons for the reduction of XRD intensity [21].

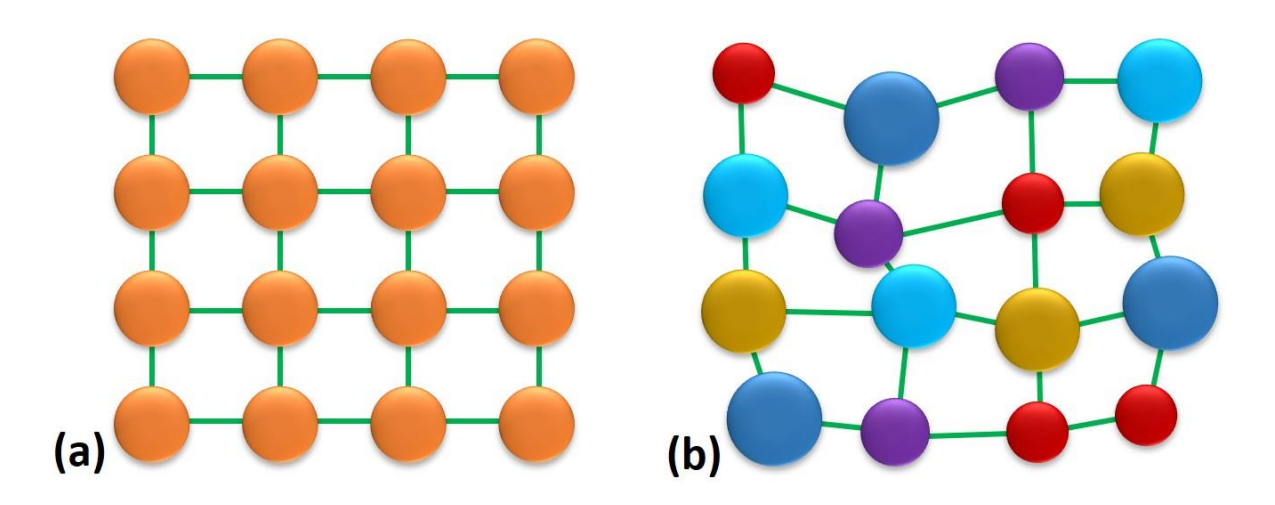


Fig. 2.3 Comparison of (a) pure metal lattice structure (b) severe distorted lattice structure of HEA.

2.3.4. Cocktail effect

Cocktail effect explains that the properties and microstructure of the alloy are the combinations of different elements present in the alloy [6]. Thus, it explains the reason for enhanced properties in these novel HEAs concepts. Although the term cocktail is not a technical term, it explains the reason for superior properties in HEAs in a descriptive manner [22]. Prof. Ranganathan also explains how an unexpected discovery of the new alloy design opens the space for superior properties for the materials community [5].

2.4. Phase prediction of HEAs

Before starting any experimental investigations, some theoretical calculations are necessary to minimize experimental errors and/or time scales of preparation. In physical metallurgy, the design of the alloy is critical to forecast the outcomes of the alloy development. The design includes whether the alloy forms a solid solution, the number of phases, etc. Specifically to HEAs, alloys consist of amorphous alloys, solid solution phases, and intermetallics. Especially solid solution phases are desirable to achieve extraordinary properties. As HEAs are concentrated alloys without a clue which solute and solvent elements are, it is difficult to predict the phases. Different methods to predict the phases are semi-empirical parameters [23,24] and computational methods. In the following sections, semi-empirical parameters and computational methods will be discussed.

2.4.1. Semi empirical parameters

Semi empirical parameters are designed mainly based on the Hume-Rothery rules. Here in this section, phase prediction based on the semi empirical parameters for HEAs will be discussed. In all the phase prediction models, few are parameter-based, and the remaining are free energy-based models [25]. Semi empirical parameters are like enthalpy of mixing (ΔH_{mix}), Omega parameter (Ω), the difference in atomic radius (δ) [8,23,26], and valence electron concentration (VEC) [9,12,27,28]. The procedure to calculate the parameters is discussed below.

The entropy of mixing value will be maximum for an equiatomic alloy. Therefore, HEAs show higher mixing entropy than conventional alloys. Comparison of (ΔH_{mix}) and (ΔS_{mix}) can decide the formation of the solid solution phase [27]. In different phases, the magnitude of (ΔH_{mix}) and (ΔS_{mix}) will overlap for HEAs. Atomic size mismatch of participating elements can improve the accuracy of phase prediction [29,30]. The difference in the atomic size enhances the lattice distortion in HEAs, thereby incrementing the strain energy. The atomic size difference in HEAs is very high; free energy will be increased, and the solid solution phase will be destabilized. Due to high lattice distortion, atoms favour order topologically, minimize energy, and lead to the formation of intermetallics [5,31]. Phase transformation will slow due to high activation energy from severe lattice distortion. This slow phase transformation leads to the formation of precipitates of nano size, amorphous phase, and elemental segregation. The atomic size difference is as follows:

$$\delta = \sqrt{\sum_{i=1}^{n} c_i \left(1 - \frac{r_i}{\bar{r}}\right)^2}...$$
(2.5)

 $\overline{r} = \sum_{i=1}^n c_i r_i$ (is the average atomic radius)

 c_i : Atomic percent of the i^{th} element

r_i: atomic radius of the ith element

The term ΔH_{mix} and δ decides whether the alloy forms a solid solution phase. If the atomic size difference $\delta \leq 6.6$, the alloy forms a solid solution phase.

$$\Delta H_{mix} = \sum_{i=1,\,i\neq j}^n \Omega_{ij} c_i\,c_j$$
(2.6)

$$\Omega_{ij} = 4\Delta H_{AB}^{mix} \qquad (2.7)$$

c_i: Atomic percent of the ith element

 c_i : Atomic percent of the j^{th} element

 ΔH_{AB}^{mix} : Enthalpy of mixing of binary pairs

With respect to ΔH_{mix} if the ΔH_{mix} value falls in the below-mentioned range, then the alloys form a solid solution phase.

$$-11.6 \text{ kJ/mol} \le \Delta H_{\text{mix}} \le 3.2 \text{ kJ/mol}$$

Zhang et al. introduced a new parameter (Ω) having a parameters ΔH_{mix} , ΔS_{mix} , and T_{m} . Zhang reported that the alloys form a solid solution phase if the Ω parameter falls in the range mentioned below.

$$\Omega \ge 1.1$$

$$\Omega = \frac{T_{\rm m}\Delta S_{\rm mix}}{|\Delta H_{\rm mix}|} \tag{2.8}$$

T_m: Melting temperature of the alloy

$$\Delta S_{mix} = -R \sum_{i=1}^{n} c_i lnc_i$$

c_i: Atomic percent of the ith element

R: Gas constant

 ΔH_{mix} : Shown in equation 2.6

Above mentioned parameters decide whether the alloy forms a solid solution, intermetallic or amorphous phase. To know the crystal structure of the alloy, Battezzati et al. [32] and Guo et al. [5,31] suggested a parameter valence electron concentration (VEC). The range of VEC decides the crystal structure of the alloy, whether it is a FCC, BCC, or HCP. The range of the VEC is mentioned below and formulae to evaluate the VEC.

VEC
$$\geq$$
 8.0 (Single FCC phase)
VEC \leq 6.87 (Single BCC phase)
VEC \approx 2.80 (Single HCP phase)
VEC $=\sum_{i=1}^{n} c_i$ (VEC)_i.....(2.9)

All the above mentioned semi empirical parameters can be used together to predict the phase and phase type of an alloy desired to manufacture. But the highest possible efficacy of the semi empirical parameters is only 72 % which is relatively low to depend only on these semi empirical parameters. Thus, these semi empirical parameters can only be used as a complementary method to other techniques for designing new alloys.

2.4.2. CALPHAD methods

Compared to the semi empirical parameters, it is known that CALPHAD calculations give the best phase prediction [5]. This is because CALPHAD involves so many thermodynamics databases generated using experimental outcomes. CALPHAD was unsuccessful for HEAs in the initial stages due to insufficient databases. Recently thermodynamic databases were

established for these novel HEAs. Thermo-Calc started its journey from the TCHEA1 database to now at the TCHEA6 database. Recently, CALPHAD was mainly used for various HEAs to understand the phase diagram and phase fraction plots before synthesizing the alloy.

2.5. Taxonomy of high-entropy alloys

High-entropy alloys are classified into many varieties based on the type of elements used, as shown in Fig. 2.4. From its inception in 2004, many different alloys were developed with vast compositional space. A wide variety of elements are used in developing HEAs, like transition metals, metalloids, alkaline earth metals, and non-metals [9]. Generally, based on the elements chosen from the periodic table, those are called that family of alloys. Various families of alloys are refractory HEAs, 3d transition alloys, light metal HEAs, precious metal HEAs, lanthanide transition HEAs, interstitial compound HEAs, and brass and bronze HEAs [9]. Among the mentioned HEAs above, the two most famous alloy families are the Cantor group (3d transition alloys) [3] and the Senkov group (refractory metals) [33]. In the present work, the alloy development is mainly focused on employing refractory metals, leading to the manufacturing of various refractory multi-principal element alloys.

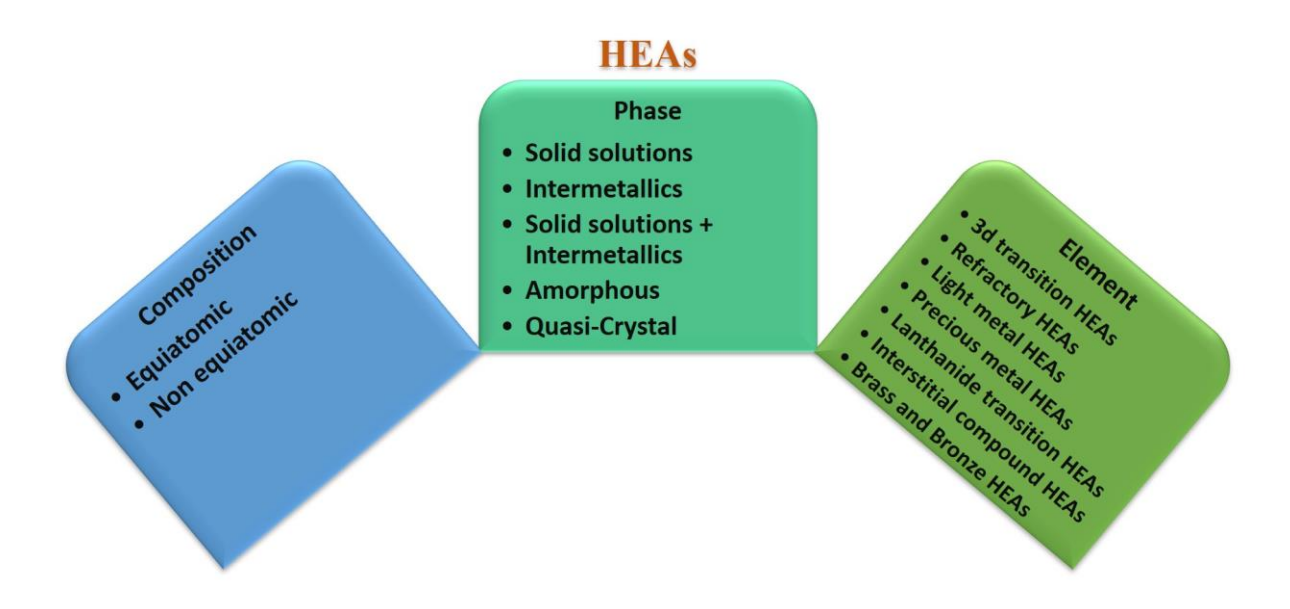


Fig. 2.4 Classification of HEAs based on composition, phase type, and elements used.

2.6. Expansion of high-entropy alloys field

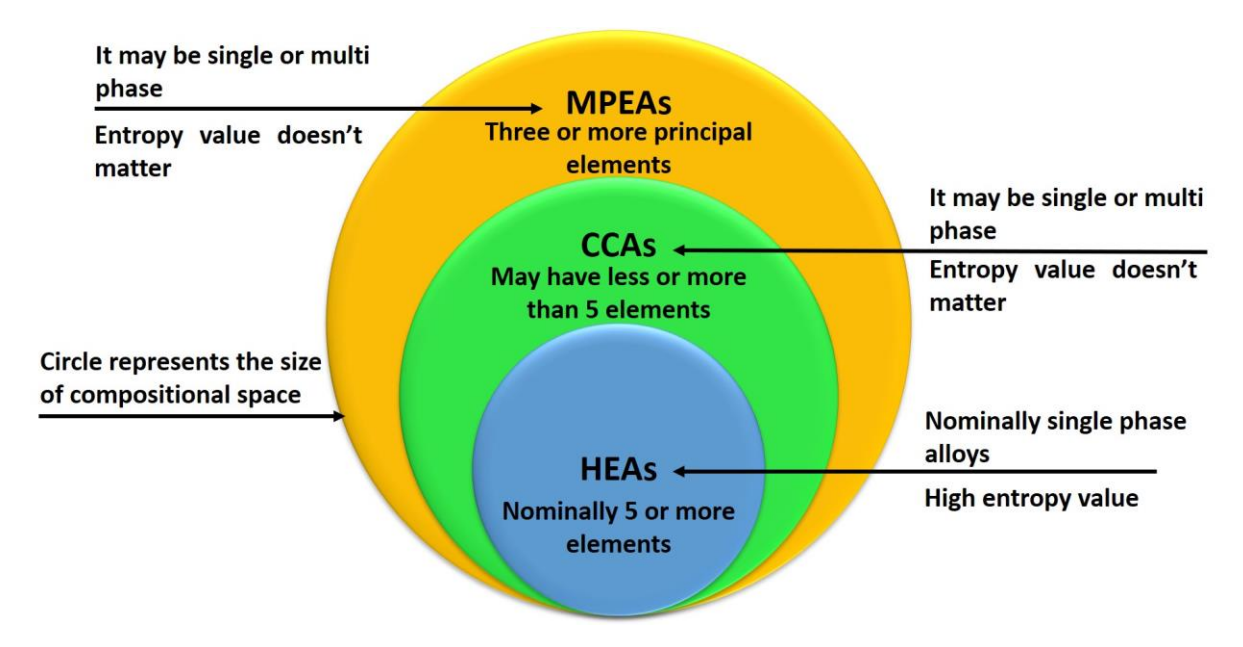


Fig. 2.5 Schematic showing the size of compositional space of different high-entropy alloys field

It is well known that after 2004 the research on high-entropy alloys had good attention in the scientific community [1,3]. Initially, these alloys are aimed only for the single phase because it is against the earlier (the year 2004) expectation of multi-phase structure and intermetallics. It is also that only equiatomic alloys were the attention with a single phase. Later researchers started developing non-equiatomic alloys with exceptional mechanical properties. With the advancement of the alloy design strategy, this high-entropy alloy field expanded to a large compositional space different from the initial high-entropy alloy definition, shown in Fig. 2.5. Many reports also aimed at the multi-phase structure in these alloys to improve the mechanical properties further, and composition concentration may be equiatomic or nonequiatomic. As a result, the initial definition of high-entropy alloys is unsuitable for the changes in new alloy designs. Therefore, they named them multi-principal element alloys (MPEAs) and complex concentrated alloys (CCAs). The new titles, like MPEAs and CCAs, have no restrictions on the number of participating elements and entropy value [34].

2.7. Refractory multi-principal element alloys

In 2010 refractory high-entropy alloys were introduced by Senkov et al. [33]. MoNbTaW was the first refractory HEA developed by the Senkov group with excellent mechanical properties. Later, many RHEAs/RMPEAs are developed with various refractory elements like Mo, Nb, Ta, Ti, W, Zr, Hf, V, and Cr. Generally, elements with melting points greater than the Fe melting point are called as high melting point elements [35]. These RMPEAs are mainly aimed for high-temperature applications. All the above are transition elements with high melting points, electrical resistance, and mechanical strength [35]. Till 2010 studies on these RMPEAs were not focused. Recently many researchers and this work also focused on the RMPEAs. In early 2004 the focus was only on the 3d transition elements to develop MPEAs.

2.7.1. Fundamental properties of refractory elements

This section will discuss all the properties of the refractory elements used in this work. Properties like density, atomic weight, melting point, crystal structure, lattice constant, Young's modulus, and atomic radius are shown in Table 2.1. In this work, the lowest melting point element used is Ti, whereas the highest melting point used is W. Similarly, the Lowest density element used is Ti and whereas W is the highest density element. The elements mentioned in Table 2.1 is used in various RMPEAs to achieve a high-strength material at high temperatures. Many reports suggested that these RMPEAs have great potential for aerospace applications [36–38].

Table 2.1 Physical properties of the most used refractory elements in the development of RMPEAs

Element	Crystal	Atomic	Atomic	Melting	Density	Lattice	Youngs's
	structure	radius,	weight,	temperature	(g/cc)	parameter	modulus
	@ 298	(Å)	(g/mol)	(K)		(Å)	(GPa)
	K						
Mo	BCC	1.36	95.95	2896	10.22	3.14	329
Nb	BCC	1.43	92.90	2750	8.57	3.30	105
Ta	BCC	1.43	180.95	3290	16.65	3.30	186
Ti	НСР	1.462	47.86	1941	4.51	2.95, 4.68	116
W	BCC	1.37	183.84	3695	19.25	3.16	411

2.7.2. Applications of refractory multi-principal element alloys

MoNbTaW is the first refractory alloy developed in 2010 by Senkov et al. [33]. This alloy exhibited extraordinary mechanical properties, as shown in Fig. 2.6, with the only concern being high density [33].

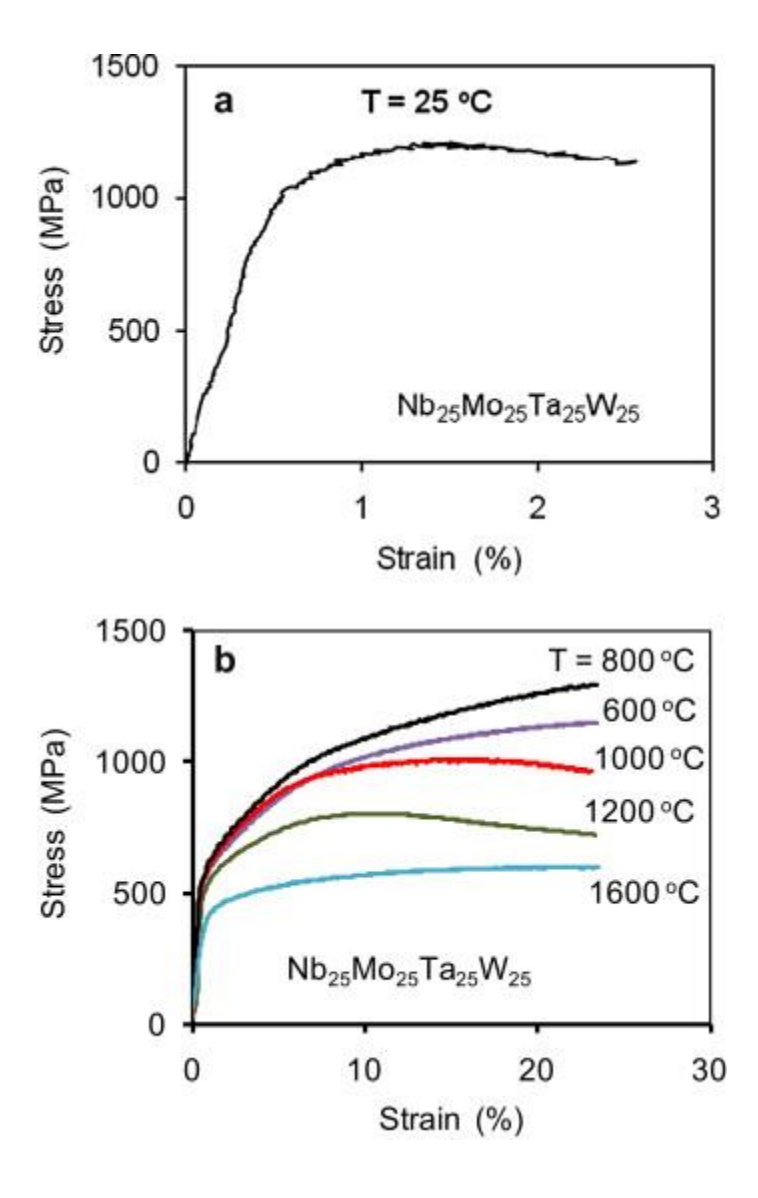


Fig. 2.6 Compressive strength of the equiatomic MoNbTaW alloy (a) room temperature and (b) elevated temperatures [39].

These RMPEAs, by the name itself, say that alloys are made up of refractory elements with high melting points. RMPEAs have great potential applications in aerospace and defence, where material undergoes extreme environments [40]. Most reports envisaged these alloys could be used as a structural material at high temperatures with extraordinary strength. These

alloys also exhibited good corrosion resistance that can be used in chemical industries for heat exchangers and gas turbine engines operating on the ground [36]. The recent interest in low-density RMPEAs is that these alloys can replace the superalloys of gas turbine engines in flight vehicles. In one most recognized RMPEA, MoNbTaW has good high-temperature strength, yet this alloy has a drawback of high density. This hinders its usage for flight vehicle applications. Few researchers explored the possibility of decreasing the overall density by altering the composition of the alloy using another low-density element addition. D G Kalali et al. developed a high-strength, low-density alloy MoNbTaTiW based on the MoNbTaW alloy where Ti has been added [41]. Nuclear power plants also require these high-strength materials to sustain high temperatures. Vanadium was focused on developing HEAs for nuclear applications [42]. Two such alloys, VCrMnTi and VCrMn are developed and investigated due to low activation elements [42]. Both alloys resulted in a single BCC phase favorable for fusion reactor applications. Some other RMPEAs have also shown some favorable conditions for nuclear applications [43–45]. Few limited room temperatures applications like WC-based drill bits and medical applications are not explored effectively [46,47].

2.7.3. Mechanical properties of refractory multi-principal element alloys

Since the inception of high-entropy alloys in 2004, the primary interest of these alloys has been extraordinary mechanical properties [1,3]. From 2010 RMPEAs showed extraordinary hightemperature mechanical properties [33]. RMPEAs have a good scope of application in flight vehicle parts operating at high temperatures. The Interest of research on RMPEAs has increased globally, and the focus of the present study is also on RMPEAs. Senkov et al. introduced two novel RMPEAs, MoNbTaW and MoNbTaVW, with extraordinary mechanical properties [39]. Two are the BCC alloys with a microhardness value of 4.45 GPa and 5.25 GPa for the MoNbTaW and MoNbTaVW alloys, respectively [39]. Hardness increment in the MoNbTaVW is due to the element V with smaller atomic radii enhancing the lattice strain in the lattice. Solid solution strengthening was also enhanced due to variations in atomic radius and elastic modulus between the participating elements after the addition of V. Hightemperature compressive strengths are also evaluated from room temperature to 1600 °C. At 1600 °C the compressive yield strength of the MoNbTaW is 405 MPa, whereas the compressive yield strength of the MoNbTaVW is 477 MPa. The compressive yield strength decreases from room temperature to 1600 °C, but the strength at 1600 °C is high compared to various conventional or superalloys as shown in Fig. 2.7.

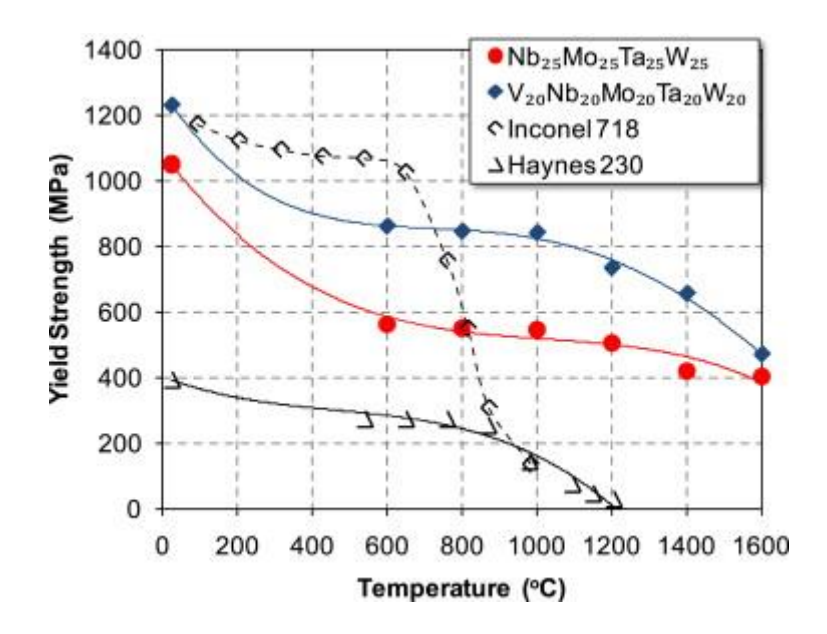


Fig. 2.7 Compressive yield strength of the MoNbTaW and MoNbTaVW at different temperatures compared with Haynes 230 and Inconel 718 superalloys [39].

After 2011, several alloys based on MoNbTaW were discussed in the literature. One such quaternary alloy is MoNbTaV which showed excellent mechanical properties superior to MoNbTaW alloy [48]. The yield strength of the MoNbTaV (1.5 GPa) is more than the yield strength of the MoNbTaW (1 GPa). Microhardness of both the alloys is 4.94 GPa and 4.45 GPa for the MoNbTaV and MoNbTaW, respectively. Ti is also added to the MoNbTaW alloy to improve the plastic strain of the MoNbTaW alloy, which was very low (1.5 %). Now the compressive yield strength of the MoNbTaTiW alloys resulted in 1455 MPa, which was far higher than the MoNbTaW alloy (996 MPa). In most RMPEAs, the strengthening is contributed to solid solution strengthening due to lattice distortion. Since 2010 many studies based on the MoNbTaW alloy have been discussed in the literature with superior mechanical properties [49–54]. Some review papers also discussed the mechanical properties of the various RMPEAs [35,55,56].

Dasari et al. [57] developed two alloys, Al_{0.5}NbTa_{0.8}Ti_{1.5}V_{0.2}Zr and Al_{0.5}Mo_{0.5}NbTa_{0.5}TiZr, that imitate the microstructure of Ni-based superalloys, with a matrix phase of ordered BCC consisting of a disordered BCC precipitate as shown in Fig. 2.8. The spinodal decomposition of phases is explained using the free energy diagrams. This spinodal decomposition has an implication on the mechanical properties.

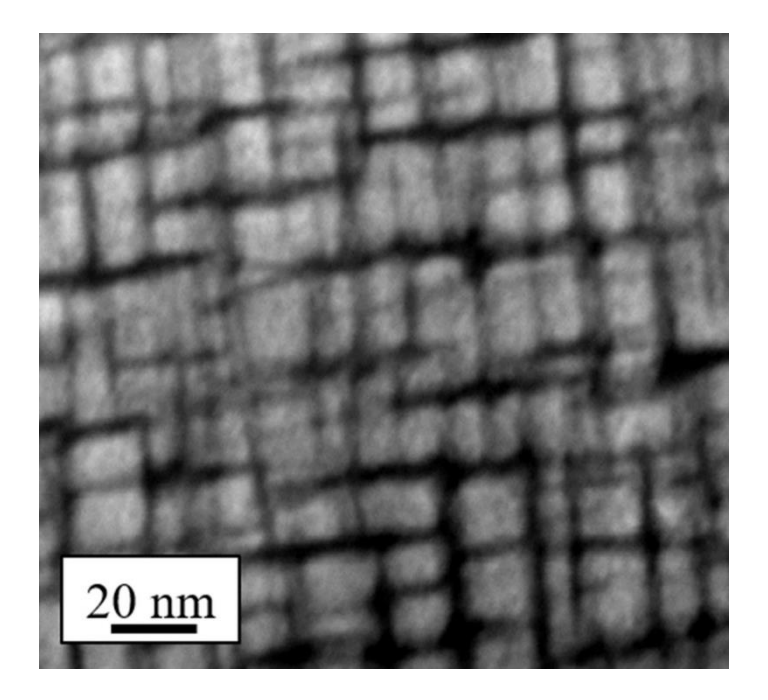


Fig. 2.8 High-angle annular dark-field scanning transmission electron microscopy micrograph of Al_{0.5}NbTa_{0.8}Ti_{1.5}V_{0.2}Zr alloy showing the BCC + B2 checkered pattern similar to Ni-based superalloy [57].

Couzinié et al. [58] discussed the high-temperature (600 °C) deformation mechanisms in a Al_{0.5}NbTa_{0.8}Ti_{1.5}V_{0.2}Zr alloy with BCC+B2 microstructure. The compressive yield strength of the alloy at 600 °C is 1186 MPa after a true strain of 0.047. The compressive yield strength of the Al_{0.5}NbTa_{0.8}Ti_{1.5}V_{0.2}Zr alloy is far better than the alloys with single BCC phase such as MoNbTaW (561 MPa) and MoNbTaVW (862 MPa).

2.8. Indentation size effect in refractory multi-principal element alloys

Understanding the mechanical behaviour of novel materials is essential to step further into application. It is always curious to understand the length-scale mechanical properties as microstructural features always influence mechanical properties. It is well known that the mechanical properties of micro/macro size features are well addressed in the literature. It is clear that the strength of the material changes when the feature size is less than 100 nm. From the well-known Hall-Petch effect, it is clear that if the microstructural feature is in the nm regime, the strength of the material increases when compared to the counterpart material with a micron regime feature size. It is known that the increment in the strength will be seen when the indented volume is very low, and the deformation happens under limited defects.

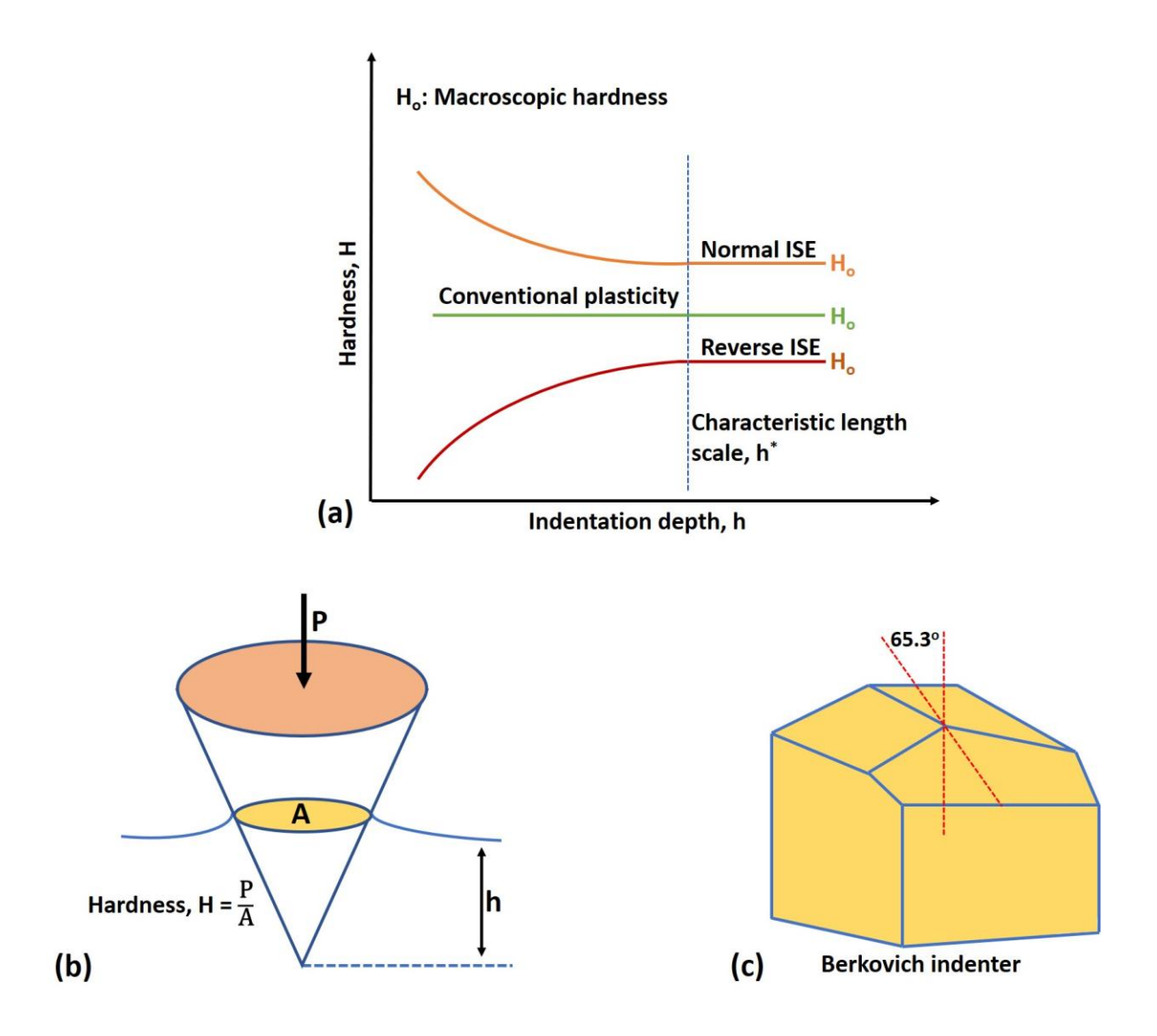


Fig. 2.9 Schematic showing (a) Variation of hardness with the increase in indentation depth (Normal ISE, Conventional plasticity, and Reverse ISE) (b) Hardness is the ratio of indentation load and projected area (c) Berkovich indenter with a half angle of 65.3°.

While performing the indentation, a size-dependent phenomenon can be observed with a decrease in indentation load, and the hardness will be increased. This phenomenon is called as indentation size effect [59]. This is often observed while using self-similar indenters like cones and pyramids [60–62], where hardness is the ratio of applied load to the projected contact area. In some instances, hardness decrement is also observed with the decrease in the indentation load, and it is termed reverse ISE, shown in Fig. 2.9 [63–66].

Chen and Hendrickson [65] performed indentation studies on the high-purity Ag. In this study, it is observed that Vickers hardness is increased with the indentation depth, whereas deceased

at the smaller depths. Hardness is evaluated using the measurement of the plastic residual

contact that appeared after indentation using the geometrically self-similar diamond indenter (centreline to face angle is 68°) [65–68]. It is known that from the conventional plasticity theory, there should not be any variation in the hardness with the indentation depth [66]. Initially, it was presumed that the reason for the ISE during indentation was sample surface preparation problems like hard surface oxides, surface roughness, and tip blunt of the indenter instead of actual material effect [69]. To understand the actual reasons for the ISE, indentation experiments are conducted on various noble metals for which a proper sample surface is maintained. These studies show that the actual reason for ISE is more fundamental than surface roughness problems [69]. Some researchers reported that the limited number of dislocations participating in the deformation during small load indentation is the reason for ISE [64,66]. After the entry of nanoindentation instruments in the research community, research interest in understanding the ISE was started again in the 1990s. Most of the research on ISE was established from 1950 to the 1970s [61,70–75]. The indent residue impression will be measured using imaging techniques in the Vickers hardness to estimate the hardness of the material. In the nanoindentation, the indent impression is measured from the indentation load (P) indentation depth (h) curves obtained from the nanoindentation experiments. This nanoindentation technique helped researchers to estimate the hardness of small volumes of the order of a few nm [74]. MacElhaney et al. showed a procedure to obtain the ISE data from the indentation experiments [76]. MacElhaney et al. performed the experiments with a Berkovich indenter (Shown in Fig. 2.9.) on single crystal Cu (1 1 1). Berkovich indenter and Vickers indenter have the same area-to-depth relationship. This resulted in using Berkovich indenter in nanoindentation experiments which avoids the damage of chisel edge tip defect. This edge tip defect will destroy the geometric self-similarity at smaller depths. Among the various fundamental reasons, strain gradient plasticity theory well explains the ISE

Among the various fundamental reasons, strain gradient plasticity theory well explains the ISE [77]. Strain gradient plasticity has been reported in various conventional dilute materials, including single crystals, polycrystalline materials, solid solutions, etc. [78,79], and was explained by the model proposed by Nix and Gao [80]. Recently ISE is also explained in a few MPEAs based on the strain gradient plasticity theory [81,82]. According to the Nix-Gao model [80], the characteristic nature of depth-dependent hardness can be written as

$$\frac{H}{H_0} = \sqrt{1 + \frac{h^*}{h}}.$$
 (2.10)

$$H_0 = 3\sqrt{3}\alpha Gb\sqrt{\rho_{SSD}}....(2.11)$$

$$h^* = \left(\frac{81}{2}\right) b\alpha^2 \tan^2\theta \left(\frac{G}{H_0}\right)^2 \dots (2.12)$$

Where H is hardness at a given depth (h), H_0 is a depth-independent hardness that arises only from statistically stored dislocations; h^* is the length scale that characterizes the depth dependence of hardness and is influenced by the shape of the indenter, shear modulus (G) and H_0 . As H_0 is influenced by the density of statistically stored dislocations (ρ_{SSD}), h^* can't be considered as a constant, and α is a constant of 0.5.

2.9. Strengthening mechanisms in refractory multi-principal element alloys

Mechanical properties of the materials can be tailored with the help of various strengthening contributions involved in the materials. Literature suggests that strengthening mechanisms of the conventional materials can be used/extrapolated to the MPEAs.

- Reduction of grain size[83,84].
- Inducing the short-range order clusters into the matrix of the material [85,86].
- Distribution of nano precipitates into the matrix of the material [18,87,88].
- Enhancement of the dislocation density [89].
- Improving the nano twins density [90–92].

All the above techniques will enhance the following strengthening contributions to enhance the strength of the material. Major strengthening contributions like frictional stress, Hall-Petch strengthening, Taylor hardening, and Solid solution strengthening will be discussed in detail.

2.9.1. Frictional stress

Strengthening contribution from the frictional stress is arises from the inherent resistance offered by the lattice to the mobile dislocations. In these novel MPEAs, the everchanging chemical nature at the atomic scale is expected to offer enhanced resistance to mobile dislocations in comparison to the lattice of pure metals. The data for the frictional stress of the individual elements is well addressed in the literature [93], whereas frictional stress for the novel MPEAs is not available in the literature. In the present work, the frictional stress of the various alloys is calculated using the rule of mixtures procedure, a similar procedure followed elsewhere [41,94,95]. Frictional stress (σ_0) is calculated using equation 2.13.

$$\sigma_0 = \Sigma \left(c_i \times \sigma_o^i \right)$$
....(2.13)

 c_i : Atomic percent of the i^{th} element

 $\sigma_o^i \colon \text{Frictional stress of the } i^\text{th} \text{ element at room temperature}$

2.9.2. Hall-Petch strengthening

Hall-Petch strengthening/Grain boundary strengthening significantly contributes to the strength of the alloy among various strengthening contributions. E.O Hall and N.J Petch, two pioneers in the field, deduced a theory of Hall-Petch strengthening that how the strength of the alloy varies with change in the grain size [96–100]. Hall-Petch strengthening states that the volume fraction of grain boundaries will be high in the alloy if the grain size is small, enabling them to act as a barrier to the dislocation movement as shown in Fig. 2.10. Random orientation of atoms in the grain boundaries hinders the movement of dislocation and thereby increases the strength of the material, which can be seen in equation 2.14. Extensive experimental investigations over several decades on wide variety of metals and alloys resulted in the pictorial representation of influence of grain size on yield strength as shown in Fig. 2.11. From the microcrystalline regime to an average of grain size 100 nm, the Hall-Petch type of behaviour was observed, whereas between the grain sizes 100 nm to 10 nm, strength enhancement was seen with decrement in grain size but with a different Hall-Petch slope at grain sizes of around 10 nm and below a negative Hall-Petch slope was observed in such metals and alloys indicating negative Hall-Petch behaviour.

$$\sigma_y = \sigma_o + \frac{k}{\sqrt{d}} \dots (2.14)$$

 σ_{v} : Yield strength of the alloy

 σ_0 : Frictional stress of the alloy

k: Hall-Petch constant

d: Grain size of the alloy

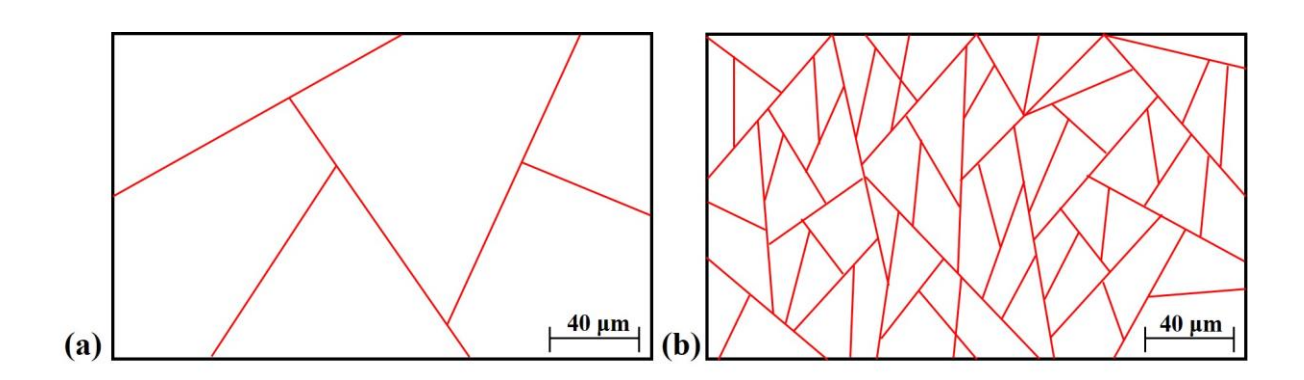


Fig. 2.10 Schematic showing (a) coarse grain size and (b) finer grain size. In fig 2.9 (b) it is clear that at finer grain size the number of obstacles in the form of grain boundaries will be more for the mobile dislocations that leads to strength enhancement.

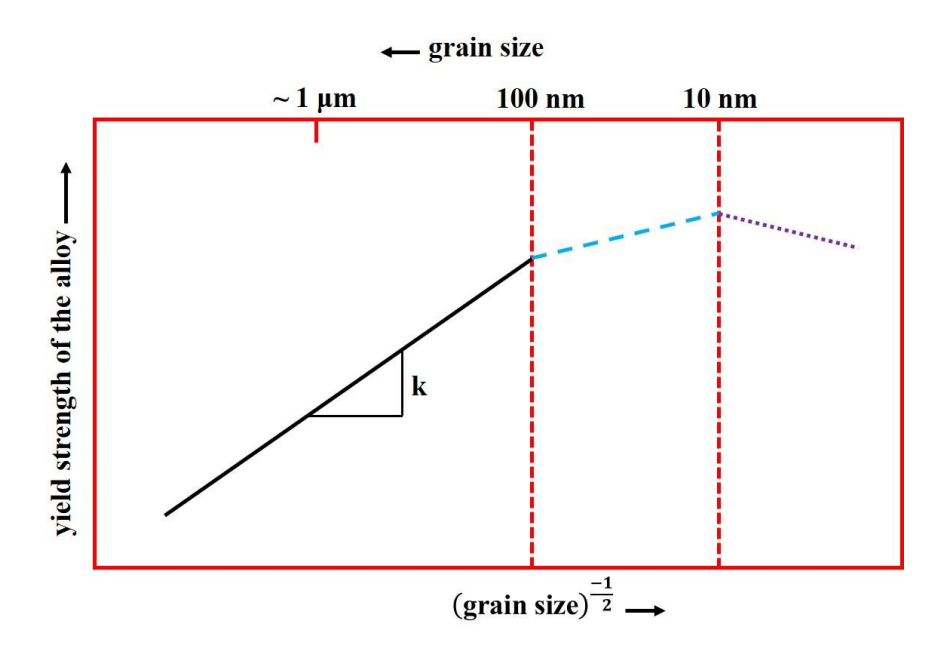


Fig. 2.11 Schematic representation of yield strength of the alloy as a function of grain size.

Dislocations pileup near the grain boundaries and develop stress on the dislocation near the grain boundary, which influences the easy movement of the dislocation to the next grain in the large grain-size alloys. The dislocation pileup in the alloy with smaller grains will be minimal; therefore, the grain boundary hinders dislocation movement to the adjacent grain.

Liu et al. fabricated ultra-fine MoNbTaTiV RMPEA using mechanical alloying with subsequent Spark Plasma Sintering to take advantage of grain boundary and solid solution strengthening [101]. MoNbTaTiV alloy sintered at a temperature of 1600 °C and achieved two phases with average grain sizes of 0.58 μm and 0.18 μm. The microhardness is exceptionally high, with a value of 524 HV. Qing Liu et al. reported that high strength is attributed to Hall-Petch and Solid Solution Strengthening. Opting for the powder metallurgy route is always desirable to achieve the alloy with finer microstructural features.

Pan et al. fabricated MoNbTaW and Mo₂₃Nb₂₃Ta₂₃W₂₃Ti₈ RMPEAs using the MA+SPS route [102]. After sintering the alloys, they achieved a grain size of less than 1 μm. The microhardness of the MoNbTaW alloy using the MA+SPS route is 7.78 GPa, which is much higher than the similar alloy developed using the melting and casting route [49]. This indicates

how the grain size influences the strength of the alloy. In the present thesis work, one of the significant contributions is from the Hall-Petch strengthening.

2.9.3. Taylor hardening

Taylor hardening is also known as strain hardening and dislocation hardening. Taylor hardening contributes to overall strengthening when dislocation-dislocation interactions take place during the deformation of the alloys. Taylor hardening can be estimated using equation 2.15 mentioned below.

$$\Delta\sigma_{SH} = M\alpha Gb\sqrt{\rho_{SSD}}....(2.15)$$

M: Taylor factor (=3.06 for both BCC and FCC alloys)

α: Correction factor is taken as 0.3

G: Shear modulus $\left(=\frac{E}{2(1+\theta)}\right)$

E: Elastic modulus

θ: Poissons ratio

b: Burgers vector ($|\mathbf{b}| = \frac{a}{2}\sqrt{3}$ for BCC and $|\mathbf{b}| = \frac{a}{2}\sqrt{2}$ for FCC)

 $\rho_{SSD} :$ Statistically stored dislocations ($\rho_{SSD} = 2\sqrt{3} \, \frac{\epsilon}{Db})$

ε: Lattice microstrain

D: Grain size of the alloy

Duan et al. fabricated a MoNbTaTiVZr RMPEA using vacuum arc melting and subsequent high-pressure torsion (HPT) at room temperature [103]. The corresponding alloy resulted in a dual-phase (BCC + BCC) structure, one with Zr rich and another with Zr depleted. In general HPT process is used for grain refinement and increasing the dislocation density. In the MoNbTaTiVZr RMPEA, no new phases are observed after the HPT, but the grain refinement has happened, and an increment in the dislocation density is observed. Thus increment in the dislocation density is directly proportional to Taylor hardening, and the alloy showed excellent hardness with enough contribution of Taylor hardening.

Wu et al. fabricated a novel Hf₂₅Nb₂₅Ti₂₅Zr₂₅ RMPEA using a vacuum arc melting route [104]. After XRD analysis in the as-cast and heat treatment conditions, a single BCC phase was observed. There was no change in the crystal structure after the homogenization. Interestingly, the yield strength and ultimate tensile strength of the alloy are much higher than most of the FCC HEAs. A TEM study has been performed after preparing the electron transparent region using ion milling to understand the mechanism in detail. During the tensile deformation process

in the alloy mentioned above, dislocation multiplication (Taylor hardening) helped in the improvement of the plasticity in the alloy.

2.9.4. Solid solution strengthening

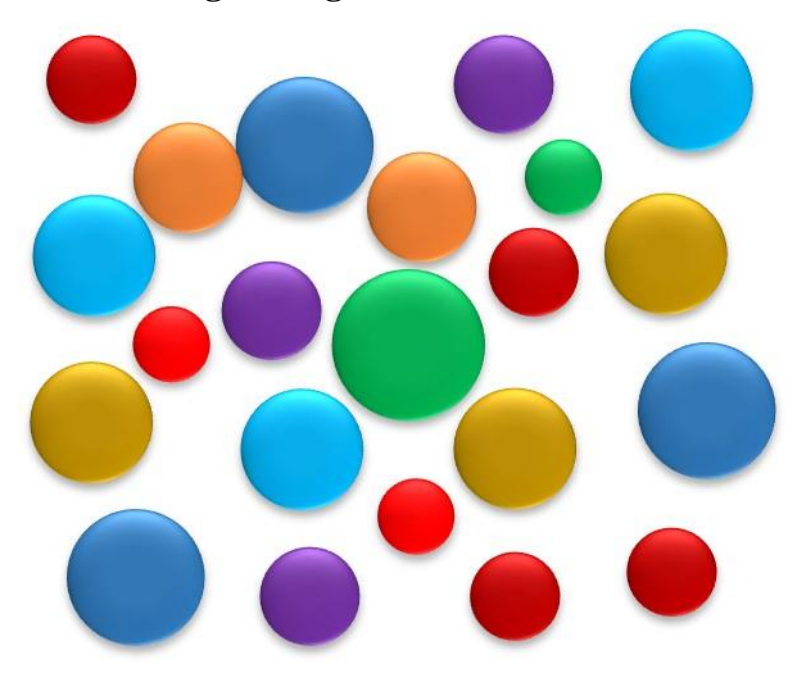


Fig. 2.12 Atoms in the multi-principal element alloy are distributed randomly, increasing the lattice distortion and hindering the movement of the dislocations, thereby enhancing the solid solution strengthening of the alloy.

Fig. 2.12. shows that in the MPEA, atoms are randomly distributed in the lattice, which imparts the lattice distortion and increases the strength of the alloy. In conventional alloys, the solute atoms increase the lattice distortion to some extent which increases the strength of the alloy. In MPEAs, the concentration of different elements is high, so it is impossible to define solute and solvent in the composition. Solid solution strengthening has been expected to be the predominant contribution in these MPEAs because these are highly concentrated solid solutions. The differences in the atomic radii and shear moduli values of the respective individual elements are believed to contribute to the overall solid solution strengthening of the MPEAs. Methodology for the theoretical calculation of SSS was initially offered by Labusch [105,106], and the same was utilized for several MPEAs [52,107], If an alloy has 'n' elements, there will be a strengthening contribution from each element for the SSS. SSS of the ith element is given by

$$\Delta \sigma_{i} = AGf_{i}^{\frac{4}{3}}c_{i}^{\frac{2}{3}}...$$
 (2.16)

c_i: Atomic percent of the ith element

A: Material constant with a value of 0.04 [108]

f_i: Mismatch parameter of the ith element

$$f_i = \sqrt{\delta_{Gi}^2 + \alpha^2 \delta_{ri}^2}.$$
 (2.17)

 $\delta_{ri} \text{:}$ Atomic size mismatch parameter of the i^{th} element

 δ_{Gi} : Atomic modulus mismatch parameter of the i^{th} element

α: 9, interaction force between the screw and edge dislocations with the solute atom

For BCC, $\delta_{ri} = \frac{9}{8} \Sigma C_j \delta_{rij}$, the i^{th} atom will have 8 nearest neighboring atoms in a BCC lattice, therefore the fraction $\frac{9}{8}$ is considered. For FCC, $\delta_{ri} = \frac{13}{12} \Sigma C_j \delta_{rij}$, the i^{th} atom will have 12 neighboring atoms in a FCC lattice, therefore the fraction $\frac{13}{12}$ is considered.

Similarly, atomic modulus mismatch was also calculated using the below formulae

For BCC,
$$\delta_{Gi} = \frac{9}{8} \Sigma C_j \delta_{Gij}$$
; For FCC, $\delta_{Gi} = \frac{13}{12} \Sigma C_j \delta_{Gij}$

Atomic radii mismatch and atomic modulus mismatch for various binaries can be calculated by using the following formulae:

$$\delta_{rij} = \frac{2 \times (r_i - r_j)}{(r_i + r_i)}; \qquad \qquad \delta_{Gij} = \frac{2 \times (G_i - G_j)}{(G_i + G_i)}$$

 r_i is the atomic radius of the respective element. G_i is shear modulus of the respective element. Using Gypen and Deruyttere approach [109], the SSS of the corresponding can be calculated using the below formulae mentioned in the

$$\Delta \sigma_{\rm sss} = \left(\Sigma \Delta \sigma_{\rm i}^{\frac{3}{2}} \right)^{\frac{2}{3}} \tag{2.18}$$

Liu et al. fabricated a novel NbTaHfZrTi RMPEA with a single BCC phase, which exhibited a moderate yield strength [110]. To further enhance the strength of the alloy using the concept of solid solution strengthening, authors added Fe (smaller atomic radii compared to other participating elements) into the alloy, which enhanced the yield strength up to 970 MPa (approx.). This didn't show any effect on the strain of the alloy, which is 17.5 % (approx.). But due to the addition of Fe, after some aging treatment, new brittle Hf₂Fe precipitates are formed, which shows an effect on the ductility of the alloy.

Wang et al. fabricated a series of novel lightweight Zr_{1.2}V_{0.8}NbTi_xAl_y (Ti_xAl_y) RMPEAs [111]. In this series of alloys, authors modified the concentration of the Ti and Al of the alloy mentioned above to suppress the B2 and C14 precipitates. Among various alloys, Ti_{3.6}Al_{0.6} alloy showed specific yield strength of 40 % more than the other developed series of alloys. Wang et al. reported that this high strength in the alloy is due to solid solution strengthening resulting from the lattice distortion in the alloy and short-range chemical ordering.

2.9.5. Twin boundary strengthening

Twinning results in the formation of the twin boundaries within the crystal, forming another crystal within the primary crystal [112]. Different types of twin formation are possible, such as during the growth of the crystal, due to the mechanical loading and due to the annealing treatments to the material [112,113]. Twin boundaries that separate the primary crystal can hinder the dislocation motion and thus help in the improvement of the strength of the material, as shown in Fig. 2.13

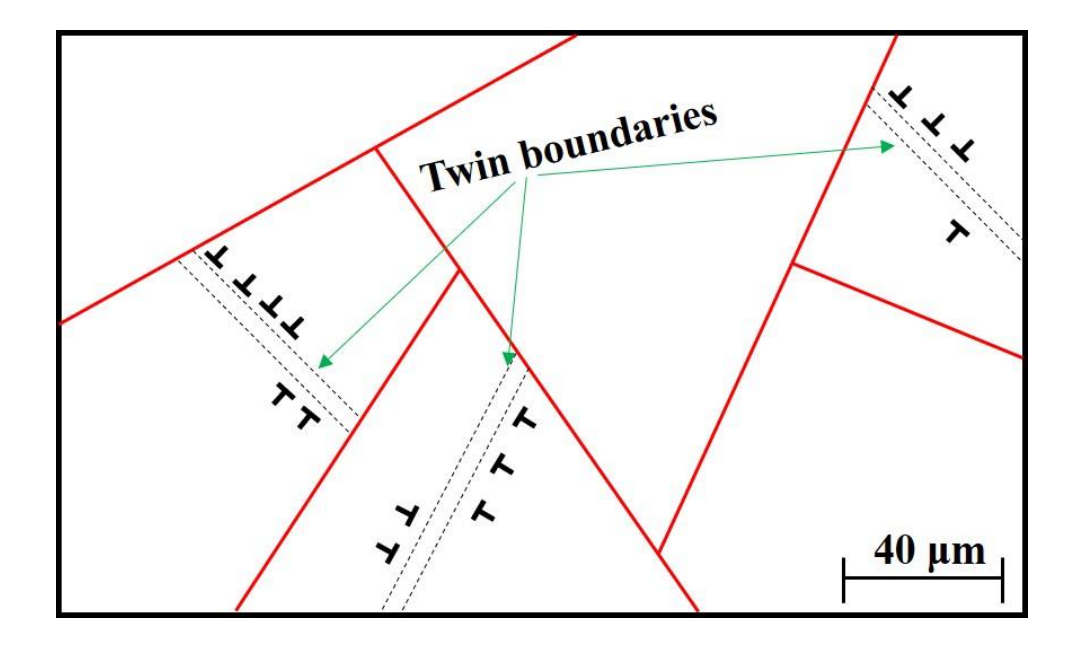


Fig. 2.13 Schematic to show how dislocations are hindered at twin boundaries

2.9.6. Precipitation strengthening

Precipitate formation in the matrix hinders the dislocation motion [114]. During the dislocation movement through the precipitate, it may bypass the precipitate by forming the loop or cutting it. Dislocation shears the precipitate when the size of the precipitate is small, thus providing

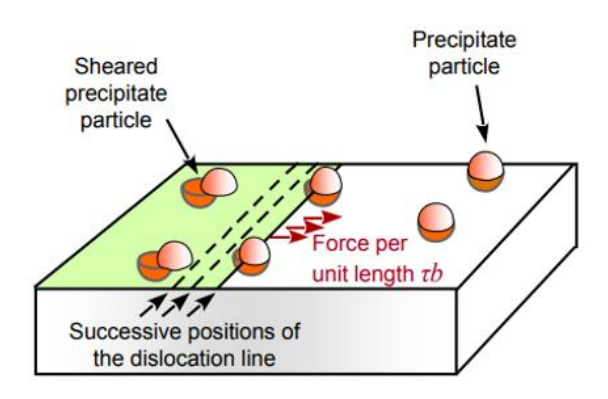
strengthening. If the size of the precipitate is above a certain size, dislocation forms a looping around the precipitate instead of shearing. Orowan stress, the stress required to move the dislocation between the precipitates separated by a distance 'L' is given by equation (2.19)

$$\tau_o = \frac{Gb}{L} \dots (2.19)$$

G: Shear modulus

b: Burgers vector

L: Precipitate spacing



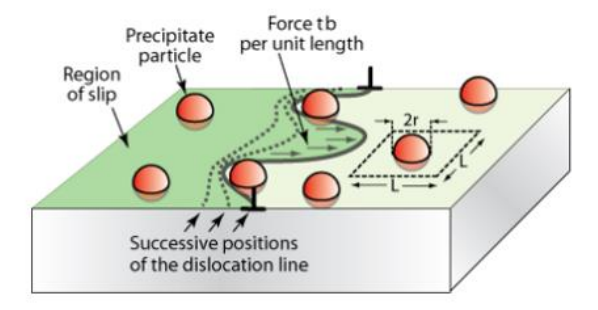


Fig. 2.14 Schematic of precipitation hardening mechanism [114]

2.9.7. Dispersion strengthening

In the dispersion strengthening mechanism, metallic material is added to the matrix as a dispersoids to strengthen the matrix material [114]. Unlike other strengthening mechanisms, the advantage of dispersion strengthening is that the dispersoids material can be chosen to have high-temperature strength. Thus, the strength achieved due to dispersion strengthening can be maintained even at high temperatures. The mechanism of dislocation interaction with dispersoids is similar to precipitation strengthening as shown in Fig. 2.14.

References

[1] J.W. Yeh, S.K. Chen, S.J. Lin, J.Y. Gan, T.S. Chin, T.T. Shun, C.H. Tsau, S.Y. Chang, Nanostructured high-entropy alloys with multiple principal elements: Novel alloy design concepts and outcomes, Adv. Eng. Mater. 6 (2004) 299–303. https://doi.org/10.1002/adem.200300567.

- [2] S. Gorsse, J.-P. Couzinié, D.B. Miracle, From high-entropy alloys to complex concentrated alloys [Des alliages à haute entropie aux alliages concentrés complexes], Comptes Rendus Phys. 19 (2018) 721–736.
- [3] B. Cantor, I.T.H. Chang, P. Knight, A.J.B. Vincent, Microstructural development in equiatomic multicomponent alloys, Mater. Sci. Eng. A. 375–377 (2004) 213–218. https://doi.org/10.1016/j.msea.2003.10.257.
- [4] C S Smith, Four outstanding researchers in metallurgical history. American Society for Testing and Materials, ASTM, Philadelphia, 1963.
- [5] B.S. Murty, J.W. Yeh, S. Ranganathan, P.P. Bhattacharjee, High-entropy alloys: basic concepts, High-Entropy Alloy. (2019) 13–30. https://doi.org/10.1016/b978-0-12-816067-1.00002-3.
- [6] J.W. Yeh, Recent progress in high-entropy alloys, Ann. Chim. Sci. Des Mater. 31 (2006) 633–648.
- [7] J.W. Yeh, Alloy design strategies and future trends in high-entropy alloys, Jom. 65 (2013) 1759–1771. https://doi.org/10.1007/s11837-013-0761-6.
- [8] M.H. Tsai, J.W. Yeh, High-entropy alloys: A critical review, Mater. Res. Lett. 2 (2014) 107–123. https://doi.org/10.1080/21663831.2014.912690.
- [9] D.B. Miracle, O.N. Senkov, A critical review of high entropy alloys and related concepts, Acta Mater. 122 (2017) 448–511. https://doi.org/10.1016/j.actamat.2016.08.081.
- [10] C. Ng, S. Guo, J. Luan, S. Shi, C.T. Liu, Entropy-driven phase stability and slow diffusion kinetics in an Al 0.5CoCrCuFeNi high entropy alloy, Intermetallics. 31 (2012) 165–172. https://doi.org/10.1016/j.intermet.2012.07.001.
- [11] K.Y. Tsai, M.H. Tsai, J.W. Yeh, Sluggish diffusion in Co-Cr-Fe-Mn-Ni high-entropy alloys, Acta Mater. 61 (2013) 4887–4897. https://doi.org/10.1016/j.actamat.2013.04.058.
- [12] Y. Zhang, T.T. Zuo, Z. Tang, M.C. Gao, K.A. Dahmen, P.K. Liaw, Z.P. Lu, Microstructures and properties of high-entropy alloys, Prog. Mater. Sci. 61 (2014) 1–

- 93. https://doi.org/10.1016/j.pmatsci.2013.10.001.
- [13] M. Vaidya, K.G. Pradeep, B.S. Murty, G. Wilde, S.V. Devinsky, Bulk tracer diffusion in CoCrFeNi and CoCrFeMnNi high entropy alloys, Acta Mater. 146 (2018) 211–224. https://doi.org/10.1557/jmr.2018.162.
- [14] Z. Li, C.C. Tasan, H. Springer, B. Gault, D. Raabe, Interstitial atoms enable joint twinning and transformation induced plasticity in strong and ductile high-entropy alloys, Nat. Publ. Gr. 1–7 (2017). https://doi.org/10.1038/srep40704.
- [15] Z. Li, Strong and Ductile Non-equiatomic High-Entropy Alloys: Design, Processing, Microstructure, and Mechanical Properties, JOM. 69 (2017) 2099–2106. https://doi.org/10.1007/s11837-017-2540-2.
- [16] C. Tong, M. Chen, S. Chen, J. Yeh, T. Shun, S. Lin, S. Chang, Mechanical Performance of the Al x CoCrCuFeNi High-Entropy Alloy System with Multiprincipal Elements, 36 (2005) 1263–1271.
- [17] Z. Li, C. Cem, K. Gokuldoss, D. Raabe, Acta Materialia A TRIP-assisted dual-phase high-entropy alloy: Grain size and phase fraction effects on deformation behavior, Acta Mater. 131 (2017) 323–335. https://doi.org/10.1016/j.actamat.2017.03.069.
- [18] J.Y. He, H. Wang, H.L. Huang, X.D. Xu, M.W. Chen, Y. Wu, X.J. Liu, T.G. Nieh, K. An, Z.P. Lu, A precipitation-hardened high-entropy alloy with outstanding tensile properties, Acta Mater. 102 (2016) 187–196. https://doi.org/10.1016/j.actamat.2015.08.076.
- [19] C. Lai, S. Lin, J. Yeh, S. Chang, Preparation and characterization of AlCrTaTiZr multielement nitride coatings, Surf. Coatings Technol. 201 (2006) 3275–3280. https://doi.org/10.1016/j.surfcoat.2006.06.048.
- [20] Y.F. Kao, T.J. Chen, S.K. Chen, J.W. Yeh, Microstructure and mechanical property of as-cast, -homogenized, and -deformed AlxCoCrFeNi (0 ≤ x ≤ 2) high-entropy alloys, J. Alloys Compd. 488 (2009) 57–64. https://doi.org/10.1016/j.jallcom.2009.08.090.
- [21] J.W. Yeh, S.Y. Chang, Y. Der Hong, S.K. Chen, S.J. Lin, Anomalous decrease in X-ray diffraction intensities of Cu-Ni-Al-Co-Cr-Fe-Si alloy systems with multi-principal elements, Mater. Chem. Phys. 103 (2007) 41–46. https://doi.org/10.1016/j.matchemphys.2007.01.003.
- [22] S. Ranganathan, Alloyed pleasures: Multimetallic cocktails, Curr. Sci. 85 (2003) 1404–1406.
- [23] X. Yang, Y. Zhang, Prediction of high-entropy stabilized solid-solution in multicomponent alloys, Mater. Chem. Phys. 132 (2012) 233–238.

- https://doi.org/10.1016/j.matchemphys.2011.11.021.
- [24] S. Guo, C. Ng, J. Lu, C.T. Liu, Effect of valence electron concentration on stability of fcc or bcc phase in high entropy alloys, J. Appl. Phys. 109 (2011). https://doi.org/10.1063/1.3587228.
- [25] J.H. Li, M.H. Tsai, Theories for predicting simple solid solution high-entropy alloys: Classification, accuracy, and important factors impacting accuracy, Scr. Mater. 188 (2020) 80–87. https://doi.org/10.1016/j.scriptamat.2020.06.064.
- [26] E.J. Pickering, N.G. Jones, High-entropy alloys: a critical assessment of their founding principles and future prospects, Int. Mater. Rev. 61 (2016) 183–202. https://doi.org/10.1080/09506608.2016.1180020.
- [27] S. Guo, C.T. Liu, Phase stability in high entropy alloys: Formation of solid-solution phase or amorphous phase, Prog. Nat. Sci. Mater. Int. 21 (2011) 433–446. https://doi.org/10.1016/S1002-0071(12)60080-X.
- [28] K.K. Alaneme, M.O. Bodunrin, S.R. Oke, Processing, alloy composition and phase transition effect on the mechanical and corrosion properties of high entropy alloys: A review, J. Mater. Res. Technol. 5 (2016) 384–393. https://doi.org/10.1016/j.jmrt.2016.03.004.
- [29] Y. Zhang, Y.J. Zhou, J.P. Lin, G.L. Chen, P.K. Liaw, Solid-solution phase formation rules for multi-component alloys, Adv. Eng. Mater. 10 (2008) 534–538. https://doi.org/10.1002/adem.200700240.
- [30] S. Guo, Q. Hu, C. Ng, C.T. Liu, More than entropy in high-entropy alloys: Forming solid solutions or amorphous phase, Intermetallics. 41 (2013) 96–103. https://doi.org/10.1016/j.intermet.2013.05.002.
- [31] Y.J. Zhou, Y. Zhang, F.J. Wang, G.L. Chen, Phase transformation induced by lattice distortion in multiprincipal component CoCrFeNi Cux Al1-x solid-solution alloys, Appl. Phys. Lett. 92 (2008) 1–4. https://doi.org/10.1063/1.2938690.
- [32] M.G. Poletti, L. Battezzati, Electronic and thermodynamic criteria for the occurrence of high entropy alloys in metallic systems, Acta Mater. 75 (2014) 297–306. https://doi.org/10.1016/j.actamat.2014.04.033.
- [33] O.N. Senkov, G.B. Wilks, D.B. Miracle, C.P. Chuang, P.K. Liaw, Refractory highentropy alloys, Intermetallics. 18 (2010) 1758–1765. https://doi.org/10.1016/j.intermet.2010.05.014.
- [34] N. Birbilis, S. Choudhary, J.R. Scully, M.L. Taheri, A perspective on corrosion of multiprincipal element alloys, Npj Mater. Degrad. 5 (2021) 1–8.

- https://doi.org/10.1038/s41529-021-00163-8.
- [35] E. Savitskii, Physical metallurgy of refractory metals and alloys, Springer Science & Business Media, 2012.
- [36] O.N. Senkov, D.B. Miracle, K.J. Chaput, J.P. Couzinie, Development and exploration of refractory high entropy alloys A review, J. Mater. Res. 33 (2018) 3092–3128. https://doi.org/10.1557/jmr.2018.153.
- [37] H. Harada, N. Rene, High Temperature Materials for Gas Turbines: The Present and Future, Proc. Int. Gas Turbine Congr. 2003. (2003) 1–9.
- [38] S.K. Dewangan, A. Mangish, S. Kumar, A. Sharma, B. Ahn, V. Kumar, A review on High-Temperature Applicability: A milestone for high entropy alloys, Eng. Sci. Technol. an Int. J. 35 (2022) 101211. https://doi.org/10.1016/j.jestch.2022.101211.
- [39] O.N. Senkov, G.B. Wilks, J.M. Scott, D.B. Miracle, Mechanical properties of Nb25Mo25Ta 25W25 and V20Nb20Mo 20Ta20W20 refractory high entropy alloys, Intermetallics. 19 (2011) 698–706. https://doi.org/10.1016/j.intermet.2011.01.004.
- [40] The Minerals, Metals & Materials Society (TMS), Defining Pathways for Realizing the Revolutionary Potential of High Entropy Alloys (Pittsburgh, PA: TMS 2021).
- [41] D.G. Kalali, S. Antharam, M. Hasan, P.S. Karthik, P.S. Phani, K. Bhanu Sankara Rao, K. V. Rajulapati, On the origins of ultra-high hardness and strain gradient plasticity in multi-phase nanocrystalline MoNbTaTiW based refractory high-entropy alloy, Mater. Sci. Eng. A. 812 (2021) 141098. https://doi.org/10.1016/j.msea.2021.141098.
- [42] P.J. Barron, A.W. Carruthers, J.W. Fellowes, N.G. Jones, H. Dawson, E.J. Pickering, Towards V-based high-entropy alloys for nuclear fusion applications, Scr. Mater. 176 (2020) 12–16. https://doi.org/10.1016/j.scriptamat.2019.09.028.
- [43] O.A. Waseem, H.J. Ryu, Powder Metallurgy Processing of a Wx TaTiVCr High-Entropy Alloy and Its Derivative Alloys for Fusion Material Applications, Sci. Rep. 7 (2017) 1–14. https://doi.org/10.1038/s41598-017-02168-3.
- [44] E.J. Pickering, A.W. Carruthers, P.J. Barron, S.C. Middleburgh, D.E.J. Armstrong, A.S. Gandy, High-entropy alloys for advanced nuclear applications, Entropy. 23 (2021) 1–28. https://doi.org/10.3390/e23010098.
- [45] A. Kareer, J.C. Waite, B. Li, A. Couet, D.E.J. Armstrong, A.J. Wilkinson, Short communication: 'Low activation, refractory, high entropy alloys for nuclear applications,' J. Nucl. Mater. 526 (2019) 0–5. https://doi.org/10.1016/j.jnucmat.2019.151744.
- [46] G. Popescu, B. Ghiban, C.A. Popescu, L. Rosu, R. Truscă, I. Carcea, V. Soare, D.

- Dumitrescu, I. Constantin, M.T. Olaru, B.A. Carlan, New TiZrNbTaFe high entropy alloy used for medical applications, IOP Conf. Ser. Mater. Sci. Eng. 400 (2018). https://doi.org/10.1088/1757-899X/400/2/022049.
- [47] A. Ostovari Moghaddam, J. Pasandideh, A. Abdollahzadeh, N.A. Shaburova, E. Trofimov, On the application of NbTaTiVW refractory high entropy alloy particles in the manufacturing process of WC based matrix body drill bits, Int. J. Refract. Met. Hard Mater. 99 (2021) 105608. https://doi.org/10.1016/j.ijrmhm.2021.105608.
- [48] H. Yao, J.W. Qiao, M.C. Gao, J.A. Hawk, S.G. Ma, H. Zhou, MoNbTaV medium-entropy alloy, Entropy. 18 (2016) 1–15. https://doi.org/10.3390/e18050189.
- [49] O.N. Senkov, C.F. Woodward, Microstructure and properties of a refractory NbCrMo0.5Ta0.5TiZr alloy, Mater. Sci. Eng. A. 529 (2011) 311–320. https://doi.org/10.1016/j.msea.2011.09.033.
- [50] H.W. Yao, J.W. Qiao, M.C. Gao, J.A. Hawk, S.G. Ma, H.F. Zhou, Y. Zhang, NbTaV-(Ti,W) refractory high-entropy alloys: Experiments and modeling, Mater. Sci. Eng. A. 674 (2016) 203–211. https://doi.org/10.1016/j.msea.2016.07.102.
- [51] B. Zhang, M.C. Gao, Y. Zhang, S.M. Guo, Senary refractory high-entropy alloy CrxMoNbTaVW, Calphad Comput. Coupling Phase Diagrams Thermochem. 51 (2015) 193–201. https://doi.org/10.1016/j.calphad.2015.09.007.
- [52] B. Kang, J. Lee, H.J. Ryu, S.H. Hong, Ultra-high strength WNbMoTaV high-entropy alloys with fine grain structure fabricated by powder metallurgical process, Mater. Sci. Eng. A. 712 (2018) 616–624. https://doi.org/10.1016/j.msea.2017.12.021.
- [53] O.A. Waseem, J. Lee, H.M. Lee, H.J. Ryu, The effect of Ti on the sintering and mechanical properties of refractory high-entropy alloy TixWTaVCr fabricated via spark plasma sintering for fusion plasma-facing materials, Mater. Chem. Phys. 210 (2018) 87–94. https://doi.org/10.1016/j.matchemphys.2017.06.054.
- [54] Z.D. Han, N. Chen, S.F. Zhao, L.W. Fan, G.N. Yang, Y. Shao, K.F. Yao, Effect of Ti additions on mechanical properties of NbMoTaW and VNbMoTaW refractory high entropy alloys, Intermetallics. 84 (2017) 153–157. https://doi.org/10.1016/j.intermet.2017.01.007.
- [55] J. Chen, X. Zhou, W. Wang, B. Liu, Y. Lv, W. Yang, D. Xu, Y. Liu, A review on fundamental of high entropy alloys with promising high-temperature properties, J. Alloys Compd. 760 (2018) 15–30. https://doi.org/10.1016/j.jallcom.2018.05.067.
- [56] J.P. Couzinié, O.N. Senkov, D.B. Miracle, G. Dirras, Comprehensive data compilation on the mechanical properties of refractory high-entropy alloys, Data Br. 21 (2018) 1622–

- 1641. https://doi.org/10.1016/j.dib.2018.10.071.
- [57] S. Dasari, V. Soni, A. Sharma, O.N. Senkov, D.B. Miracle, H.L. Fraser, Y. Wang, R. Banerjee, Concomitant Clustering and Ordering Leading to B2 + BCC Microstructures in Refractory High Entropy Alloys, Trans. Indian Inst. Met. 75 (2022) 907–916. https://doi.org/10.1007/s12666-021-02518-w.
- [58] J.P. Couzinié, M. Heczko, V. Mazánová, O.N. Senkov, M. Ghazisaeidi, R. Banerjee, M.J. Mills, High-temperature deformation mechanisms in a BCC+B2 refractory complex concentrated alloy, Acta Mater. 233 (2022). https://doi.org/10.1016/j.actamat.2022.117995.
- [59] M. Atkinson, Origin of the size effect in indentation of metals, Int. J. Mech. Sci. 33 (1991) 843–850. https://doi.org/10.1016/0020-7403(91)90006-O.
- [60] T.F. Page, W.C. Oliver, C.J. McHargue, The deformation behavior of ceramic crystals subjected to very low load (nano)indentations, J. Mater. Res. 7 (1992) 450–473. https://doi.org/10.1557/JMR.1992.0450.
- [61] N.A. Stelmashenko, M.G. Walls, L.M. Brown, Y. V. Milman, Microindentations on W and Mo oriented single crystals: An STM study, Acta Metall. Mater. 41 (1993) 2855–2865. https://doi.org/10.1016/0956-7151(93)90100-7.
- [62] D. Kiener, K. Durst, M. Rester, A.M. Minor, Revealing deformation mechanisms with nanoindentation, Jom. 61 (2009) 14–23. https://doi.org/10.1007/s11837-009-0036-4.
- [63] K. Sangwal, On the reverse indentation size effect and microhardness measurement of solids, Mater. Chem. Phys. 63 (2000) 145–152. https://doi.org/10.1016/S0254-0584(99)00216-3.
- [64] N. Gane, Proceedings of the Royal Society of London Series a-Mathematical and Physical Sciences, 317 (1970) 367.
- [65] C.C. and A. Hendrickson, The Science of Hardness Testing and Its Research Application, SAM, Metals Park, OH, 1973.
- [66] D. Tabor, in Microindentation techiques in materials science and engineering, ASTM STP 889 (P. Blau and B. Lawn, eds.), ASTM, Philadelphia, 1986.
- [67] E. H. Bückle, The Science of hardness testing and its research applications, ASME, Metals Park, OH, 1973.
- [68] B.W. Mott, Microindentation Hardness Testing, Butterworths, London, 1957.
- [69] G.M. Pharr, E.G. Herbert, Y. Gao, The indentation size effect: A critical examination of experimental observations and mechanistic interpretations, Annu. Rev. Mater. Res. 40 (2010) 271–292. https://doi.org/10.1146/annurev-matsci-070909-104456.

[70] Oliver, W.C. and Pharr, G.M., An Improved Technique for Determining Hardness and Elastic Modulus Using Load and Displacement Sensing Indentation Experiments. J. 55 Chapter 3 Experimental details Mater. Res., 7 (1992) 1564-1583. https://doi.org/10.1557/JMR.1992.1564...

- [71] W.J. Poole, M.F. Ashby, N.A. Fleck, Micro-hardness of annealed and work-hardened copper polycrystals, Scr. Mater. 34 (1996) 559–564. https://doi.org/10.1016/1359-6462(95)00524-2.
- [72] Tangyunyong P, Thomas RC, Houston JE, Michalske TA, Crooks RM, Howard AJ. Nanometer-scale mechanics of gold films. Phys Rev Lett, 71 (1993) 3319-3322. doi: 10.1103/PhysRevLett.71.3319.
- [73] Oliver, W., & Pharr, G. Measurement of hardness and elastic modulus by instrumented indentation: Advances in understanding and refinements to methodology. J. Mater. Res., 19 (2004) 3-20. doi:10.1557/jmr.2004.19.1.3.
- [74] J.B. Pethicai, R. Hutchings, W.C. Oliver, J.B. Pethicat, W.C. Oliver\$, Philosophical Magazine A Hardness measurement at penetration depths as small as 20 nm Hardness measurement at penetration depths as small as 20 nm, 48 (1983) 593–606. https://doi.org/10.1080/01418618308234914.
- [75] Q. Ma, D.R Clarke, Size dependent hardness of silver single crystals. Journal of Materials Research 10 (1995) 853–863. https://doi.org/10.1557/JMR.1995.0853.
- [76] K.W. McElhaney, J.J. Vlassak, W.D. Nix, Determination of indenter tip geometry and indentation contact area for depth-sensing indentation experiments, J. Mater. Res. 13 (1998) 1300–1306. https://doi.org/10.1557/JMR.1998.0185.
- [77] N.K. Mukhopadhyay, P. Paufler, Micro- and nanoindentation techniques for mechanical characterisation of materials, Int. Mater. Rev. 51 (2006) 209–245. https://doi.org/10.1179/174328006X102475.
- [78] K. Durst, O. Franke, A. Böhner, M. Göken, Indentation size effect in Ni-Fe solid solutions, Acta Mater. 55 (2007) 6825–6833. https://doi.org/10.1016/j.actamat.2007.08.044.
- [79] A.A. Elmustafa, D.S. Stone, Stacking fault energy and dynamic recovery: Do they impact the indentation size effect?, Mater. Sci. Eng. A. 358 (2003) 1–8. https://doi.org/10.1016/S0921-5093(03)00293-4.
- [80] W.D. Nix, H. Gao, Indentation size effects in crystalline materials: A law for strain gradient plasticity, J. Mech. Phys. Solids. 46 (1998) 411–425. https://doi.org/10.1016/S0022-5096(97)00086-0.

[81] H. Zaid, J.W. Stremfel, K. Tanaka, M. Liao, M.S. Goorsky, J.M. Yang, S. Kodambaka, Mechanical properties of compositionally-rich body-centered cubic VNbTaMoW alloy, Materialia. 12 (2020) 8–13. https://doi.org/10.1016/j.mtla.2020.100746.

- [82] B.B. Palei, T. Dash, S.K. Biswal, Graphene reinforced aluminum nanocomposites: synthesis, characterization and properties, J. Mater. Sci. 57 (2022) 8544–8556. https://doi.org/10.1007/s10853-022-07043-9.
- [83] B. Schuh, F. Mendez-Martin, B. Völker, E.P. George, H. Clemens, R. Pippan, A. Hohenwarter, Mechanical properties, microstructure and thermal stability of a nanocrystalline CoCrFeMnNi high-entropy alloy after severe plastic deformation, Acta Mater. 96 (2015) 258–268. https://doi.org/10.1016/j.actamat.2015.06.025.
- [84] J. Moon, Y. Qi, E. Tabachnikova, Y. Estrin, W.M. Choi, S.H. Joo, B.J. Lee, A. Podolskiy, M. Tikhonovsky, H.S. Kim, Microstructure and Mechanical Properties of High-Entropy Alloy Co20Cr26Fe20Mn20Ni14 Processed by High-Pressure Torsion at 77 K and 300 K, Sci. Rep. 8 (2018) 1–12. https://doi.org/10.1038/s41598-018-29446-y.
- [85] R. Zhang, S. Zhao, J. Ding, Y. Chong, T. Jia, C. Ophus, M. Asta, R.O. Ritchie, A.M. Minor, Short-range order and its impact on the CrCoNi medium-entropy alloy, Nature. 581 (2020) 283–287. https://doi.org/10.1038/s41586-020-2275-z.
- [86] Z. Lei, X. Liu, Y. Wu, H. Wang, S. Jiang, S. Wang, X. Hui, Y. Wu, B. Gault, P. Kontis, D. Raabe, L. Gu, Q. Zhang, H. Chen, H. Wang, J. Liu, K. An, Q. Zeng, T.G. Nieh, Z. Lu, Enhanced strength and ductility in a high-entropy alloy via ordered oxygen complexes, Nature. 563 (2018) 546–550. https://doi.org/10.1038/s41586-018-0685-y.
- [87] T. Yang, Y.L. Zhao, Y. Tong, Z.B. Jiao, J. Wei, J.X. Cai, X.D. Han, D. Chen, A. Hu, J.J. Kai, K. Lu, Y. Liu, C.T. Liu, Multicomponent intermetallic nanoparticles and superb mechanical behaviors of complex alloys, Science (80-.). 362 (2018) 933–937. https://doi.org/10.1126/science.aas8815.
- [88] Y.J. Liang, L. Wang, Y. Wen, B. Cheng, Q. Wu, T. Cao, Q. Xiao, Y. Xue, G. Sha, Y. Wang, Y. Ren, X. Li, L. Wang, F. Wang, H. Cai, High-content ductile coherent nanoprecipitates achieve ultrastrong high-entropy alloys, Nat. Commun. 9 (2018) 1–8. https://doi.org/10.1038/s41467-018-06600-8.
- [89] U. Sunkari, S.R. Reddy, B.D.S. Rathod, S.S.S. Kumar, R. Saha, S. Chatterjee, P.P. Bhattacharjee, Heterogeneous precipitation mediated heterogeneous nanostructure strength-ductility enhances synergy in severely cryo-rolled and annealed CoCrFeNi2.1Nb0.2 Sci. (2020)high entropy alloy, Rep. 10 1–9. https://doi.org/10.1038/s41598-020-63038-z.

[90] J. Su, D. Raabe, Z. Li, Hierarchical microstructure design to tune the mechanical behavior of an interstitial TRIP-TWIP high-entropy alloy, Acta Mater. 163 (2019) 40– 54. https://doi.org/10.1016/j.actamat.2018.10.017.

- [91] Z. Li, K.G. Pradeep, Y. Deng, D. Raabe, C.C. Tasan, Metastable high-entropy dual-phase alloys overcome the strength-ductility trade-off, Nature. 534 (2016) 227–230. https://doi.org/10.1038/nature17981.
- [92] P.M. C. Kittel, P. McEuen, Introduction to solid state physics, Wiley New York, 1996.
- [93] Z.C. Cordero, B.E. Knight, C.A. Schuh, Six decades of the Hall–Petch effect a survey of grain-size strengthening studies on pure metals, Int. Mater. Rev. 61 (2016) 495–512. https://doi.org/10.1080/09506608.2016.1191808.
- [94] R.S. Ganji, P. Sai Karthik, K. Bhanu Sankara Rao, K. V. Rajulapati, Strengthening mechanisms in equiatomic ultrafine grained AlCoCrCuFeNi high-entropy alloy studied by micro- and nanoindentation methods, Acta Mater. 125 (2017) 58–68. https://doi.org/10.1016/j.actamat.2016.11.046.
- [95] R. Sriharitha, B.S. Murty, R.S. Kottada, Alloying, thermal stability and strengthening in spark plasma sintered AlxCoCrCuFeNi high entropy alloys, J. Alloys Compd. 583 (2014) 419–426. https://doi.org/10.1016/j.jallcom.2013.08.176.
- [96] E.O. Hall, The deformation and ageing of mild steel: III Discussion of results, Proc. Phys. Soc. Sect. B. 64 (1951) 747–753. https://doi.org/10.1088/0370-1301/64/9/303.
- [97] S. Chen, K.K. Tseng, Y. Tong, W. Li, C.W. Tsai, J.W. Yeh, P.K. Liaw, Grain growth and Hall-Petch relationship in a refractory HfNbTaZrTi high-entropy alloy, J. Alloys Compd. 795 (2019) 19–26. https://doi.org/10.1016/j.jallcom.2019.04.291.
- [98] Y. Xie, Y. Luo, T. Xia, W. Zeng, J. Wang, J. Liang, D. Zhou, D. Zhang, Grain growth and strengthening mechanisms of ultrafine-grained CoCrFeNiMn high entropy alloy matrix nanocomposites fabricated by powder metallurgy, J. Alloys Compd. 819 (2020) 152937. https://doi.org/10.1016/j.jallcom.2019.152937.
- [99] M.F. Ashby, The deformation of plastically non-homogeneous materials, Philos. Mag. 21 (1970) 399–424. https://doi.org/10.1080/14786437008238426.
- [100] K.S. Kumar, H. Van Swygenhoven, S. Suresh, Mechanical behavior of nanocrystalline metals and alloys, Acta Mater. 51 (2003) 5743–5774. https://doi.org/10.1016/j.actamat.2003.08.032.
- [101] Q. Liu, G. Wang, X. Sui, Y. Liu, X. Li, J. Yang, Microstructure and mechanical properties of ultra-fine grained MoNbTaTiV refractory high-entropy alloy fabricated by spark plasma sintering, J. Mater. Sci. Technol. 35 (2019) 2600–2607.

- https://doi.org/10.1016/j.jmst.2019.07.013.
- [102] J. Pan, T. Dai, T. Lu, X. Ni, J. Dai, M. Li, Microstructure and mechanical properties of Nb25Mo25Ta25W25 and Ti8Nb23Mo23Ta23W23 high entropy alloys prepared by mechanical alloying and spark plasma sintering, Mater. Sci. Eng. A. 738 (2018) 362–366. https://doi.org/10.1016/j.msea.2018.09.089.
- [103] C. Duan, M. Reiberg, P. Kutlesa, X. Li, R. Pippan, E. Werner, Strain-hardening properties of the high-entropy alloy MoNbTaTiVZr processed by high-pressure torsion, Contin. Mech. Thermodyn. 34 (2022) 475–489. https://doi.org/10.1007/s00161-021-01065-5.
- [104] Y.D. Wu, Y.H. Cai, T. Wang, J.J. Si, J. Zhu, Y.D. Wang, X.D. Hui, A refractory Hf25Nb25Ti25Zr25 high-entropy alloy with excellent structural stability and tensile properties, Mater. Lett. 130 (2014) 277–280. https://doi.org/10.1016/j.matlet.2014.05.134.
- [105] I. Toda-Caraballo, P.E.J. Rivera-Díaz-Del-Castillo, Modelling solid solution hardening in high entropy alloys, Acta Mater. 85 (2015) 14–23. https://doi.org/10.1016/j.actamat.2014.11.014.
- [106] R. Labusch, A Statistical Theory of Solid Solution Hardening, Phys. Status Solidi. 41 (1970) 659–669. https://doi.org/10.1002/pssb.19700410221.
- [107] O.N. Senkov, J.M. Scott, S. V. Senkova, D.B. Miracle, C.F. Woodward, Microstructure and room temperature properties of a high-entropy TaNbHfZrTi alloy, J. Alloys Compd. 509 (2011) 6043–6048. https://doi.org/10.1016/j.jallcom.2011.02.171.
- [108] W. Guo, B. Liu, Y. Liu, T. Li, A. Fu, Q. Fang, Y. Nie, Microstructures and mechanical properties of ductile NbTaTiV refractory high entropy alloy prepared by powder metallurgy, J. Alloys Compd. 776 (2019) 428–436. https://doi.org/10.1016/j.jallcom.2018.10.230.
- [109] L.A. Gypen, A. Deruyttere, Multi-component solid solution hardening Part 1 Proposed model, J. Mater. Sci. 12 (1977) 1028–1033. https://doi.org/10.1007/BF00540987.
- [110] F. Liu, B. Wang, L. Wang, Y. Xue, Solid-solution strengthening of Ti-Zr-Hf-Nb-Ta-Fe refractory high-entropy alloy, J. Phys. Conf. Ser. 2383 (2022). https://doi.org/10.1088/1742-6596/2383/1/012141.
- [111] L.W. Liang Wang, Songshen Chen, Bolun li, Tangqing Cao, Benpeng Wang, Y.X. Yang Ren, Jun Liang, Lightweight Zr1.2V0.8NbTixAly high-entropy alloys with high tensile strength and ductility, Mater. Sci. Eng. A. 814 (2021) 141234.
- [112] J. Hirth, J.P. Lothe, Theory of Dislocations, 2nd ed, Krieger Publishing, Malabar, FL,

1992.

[113] J.W. Christian, S. Mahajan, Deformation twinning, Prog. Mater. Sci. 39 (1995) 1–157. https://doi.org/10.1016/0079-6425(94)00007-7.

[114] M. Ashby, H. Shercliff, D. Cebon, Materials Engineering, Science, Processing and Design, 2007.

Chapter 3 Experimental details

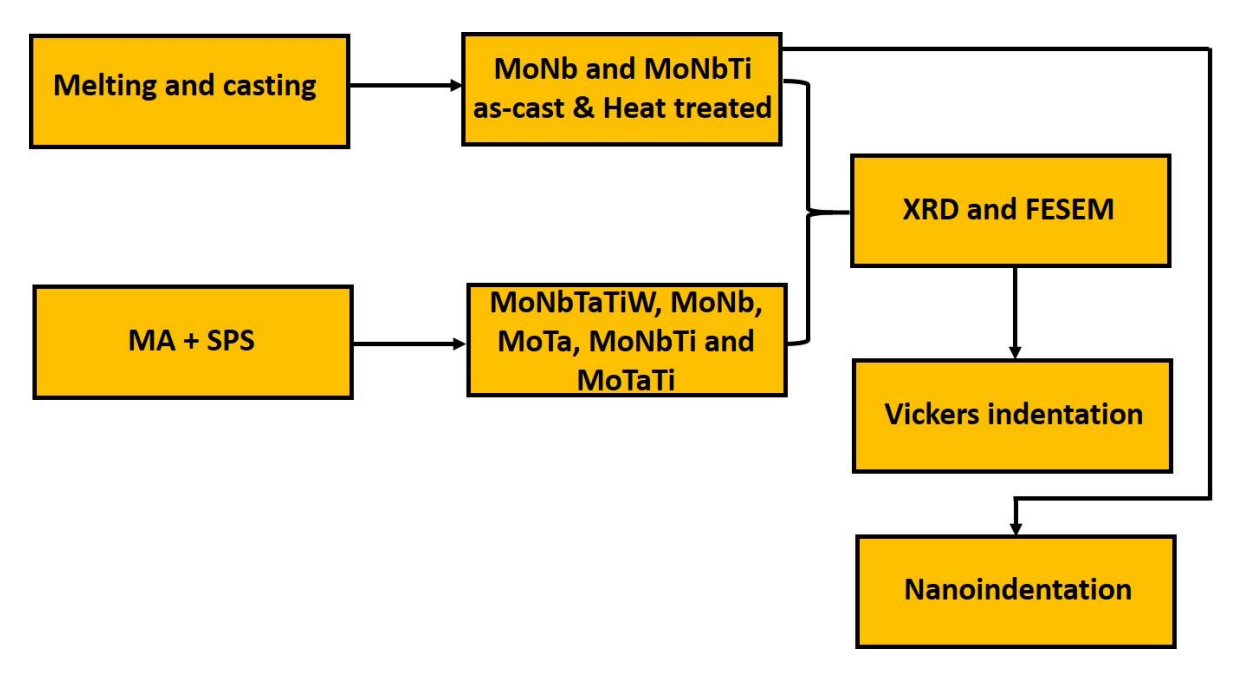


Fig. 3.1 Flow chart of the experimental procedures adapted in the current investigation

3.1. Materials used

In the present work, Mo, Nb, Ta, Ti, W, and Fe elemental powders and/or granules with purity >99.5 % are used to manufacture various alloys in two different processing routes via MA+SPS and melting and casting. The physical properties of the respective elements are shown in Table 3.1.

Table 3.1 Physical properties of elements used in this work to fabricate various RMPEAs

Element	Mo	Nb	Ta	Ti	W	Fe
Atomic	42	41	73	22	74	26
number						
Crystal	BCC	BCC	BCC	НСР	BCC	BCC
structure						
(@ 298 K)						
Atomic	1.36	1.43	1.43	1.46	1.37	1.24
radius, (Å)						
Atomic	95.95	92.90	180.95	47.86	183.84	55.84
weight,						
(g/mol)						
Melting	2896	2750	3290	1941	3695	1811
temperature						
(K)						
Density	10.22	8.57	16.65	4.51	19.25	7.87
(g/cc)						
Lattice	3.14	3.30	3.30	2.95, 4.68	3.16	2.86
parameter						
(Å)						
Youngs's	329	105	186	116	411	211
modulus						
(GPa)						

3.2. Processing of refractory multi-principal element alloys with finer microstructural features

Processing of the nanocrystalline (1 nm to 100 nm) RMPEAs has a significant advantage of high strength and homogeneous microstructure compared to coarse-grained counterparts [1]. Researchers like Gleiter and Koch have contributed significantly to the understanding and advancement of the science of nanostructured materials [2,3]. It is well understood and well documented that refined microstructural features (matrix grain size and/or second phase dimensions) would contribute enhancement to the hardness/strength of structural engineering

materials. Therefore, this aspect is also explored and RMPEAs with refined microstructural features are developed in the present study and associated strengthening characteristics are studied. In the present work, all the nanocrystalline RMPEAs are synthesized via the MA+SPS route, which is a top-down approach. In further sections, experimental details with respect to mechanical alloying and spark plasma sintering will be discussed.

3.2.1. Mechanical alloying

In the most available literature, mechanical alloying (top-down approach) is the primary technique for synthesizing nanocrystalline MPEAs [4,5]. The ball milling facility will generally form an alloy with 'n' number of elements. The initial elemental powder particle size will be in microns. After continuous milling for hours, the milled powder crystallite size will be reduced to the nanoscale. In this work, the milling process is undergone in an argon atmosphere to avoid contaminating the elemental powder with the surrounding atmosphere. Milling was stopped after sufficient reduction of the crystallite size was observed. The milling parameters used in this work are shown in Table 3.2 and the schematic of the ball milling process is shown in Fig. 3.2. In the high-energy ball milling facility, two vials are loaded with equal weight, and the movement of these vials will be in ' ∞ ' shape. The velocity of each vial is in the order of 5 m/s, the clamp speed motion is 1200 rpm, and the length of the vial is 5 cm [6]. For every one-hour run of the mill, a break of 20 mins is given to cool down the motor in the mill. Samples of minimal quantity are collected every 5 h to perform the XRD and understand the phase formation and crystallite size.

Table 3.2 Parameters used during mechanical alloying in the high-energy ball mill

Type of mill	High-energy ball mill	
Make	SPEX 8000D shaker mill	
Milling media	Hardened steel	
Milling condition	Dry	
Milling temperature	Room temperature	
Milling atmosphere	Argon	
Ball-to-powder ratio	5:1	

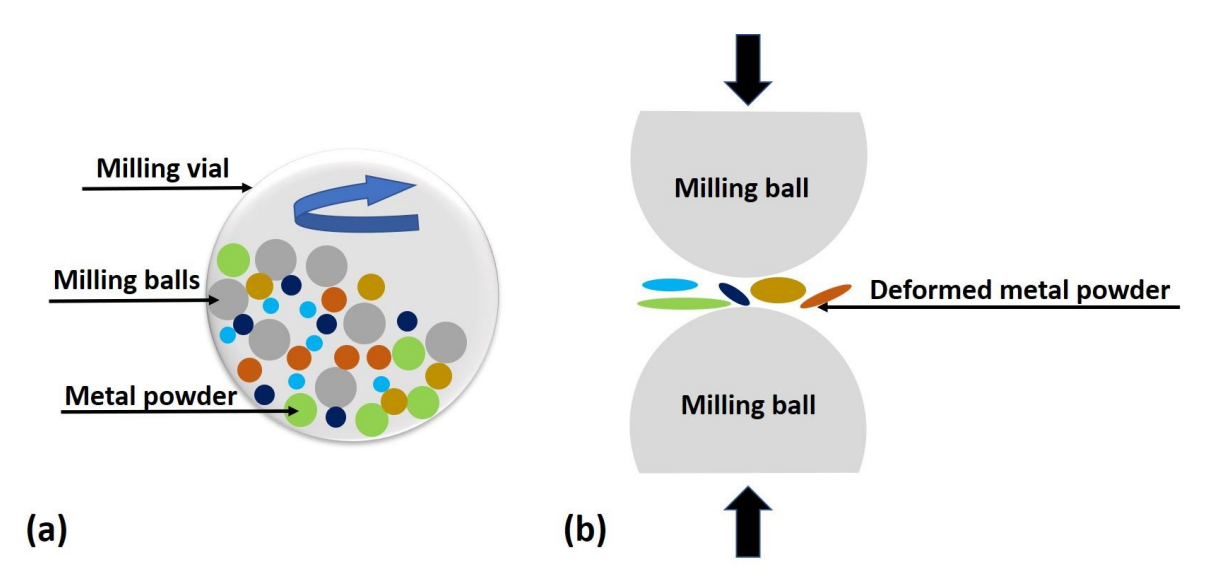


Fig. 3.2 Schematic of the milling process in the high-energy ball mill. (a) Metal powder and metal balls in the milling vial (b) metal powder is fracturing in between the two metal balls hitting with high velocity.

3.2.2. Spark plasma sintering

Among the various types of sintering techniques for powder material, spark plasma sintering (SPS) is the technique with a fast heating rate. In this process, both uniaxial pressure and DC pulsed current are applied simultaneously. Due to the high heating rate, the required temperature to form a neck between the particles will reach in a few minutes, and simultaneous pressure helps in the formation of dense material. There will not be enough time for grain growth in this process due to fast operation. Therefore, the crystallite size will be slightly increased/maintained after SPS [7–9]. In Table 3.3, the SPS parameters used in the present work are mentioned, and the schematic of the SPS equipment is shown in Fig. 3.3.

Table 3.3 Parameters used during spark plasma sintering to sinter the milled powders in this work

Type of Press	Spark plasma sintering		
Make (Available at ARCI Hyderabad)	DR SINTER 1050 apparatus		
	(SPS Syntex Inc., Tokyo, Japan)		
Uniaxial pressure applied	80 MPa		
Sintering temperature for MoNbTaTiW and	1473 K		
MoNb alloys			
Sintering temperature for MoNbTi alloy	1273 K		
Sintering temperature for MoTa alloy	1573 K		
Sintering temperature for MoTaTi alloy	1373 K		
Heating rate for all the alloys	7.21 K/s		
Holding time for all the alloys	15 min		
Sintering atmosphere	Argon		
Die material	Graphite (die, punches, and foil 0.2 mm		
	thick)		

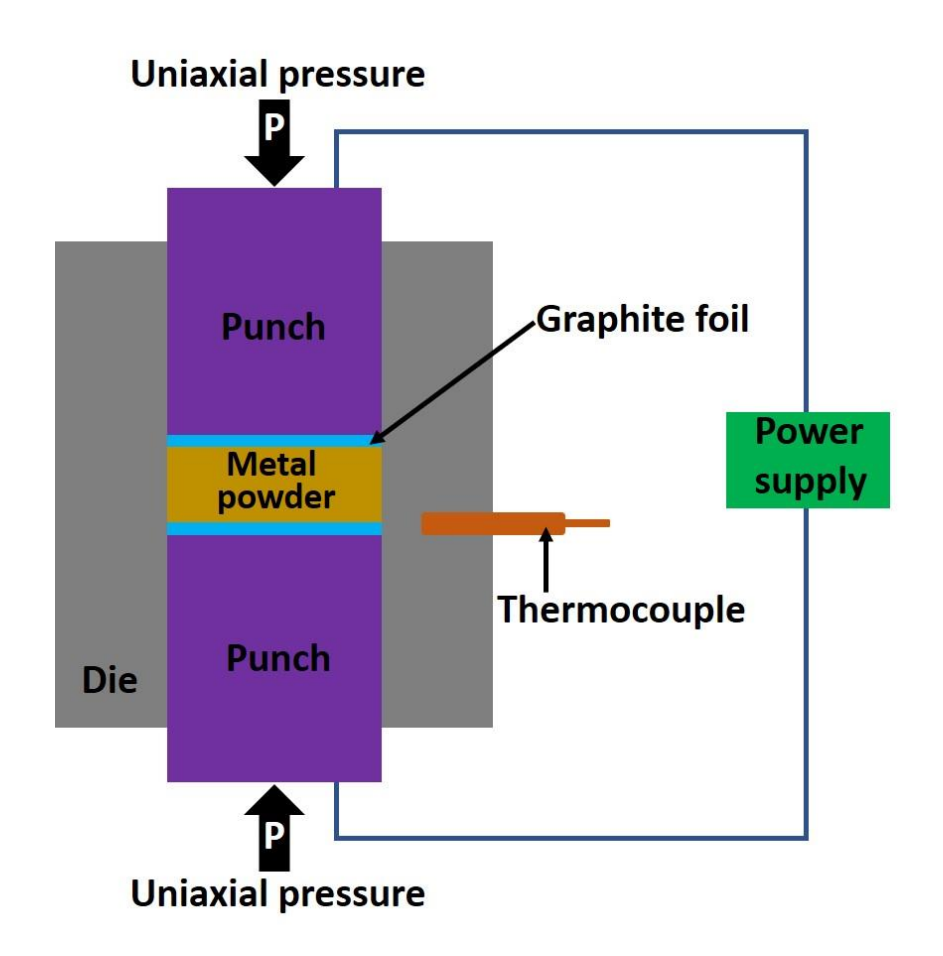


Fig. 3.3 Schematic of the spark plasma sintering equipment used in this work

3.3. Processing of refractory multi-principal element alloys with coarser microstructural features

Manufacturing of MPEAs using conventional melting and casting routes results in alloys with micron-level grain sizes. The alloys prepared through the powder metallurgy route are often thermodynamically unstable. Given the supply of some amount of energy, they tend to transform into other stable configurations with the minimum possible amount of free energy. It has been a practice for several centuries to develop new materials that possess equilibrium microstructures using melting and casting [10]. In the current study, arc melting has been used to develop these novel RMPEAs by adapting the following process parameters as outlined in Table 3.4. Due to the concentration of all the participating elements being high during solidification after melting; there will be elemental segregation in the melting and casting route. Although several melting and casting routes are available to fabricate the alloys with micronscale grain sizes, vacuum arc melting is used to manufacture the alloy in this work.

Table 3.4 Parameters used during vacuum arc melting in this work

Vacuum	10 ⁻⁶ mbar
Getter	Titanium
Number of times inert gas purging	4
Number of times remelting	5

3.3.1. Vacuum arc melting

Vacuum arc melting (VAM) is the most used processing technique to manufacture various MPEAs with coarse grains [11–18]. In this work, melting is performed using the melting unit supplied by Mansha Vacuum Technologies Pvt ltd. A schematic of the melting unit is shown in Fig. 3.4. In the melting process, the copper hearth inside the chamber is cleaned thoroughly without any foreign particles/dust. Then a Ti getter is placed in one cavity of the Cu hearth, which will be melted before the melting of the actual alloy to absorb traces of oxygen, if any. After loading the Ti getter, the raw material is loaded, which needs to be melted. Now the chamber is evacuated until the pressure reaches to the negative pressure of 10⁻⁶ mbar. After the appropriate vacuum is reached, the raw material is melted using the Tungsten electrode for which power is supplied using the TIG transformer. This melting process is performed 5 to 6

times by flipping the melt, such that melting has happened homogeneously without any elemental segregation.

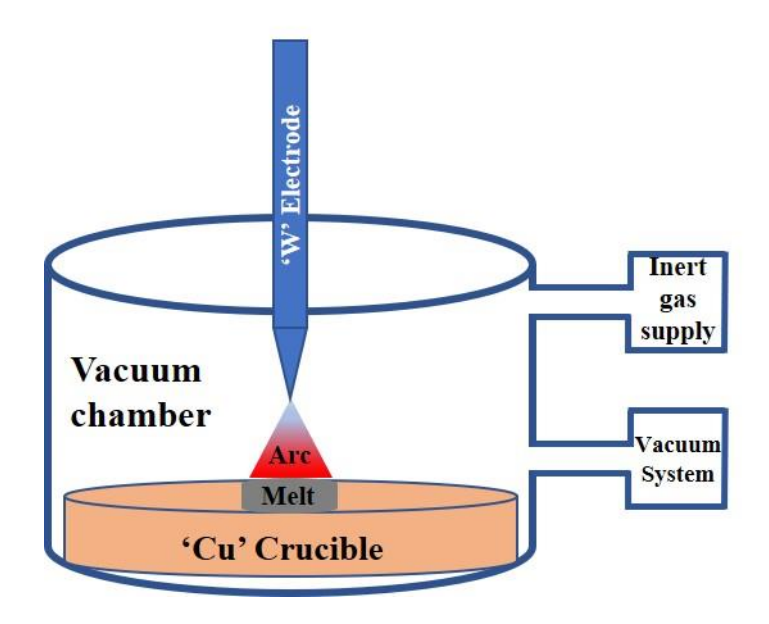


Fig. 3.4 Schematic of the Vacuum arc melting system used in this work

3.4. Structural and mechanical characterization

The sintered sample surface will have graphite foil used between the punch and the milled powder during the sintering process. The graphite layer needs to be removed for further density measurements. After removing the graphite layer on the sintered samples, the density of both sintered and cast samples must be measured. Density measurement is conducted using the Archimedes principle, which works based on the principle of Buyoncy force. The initial weight of the sample is called as dry weight and is designated as (W_D) , then the sample is to be soaked in the distilled water for 24 h, and the soaked weight will be designated as (W_S) . Now the suspended weight is measured using the Archimedes density measuring kit and designated as (W_{SU}) . Now the density of the alloy is calculated using the formulae mentioned in equation 3.1. and relative density is calculated using equation 3.2.

Density (
$$\rho$$
) = $\frac{W_D}{W_S - W_{SU}}$(3.1)

Relative density (
$$\rho$$
 %) = Density (ρ) × $\frac{1}{\text{Theoretical density}}$ × 100.....(3.2)

Now all the samples are metallographically polished with emery papers of grit size 800 to 2000. Subsequently, the samples were polished with $0.3~\mu m$ Alumina and $0.05~\mu m$ Alumina, respectively. Finally, vibratory polishing in a $0.04~\mu m$ colloidal silica suspension was

performed using an automatic vibratory polishing machine (SAPHIR VIBRO-ATM) for 18 h for all the samples.

3.4.1. X-ray diffraction

In this work, the alloys manufactured are novel alloy systems without any prior information on their crystal structure and lattice constants. To understand the crystal structure, lattice constant, and crystallite size, X-ray analysis is performed using the BRUKER D8 ADVANCE machine. The copper target produces Monochromatic wavelength X-rays from the cathode ray tube (CRT). These X-rays are incident onto the sample whose structural characterization needs to be performed. X-rays generated from the CRT are filtered using Nickel filters where the K β radiation is stripped, and only K α radiations (λ = 1.54 Å) are allowed to fall on the sample. If Bragg's law mentioned in equation 3.3 satisfies, constructive interference will be produced. A Schematic of the X-rays interaction with the atomic planes is shown in Fig. 3.5. Parameters used for the experiment are shown in Table 3.5.

$$n\lambda = 2d\sin\theta....(3.3)$$

λ: Wavelength of the X-rays

d: Interplanar spacing

θ: Diffraction angle

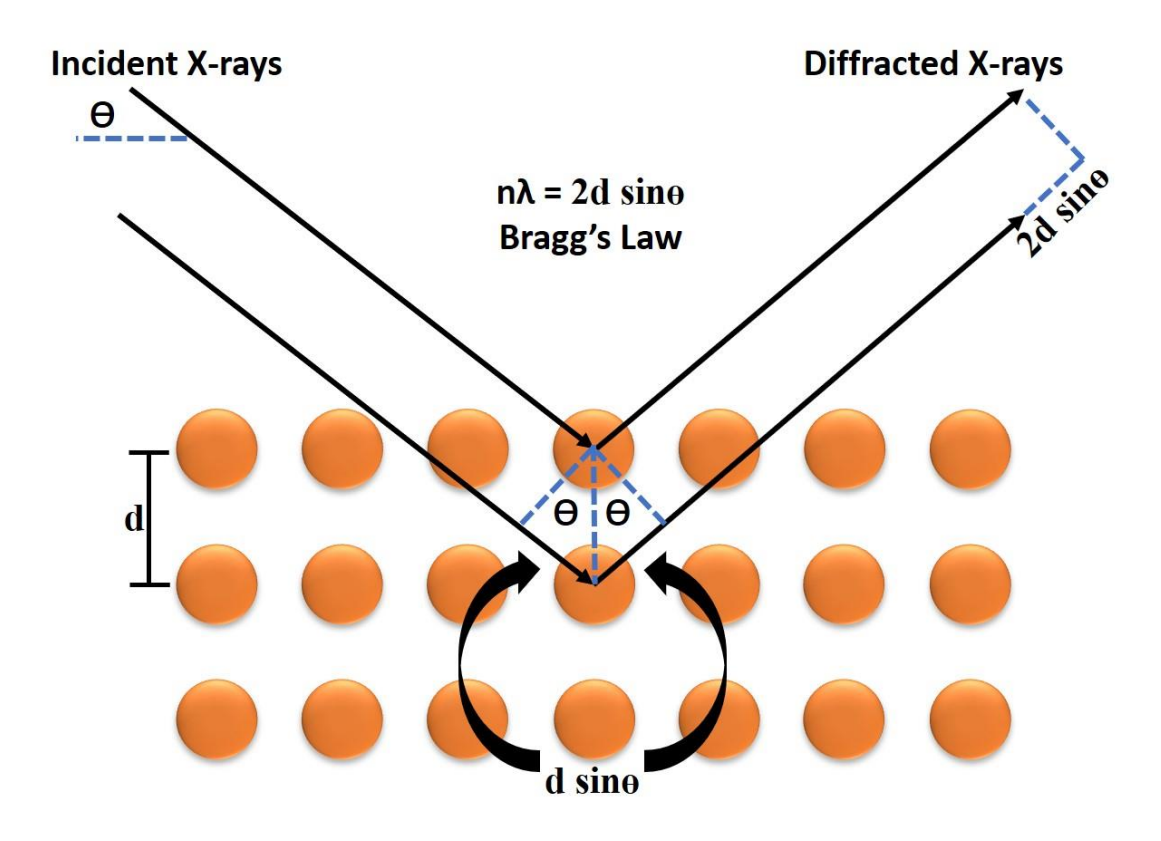


Fig. 3.5 Principle of the X-ray diffraction.

Table 3.5 Parameters used for the XRD analysis

Parameter	Value
Scan range (2θ)	20° to 120°
Step size	0.02°
Scan speed	1 s/step
Wavelength	1.54 Å

The detector receives the diffracted X-rays, plotted as a X-ray diffractogram. From the X-ray diffractogram, 2θ values are noted, and the d-spacing values are calculated using equation 3.3. Each reflection in the diffractogram is indexed with Miller indices using analytical or mathematical methods for indexing [19]. For the cubic crystal systems, equation 3.4 is used to calculate the lattice parameter. Nelson-Riley extrapolation function is sued to estimate the precise lattice parameter, shown in equation 3.5. Error in the measurements of lattice parameter is possible as we proceed with the higher-angle reflections as the term $\sin\theta$ involved in the calculations, and also error percentage will increase with an increase in θ . The Nelson-Riley function results in a straight line, and by extrapolating to Y-axis, its intercept gives the precise lattice parameter.

$$\frac{1}{d^2} = \frac{h^2 + k^2 + l^2}{a^2}...(3.4)$$

$$\frac{\cos^2\theta}{\sin\theta} + \frac{\cos^2\theta}{\theta}.$$
 (3.5)

a: Lattice parameter

In the RMPEAs processed through the milling route, there will be a reduction in the crystallite size with an increase in milling time, and peak broadening happens with the decrease in the crystallite size. To estimate the crystallite size, Scherrer formulae is used shown in equation 3.6.

$$L = \frac{k\lambda}{\beta\cos\theta} \dots (3.6)$$

L: Crystallite size

k: Shape factor (0.94 for cubic structures)

β: Full-width half maximum

Peak broadening will also have an effect of instrumental effect, which needs to be subtracted from the observed peak width, as shown in equation 3.7.

$$\beta = \sqrt{\beta_o^2 + \beta_i^2}...$$
(3.7)

 β_0 : Observed peak width

β_i: Instrumental broadening peak width

 β_i is 0.045° for the XRD machine used in this work. Using the Stokes-Wilson formulae, the lattice strain (ϵ) in the alloy is calculated, which is shown in equation 3.8.

$$\varepsilon = \frac{\beta}{4\tan\theta}.$$
 (3.8)

3.4.2. Field emission scanning electron microscopy

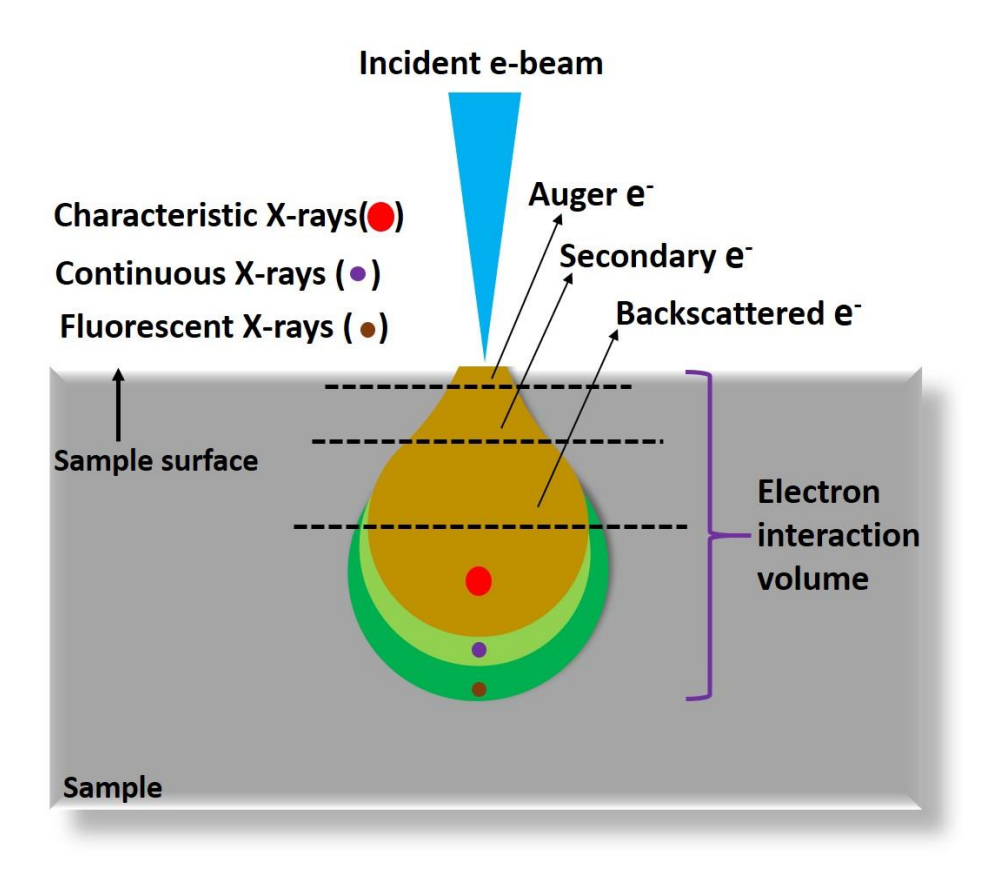


Fig. 3.6 Schematic of the electron beam interaction volume with the sample in the FESEM investigation.

FEI Nova NanoSEM 450 Field Emission Scanning Electron Microscope (FESEM) incorporated with energy dispersive spectroscopy (EDS) and Electron Back Scattered

Diffraction (EBSD) detectors were used for the microstructural characterization and chemical analysis. The Field emission gun liberates a high-energy electron beam using a tungsten filament which interacts with the sample surface and produces inelastic and elastic scattered electrons. Once the primary beam interacts with the sample surface, both backscattered and secondary electrons (BSE and SE) are generated. Inelastic scattering of the electrons will give the morphological information of the sample surface. Elastic scattering of electrons will give the Z-contrast information of the sample. Other X-rays, like Characteristic, continuous, and Fluorescent will generate along with other electrons like Auger electrons, shown in Fig. 3.6. BSE microstructures will have a phase contrast based on the atomic number difference in the elements. A single-phase material will have only one phase such that no contrast is observed, whereas, in multi-phase material, there will be a contrast between the phases. Due to inelastic scattering, secondary electrons are produced, which are useful in obtaining the sample surface morphological information. The parameters used in this work to obtain the microstructures are 15-20 keV voltage and 6 mm to 10 mm working distance.

3.4.3. Vickers indentation

Resistance to plastic deformation is known as hardness [20]. In various length scales, hardness can be measured. Vickers indentation is a technique to measure the hardness on a micron scale. In Vickers hardness, the indenter used is a diamond pyramid indenter with an included angle of 136° of the opposite faces of the pyramid. This geometrically self-similar indenter is shown in Fig. 3.7, indenting the sample. Vickers indentation is a load-dependent indentation technique where higher loads will have a higher area of contact. Vickers hardness will result in the hardness value in HV, and the formulae to evaluate the HV is shown in equation 3.9.

$$HV = \frac{1.854 \times P}{d^2}...(3.9)$$

P: Applied load on the sample

d: Average diagonal length of the indentation

the diagonal length of the indentation is measured using the microscope attached to the machine (Tinius Olsen, which was used in this work). If the indentation is performed below 1 kg, then the indentation is known as microindentation. If the applied load ranges between 1 kg to 120 kg, the indentation is called macroindentation. In this work, indentation is performed from the load range 25 g to 10 kg with a dwell time of 15 s, and an average of 10 indents is considered as the hardness value and the average of 10 indents, under given set of experimental conditions,

is considered as the hardness value and associated standard deviation is reported as the error bar.

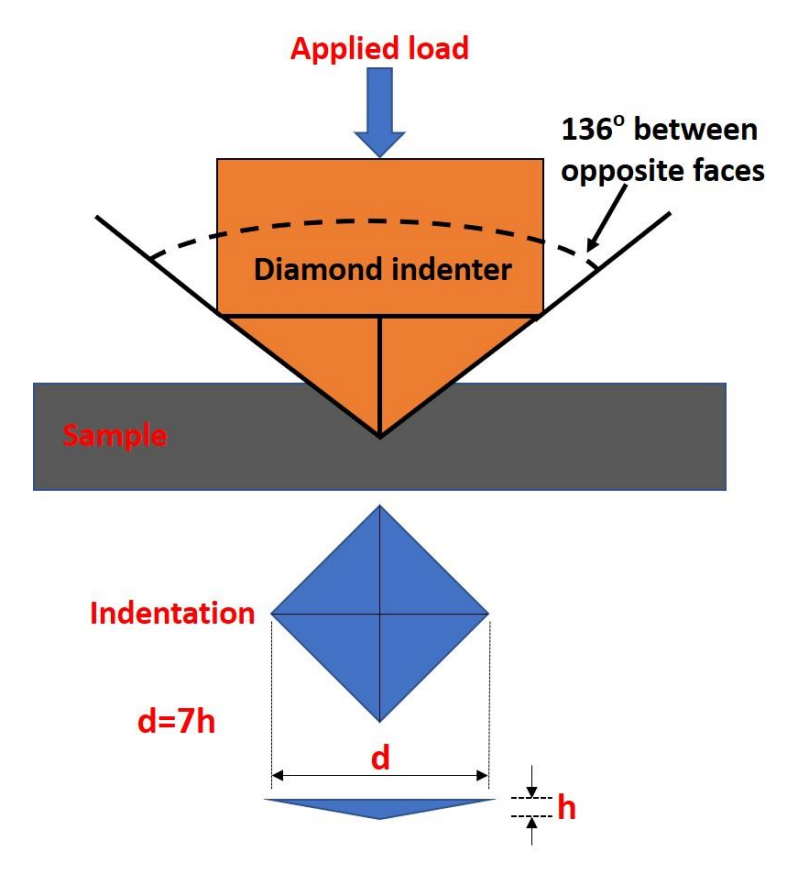


Fig. 3.7 Schematic of the Vickers indentation using a diamond indenter

3.4.4. Nanoindentation

Nanoindentation is also popularly known as depth-sensing indentation. Like Vickers indentation, this is also performed by applying the load on the sample using an indenter. In the Vickers hardness, the diagonal length is measured using the microscope. In contrast, in the nanoindentation, the contact area is measured using the analysis developed by Oliver and Pharr [21]. The method developed by Oliver and Pharr is based on the work reported by Doerner and Nix [21,22]. In the Oliver and Pharr method, the contact area is measured using the slope of the load (P) - displacement (h) unloading curve, shown in equation 3.10.

$$S = \frac{dP}{dh} = \frac{2}{\sqrt{\pi}} E_r \sqrt{A_c}.$$
(3.10)

S: Stiffness

E_r: Reduced modulus

A_c: Contact area

The effects of indentation with a non-rigid indenter are accounted using the reduced modulus. To estimate the elastic modulus of the material, equation 3.11. will be used.

$$\frac{1}{E_{\rm r}} = \frac{(1-9^2)}{E} + \frac{(1-9_{\rm i}^2)}{E_{\rm i}}...(3.11)$$

9: Poissons ratio of the material

E: Elastic modulus of the material

 θ_i : Elastic modulus of the indenter

E_i: Elastic modulus of the indenter

To estimate the hardness of the material, equation 3.12 is used

$$H = \frac{P}{A_C}...(3.12)$$

$$A_c = \sum_{n=0}^{8} c_n (h_c)^{2-n}$$
....(3.13)

The c_n coefficients are estimated by fitting the area function at different indentation depths on the test material, mostly silica, whose elastic modulus is known. h_c is the contact depth under load during nanoindentation. In this work, iMicro® nanoindenter from Nanomechanics Inc. (now KLA, Oak Ridge, TN, USA) was used for high-speed nanoindentation testing, schematic shown in Fig. 3.8. A diamond Berkovich tip was used for all the indentation tests. The area function and load frame stiffness calibration were performed as per the procedure detailed elsewhere [23]. A highspeed nanoindentation technique (Nanoblitz3D®), wherein each indent takes less than one second to perform [24], was used to obtain hardness and elastic modulus maps.

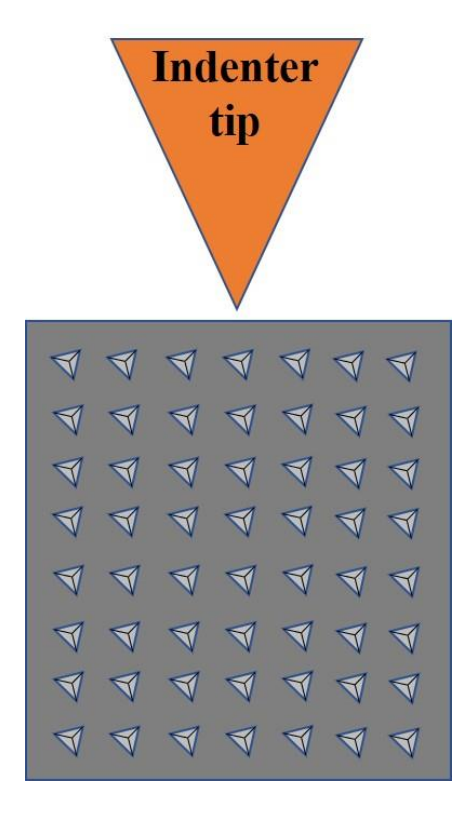


Fig. 3.8 Schematic showing the indents on the sample after high-speed nanoindentation

3.5. Heat treatment

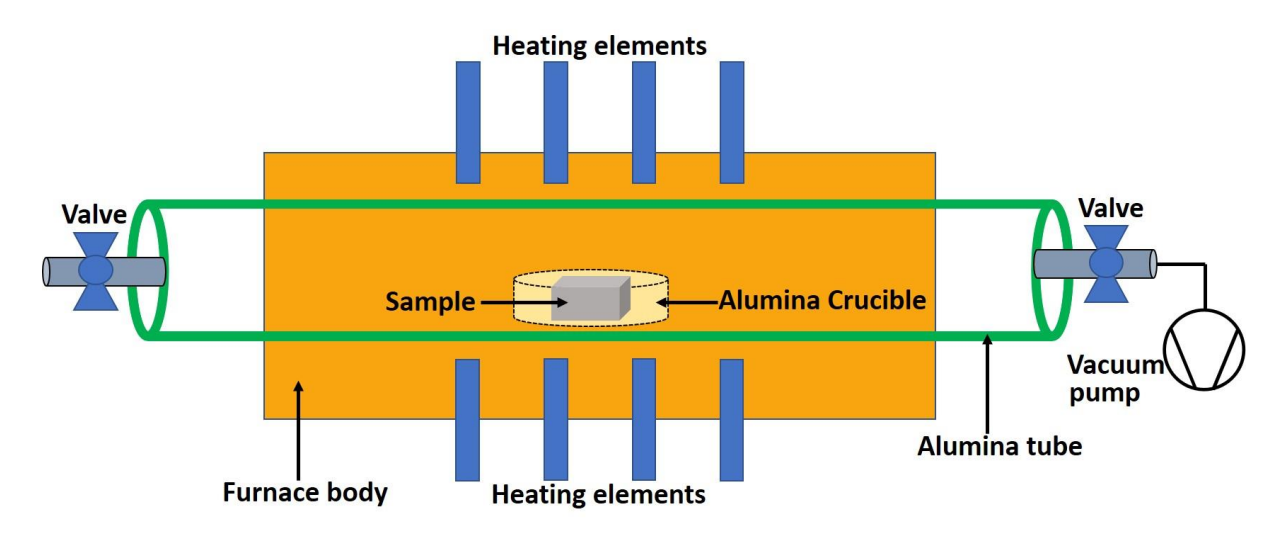


Fig. 3.9 Schematic of the tubular furnace used for the heat treatments in this work

Since the time given for solidification during arc melting was less, the as-cast samples are heat treated at different temperatures and for longer durations, so the required interdiffusion among the participating elements will happen, resulting in equilibrium microstructures. In this work,

the alloys fabricated are refractory alloys that are prone to oxidize at high temperatures. To avoid oxidation, heat treatments are performed in a tubular vacuum furnace of the capacity of running up to the maximum temperature of 1600 °C in the vacuum for up to 48 h, a schematic of the tubular furnace is shown in Fig. 3.9. This furnace has rotary and diffusion pumps to perform the heat treatments in the ultra-high vacuum of 10^{-6} mbar. First, the sample is to be loaded in an alumina crucible, and then the crucible is to be loaded into the furnace. Then the alumina tube is to be evacuated using the vacuum pumps until the pressure reaches 10^{-6} mbar. Then the furnace is to be switched on based on the heat treatment cycle.

References

- [1] C. Suryanarayana, C.C Koch, Nanocrystalline materials Current research and future directions. HyperfineInteractions 130 (2000) 5–44.
- [2] C.C. Koch, Nanostructured Materials Processing, Properties and Applications, 2nd Edition. 2006.
- [3] H. Gleiter, Nanocrystalline materials. Progress in Materials Science, 33 (1989) 223-315. https://doi.org/10.1016/0079-6425(89)90001-7
- [4] A. Kumar, A. Singh, A. Suhane, Mechanically alloyed high entropy alloys: existing challenges and opportunities, J. Mater. Res. Technol. 17 (2022) 2431–2456. https://doi.org/10.1016/j.jmrt.2022.01.141.
- [5] M. Vaidya, G.M. Muralikrishna, B.S. Murty, High-entropy alloys by mechanical alloying: A review, J. Mater. Res. 34 (2019) 664–686. https://doi.org/10.1557/jmr.2019.37.
- [6] C. Suryanarayana, Mechanical alloying and milling, Prog. Mater. Sci. 46 (2001) 1–184. https://doi.org/10.1016/S0079-6425(99)00010-9.
- [7] V. Mamedov, Spark plasma sintering as advanced PM sintering method, Powder Metall. 45 (2002) 322–328. https://doi.org/10.1179/003258902225007041.
- [8] Y.H. Han, R. Gao, I. Bajpai, B.N. Kim, H. Yoshida, A. Nieto, H.W. Son, J. Yun, B.K. Jang, S. Jhung, Z. Jingming, K.H. Hwang, F. Chen, J.F. Shackelford, S. Kim, Spark bioceramics-from transparent hydroxyapatite sintered to graphene nanocomposites: a review, Adv. Ceram. 119 (2020)57-74. Appl. https://doi.org/10.1080/17436753.2019.1691871.
- [9] S. Grasso, Y. Sakka, G. Maizza, Electric current activated/assisted sintering (ECAS): A review of patents, Sci. Technol. Adv. Mater. 10 (2009) 1906-2008.

- https://doi.org/10.1088/1468-6996/10/5/053001.
- [10] M. C. Hebeisen, H. J. Wagner, S. G. Nelson, C. A. Alexander, E. L. Foster, D. P. Moak, J. M. Blocher, Vacuum Melting and Casting of Superalloys, National Aeronautics and Space Administration Washington, D.C, 1971.
- [11] B. Akhil, A. Bajpai, K. Biswas, Microstructure and mechanical properties of the new TiZrHfReAl HCP high entropy alloy, Philos. Mag. Lett. 102 (2022) 287–298. https://doi.org/10.1080/09500839.2022.2120644.
- [12] O.N. Senkov, J.M. Scott, S. V. Senkova, D.B. Miracle, C.F. Woodward, Microstructure and room temperature properties of a high-entropy TaNbHfZrTi alloy, J. Alloys Compd. 509 (2011) 6043–6048. https://doi.org/10.1016/j.jallcom.2011.02.171.
- [13] C. Juan, M. Tsai, C. Tsai, C. Lin, W. Wang, C. Yang, S. Chen, S. Lin, J. Yeh, Enhanced mechanical properties of HfMoTaTiZr and HfMoNbTaTiZr refractory high-entropy alloys, Intermetallics. 62 (2015) 76–83. https://doi.org/10.1016/j.intermet.2015.03.013.
- [14] L. Raman, A. Anupam, G. Karthick, C.C. Berndt, A.S.M. Ang, S.V.S. Narayana Murty, D. Fabijanic, B.S. Murty, R.S. Kottada, Strengthening mechanisms in CrMoNbTiW refractory high entropy alloy, Mater. Sci. Eng. A. 819 (2021) 141503. https://doi.org/10.1016/j.msea.2021.141503.
- [15] D.G. Kalali, S. Antharam, M. Hasan, P.S. Karthik, P.S. Phani, K. Bhanu Sankara Rao, K. V. Rajulapati, On the origins of ultra-high hardness and strain gradient plasticity in multi-phase nanocrystalline MoNbTaTiW based refractory high-entropy alloy, Mater. Sci. Eng. A. 812 (2021) 141098. https://doi.org/10.1016/j.msea.2021.141098.
- [16] O.N. Senkov, G.B. Wilks, J.M. Scott, D.B. Miracle, Mechanical properties of Nb 25Mo 25Ta 25W 25 and V 20Nb 20Mo 20Ta 20W 20 refractory high entropy alloys, Intermetallics. 19 (2011) 698–706. https://doi.org/10.1016/j.intermet.2011.01.004.
- [17] O.N. Senkov, D.B. Miracle, S.I. Rao, Correlations to improve room temperature ductility of refractory complex concentrated alloys, Mater. Sci. Eng. A. 820 (2021) 141512. https://doi.org/10.1016/j.msea.2021.141512.
- [18] Z.D. Han, N. Chen, S.F. Zhao, L.W. Fan, G.N. Yang, Y. Shao, K.F. Yao, Effect of Ti additions on mechanical properties of NbMoTaW and VNbMoTaW refractory high entropy alloys, Intermetallics. 84 (2017) 153–157. https://doi.org/10.1016/j.intermet.2017.01.007.
- [19] Cullity, B.D. (1978) Elements of X-Ray Diffraction. 2nd Edition, Addison-Wesley Publishing Company Inc., Phillippines.
- [20] G. E. Dieter, Mechanical Metallurgy- McGraw-Hill Book Company, London, 1928.

- [21] Oliver, W.C. and Pharr, G.M., An Improved Technique for Determining Hardness and Elastic Modulus Using Load and Displacement Sensing Indentation Experiments. J. 55 Chapter 3 Experimental details Mater. Res., 7 (1992) 1564-1583. https://doi.org/10.1557/JMR.1992.1564.
- [22] Doerner, M.F., Nix, W.D. A method for interpreting the data from depth-sensing indentation instruments. J. Mater. Res. 1 (1986) 601–609.
- [23] P. Sudharshan Phani, W.C. Oliver, G.M. Pharr, Measurement of hardness and elastic modulus by load and depth sensing indentation: Improvements to the technique based on continuous stiffness measurement, J. Mater. Res. 36 (2021) 2137–2153. https://doi.org/10.1557/s43578-021-00131-7.
- [24] B. Vignesh, W.C. Oliver, G.S. Kumar, P.S. Phani, Critical assessment of high speed nanoindentation mapping technique and data deconvolution on thermal barrier coatings, Mater. Des. 181 (2019) 108084. https://doi.org/10.1016/j.matdes.2019.108084.

Chapter 4

Results and Discussion

4.1. Ultra high hardness and strain gradient plasticity in multi-phase nanocrystalline MoNbTaTiW based refractory high-entropy alloy

4.1.1. Introduction

Increasing the configurational entropy of a material system by adding number of elements and choosing the composition with no-bias towards any specific element has revolutionized the science of alloy development [1-4]. This also led to the realization of unprecedented mechanical properties in various alloy systems [3,5]. Although near-infinitesimal alloy compositions can be thought of by resorting to several permutations and combinations of the elements present in the periodic table with sound scientific/technological considerations [6,7], the ones based on refractory elements hold much promise in terms of realizing high temperature materials which can withstand high service temperatures and mechanical stresses than the existing materials [8]. Among refractory high-entropy alloys (RHEAs), MoNbTaW and alloys thereof have received much attention and the observed promising mechanical properties are well documented [9,10]. Majority of these investigations were performed on the samples prepared by melting and casting route. In order to realize the probable exceptional strength values, structural/microstructural refinement should be adapted [7] and multi-phase structure (combination of phases with different crystal structures) is always desirable to achieve both high strength and acceptable levels of plasticity [11] for structural engineering applications. In addition, to decrease the density of these alloys, alloying element (s) should judiciously be selected. In view of all these factors, Ti is chosen and added in equiatomic proportion to MoNbTaW composition so that its overall density is reduced and the presence of Ti is also expected to assist in retaining the high temperature properties of MoNbTaW alloy system. A combination of mechanical alloying and spark plasma sintering (SPS) was adapted to fabricate a multi-phase, nanocrystalline complex solid solutions. Depth dependence of hardness was widely studied in conventional crystalline materials [12]. However, this aspect has not been reported in recently developed high-entropy alloys. Motivated by all these factors, sintered bulk sample was characterized using Vickers microindentation to understand the bulk plastic deformation characteristics. In this paper, our efforts are presented on the origins of various

strengthening contributions, indentation size effect vis-à-vis the observed structural/microstructural features in this multi-phase concentrated alloy system.

4.1.2. Experimental procedure

Mechanical alloying (MA) was performed in SPEX 8000D shaker mill at room temperature using hardened steel milling media. The elemental raw powders (-325 mesh size mixed in nominally equiatomic composition) were of purity greater than 99.5% and stearic acid was used as process controlling agent during milling under high purity Argon atmosphere. X-ray diffraction (XRD) was done using BRUKER D8 ADVANCE equipment Cu Ka radiation $(\lambda=1.5418 \text{ Å})$ in the scan range (2 Θ) between 20° to 120° with a step size 0.02° and scan time 1sec/step. Scanning electron microscopy and elemental analysis was done using a Field emission scanning electron microscope (FEI Nova NanoSEM 450) incorporated with energy dispersive spectroscopy (EDS). The milled powders were converted into bulk objects by spark plasma sintering (SPS) Dr. SINTER 1050 apparatus (SPS Syntex Inc., Tokyo, Japan) at 1473 K at a heating rate of 7.21 K/s, holding time of 15 min and uniaxial pressure of 80 MPa. Thus obtained disc was metallographically polished for subsequent characterization and density measurements (The Archimedes principle method). Phase fractions of the microstructure are calculated using ImageJ analysis. Crystallite size was estimated from broadened X-ray peaks using the Scherrer method after accounting for instrumental broadening and lattice microstrain was obtained using the Stokes-Wilson formula. Microhardness measurements (Tinius Olsen) were done on the alloy, after careful sample preparation, at various loads in the range 25-500 g and a dwell time of 15 sec. At a given test condition, a total of 10 indentations were made and the average as well as corresponding standard deviation are reported. Nanoindentation was performed using Hysitron TI-950 nanoindenter with a peak load of 8000 µN, loading rate 1000 $\mu N/s$, and holding time of 30 s with a spacing of 5 μm between the two consecutive indents.

4.1.3. Results and discussion

Structural evolution

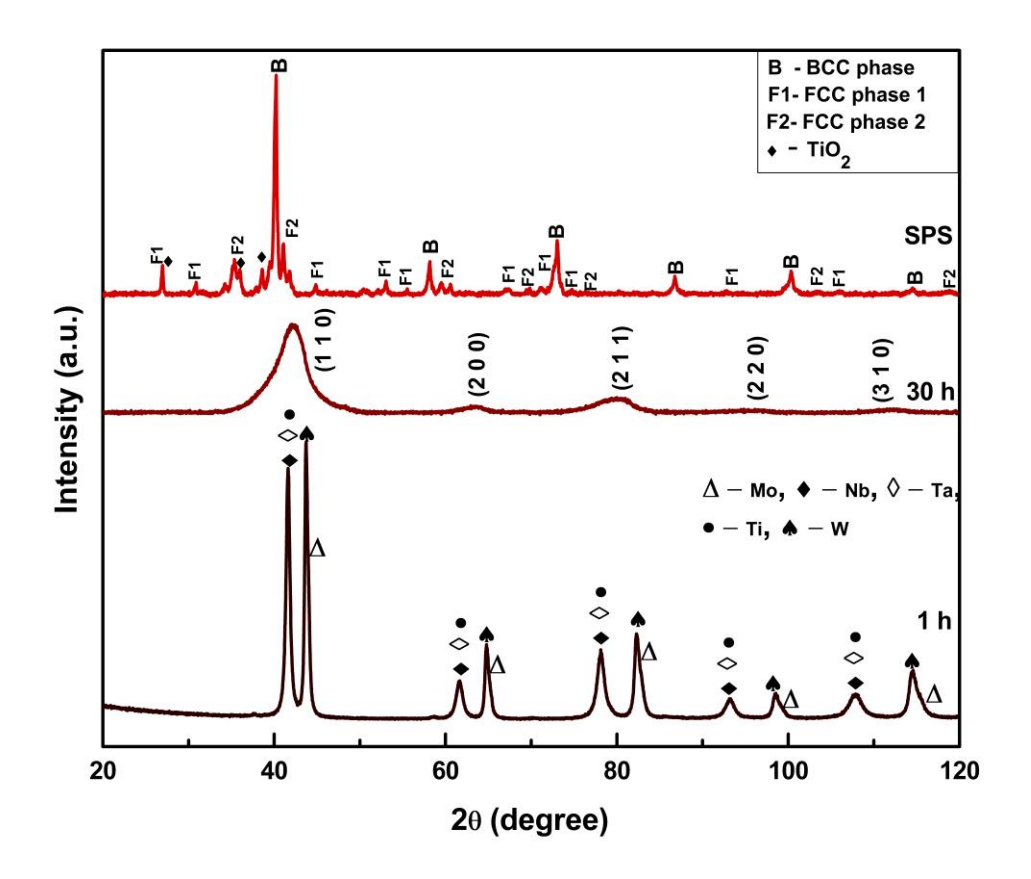


Fig. 4.1 X-ray diffractograms of 1 h milled, 30 h milled and sintered MoNbTaTiW alloy. Milling for 30 h resulted in a single phase BCC phase complex solid solution; upon sintering at 1473 K, this BCC has decomposed into a new BCC phase and two different FCC phases (FCC1, FCC2). A minor presence of TiO₂ is also noticed.

Fig. 4.1. shows X-ray diffractograms, depicting the structural variations in MoNbTaTiW alloy at the beginning of the milling (1h), after 30 h of milling and sintering at 1473 K subsequent to 30 h of milling. After 1 h of milling, it is evident that all the elements are present in their elemental form. After 30 h of milling, complete alloying has happened leading to the formation of a single phase BCC complex concentrated alloy. The interplanar spacings (d) of this phase are measured to be 2.14 Å, 1.46 Å, 1.20 Å, 1.04 Å, 0.92 Å for (110), (200), (211), (220), (310) reflections, respectively, with a crystallite size of 3 nm, microstrain of 0.029 and a lattice parameter of 2.91 \pm 0.02 Å. After sintering, it appears that as-milled BCC phase has decomposed into a new BCC phase and two FCC phases. The crystallite size of new phases

was estimated to be 22 nm, 25 nm and 22 nm for BCC, FCC1 and FCC2 phases respectively. The lattice microstrain was found to be 0.0031, 0.0031 and 0.0036 for BCC, FCC1 and FCC2 phases respectively with the lattice parameters of 3.17 Å, 5.58 Å and 4.38 Å in the same order as mentioned above. Fig. 4.2. presents BSE-SEM image of the sintered sample containing various phases as evidenced in Fig. 4.1. Primarily three types of contrast (grey, dark and bright) can be seen from Fig. 4.2. Phase quantification was done using X-ray data (Fig. 4.1) and SEM data (Fig. 4.2). There is a very close agreement among the estimations done (Table 4.1) on the phase fractions from these two methods and the average is considered for rest of the discussion in this paper. The average phase fractions are 47.52 %, 16.16 %, 36.36 % for grey phase (BCC), dark (FCC1) and bright (FCC2) respectively. X-ray data was derived from Fig. 4.1 and ImageJ analysis was done on BSE-SEM image shown in Fig. 4.3.

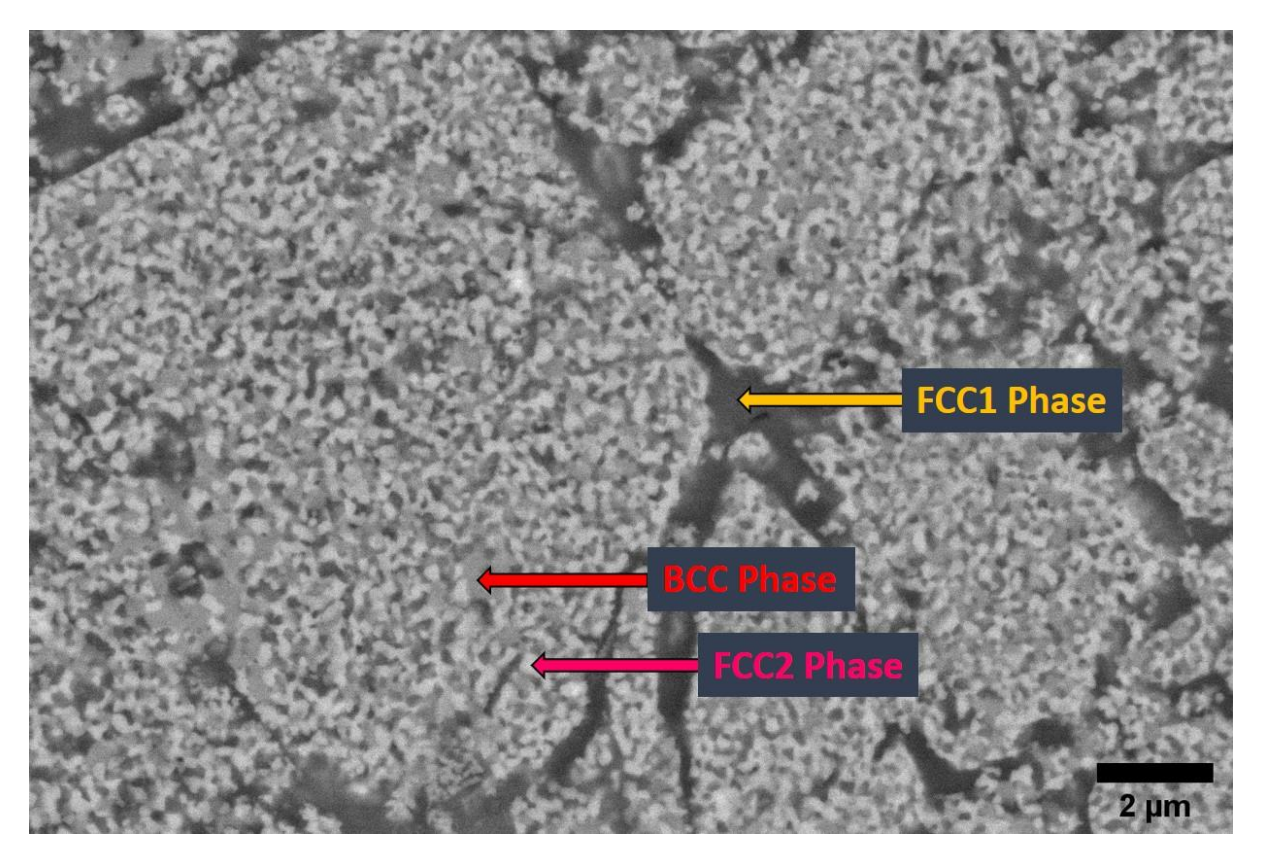


Fig. 4.2 BSE image of sintered sample showing the contrast from three different phases (Grey, dark and bright). By considering the phase fractions from both X-ray analysis and BSE-SEM analysis, Grey phase, dark phase and bright phase are confirmed as BCC, FCC1 and FCC2 respectively.

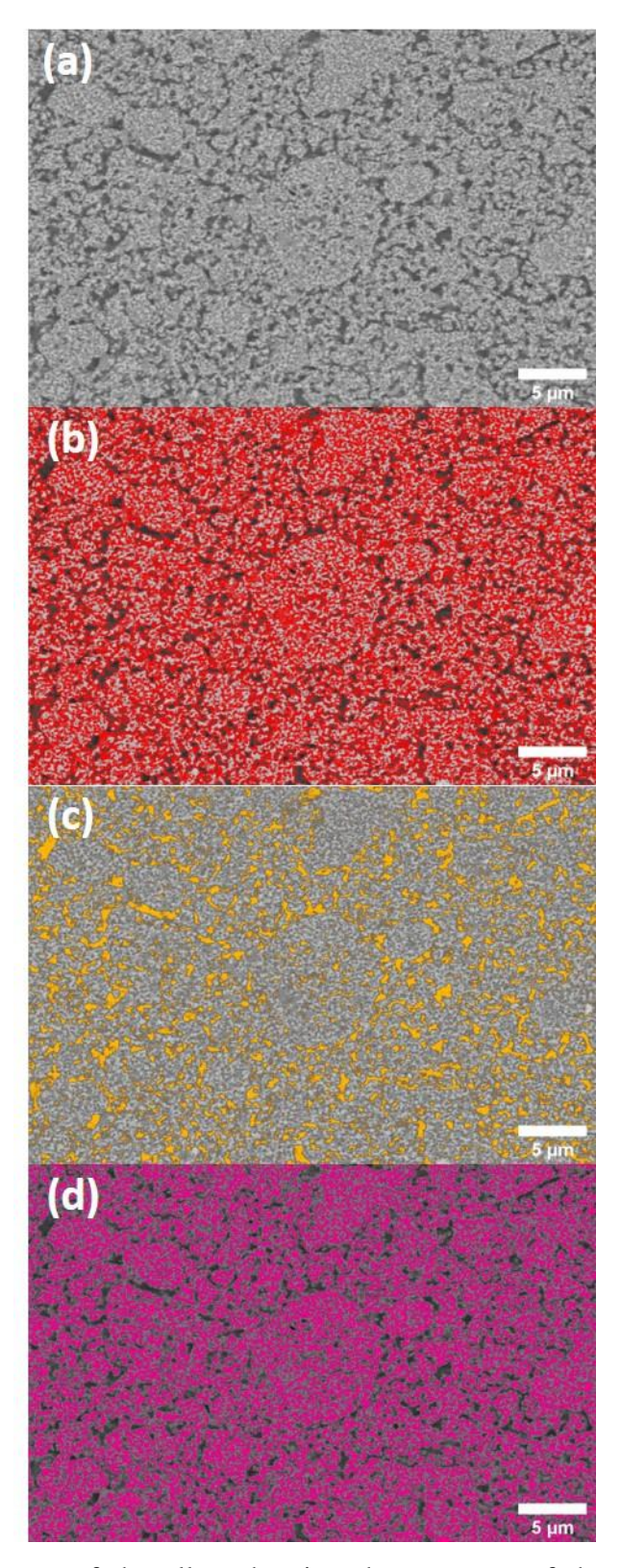


Fig. 4.3 BSE-SEM image of the alloy showing the presence of three different phases in different contrasts (grey, dark and bright) (a); location of grey phase (BCC) shown in red color in (b); location of dark phase (FCC1) shown in yellow color in (c); location of bright phase

(FCC2) shown in pink color (d). It is clear that the microstructural length scale (particle size) of the individual phases is within the sub-micron range.

Table 4.1 Amount of different phases estimated from X-ray diffractograms and BSE-SEM images

Phase	Phase percentage	Phase percentage	Average phase
	(From XRD)	(From BSE-SEM)	percentage from
			XRD and BSE-
			SEM analyses
BCC (Grey)	47.30	47.75	47.52
FCC1 (Dark)	16.83	15.49	16.16
FCC2 (Bright)	35.86	36.76	36.31

EDS analysis in SEM was done to understand the composition of the individual phases (Fig. 4.4); FCC1 is Ti-rich whereas BCC and FCC2 phases have nearly equiatomic presence of the elements. Resolving of individual composition of BCC and FCC2 phases was beyond the capability of EDS, therefore based on spot analysis at multiple locations, we accord similar compositional details to BCC and FCC1 phases for all practical reasons. Incidentally, it is also observed that Fe has entered from the milling media. It is fortuitous that Fe is also BCC, contributing to further solid solution strengthening of this alloy, although it was not intentionally added.

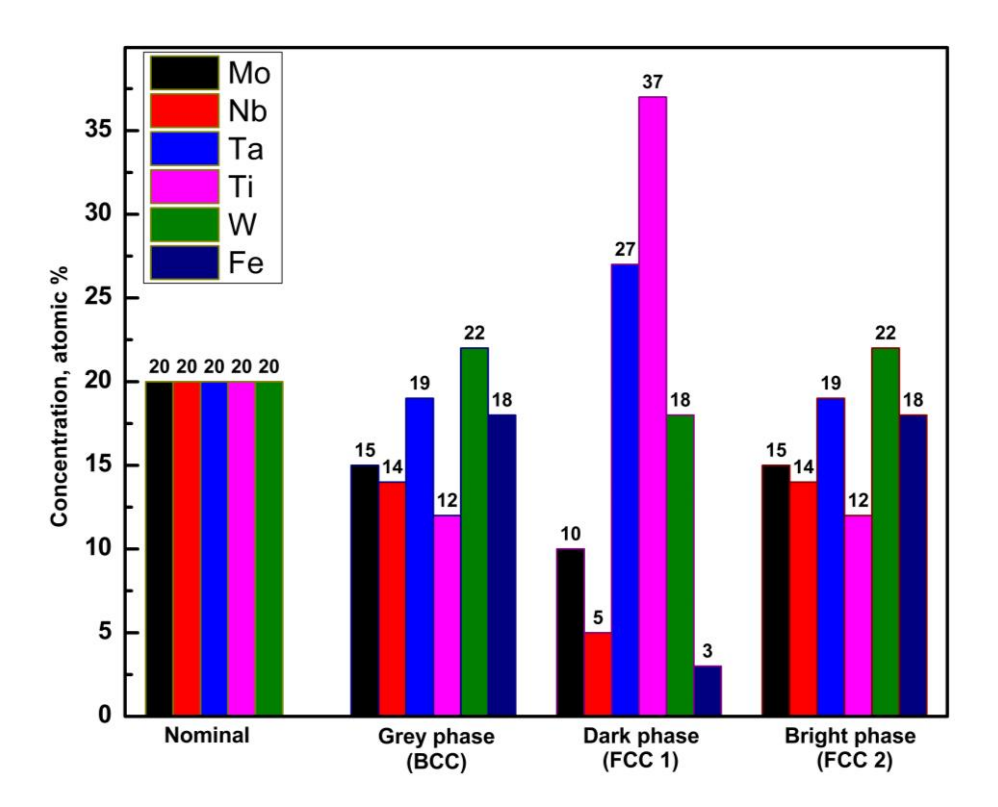


Fig. 4.4 Bar chart showing the elemental composition (at. %) in various phases observed in this alloy. This data was obtained using spot analysis in SEM-EDS. Nominal compositions was also shown for comparison purposes.

Using rule of mixtures, melting point (T_M) of this alloy is calculated to be 2914 K. SPS was done at 1473 K and it corresponds to a homologous temperature of 0.5. Normally one would expect that the as-milled BCC phase should be retained after SPS as was seen in other studies on the similar alloy system [13]. But it is to be noted that Ti (T_M=1941 K) and unintentionally present Fe (T_M=1811 K) are the low melting elements in this alloy in comparison to rest of the elements. The chosen SPS temperature of 1473 K corresponds to a homologous temperature of 0.76 in case of Ti and 0.81 in case of Fe. As a result, it is plausible to envisage interdiffusion of Ti and Fe atoms out of the complex BCC solid solution lattice which was obtained after 30 h of milling (Fig. 4.1). Further, as milled complex concentrated BCC phase has an extremely finer crystallite size of 3 nm with the presence of all the alloying elements including Fe. At this length scale (grain size being in nm range), volume fraction of interfaces such as grain boundaries, triple junctions, quadruple junctions would be significantly high fostering the interdiffusion of Ti and Fe at that high homologous temperature. As a result, the as-milled BCC lattice was made unstable leading to the formation of a different BCC phase and two other FCC (FCC1, FCC2) phases with lattice constants different from the parent milled phases. Therefore,

it is not unreasonable to imagine that Ti, Fe as well as finer grain size are responsible for the decomposition of as-milled BCC phase. The density of SPS sample was measured (using the Archimedes principle method) to be 10.14 g/cc and no pores were observed in the sample during SEM investigations indicating that full-density is achieved in this alloy.

Mechanical properties

Vickers microhardness measurements were made on the sintered sample at various loads and the corresponding data is presented in Fig. 4.5. It is very encouraging to observe very high values of hardness in the range 18.87-13.89 GPa, which are currently the highest reported values in this alloy. It is clear that as the load (indentation depth) increases, hardness decreases suggesting a very distinguishable indentation size effect (ISE). The pronounced ISE observed at low loads is exhausted at higher loads, as expected, and reaches a lower limiting value of 13.89 GPa. There is a pronounced hardness decrement at low loads (25-50 g) and it was getting saturated with the further increase in load.

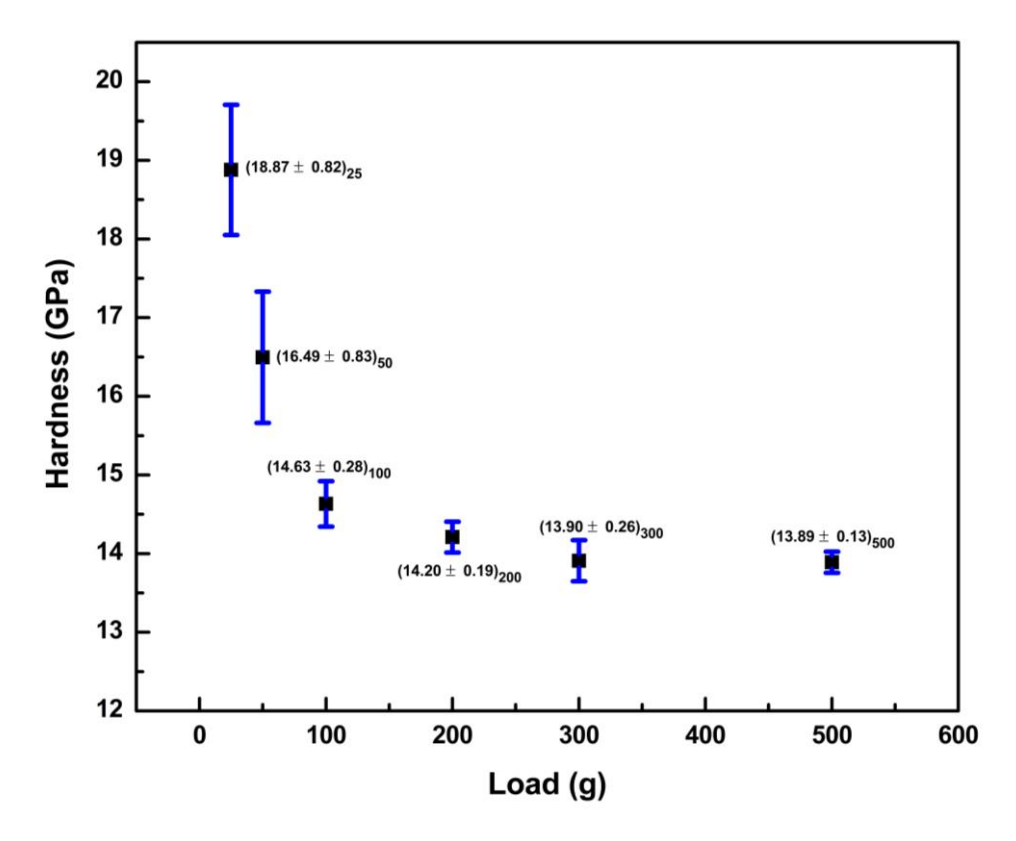


Fig. 4.5 Variation of microhardness at different indentation loads in multi-phase MoNbTaTiW-Fe alloy. A high hardness of 18.87 GPa was observed at 25 g load and a pronounced indentation size effect can be seen as the load is increased to 500 g.

The average indent diagonal lengths are 4.9 μ m, 7.4 μ m, 11.17 μ m, 16.0 μ m, 19.8 μ m, 25.63 μ m at indentation loads of 25 g, 50 g, 100 g, 200 g, 300 g, 500 g respectively. The microstructural length scale (particle size) of individual phases is in submicron range (Fig. 4.2) and the grain size is in the range 22-25 nm (Table 4.2). Hence, even at the lowest load (diagonal length of 4.9 μ m), the indent impression and thereby the associated plastic zone encompasses multiple grains and /or phases. This implies that the indentation response is a composite response of all the constituents. Further, no cracks were observed during indentation studies, suggesting that the alloy exhibits reasonable levels of plasticity. In spite of the multi-phase/ multi-grain response at low loads, wherein, numerous defects are expected to be present in the highly stressed zone near the indenter tip to facilitate deformation, it is interesting to note that the alloy exhibits ISE.

Table 4.2 Grain size and Hall-Petch strengthening contributions of various phases

Phase	Grain size (nm)	Hall-Petch Constant	Δσ _{HP} (MPa)
		(K_{HP}) $(MPa\sqrt{m}),$	
BCC	22	0.27	1820
FCC1	25	0.27	1710
FCC2	22	0.27	1820

The obtained lower limit of hardness of 13.89 GPa at 500 g load was normalized by the density (10.14 g/cc) and a comparison was made with several MoNbTaW based alloys reported in the literature (Fig. 4.6). It is highly fascinating to see that the present alloy clearly possesses a very high "density-normalized" hardness among various investigations in this family of RHEA alloys. This extremely high hardness can result from finer grains size and resultant high fraction of strain hardening arising out of dislocation-grain boundaries interactions, solid solution strengthening, lattice frictional stress, composite strengthening from multiple phases present. The details of the various strengthening mechanisms are presented in the following section.

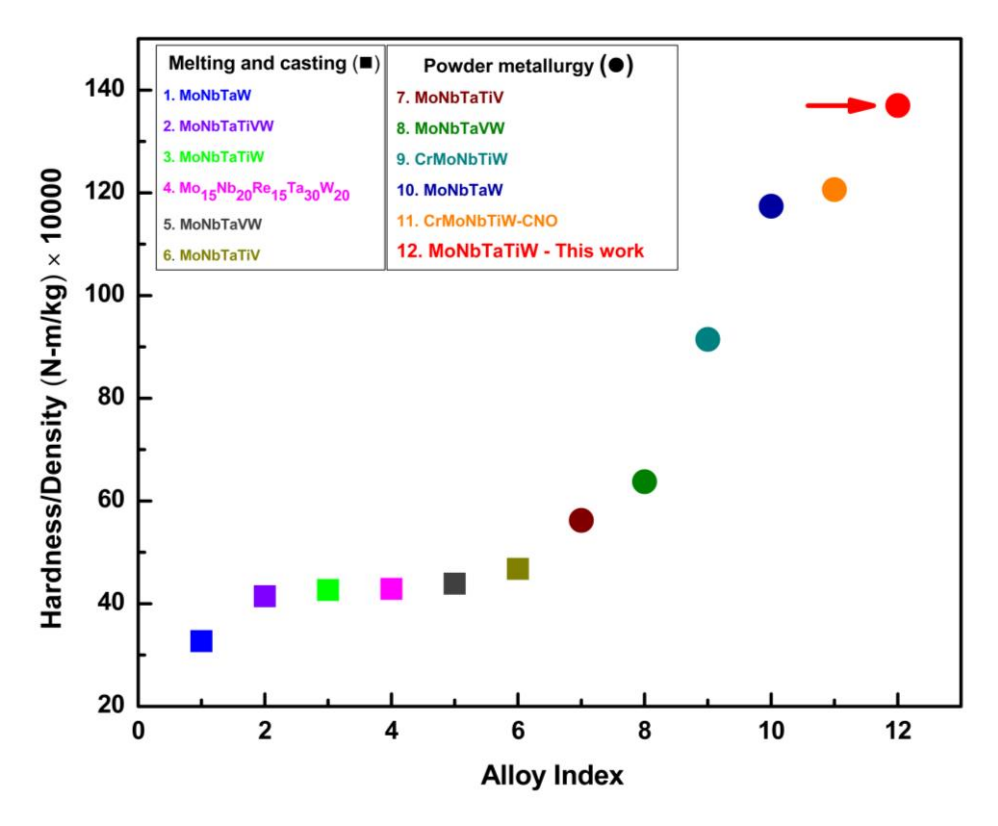


Fig. 4.6 Compilation of hardness data of similar alloys (processed by melting + casting, Powder metallurgy) from the literature [13-21]; hardness values are normalized with the densities of corresponding alloys. It is clear that the present alloy shows an exceptional absolute hardness (Fig. 4.5) and "density-normalized" hardness (indicated with an arrow).

Strengthening mechanisms

To begin, the hardness of 13.89 GPa obtained at an indentation load of 500 g (Fig. 4.5) is considered to explore the origins of strengthening in this alloy. Later the contribution from ISE will be presented. Using the Tabor's formula for metallic materials, we can write $\sigma_{flow} = \frac{H}{C}$; Where σ_{flow} is flow stress and C is the constraint factor which was observed to be around 3 for different materials [22]; flow stress of this alloy, therefore, assumes a value of 4.63 GPa. The structural (Fig. 4.1) and microstructural (Fig. 4.2 & Fig. 4.3) investigations on the present alloy reveal that it consists of three concentrated solid solution phases (BCC, FCC1, FCC2) with finer grain sizes (22 nm, 25 nm, 22 nm). Therefore it is proposed that the observed ultra-high flow stress could be originating from frictional stress offered by individual lattices, strain hardening arising from intersection of dislocations in these three different phases, Hall-Petch strengthening from the finer grain sizes of the individual phases and solid solution strengthening effects in all the three phases. Based on that, the following superposition among different plausible (independent and additive) strengthening contributions has been considered:

$$\sigma_{\text{flow}} = \{ f_{\text{BCC}} x (\sigma_{\text{o}} + \Delta \sigma_{\text{SH}} + \Delta \sigma_{\text{HP}} + \Delta \sigma_{\text{SSS}})_{\text{BCC}} + f_{\text{FCC1}} x (\sigma_{\text{o}} + \Delta \sigma_{\text{SH}} + \Delta \sigma_{\text{HP}} + \Delta \sigma_{\text{SSS}})_{\text{FCC1}} +$$

$$f_{FCC2} x \left(\sigma o + \Delta \sigma_{SH} + \Delta \sigma_{HP} + \Delta \sigma_{SSS}\right)_{FCC2} \right\} (4.1)$$

Where σ_0 is the lattice frictional stress, $\Delta\sigma_{SH}$ is dislocations hardening /strain hardening/Taylor hardening, $\Delta\sigma_{HP}$ is the Hall-Petch strengthening, $\Delta\sigma_{SSS}$ is the contribution from solid solution strengthening. The symbol 'f' represents the corresponding phase fraction of a phase.

Frictional stress (σ_0) of a given phase is calculated by, $\sigma_0 = \Sigma \left(C_i \times \sigma_0^i \right)$; where C_i is the concentration of i^{th} element constituting the phase and σ_0^i is the lattice fractional stress of the given element at room temperature reported in the literature [23]. Using this approximation, the room temperature frictional stresses of BCC, FCC1, FCC2 phases are calculated as 282 MPa, 289 MPa, 282 MPa respectively. It is to be mentioned that compositions of the individual elements of the present alloy including Fe in a given phase are taken from the EDS analysis presented in Fig. 4.4.

Taylor hardening, or strain hardening can be estimated using the equation 4.2.

$$\Delta\sigma_{SH} {=} M \; \alpha \; G \; b \; \sqrt{\rho_{SSD}}.....(4.2)$$

M is the Taylor factor (=3.06 for both fcc and bcc materials) [24], α is a correction factor (taken as 0.3 [25]). Elastic modulus of this alloy was measured, using nanoindentation, to be 217 GPa. Assuming elastic isotropy, shear modulus G was calculated, using $G = \frac{E}{2(1+\upsilon)}$; υ is the Poisson's ratio (\approx 0.33), to be 82 GPa. Statistically stored dislocation density, $\rho_{SSD} = 2\sqrt{3}\frac{\epsilon}{Db}$; ϵ is lattice microstrain; D is the grain size and b is the magnitude of the Burgers vector. From X-ray analysis (Fig. 4.1), grain size, lattice parameter and lattice microstrain were calculated for all the three phases. By making use of these values, magnitude of the Burgers vectors of individual phases and corresponding densities of statistically stored dislocations are calculated. Using this approach, contributions arising out of strain hardening due to intersection of dislocations in various phases are calculated and are shown in the Table 4.3.

Table 4.3 Lattice parameter, lattice microstrain, Burgers vector, dislocation density and strain hardening contributions of BCC, FCC1, FCC2 phases.

Phase	Lattice	Lattice	Magnitude of	$\rho_{SSD}\left(\frac{1}{m^2}\right)$	Δσ _{SH} (MPa)
Parameter	parameter, a	microstrain	Burgers	(111-7	
	(nm)	(ε)	Vector (b),		
			nm;		
			$(b) = \left(\frac{a}{2}\right)\sqrt{3},$		
			for BCC;		
			$\left(\frac{a}{2}\right)\sqrt{2}$, for		
			FCC)		
BCC	0.317	0.0031	0.274	1.7×10^{15}	866
FCC1	0.558	0.0031	0.394	1.1×10^{15}	974
FCC2	0.438	0.0036	0.31	1.8×10^{15}	993

The dependence of flow stress on grain size follows the Hall-Petch equation and the corresponding strengthening contribution can be calculated by

$$\Delta \sigma_{HP} = K_{HP} d^{-0.5}$$
....(4.3)

Hall-Petch constants (K_{HP}) are not reported for this alloy in the literature. However, Hall-Petch constant of 0.27 MPa \sqrt{m} , for the grain size range 26.9-205 μm , was reported for another equiatomic RHEA HfNbTaZrTi [26]. Since it is a nearest RHEA to the present alloy, similar Hall-Petch constants are considered for all the phases of the current alloy system with the assumption that same Hall-Petch constant is also valid from nano to micro range of grain sizes, as reported in the case of CoCrFeMnNi [27]. It is to be noted that Hall-Petch constant for a given conventional crystalline material will be usually smaller if the average grain size is in nm range [28]. However, in view of the non-availability of grain size dependent Hall-Petch slope for HEAs in general and the present RHEA in particular, it is assumed that the Hall-Petch constant reported in ref. [26] is considered for the nm range grain sizes also in the present study. As a result, the obtained grain size contributions of different phases towards strengthening are given in Table 4.2.

Solid solution strengthening (SSS) has been expected to be the predominant contribution due to the fact these are highly concentrated solid solutions. The differences in the atomic radii and shear moduli values of the respective individual elements are believed to contribute to overall

solid solution strengthening of the HEAs. Methodology for the theoretical calculation of SSS was initially offered by Labush [29,30], and the same was utilized for the several HEAs [31,32]. If there are 'n' elements in an alloy, there will be strengthening contribution from each element for the SSS.

SSS of the ith element is given by

$$\Delta\sigma_i = AGf_i^{\frac{4}{3}}C_i^{\frac{2}{3}}....(4.4)$$

 C_i — atomic percent of the i^{th} element (obtained from the EDS analysis of the respective phases using spot analysis in the present study), A is a material constant with the value of 0.04 [33], and f_i is the mismatch parameter can be obtained from the below formula, $f_i = \sqrt{\delta_{Gi}^2 + \alpha^2 \delta_{ri}^2}$; δ_{ri} is atomic size mismatch parameter, δ_{Gi} is atomic modulus mismatch of the respective i^{th}

element and α (= 9) is the interaction force between the screw and edge dislocations with the solute atom [33]. Since it is a multi-phase and heavily concentrated alloy in the present study, δ_{ri} and δ_{Gi} are calculated by considering the corresponding crystal structures.

For BCC, $\delta_{ri}=\frac{9}{8}\Sigma C_j\delta_{rij}$, the i^{th} atom will have 8 nearest neighbouring atoms in a BCC lattice, therefore the fraction $\frac{9}{8}$ is considered. For FCC, $\delta_{ri}=\frac{13}{12}\Sigma C_j\delta_{rij}$, the i^{th} atom will have 12 neighbouring atoms in a FCC lattice, therefore the fraction $\frac{13}{12}$ is considered.

Similarly, atomic modulus mismatch was also calculated using the below formulae

For BCC,
$$\delta_{Gi} = \frac{9}{8} \Sigma C_j \delta_{Gij}$$
; For FCC, $\delta_{Gi} = \frac{13}{12} \Sigma C_j \delta_{Gij}$

In the present work, the material system consists of one BCC and two FCC phases. The composition of the individual elements in the respective phases was analyzed by EDS (Fig. 4.4) and these details are considered presented in this section. Although the present authors intend to manufacture only MoNbTaTiW alloy, unwanted introduction of Fe by the processing route (Fig. 4.4) was not ignored and the corresponding composition of Fe was also considered in all the estimations. Therefore, Fe is also used as the 6th element in the SSS calculations.

Atomic radii mismatch and atomic modulus mismatch for various binaries can be calculated by using the following formulae:

$$\delta_{rij} = \frac{2 \times (r_i - r_j)}{(r_i + r_j)}; \qquad \qquad \delta_{Gij} = \frac{2 \times (G_i - G_j)}{(G_i + G_j)}$$

 r_i is the atomic radius of the respective element. G_i is shear modulus of the respective elements, and all these calculates are shown in Table 4.4. Using Gypen and Deruyttere approach [34],

the SSS of the corresponding phase of the present multi-phase alloy is calculated using equation 4.5 given below and the corresponding details are shown in Table 4.5.

Table 4.4 Atomic radius and shear modulus (G) of various participating elements in the present alloy system, taken from ref. [35]

Element	Atomic radius, Å	Shear modulus (G), GPa
Mo	1.363	123
Nb	1.429	59.5
Ta	1.430	64.7
Ti	1.462	37.3
W	1.367	152
Fe	1.241	80.4

Table 4.5 Calculated various parameters and quantities used in estimating the SSS contribution

					Shear			
					modulus			
					of alloy			
	Eleme				(G),			$\Delta\sigma_{\mathrm{sss}}$,
Phase	nt	δ_{ri}	δ_{Gi}	$\mathbf{f_i}$	GPa	C_{i}	$\Delta\sigma_{i}$	MPa
	Mo	-0.008621	0.417203	0.4243569		0.152	0.297905	
	Nb	0.0445322	-0.35216	0.5335239		0.138	0.379023	
BCC	Ta	0.0453183	-0.26418	0.4859455	82	0.184	0.405386	2120
	Ti	0.0701811	-0.81705	1.0327252		0.123	0.846818	
	W	-0.005327	0.631805	0.6336212		0.222	0.654458	
	Fe	-0.11394	-0.033	1.025993		0.181	1.086056	
	Mo	-0.04191	0.617878	0.723909		0.102	0.465428	
	Nb	0.0092955	-0.09959	0.1300624		0.051	0.029725	
FCC 1	Ta	0.010053	-0.0148	0.0916793	82	0.274	0.057201	1750
	Ti	0.0340176	-0.56125	0.6393201		0.364	0.920943	
	W	-0.038737	0.809358	0.8812529		0.178	0.876909	
	Fe	-0.143257	0.204435	1.3054229		0.031	0.461796	
	Mo	-0.008302	0.401751	0.40864		0.152	0.283285	
	Nb	0.0428828	-0.33912	0.5137638	-	0.138	0.360422	
FCC 2	Ta	0.0436398	-0.25439	0.4679475	82	0.184	0.385492	2000
	Ti	0.0675818	-0.78679	0.9944761		0.123	0.805261	
	W	-0.00513	0.608404	0.6101537		0.222	0.622341	
	Fe	-0.10972	-0.03177	0.9879932		0.181	1.032757	

$$\Delta\sigma_{\rm sss} = \left(\Sigma\Delta\sigma_{\rm i}^{\frac{3}{2}}\right)^{\frac{2}{3}}....(4.5)$$

The summary of various strengthening mechanisms that could be operating in various phases of this alloy are shown in Fig. 4.7. Now upon substituting these numbers from Fig. 4.7 and phase fractions from Table 4.1 in Eq. (4.1), we get σ_{flow} as 5040 MPa and this value corresponds

to a constraint factor of 2.74 for this RHEA, which is in good agreement with that for various metallic materials [36,37] including HEAs [37].

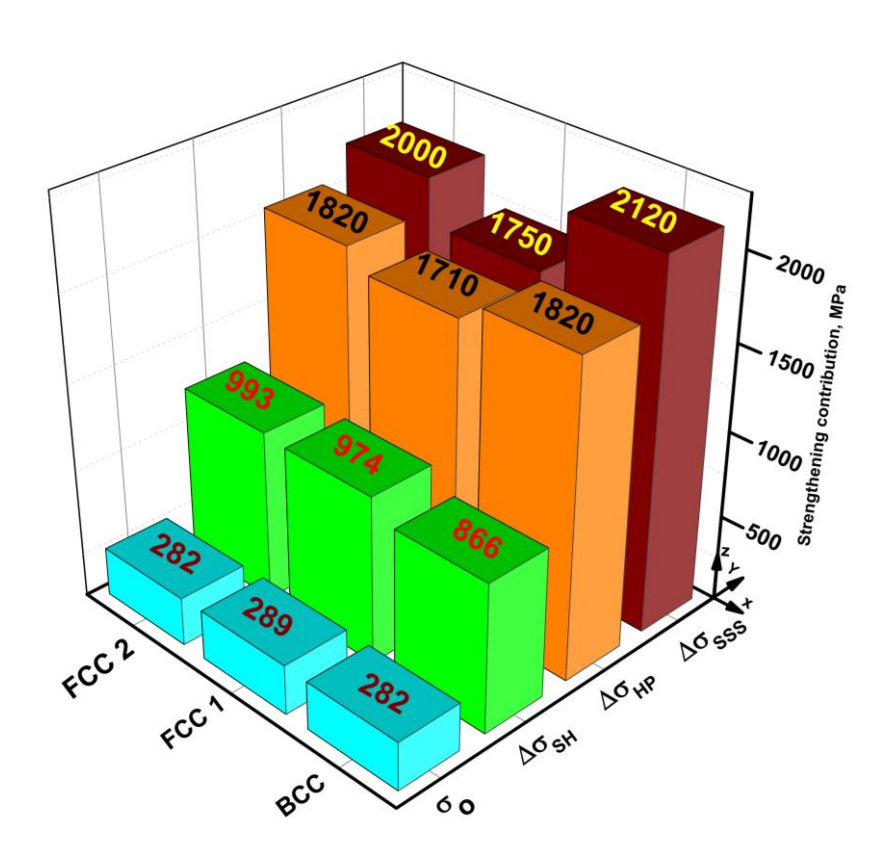


Fig. 4.7 Summary of various strengthening mechanisms operating among the various phases of the present alloy system.

It is clear that solid solution strengthening and Hall-Petch strengthening are the dominant mechanisms in all the phases with minor contributions from Taylor hardening and lattice frictional stress. Also, it may be noted that in spite of the multiple strengthening mechanism operating in this complex alloy at different length scales, a linear superposition of the individual strengthening contributions given by Eq. (4.1), can accurately explain the experimental observations of high hardness obtained in the present alloy system.

Indentation size effect

It is clear from Fig. 4.5 that this multi-phase RHEA exhibits indentation size effect. Hardness behavior of various materials evaluated by Vickers microindentation was analyzed using the Meyer power law: $P = A(y)^n$; Where P is the indentation load, A is a constant, y = average diagonal length of the residual indent, n is constant called as Meyer index that indicates

indentation size effect. For various materials this n value was found to be in the range 1.5-2.0 [38,39]. If n=2, the hardness is observed to be independent of load and if n < 2, then the material exhibits indentation size effect. For the hardness data obtained in the case of present alloy, a plot of log (P) and log (y) was made and is shown in Fig. 4.8. It is evident that Meyer power law is well followed by the present RHEA with n=1.82 which suggests that indentation size exists in the present alloy.

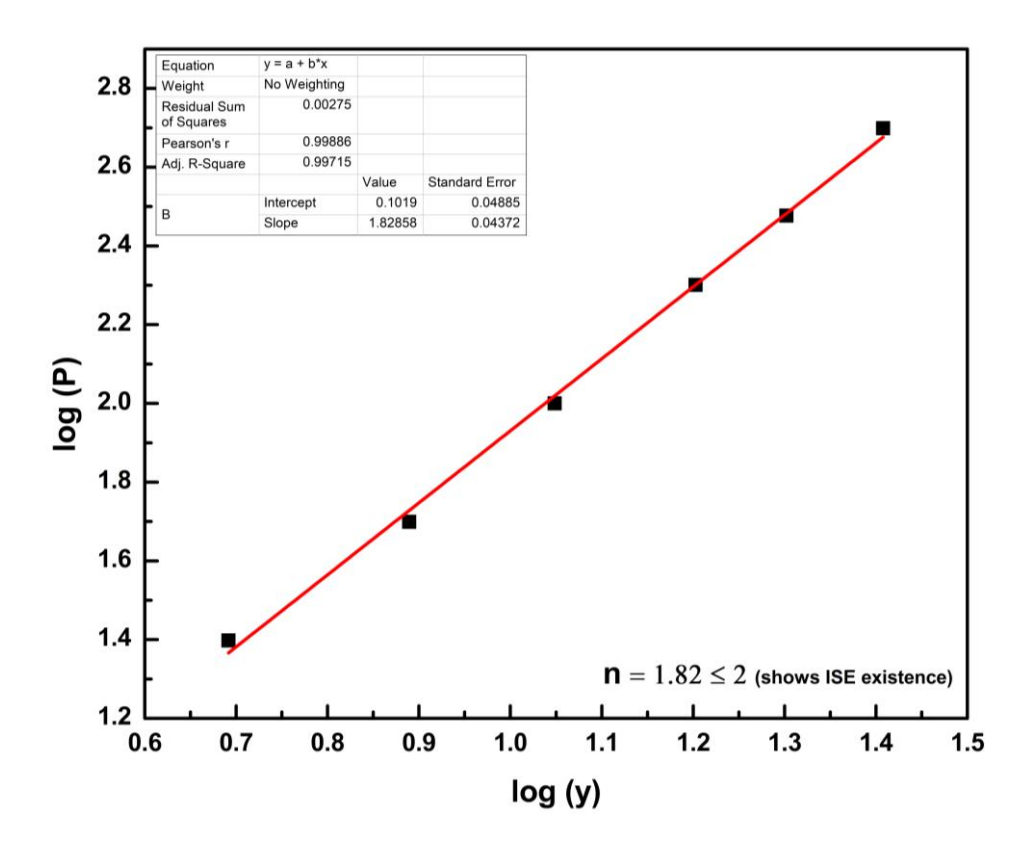


Fig. 4.8 Validation of the Vickers hardness data of the present alloy by Meyer power law. Here P is indentation load, y is average diagonal length. The analysis yields a Meyer index of 1.82 suggesting the presence of indentation size effect.

Here P is indentation load, y is average diagonal length. The analysis yields a Meyer index of 1.82 suggesting the presence of indentation size effect. The interplay between the size of the microstructural features and the deformed zone during indentation that scales with indentation depth, is important in understanding the depth dependence of hardness and this aspect has not received much attention in HEAs yet. As local structural/microstructural/chemical environment dictates the deformation behavior at finer length scales, details of deformed volume are very critical in probing the reasons for strain gradient plasticity. It has to be stressed

here that, the structural/microstructural conditions of the present alloy beneath the indenter are quite complex. The deformed volume consists of multiple phases (BCC, FCC1, FCC2) with different crystal structures. These complex solid solution phases (BCC, FCC1 and FCC2), although contain all the alloying elements, differ in composition of the respective elements. Further the grain size is observed to be around 22-25 nm.

In the current alloy, post indentation recovery at room temperature is ruled out as the multiphases are composed of high melting elements such as Mo, Nb, Ta, Ti, W and Fe. As a result room temperature may not be sufficient enough to provide enough activation energy for recovery in this system. This alloy contains multiple chemically inhomogeneous phases (BCC, FCC1, FCC2) at smaller length scales, although BCC and FCC2 were accorded identical composition owing to the practical reasons (Fig. 4.4). Based on the fact that all the phases contain all the participating elements (Fig. 4.4), comparable grain sizes (Table 4.2) and similar observed lattice microstrains (Table 4.3), it is assumed that these features are not influential in the indentation size effect observed. It shows that multi-phase structure was plastically deformed by looking at the microstructural length scales of individual phases vs Vickers diagonal lengths as mentioned above. As the deformed volume appears to contain all the three phases at all loads, chemical inhomogeneity existing among various phases of this complex multi-phase solid solution may not be the reason behind the indentation size effect.

Strain gradient plasticity has been reported in a variety of conventional dilute materials including single crystals, polycrystalline materials, solid solutions etc. [40, 41] and was explained by the model proposed by Nix and Gao [12]. According to the Nix-Gao model [12], the characteristic nature of depth-dependent hardness can be written as

$$\frac{H}{H_0} = \sqrt{1 + \frac{h^*}{h}}...(4.6)$$

$$H_0 = 3\sqrt{3}\alpha Gb\sqrt{\rho_{SSD}}....(4.7)$$

$$h^* = \left(\frac{81}{2}\right) b\alpha^2 \tan^2\theta \left(\frac{G}{H_0}\right)^2.$$
 (4.8)

Where H is hardness at a given depth (h), H_0 is depth independent hardness that arises only from statistically stored dislocations; h^* is length scale that characterizes the depth dependence of hardness and is influenced by shape of the indenter, shear modulus (G) and H_0 . As H_0 is influenced by density of statistically stored dislocations (ρ_{SSD}), h^* can't be considered as a constant.

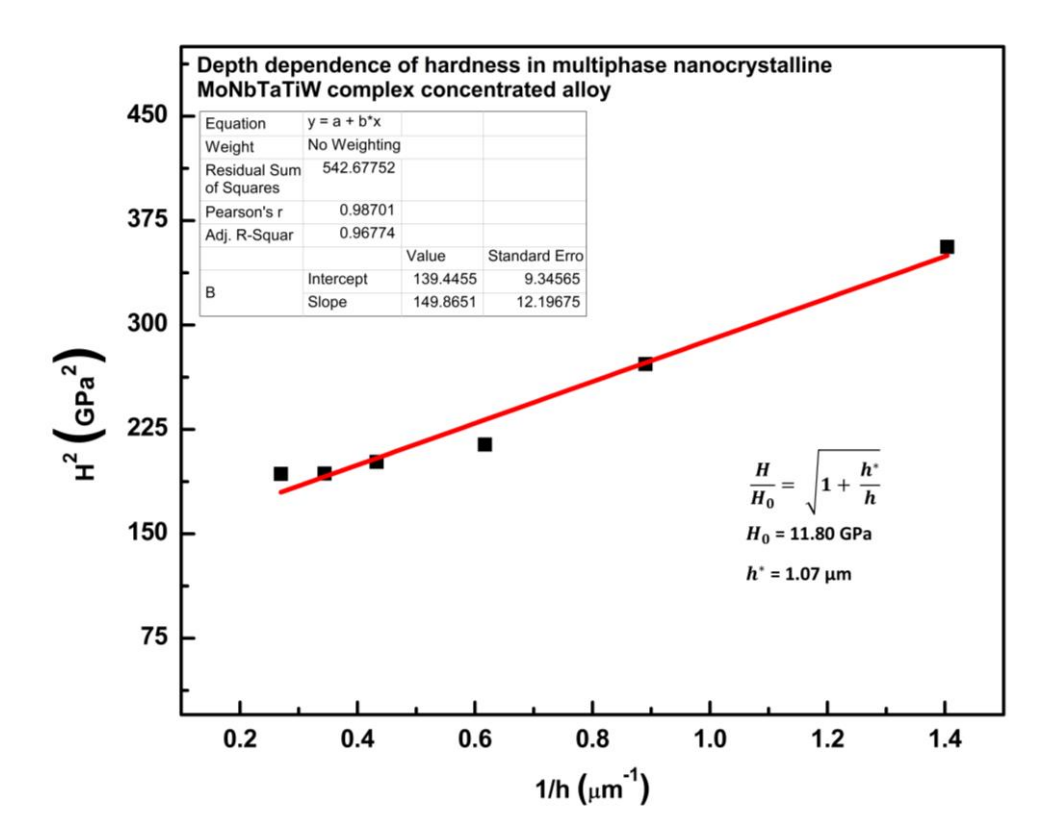


Fig. 4.9 Validation of the experimentally measured hardness data with the Nix-Gao model on strain gradient plasticity during indentation using self-symmetrical indenters [12]. In this case Vickers square based diamond pyramid indenter was used.

Indentation depth for Vickers indentation is given by, $h = 1/\{2\sqrt{2}\tan(\theta/2)\}$. From geometrical considerations for Vickers pyramidal indenter with square base, θ is 136°, $\tan(\theta/2) = 2.47$ and h = 1/(6.98); 1 is average of two diagonal lengths. A plot was made with square of the hardness (H²) on Y-axis, reciprocal of indentation depth (1/h) on X-axis and is shown in Fig. 4.9 and the data fits very well to a linear approximation following the Nix-Gao model on strain gradient plasticity involving GNDs [12]. Depth-independent hardness, characteristic length scale are calculated from this plot to be 11.80 GPa, 1.07 μ m respectively. Storage volume i.e., density of GNDs present in the characteristic length scale (h*) can be calculated using:

$$\rho_{\text{GNDs}} = \left(\frac{3}{2|b|h^*}\right) \times \tan^2\theta; \quad \text{Where } |b| = \sqrt{|b|_{BCC}^2 + |b|_{FCC1}^2 + |b|_{FCC2}^2};$$

|b| for this multi-phase alloy is calculated to be 1.58 nm, h* is 1.07 μ m (Fig. 4.9) and θ is the angle between surface of the equivalent conical indenter and the plane of the sample surface and that is 70.3° for Vickers indenter. Therefore density of GNDs is calculated to be 6.9 x 10^{15} m⁻². It should be mentioned here that the phase fraction of BCC phase is about 0.47 and the

FCC phases (FCC1, FCC2) account for a fraction of 0.53 in this alloy. The length scale of the Vickers indent vis-avis the microstructural length scales of different phases of this alloy is shown in Fig. 4.10 (a). The generation of GNDs in this three phase RHEA is schematically represented in Fig. 4.10 (b).

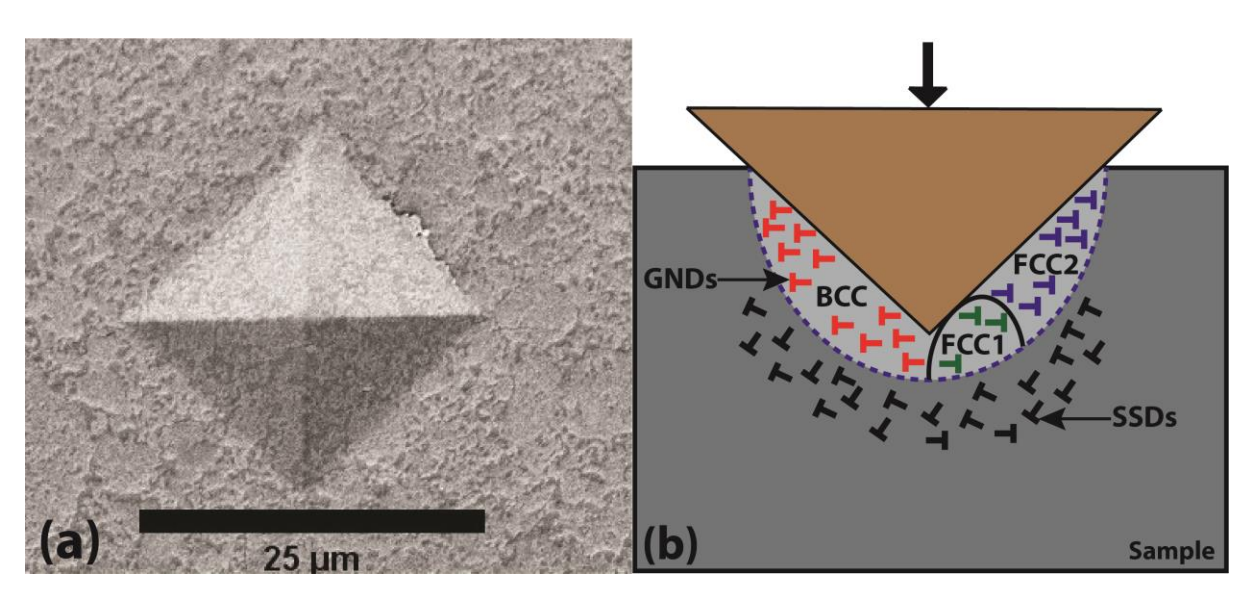


Fig. 4.10 (a) SEM topography image of the residual indent performed at 500 g load, which shows that deformation volume includes all the three different phases (BCC, FCC1, FCC2) of the alloy. (b) Schematic illustration of the probable processes that occur beneath the indenter in this multi-phase RHEA.

At room temperature, work hardening is more in solid solutions compared to elemental metals. Work hardening effects are furthermore when the material consists of a two-phase structure [25]. In this case it is a multi-phase structure and each phase is a concentrated solid solution in itself. Therefore it gave rise to pronounced work hardening effects at smaller loads. This is also supported by the observation that the solid solution strengthening is the major dominant mechanism in each individual phase (Fig. 4.7). Flow stress of individual phases are calculated as 5108 MPa, 4723 MPa, 5095 MPa for BCC, FCC1, FCC2 phases respectively (Fig. 4.7). It is clear that all the phases have comparable flow stress values with BCC being the relatively stronger (harder) phase. As BCC and FCC (FCC1, FCC2) phases seem to contain all the participating elements of this alloy, although in different proportions, chemical inhomogeneity existing among different phases is not considered as an influential factor here towards indentation size effect. Strain hardening in FCC based systems would be higher owing to the presence of more number of slip systems. But the slip characteristics of BCC based systems

would be complex at room temperature due to the operation of limited number of slip systems, often requiring thermal energy to activate more number of slip systems. Therefore in the present system, it is considered that FCC (FCC1, FCC2) phases could be accommodating more plastic strain whereas BCC phase is not expected to be strain accommodating. In order for the plastic deformation of this multi-phase alloy to be compatible and homogeneous especially at smaller loads (deformation volumes), it is expected back stress would develop at the interface of BCC/FCC phases and that would increase the hardness at small deformed volumes as observed in Fig. 4.5. This back stress would diminish as the deformed volume at higher indentation loads would have enough FCC phase fraction to account for the homogeneous plastic deformation. Therefore based on the above mentioned analysis and discussion, it is reasonable to state that the generation of GNDs in various phases of this RHEA during the initial stages of Vickers indentation coupled with the back stress exerted by the inter-phase boundaries (FCC/BCC) is probably be the reason for the observed strain gradient plasticity.

4.1.4. Summary

Fully dense multi-phase nanocrystalline MoNbTaTiW complex concentrated alloy was prepared using ball milling followed by SPS. Single phase BCC structure obtained after milling for 30 h has transformed to a new BCC and two FCC (FCC1, FCC2) phases with different lattice constants. Some amount of Fe has also entered the alloy from the milling media. It appears that very fine nanocrystalline structure coupled with the presence of relatively low melting elements such as Ti and Fe aids the phase decomposition during SPS. BCC phase fraction is about 47% and the remaining fraction constitutes FCC1 and FCC2 phases. Exceptionally high hardness in the range 18.87-13.89 GPa was observed in this multi-phase alloy which is the highest reported till now in the family of alloys based on MoNbTaW composition. "Density-normalized" hardness is also remarkably high for this alloy making as an attractive candidate material for structural applications. Detailed analysis on probable strengthening mechanisms suggest that solid solution strengthening and Hall-Petch strengthening are the major strengthening mechanisms in this alloy. The hardness data of this alloy was observed to follow the Meyer hardening power law with an index of 1.82 suggesting the presence of indentation size effect. The strain gradient plasticity of this multi-phase RHEA was explained based on the considerations of GNDs that exists owing to the multi-phase structure with different crystal structures (BCC, FCC1, FCC2), by using the Nix-Gao model by incorporating the structural/microstructural features arising out of multi-phase structure in

this alloy. The plastic incompatibility is expected to arise from the different slip characteristics of BCC and FCC phases at room temperature at smaller indentation loads, leading to the generation of back stress at interphase (BCC/FCC) boundaries. The depth-independent hardness of 11.8 GPa and the characteristic length scale of 1.07 μ m were obtained in the analysis.

References

- [1] Yeh J W, Chen S K, Lin S J, Gan J Y, Chin T S, Shun T T, Tsua C H, and Chang S Y, Nanostructured high entropy alloys with multiple principal elements: novel alloy design concepts and outcomes, Adv Eng Mater. 6 (2004) 299-303.
- [2] B. Cantor, I.T.H. Chang, P. Knight, A.J.B. Vincent, Microstructural development in equiatomic multicomponent alloys, Mater. Sci. Eng. A. 375-377 (2004) 213-218.
- [3] Murty B S, Yeh J W, and Ranganathan S, Bhattacharjee P P, High-Entropy Alloys, second ed., Elsevier, United States, 2019.
- [4] Miracle D B, and Senkov O N, A critical review of high entropy alloys and related concepts, Acta Mater. 122 (2017) 448-511.
- [5] B. Gludovatz, A. Hohenwarter, D. Catoor, E.H. Chang, E.P. George, R.O. Ritchie, A fracture-resistant high-entropy alloy for cryogenic applications, Science 345 (2014) 1153-1158.
- [6] M.H. Tsai, J.W. Yeh, High-entropy alloys: a critical review, Mater. Res. Lett. 2 (2014) 107-123.
- [7] Ganji R S, Sai Karthik P, Bhanu Sankara Rao K, and Rajulapati K V, Strengthening mechanisms in equiatomic ultrafine grained AlCoCrCuFeNi high-entropy alloy studied by micro- and nanoindentation methods, Acta Mater. 125 (2017) 58-68.
- [8] Davis, J R, ASM specialty handbook: Heat-resistant materials, ASM International, United State, 1997.
- [9] Senkov O N, Wilks G B, Miracle D B, Chuang C P, and Liaw P K, Refractory high-entropy alloys, Intermetallics. 18 (2010) 1758-1765.
- [10] Ganji R S, Rajulapati K V, and Bhanu Sankara Rao K, Development of a Multi-phase AlCuTaVW High-Entropy Alloy Using Powder Metallurgy Route and its Mechanical Properties, Trans. Indian Inst. Met. 73 (2020) 613–618.
- [11] Z. Li, K.G. Pradeep, Y. Deng, D. Raabe, C.C. Tasan, Metastable high-entropy dual-phase alloys overcome the strength-ductility trade-off, Nature. 534 (2016) 227-230.

[12] W.D. Nix, H. Gao, Indentation size effects in crystalline materials: A law for strain gradient plasticity, J. Mech. Phys. Solids. 46 (1998) 411-425.

- [13] O.N. Senkov, G.B. Wilks, J.M. Scott, D.B. Miracle, Mechanical properties of Nb₂₅Mo₂₅Ta₂₅W₂₅ and V₂₀Nb₂₀Mo₂₀Ta₂₀W₂₀ refractory high entropy alloys, Intermetallics. 19 (2011) 698-706.
- [14] Z.D. Han, N. Chen, S.F. Zhao, L.W. Fan, G.N. Yang, Y. Shao, K.F. Yao, Effect of Ti additions on mechanical properties of NbMoTaW and VNbMoTaW refractory high entropy alloys, Intermetallics. 84 (2017) 153-157.
- [15] U. Bhandari, C. Zhang, C. Zeng, S. Guo, S. Yang, Computational and experimental investigation of refractory high entropy alloy Mo₁₅Nb₂₀Re₁₅Ta₃₀W₂₀, J. Mater. Res. Technol. 9 (2020) 8929-8936.
- [16] H.W. Yao, J.W. Qiao, J.A. Hawk, H.F. Zhou, M.W. Chen, M.C. Gao, Mechanical properties of refractory high-entropy alloys: Experiments and modeling, J. Alloys Compd. 696 (2017) 1139-1150.
- [17] Q. Liu, G. Wang, X. Sui, Y. Liu, X. Li, J. Yang, Microstructure and mechanical properties of ultra-fine grained MoNbTaTiV refractory high-entropy alloy fabricated by spark plasma sintering, J. Mater. Sci. Technol. 35 (2019) 2600-2607.
- [18] B. Kang, J. Lee, H.J Ryu, S.H. Hong, Ultra-high strength WNbMoTaV high-entropy alloys with fine grain structure fabricated by powder metallurgical process, Mater. Sci. Eng. A. 712 (2018) 616-624.
- [19] L. Raman, K. Guruvidyathri, G. Kumari, S.V.S. Narayana Murty, R.S. Kottada, B.S. Murty, Phase evolution of refractory high-entropy alloy CrMoNbTiW during mechanical alloying and spark plasma sintering, J. Mater. Res. 34 (2019) 756-766.
- [20] J.A. Smeltzer, C.J. Marvel, B.C. Hornbuckle, A.J. Roberts, J.M. Marsico, A.K. Giri, K.A. Darling, J.M. Rickman, H.M. Chan, M.P. Harmer, Achieving ultra hard refractory multiprincipal element alloys via mechanical alloying, Mater. Sci. Eng. A. 763 (2019) 138140.
- [21] S. Lv, Y. Zu, G. Chen, B. Zhao, X. Fu, W. Zhou, A multiple nonmetallic atoms co-doped CrMoNbWTi refractory high-entropy alloy with ultra-high strength and hardness, Mater. Sci. Eng. A. 795 (2020) 140035.
- [22] Tabor D, The Hardness of Metals, Illustrated ed., OUP Oxford, United Kingdom, 2000.
- [23] Z.C. Cordero, B.E. Knight, C.A. Schuh, Six decades of the Hall–Petch effect a survey of grain-size strengthening studies on pure metals, Int. Mater. Rev. 61 (2016) 495-512.
- [24] T.H. Courtney, Mechanical Behavior of Materials, Second ed., McGraw Hill Education, New York, 2012, pp.179e181.

[25] M.F. Ashby, The deformation of plastically non-homogeneous materials, Philos. Mag. 21 (1970) 399-424.

- [26] S. Chen, K.K. Tseng, Y. Tong, W. Li, C.W. Tsai, J.W. Yeh, P.K. Liaw, Grain growth and Hall-Petch relationship in a refractory HfNbTaZrTi high-entropy alloy, J. Alloys Compd. 795 (2019) 19-26.
- [27] Y. Xie, Y. Luo, T. Xia, W. Zeng, J. Wang, J. Liang, D. Zhou, D. Zhang, Grain growth and strengthening mechanisms of ultrafine-grained CoCrFeNiMn high entropy alloy matrix nanocomposites fabricated by powder metallurgy, J. Alloys Compd. 819 (2020) 152937.
- [28] K.S. Kumar, H. Van Swygenhoven, S. Suresh, Mechanical behavior of nanocrystalline metals and alloys, Acta Mater. 51 (2003) 5743-5774.
- [29] R. Labusch, A Statistical Theory of Solid Solution Hardening, Phys. Status Solidi. 41 (1970) 659-669.
- [30] I. Toda-Caraballo, P.E.J. Rivera-Diaz-Del-Castillo, Modelling solid solution hardening in high entropy alloys, Acta Mater. 85 (2015) 14-23.
- [31] B. Kang, J. Lee, H.J. Ryu, S.H. Hong, Ultra-high strength WNbMoTaV high-entropy alloys with fine grain structure fabricated by powder metallurgical process, Mater. Sci. Eng. A. 712 (2018) 616-624.
- [32] O.N. Senkov, J.M. Scott, S.V. Senkova, D.B. Miracle, C.F. Woodward, Microstructure and room temperature properties of a high-entropy TaNbHfZrTi alloy, J. Alloys Compd. 509 (2011) 6043-6048.
- [33] W. Guo, B. Liu, Y. Liu, T. Li, A. Fu, Q. Fang, Y. Nie, Microstructures and mechanical properties of ductile NbTaTiV refractory high entropy alloy prepared by powder metallurgy, J. Alloys Compd. 776 (2019) 428-436.
- [34] L.A. Gypen, A. Deruyttere, Multi-component solid solution hardening Part 1 Proposed mode, J. Mater. Sci. 12 (1977) 1028-1033.
- [35] W. Martienssen, H. Warlimont, Handbook of Condensed Matter and Materials Data, First ed., Springer, New York, 2005.
- [36] I.M. Hutchings, The contributions of David Tabor to the science of indentation hardness, J. Mater. Res. 24 (2009) 581-589.
- [37] P. Zhang, S.X. Li, Z.F. Zhang, General relationship between strength and hardness, Mater. Sci. Eng. A. 529 (2011) 62-73.
- [38] G.M. Pharr, E.G. Herbert, Y. Gao, The indentation size effect: A critical examination of experimental observations and mechanistic interpretations, Annu. Rev. Mater. Res. 40 (2010) 271-292.

[39] X.J. Ren, R.M. Hooper, C. Griffiths, J.L. Henshall, Indentation-size effects in single-crystal MgO, Philos. Mag. A. 82 (2002) 2113-2120.

- [40] A.A. Elmustafa, D.S. Stone, Stacking fault energy and dynamic recovery: Do they impact the indentation size effect?, Mater. Sci. Eng. A. 358 (2003) 1-8.
- [41] K. Durst, O. Franke, A. Bohner, M. Goken, Indentation size effect in Ni-Fe solid solutions, Acta Mater. 55 (2007) 6825-6833.

4.2. Ultra-hard, multi-phase nanocrystalline MoTa and MoTaTi based multi-principal element alloys

4.2.1. Introduction

Refractory multi-principal element alloys (RMPEAs) have received a tremendous interest recently owing to their potential towards replacing the existing Ni-based superalloys and other high temperature structural materials. MoNbTaW based MPEAs are being envisaged for future high temperature applications [1]. Although this class of alloys provide high strength and high temperature stability, they suffer from larger densities owing to the presence of elements such as Ta. High absolute and high "density-normalized" hardness were reported in Ti-containing multi-phase MoNbTaW alloy prepared by ball milling (BM) and spark plasma sintering (SPS) [2]. Therefore to better understand the phase formation, phase stability, two element (MoTa) and three element (MoTaTi) strategies are adapted; further Ti was chosen to reduce the overall density of the alloy. Thus, proposed alloys are prepared by BM and SPS. Iron has entered the alloys as a contaminant, and it is also considered as another alloying element (although unintentionally added). Vickers indentation has revealed an extremely high hardness as well as highly significant "density-normalized" hardness in these new alloys aimed for high temperature applications.

4.2.2. Experimental procedure

Elemental powders Mo, Ta, and Ti were procured from Alfa Aesar with purity greater than 99.95 % with a -325 mesh size. MoTa and MoTaTi compositions weighed 10 g each and were milled for a total duration of 30 h in SPEX 8000D shaker mill and stopped at 30 h after achieving a saturated nanocrystalline grain structure structure. Ball to powder ratio is maintained at 5:1. The powders milled for 30 h of both the compositions are sintered using the Dr. SINTER 1050 apparatus with a heating rate of 7.21 K/s, uniaxial pressure of 80 MPa, and holding time of 15 min. The adapted sintering temperatures of 1573 K and 1373 K for MoTa and MoTaTi alloys correspond to more than 0.5Tm of the respective alloys, considering the rule of mixtures while estimating the melting temperatures. The density of the sintered sample is measured using the Archimedes principle method. X-ray diffraction (XRD) is performed on milled powders at an interval of 5 h up to 30 h using BRUKER D8 ADVANCE equipment (Cu K α radiation, λ =1.5419 Å; 2 Θ between 20° to 120°; scan time 1 sec/step; step size 0.02°). Microstructural features and elemental information are obtained using a field emission

scanning electron microscope (FEI Nova NanoSEM 450) incorporated with energy dispersive spectroscopy (EDS) detector. Vickers hardness measurements are performed using Tinius Olsen equipment with load 0.25-9.81 N and dwell time of 15 s.

4.2.3. Results and discussion

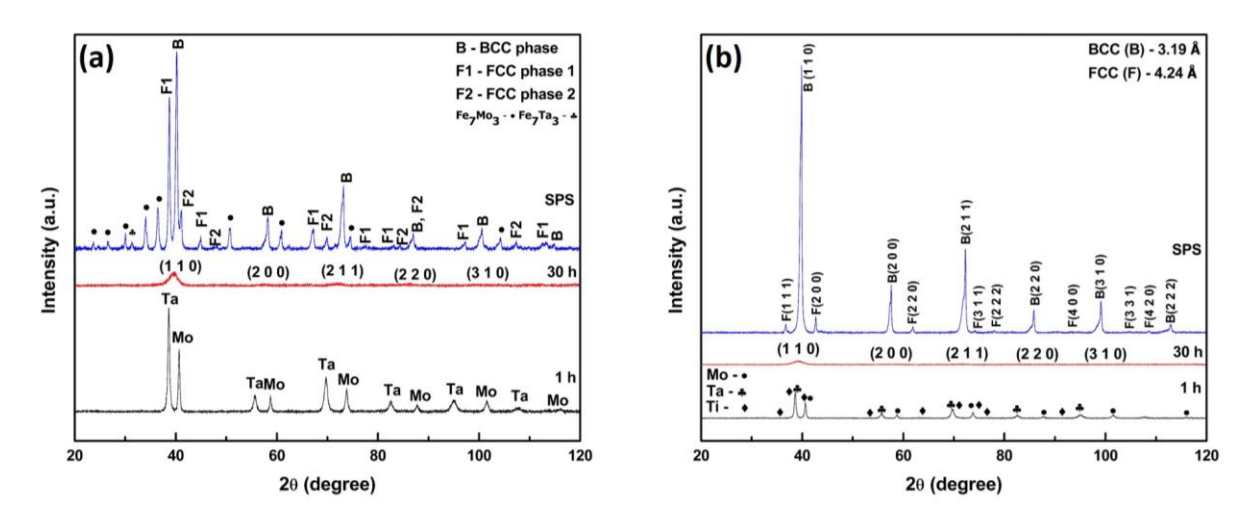


Fig. 4.11 (a) X-ray diffractograms of MoTa alloy at 1 h, 30 h of ball milling and after SPS (b) X-ray diffractograms of MoTaTi alloy at 1 h, 30 h and after SPS.

30 h ball milled powder for both the alloys MoTa and MoTaTi reveals a single BCC phase crystal structure from Fig. 4.11 with lattice parameters of 3.22 Å and 3.24 Å for MoTa and MoTaTi alloys respectively. Milling for 30 h resulted in the decrement of crystallite size up to 4 nm and 3 nm for MoTa and MoTaTi alloys, respectively. Lattice strain evaluated using the Stokes-Wilson method showed a value of 0.018 and 0.025 for MoTa and MoTaTi alloys respectively.

MoTa and MoTaTi alloys are sintered into a 15x5 mm² disks using SPS. XRD from Fig. 4.11 shows that the single BCC phase of both the alloys resulted in a multi-phase structure after sintering. It is evident from the literature that milling in the hardened steel milling media results in unintended Fe addition into the alloy [2,3]. Here in the MoTa alloy, the 1573 K SPS temperature corresponds to a homologous temperature of 0.87 for Fe, leading to the interdiffusion of Fe in the alloy, resulting in BCC, FCC1, and FCC2 phases compared to the single BCC phase of the as-milled condition. Similarly, 1373 K SPS temperature for MoTaTi alloy corresponds to a homologous temperature of 0.76 for Fe and 0.71 for Ti, leading to the interdiffusion of Fe and Ti from the as-milled alloy after sintering and resulting in BCC and FCC phases. In the MoTa alloy corresponding lattice parameters of the respective phases are

 $a_{BCC} = 3.16$ Å, $a_{FCC1} = 4.03$ Å and $a_{FCC2} = 3.81$ Å and a minor fraction of FeMo and FeTa compounds are also observed (Fig. 4.11). In the MoTaTi alloy BCC phase has a lattice parameter of 3.19 Å, and the FCC phase has a lattice parameter of 4.24 Å. The final crystallite size after sintering in the MoTa alloy for the respective phases is like for BCC – 30 nm, FCC1 – 24 nm, and FCC2 – 26 nm. In the MoTaTi alloy BCC phase has a crystallite size of 21 nm, and the FCC phase has a crystallite size of 36 nm.

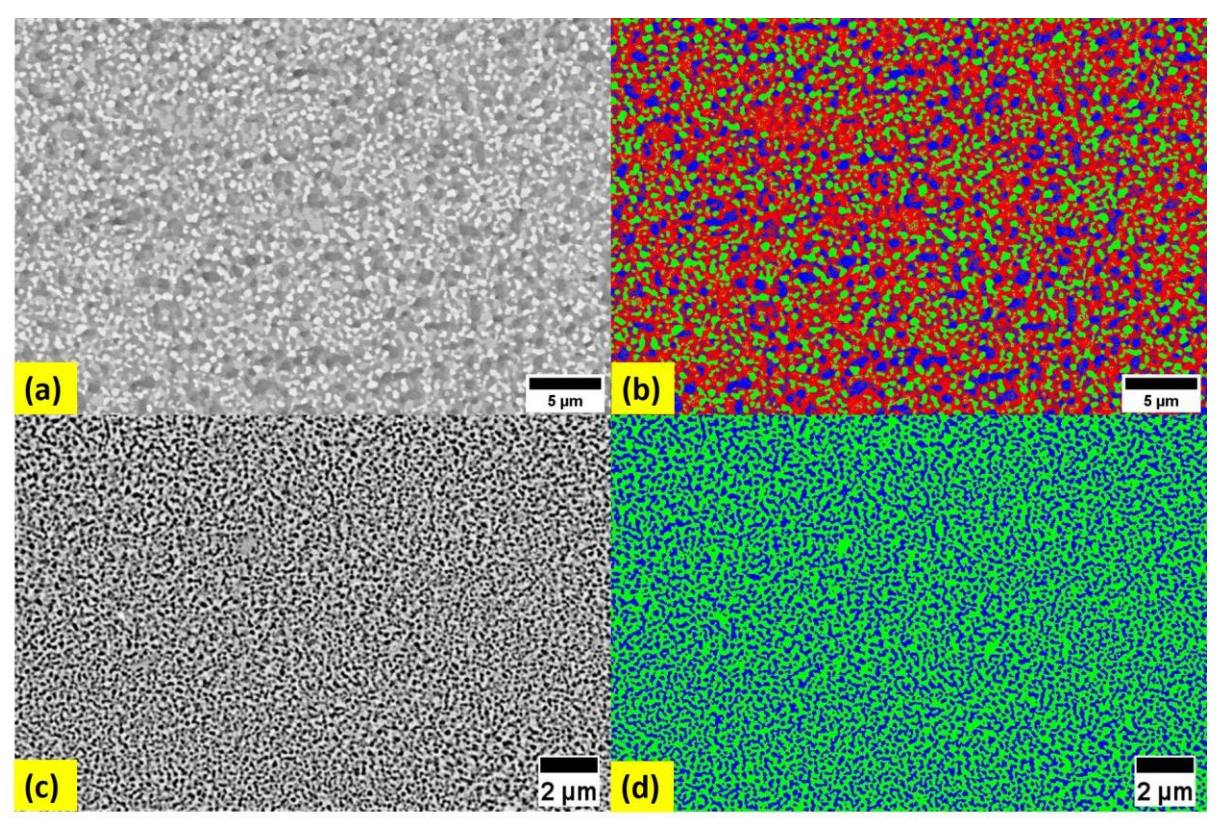


Fig. 4.12 (a) FESEM-BSE microstructure of MoTa (Fe) alloy; (b) Colour contrast microstructure of MoTa (Fe) alloy, obtained from (a) using ImageJ, that shows three different phases (red, blue, green) formed after sintering; (c) FESEM-BSE microstructure of MoTaTi (Fe) alloy; (d) Colour contrast microstructure of MoTaTi (Fe) alloy, obtained from (c) using ImageJ, that shows two different phases (green, blue).

FESEM microstructures of the respective MoTa (Fe) and MoTaTi (Fe) alloys are shown in Fig. 4.12. Three phase contrast (red, blue and green) is observed from the MoTa (Fe) alloy (Fig. 4.12 a&b). EDS analysis of the MoTa alloy shows that the alloy has a Fe of 7.3 % along with 48.9 % Mo and 43.8 % of Ta, although the Mo and Ta have an actual nominal composition of 50 % each. Two phase contrast (green and blue) is observed from the MoTaTi alloy, as shown in Fig. 4.12 (c&d). EDS analysis of the MoTaTi alloy shows that the alloy has a Fe of 4 %

along with 32.5 % Mo, 31.3 % of Ta, and 32.2% of Ti. The actual nominal composition of Mo, Ta, and Ti in the MoTaTi alloys is 33.33 % each. Clear presence of Fe (entered during processing) is observed in both the alloys from the XRD analysis and EDS analysis.

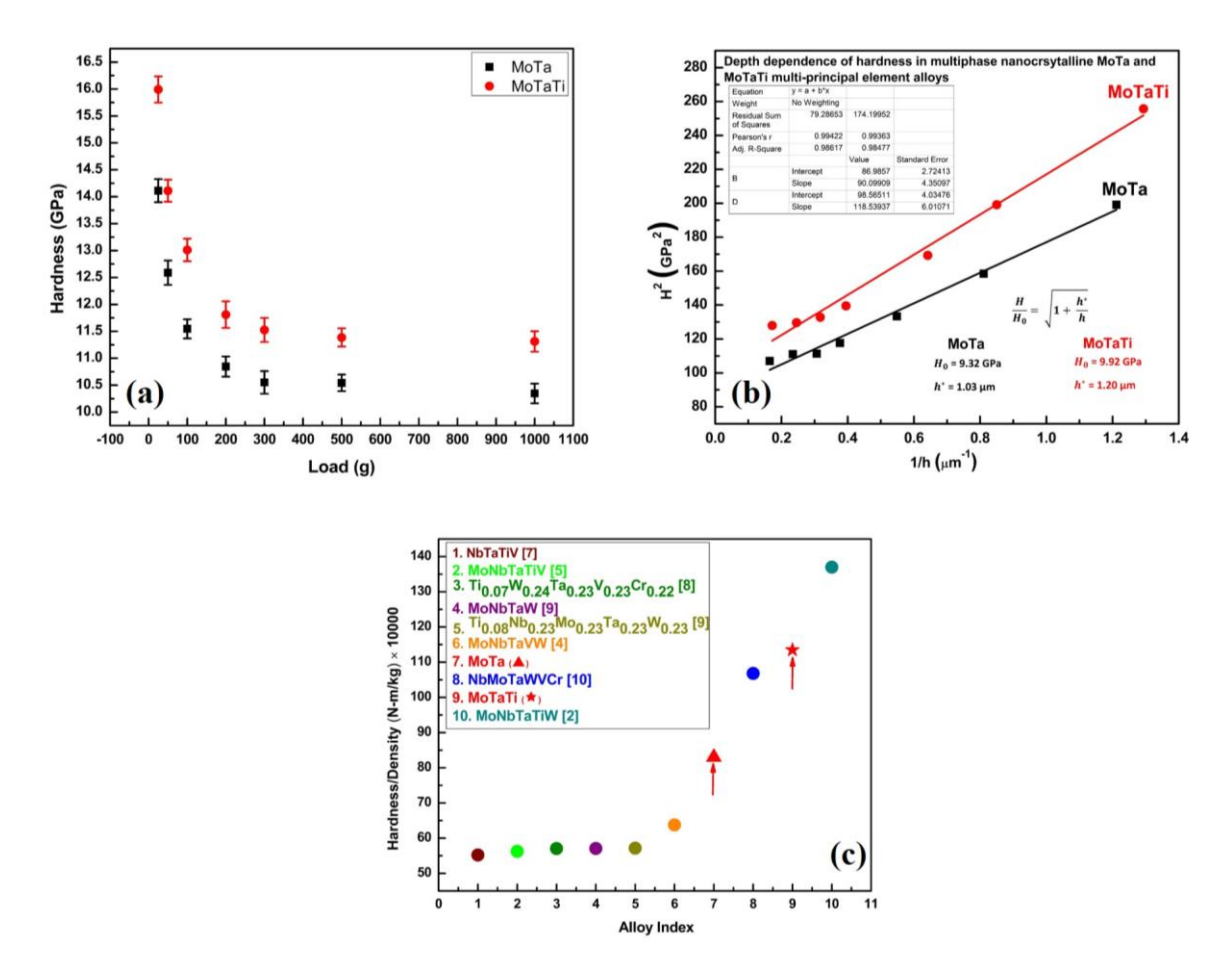


Fig. 4.13 (a) Variation microhardness in MoTa (Fe) and MoTaTi (Fe) alloys with load upto 9.81 N. A pronounced indentation size effect (ISE) was observed for both the alloys. (b) Observed ISE clearly follows the Nix-Gao model proposed considering the geometrically necessary dislocations and multi-phase structure [2]. (c) "Density-normalized" hardness of various tantalum containing alloys manufactured using the powder metallurgy route compared with the values obtained in the present work (shown with upward arrows).

From Fig. 4.13 (a), it is evident that, for MoTa (Fe) alloy, the hardness is varied from 14.11 ± 0.21 GPa to 10.34 ± 0.18 GPa in the load range of 0.25 to 9.81 N. In the MoTaTi alloy, hardness varies from 15.99 ± 0.24 GPa to 11.31 ± 0.19 GPa in the load range of 0.25 to 9.81 N. In both the alloys, hardness decreased with an increase in the load, which infers an apparent indentation size . The absolute hardness values for both the alloys are extremely high compared to other RHEAs or RMPEAs [4,5]. To understand about the depth independent hardness and

corresponding depth up to which ISE persists Nix-Gao plots [2,6] are generated for both the alloys and shown in Fig. 4.13 (b). Depth independent hardness is evaluated from the Nix-Gao plot for MoTa alloy is 9.32 GPa with a characteristic length scale of 1.03 μ m. For MoTaTi alloy, depth independent hardness is 9.92 GPa with a characteristic length scale of 1.20 μ m. These are highly significant numbers suggesting the potential of these alloys for high strength applications.

The hardness of both the alloys is normalized with densities of 12.70 g/cc and 10.03 g/cc for MoTa and MoTaTi alloys respectively and compared with the "density-normalized" hardness of similar family of alloys reported in the literature (Fig. 4.13 (c)). MoTa and MoTaTi alloys showed an exceptional "density-normalized" hardness (shown with arrows) compared to other alloys. The major drawback with tantalum containing RMPEAs [1] is their high density, coming from the absolute density of tantalum (16.6 g/cc). The alloys in the present investigation MoTa and MoTaTi contain less number of elements but offer extremely high hardness compared to three-, four-, five-element containing MPEAs that contain Ta. Therefore, by adapting careful alloying strategies the hardness/density of these new alloys can be further enhanced for future high strength and high temperature applications.

4.2.4. Summary

- 1) Single phase BCC structures were observed after ball milling of MoTa and MoTaTi alloys. Fe has entered the systems from milling media.
- 2) Spark plasma sintering resulted in formation of three phase structure in MoTa (Fe), two phase structure in MoTaTi (Fe) alloys respectively. Presence of Ti and Fe in these alloys triggers the phase transformations leading to the multi-phase structures.
- 3) Extremely high hardness values are observed in both the alloy systems with a very clear ISE. The ISE follows the considerations according to the Nix-Gao model and the characteristic multi-phase structure of these alloys.
- 4) These extraordinarily high hardness values could be originating from the high frictional stress, nanocrystallinity, multi-phase structure, solid solution strengthening etc.
- 5) A very significant "density-normalized" hardness was attained by these two alloys highlighting the potential advantages for future high strength, high temperature applications.

References

[1] O.N. Senkov, D.B. Miracle, K.J. Chaput, J.P. Couzinie, Development and exploration of refractory high entropy alloys - A review, J. Mater. Res. 33 (2018) 3092–3128.

- [2] D.G. Kalali, S. Antharam, M. Hasan, P.S. Karthik, P.S. Phani, K. Bhanu Sankara Rao, K. V. Rajulapati, On the origins of ultra-high hardness and strain gradient plasticity in multi-phase nanocrystalline MoNbTaTiW based refractory high-entropy alloy, Mater. Sci. Eng. A. 812 (2021) 141098.
- [3] J.A. Smeltzer, C.J. Marvel, B.C. Hornbuckle, A.J. Roberts, J.M. Marsico, A.K. Giri, K.A. Darling, J.M. Rickman, H.M. Chan, M.P. Harmer, Achieving ultra hard refractory multiprincipal element alloys via mechanical alloying, Mater. Sci. Eng. A. 763 (2019).
- [4] B. Kang, J. Lee, H.J. Ryu, S.H. Hong, Ultra-high strength WNbMoTaV high-entropy alloys with fine grain structure fabricated by powder metallurgical process, Mater. Sci. Eng. A. 712 (2018) 616–624.
- [5] Q. Liu, G. Wang, X. Sui, Y. Liu, X. Li, J. Yang, Microstructure and mechanical properties of ultra-fine grained MoNbTaTiV refractory high-entropy alloy fabricated by spark plasma sintering, J. Mater. Sci. Technol. 35 (2019) 2600–2607.
- [6] W.D. Nix, H. Gao, Indentation size effects in crystalline materials: A law for strain gradient plasticity, J. Mech. Phys. Solids. 46 (1998) 411–425.
- [7] W. Guo, B. Liu, Y. Liu, T. Li, A. Fu, Q. Fang, Y. Nie, Microstructures and mechanical properties of ductile NbTaTiV refractory high entropy alloy prepared by powder metallurgy, J. Alloys Compd. 776 (2019) 428–436.
- [8] O.A. Waseem, J. Lee, H.M. Lee, H.J. Ryu, The effect of Ti on the sintering and mechanical properties of refractory high-entropy alloy TixWTaVCr fabricated via spark plasma sintering for fusion plasma-facing materials, Mater. Chem. Phys. 210 (2018) 87–94.
- [9] J. Pan, T. Dai, T. Lu, X. Ni, J. Dai, M. Li, Microstructure and mechanical properties of Nb25Mo25Ta25W25 and Ti8Nb23Mo23Ta23W23 high entropy alloys prepared by mechanical alloying and spark plasma sintering, Mater. Sci. Eng. A. 738 (2018) 362–366.
- [10] Y. Long, X. Liang, K. Su, H. Peng, X. Li, A fine-grained NbMoTaWVCr refractory highentropy alloy with ultra-high strength: Microstructural evolution and mechanical properties, J. Alloys Compd. 780 (2019) 607–617.

4.3. Low-dense, multi-phase nanocrystalline MoNb (Fe) and MoNbTi (Fe) based multi-principal element alloys

4.3.1. Introduction

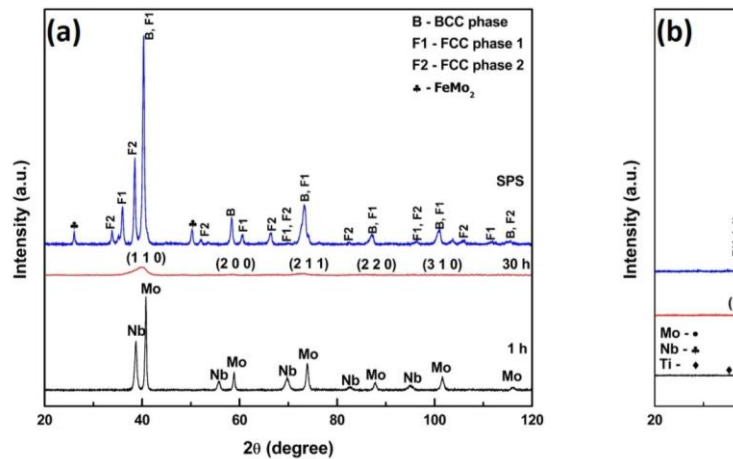
High-temperature materials are always a primary interest in the field of aerospace applications as turbine engines operate in extreme environmental conditions [1]. Specifically, turbine blades manufactured using Ni-based superalloys are used up to 1200 °C [2]. This operating temperature limitation is due to the melting points of the Ni-based superalloys. To enhance the operating temperature of the turbine blades. In recent times, the scientific community has focused on refractory high-entropy alloys (RHEAs)/multi-principal element alloys (MPEAs) consisting of refractory elements [3,4]. Further, alloys with high strength-to-weight ratios are desired for aerospace applications.

Our earlier reports on nanocrystalline refractory alloys showed extraordinary hardness [5] and "density-normalized" hardness numbers [4]. To improve the "density-normalized" hardness further, in the present work, the high-density element Ta in the previous work [5] is replaced with the Nb to decrease the overall density of the alloy without any effect on its hardness numbers. Thus, the alloys developed in this work showed an extraordinary density-normalized hardness compared to any other Nb-containing alloys aiming for high-temperature aerospace applications.

4.3.2. Experimental procedure

MoNb and MoNbTi equiatomic compositions are milled up to 30 h in ball milling (SPEX 8000D) using hardened steel vials with a ball-powder ratio of 5:1. X-ray diffraction (XRD) is performed using BRUKER D8 ADVANCE with Parameters Cu K α radiation; λ =1.5419 Å; 2 Θ between 20° to 120°; step size 0.02°; scan time 1 s/step. Lattice strain is calculated using the Stokes-Wilson method. 30 h milled powder is sintered using spark plasma sintering (SPS) with a heating rate of 7.21 K/s, uniaxial pressure of 80 MPa, and holding time of 15 min (Equipment: Dr. SINTER 1050). The corresponding sintering temperatures for MoNb (Fe) and MoNbTi (Fe) are 1473 K and 1273 K. Field emission scanning electron microscope (FEI Nova NanoSEM 450) equipped with an energy dispersive spectroscopy (EDS) detector is used for microstructural characterization. Hardness measurements: Tinius Olsen with a dwell time of 15 s. Density measurements using the Archimedes principle.

4.3.3. Results and discussion



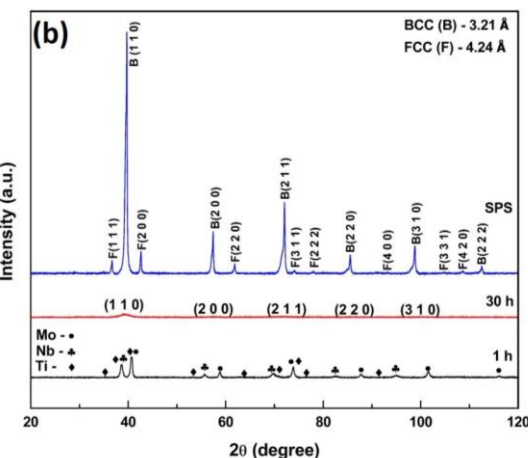


Fig. 4.14 (a) X-ray diffractograms of MoNb (Fe) alloy and (b) X-ray diffractograms of MoNbTi (Fe) alloy at different processing conditions.

Fig. 4.14 (a & b) shows the XRD diffractograms of MoNb (Fe) and MoNbTi (Fe) alloys at different processing conditions like 1 h milled powder, 30 h milled powder, and after SPS. At 30 h milled condition, MoNb (Fe) and MoNbTi (Fe) alloys have a single BCC phase structure. Lattice parameters corresponding to MoNb (Fe) and MoNbTi (Fe) alloys after 30 h milled condition are 3.18 Å and 3.22 Å, respectively. After 30 h of milling, the final crystallite size is 4 nm and 3 nm for MoNb (Fe) and MoNbTi (Fe) alloys, respectively. A lattice strain of 0.021 and 0.025 are observed for MoNb (Fe) and MoNbTi (Fe) alloys after 30 h of milling.

A 15 mm diameter and 5 mm thickness sintered samples (with multi-phase structure) are obtained after SPS with a sintered density of 9.33 g/cc and 7.67 g/cc, respectively, for MoNb (Fe) and MoNbTi (Fe) alloys. MoNbTi (Fe) can be considered as one of the low-density (7.67 g/cc) alloys compared to the various Nb-based commercial alloys like C-103 (8.85 g/cc), C-129Y (9.5 g/cc), and C3009 (10.1 g/cc) for the use of aerospace applications [6]. In the MoNb (Fe) alloy, Fe has a homologous temperature of 0.81 with respect to the 1473 K SPS temperature, which contributed to the interdiffusion of Fe in the alloy and eventually formed into the multi-phase structure (BCC, FCC1 and FCC2). Fe and Ti have a homologous temperature of 0.70 and 0.65, respectively, in the MoNbTi (Fe) alloy with respect to the 1273 K SPS temperature. Thus, Fe and Ti interdiffusion contributed to the formation of BCC and FCC phases after sintering. Lattice parameters corresponding to different phases of MoNb (Fe) alloy are BCC (a) = 3.16 Å, FCC1 (a) = 4.47 Å and FCC2 (a) = 4.67 Å and a minor fraction of FeMo compounds are also observed (Fig. 4.14). Lattice parameters corresponding to different

phases of MoNbTi (Fe) alloy are BCC (a) = 3.21 Å, and FCC (a) = 4.24 Å. The crystallite size for different phases in the MoNb (Fe) alloy is BCC - 14 nm, FCC1 - 14 nm, and FCC2 - 19 nm with a minor fraction of FeMo compound (Fig. 4.14(a)). In the MoNbTi (Fe) alloy, the crystallite size of the BCC phase is 36 nm, and the FCC phase is 44 nm.

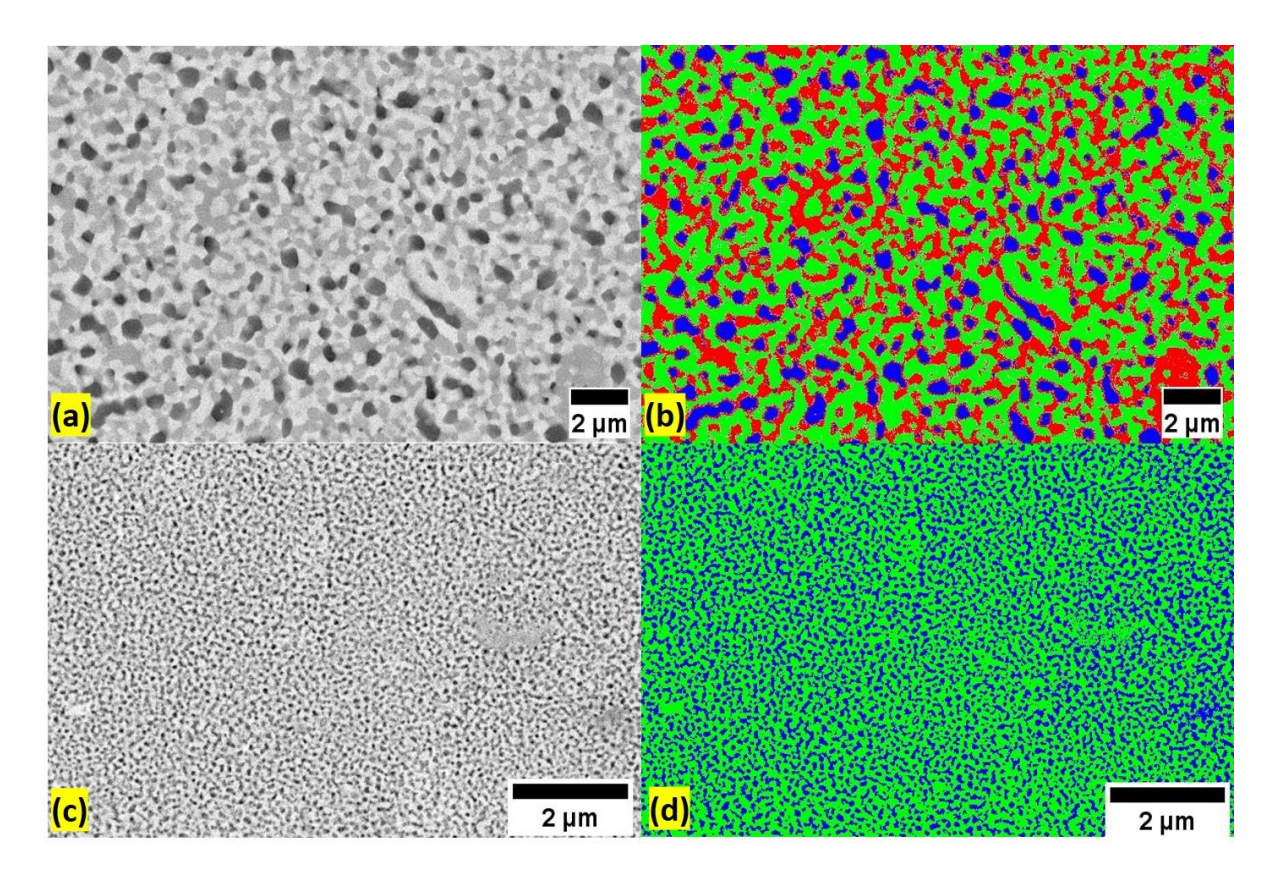


Fig. 4.15 (a) FESEM-BSE microstructure of MoNb (Fe) alloy; (b) Colour contrast microstructure of MoNb (Fe) alloy that shows three different phases (red, blue, green); (c) FESEM-BSE microstructure of MoNbTi (Fe) alloy; (d) Colour contrast microstructure of MoNbTi (Fe) alloy that shows two different phases (green, blue). All the microstructures are of the sintered condition.

FESEM-BSE microstructures of the MoNb (Fe) and MoNbTi (Fe) alloys are shown in Fig. 4.15. Fig. 4.15 (a&b) show the multi-phase contrast (red, blue and green) in the MoNb (Fe) alloy. Fe of 3.5 % with 51.7 % Mo and 44.8 % Nb were observed from the EDS analysis in the MoNb (Fe) alloy. The actual nominal composition of the Mo and Nb in the MoNb alloy is 50 % each. Fig. 4.15 (c&d) also shows the multi-phase contrast (green and blue) in the MoNbTi (Fe) alloy. Fe of 1.7 %, Mo of 36.2 %, Nb of 31.7 %, and 30.4 % of Ti were observed from the EDS analysis in the MoNbTi (Fe) alloy, and the actual nominal composition was 33 % each in

the MoNbTi alloy. XRD and EDS analysis revealed that a clear presence of Fe resulted from the milling media during the processing of elemental powder in the high-energy ball mill.

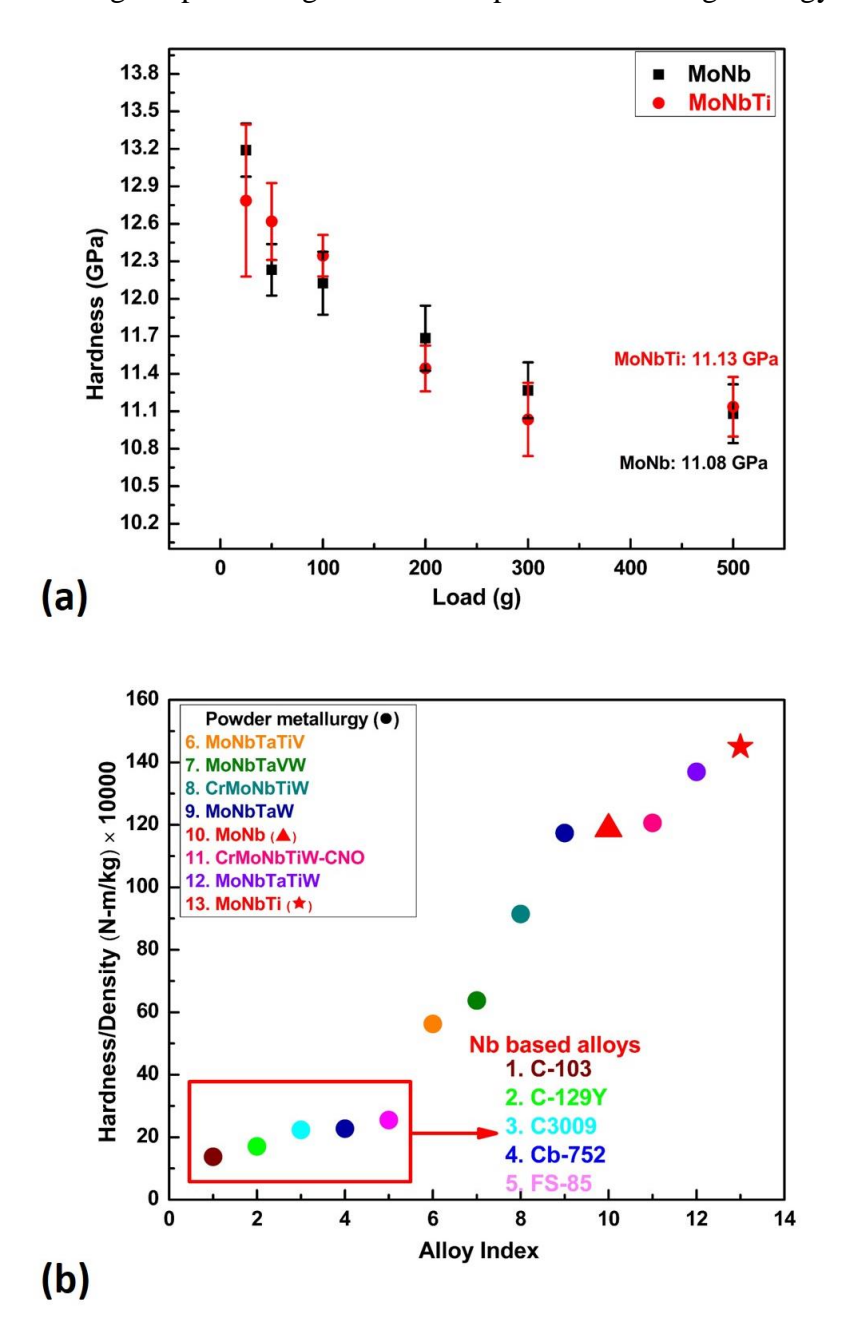


Fig. 4.16 (a) Microhardness details of the MoNb (Fe) and MoNbTi (Fe) alloys at different loads. (b) "Density-normalized" hardness of various Niobium-containing alloys processed via powder metallurgy route. Further, some Niobium-based commercial alloys are also compared with the values obtained in the present work [4,6–11].

The hardness ranges from 13.19 ± 0.21 GPa to 11.08 ± 0.23 GPa in the 25 to 500 g load range for MoNb (Fe) alloy, shown in Fig. 4.16 (a). Hardness varies from 12.78 ± 0.60 GPa to 11.13

± 0.23 GPa in the 25 g to 500 g load range for MoNbTi (Fe) alloy, shown in Fig. 4.16 (a). The obtained hardness numbers are normalized with densities of MoNb (Fe) and MoNbTi (Fe) alloys. Further, the numbers are with the "density-normalized" hardness of various Niobium-containing alloys processed using the powder metallurgy route and also some Niobium-based commercial alloys reported in the literature (Fig. 4.16 (b)). MoNb (Fe) and MoNbTi (Fe) alloys showed exceptional "density-normalized" hardness compared to various other commercially available Niobium-based alloys. Therefore, alloys developed in this work (MoNb (Fe) and MoNbTi (Fe)) are beneficial for high "strength-to-weight" aerospace applications. Further, considering the cost of the alloys, the alloys developed in this work are more cost-effective than most of the commercially available Nb-based alloys like C-103 (medium strength alloy, 10 wt % Hf), C-129Y (10 wt % Hf), and C-3009 (High strength alloy, 30 wt % Hf). This is because, in most of the Nb-based alloys, Hf is one of the costliest (approx. 1200 USD/kg) elements involved in the production [12]. Hence MoNbTi (Fe) alloy developed in this work has a massive potential for high strength-to-weight applications.

4.3.4. Summary

- High energy ball milling of the elemental powders in two different compositions, MoNb and MoNbTi, in equiatomic proportions, resulted in single-phase BCC after 30 h of milling. Fe, an unintentional guest from the milling media.
- A three-phase structure in MoNb (Fe) and a two-phase structure in MoNbTi (Fe) alloy were observed after SPS. The high homologous temperatures of Ti and Fe contributed to the phase transformations after sintering compared to the as-milled condition.
- MoNbTi (Fe) alloy can be considered as one of the lowest density alloys (7.67 g/cc) compared to the various commercially available Nb-based alloys like C-103 (8.85 g/cc), C-129Y (9.5 g/cc), C3009 (10.1 g/cc), Cb-752 (9.03 g/cc), and FS-85 (10.61 g/cc).
- A high "density-normalized" hardness observed in this work indicates that MoNbTi (Fe) is a good candidate for low-density aerospace applications.
- The cost of the MoNbTi (Fe) alloy will be significantly less when compared to commercially available Nb-based alloys due to the absence of Hf.

References

[1] H. Harada, N. Rene, High Temperature Materials for Gas Turbines: The Present and Future, Proc. Int. Gas Turbine Congr. 2003. (2003) 1–9.

[2] J.H. Perepezko, The hotter the engine, the better, Science. 326 (2009) 1068–1069.

- [3] O.N. Senkov, G.B. Wilks, D.B. Miracle, C.P. Chuang, P.K. Liaw, Refractory highentropy alloys, Intermetallics. 18 (2010) 1758–1765.
- [4] D.G. Kalali, S. Antharam, M. Hasan, P.S. Karthik, P.S. Phani, K. Bhanu Sankara Rao, K. V. Rajulapati, On the origins of ultra-high hardness and strain gradient plasticity in multi-phase nanocrystalline MoNbTaTiW based refractory high-entropy alloy, Mater. Sci. Eng. A. 812 (2021) 141098.
- [5] D.G. Kalali, P.S. Karthik, K.B. Sankara, K. V Rajulapati, Ultra-hard, multi-phase nanocrystalline MoTa and MoTaTi based concentrated refractory alloys, Mater. Lett. 324 (2022) 132768.
- [6] H.E. McCoy, R.L. Stephenson, J.R. Weir, Mechanical Properties of Some Refractory Metals and their Alloys, Ornl-3593. (1964) 48 pp.
- [7] L. Raman, K. Guruvidyathri, G. Kumari, S.V.S. Narayana Murty, R.S. Kottada, B.S. Murty, Phase evolution of refractory high-entropy alloy CrMoNbTiW during mechanical alloying and spark plasma sintering, J. Mater. Res. 34 (2019) 756–766.
- [8] B. Kang, J. Lee, H.J. Ryu, S.H. Hong, Ultra-high strength WNbMoTaV high-entropy alloys with fine grain structure fabricated by powder metallurgical process, Mater. Sci. Eng. A. 712 (2018) 616–624.
- [9] S. Lv, Y. Zu, G. Chen, B. Zhao, X. Fu, W. Zhou, A multiple nonmetallic atoms co-doped CrMoNbWTi refractory high-entropy alloy with ultra-high strength and hardness, Mater. Sci. Eng. A. 795 (2020) 140035.
- [10] Q. Liu, G. Wang, X. Sui, Y. Liu, X. Li, J. Yang, Microstructure and mechanical properties of ultra-fine grained MoNbTaTiV refractory high-entropy alloy fabricated by spark plasma sintering, J. Mater. Sci. Technol. 35 (2019) 2600–2607.
- [11] B. Kang, J. Lee, H.J. Ryu, S.H. Hong, Ultra-high strength WNbMoTaV high-entropy alloys with fine grain structure fabricated by powder metallurgical process, Mater. Sci. Eng. A. 712 (2018) 616–624.
- [12] O.N. Senkov, S.I. Rao, T.M. Butler, K.J. Chaput, Ductile Nb alloys with reduced density and cost, J. Alloys Compd. 808 (2019) 151685.

4.4.Role of Ti on the microstructure and mechanical properties of MoNbTi multi-principal element alloy: Performance of the multi-principal element alloys

4.4.1. Introduction

The recent development of cost-effective medium entropy alloys (MEAs) with refractory and non-refractory transition elements showed extraordinary mechanical properties at both room temperature and elevated temperatures comparable to high entropy alloys (HEAs) [1–8]. In the family of non-refractory MEAs, CoCrNi showed excellent mechanical properties like their counterpart HEAs [9]. In the case of refractory HEAs, most participating elements are of high density, resulting in denser HEAs which is undesirable for high-temperature aerospace applications which require a high strength-to-weight ratio. In this direction, prior literature suggests that adding both Al and Ti decreases the overall density of the alloy in the refractory HEAs [10,11]. Specifically, the addition of Ti substantially affects the overall behaviour of the MEAs, like improved specific strength. It is also reported that severe lattice distortion between the participating elements enhances the strength of the alloy [12,13]. Ti mainly serves the purpose of increasing the lattice distortion in the alloy as it differs with atomic radius and shear modulus compared to several other refractory elements. Various refractory MEAs reported till now have a similar strength to their counterpart HEAs [14,15]. Qi and Chrzan, using their theoretical studies, mentioned that adding Ti, Zr, and Hf to the group 6 elements enhances the ductility of the alloy, resulting in a shear fracture rather than a cleavage fracture [16]. Segregation of the solute elements to the grain boundaries leads to grain growth stagnation [17] and inhibition of grain growth helps in the enhancement of mechanical properties.

This work provides insights on the effect of Ti addition on density, microstructure, and mechanical properties of MoNb alloy. To this end, equiatomic MoNb and MoNbTi alloys are developed and microstructural and mechanical property measurements are reported. A theoretical analysis is presented by considering the major strengthening contributions in medium HEAs to systematically determine the effect of the number of elements and their density on the "density-normalized" strength. Also, we provide insights on the optimal number of elements required to achieve high "density-normalized" strength at low cost. This work shows that very high "density-normalized" strength can be achieved by the appropriate choice of fewer elements.

4.4.2. Experimental procedure

Elemental powders of Mo (99.99 %), Nb (99.8 %), and Ti (99.5 %) were procured from M/s Alfa Aesar with a -325 mesh size. They were handled under a high-purity argon atmosphere in a glove box during various stages of processing. Initially, powders corresponding to MoNb and MoNbTi equiatomic compositions were weighed to a total of 10 g. The weighed powders were transferred individually to the vacuum arc melting furnace. Ti getter was placed inside the furnace to absorb the traces of oxygen, if present during the melting process. After achieving a vacuum level of 10⁻⁶ mbar inside the furnace, melting was carried out with a tungsten electrode. The cast product was flipped for 5 times during the melting process and remelted to achieve a homogenous composition in the corresponding alloys. Homogenization was performed at 1673 K for 24 h with a heating rate of 4.6 K/s in a tubular furnace equipped with high purity argon atmosphere to facilitate diffusion among different elements in these alloys under equilibrium conditions. Equilibrium phase diagrams and phase fraction plots are drawn using Thermo Calc TCHEA6 thermodynamic database.

All the alloys were metallographically polished to a mirror-like surface finish for microscopic examinations and density measurements (The Archimedes principle method). The density of MoNb and MoNbTi alloys was found to be 9.39 g/cc and 7.82 g/cc, respectively. X-ray diffraction (XRD) was conducted using BRUKER D8 ADVANCE equipment with Cu K α radiation (λ =1.5419 Å) in the scan range (2 Θ) between 20 0 to 120 0 with a scan time of 1 sec/step and a step size of 0.02 0 to determine the crystal structure and/or phase stability of the corresponding alloys. Lattice microstrain is calculated using the Stokes-Wilson method [18]. The microstructure was recorded using a field emission scanning electron microscope (FESEM, FEI Nova NanoSEM 450) at 20 kV accelerating voltage with a 10 mm working distance, and elemental analysis was carried out using energy dispersive spectroscopy (EDS) incorporated into FESEM. Electron backscattered diffraction (EBSD) studies were also performed on the alloys to understand the grain size distribution/orientation. Macro Vickers hardness measurements (Tinius Olsen) were carried out at different loads with a dwell time of 15 sec. A total of 10 indentations were performed, and the average and corresponding standard deviation were reported.

4.4.3. Results

Structural evolution

Calculation of Phase Diagram

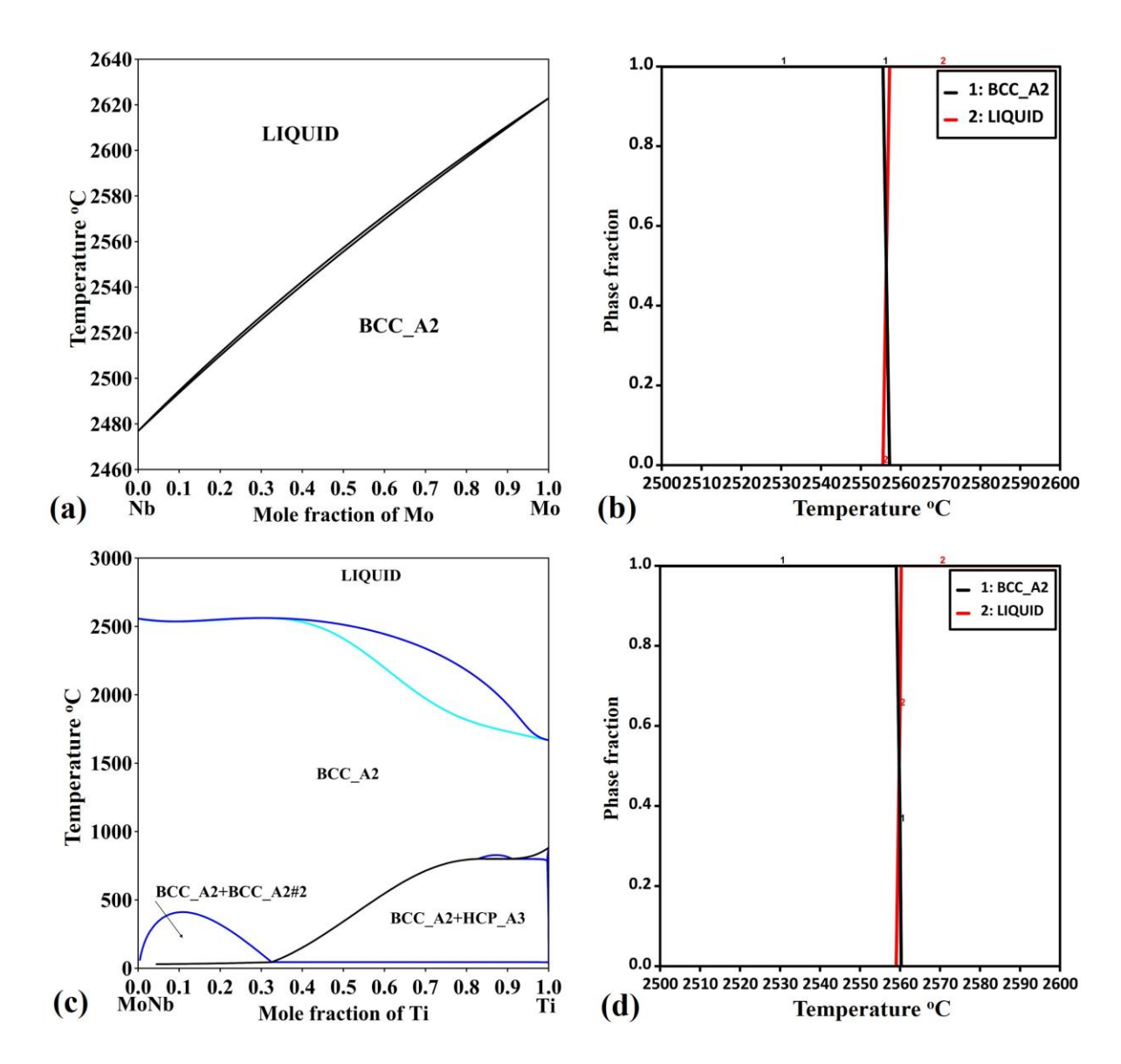


Fig. 4.17 Equilibrium phase diagram of MoNb alloy (a), vertical section of the $(MoNb)_{1-x}Ti_x$ phase diagram (c), Phase fraction plots of MoNb (b) and MoNbTi (d) alloys with temperature scale from 2500 °C to 2600 °C.

Fig. 4.17 (a & b) shows the equilibrium phase diagram and phase fraction plot of the MoNb alloy. The binary phase diagram of MoNb alloy is well addressed in the literature, it is an isomorphous system with a single BCC phase (BCC_A2), and it can be seen in Fig. 4.17 (a). As Ti is added in the present work, a vertical section of (MoNb)_{1-x}Ti_x phase diagram is drawn,

as shown in Fig. 4.17 (c). Interestingly, at the equiatomic composition in the vertical section of (MoNb)_{1-x}Ti_x phase diagram, a single BCC phase (BCC_A2) is observed over the complete range of temperatures (room temperature to the melting point of the alloy). The left side of the equiatomic composition in vertical section of (MoNb)_{1-x}Ti_x phase diagram leads to two BCC phases, whereas the right side leads to one BCC and one HCP phase. Fig. 4.17 (b) shows the phase fraction plot of the MoNb alloy obtained for an equiatomic composition with temperature on the abscissa and phase fraction on the ordinate. BCC_A2 and LIQUID are the solidus and liquidus lines of the corresponding MoNb alloy phase diagram shown in the phase fraction plot, respectively. A vertical line drawn at any abscissa point up to the solidus line, the complete phase fraction corresponds to BCC_A2, after which it transforms into a liquid phase. Fig. 4.17 (d) shows the phase fraction plot of the MoNbTi alloy obtained for an equiatomic composition. Further, it indicates that up to around 2560 °C, only a single BCC phase is stable, after which congruent melting occurs to transform into liquid phase.

Crystal structure

Fig. 4.18 shows the X-ray diffractograms obtained for both the MoNb and MoNbTi alloys in as-cast and homogenized conditions [19]. In MoNb alloy, the as-cast condition confirms a single BCC phase with a lattice parameter of 3.22 Å, and the corresponding homogenized condition also has a single BCC phase with a lattice parameter of 3.21 Å. In MoNbTi alloy, the as-cast and homogenized conditions confirm that both have a single BCC phase with no change in the lattice parameter of value 3.23 Å. Further, Ti addition does not alter the crystal structure. Homogenization at 1673 K for 24 h also does not result in any phase transformation, indicating that these alloys are thermally stable even at 1673 K. Hence, it is clear that single phase BCC structure is the most stable structure in these two alloys.

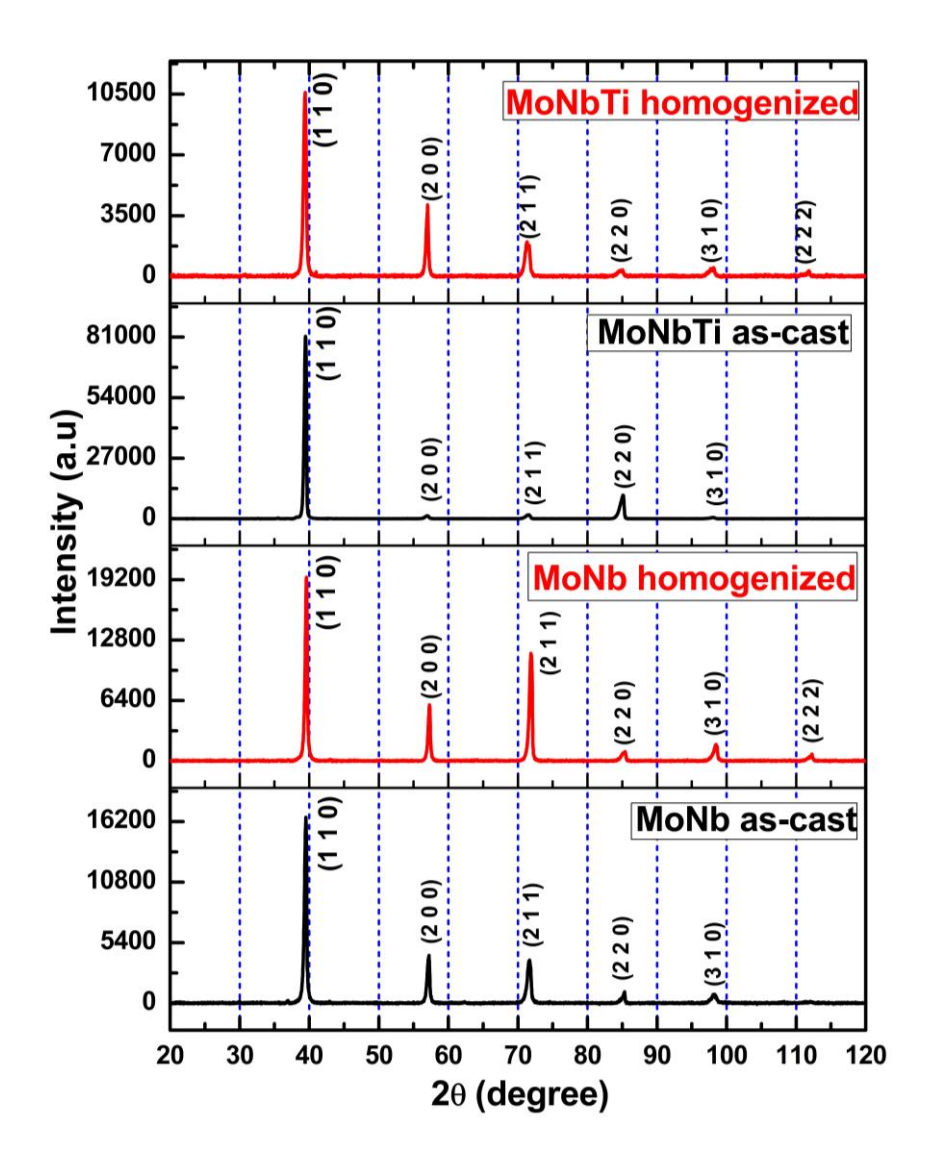


Fig. 4.18 X-ray diffractograms of equiatomic MoNb and MoNbTi alloys in as-cast and homogenized conditions (from bottom to top). In all the cases a single BCC phase was observed [19].

Microstructure and elemental distribution

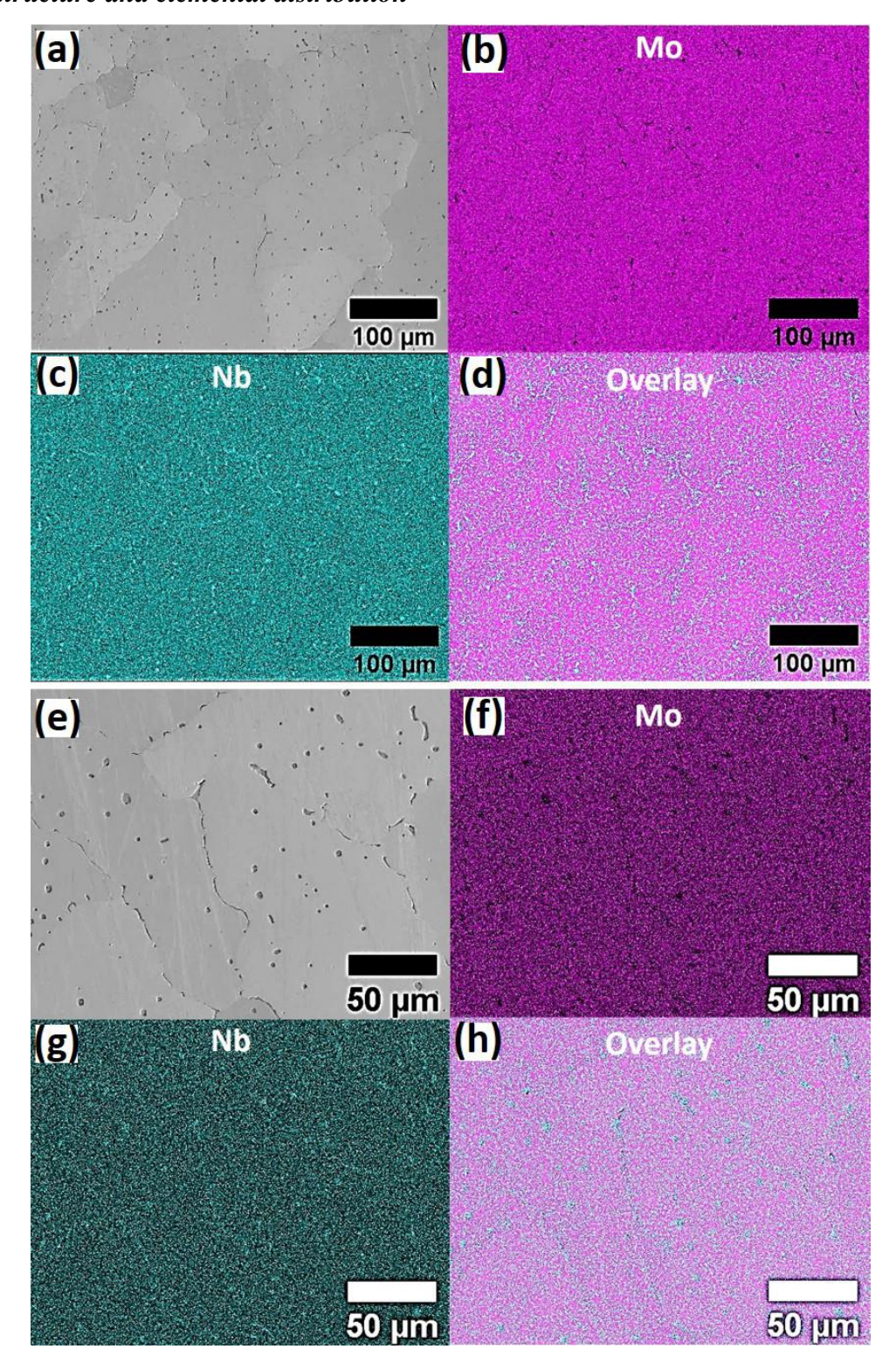


Fig. 4.19 (a) BSE micrograph of MoNb as-cast alloy, (b) elemental distribution of Mo in as-cast MoNb alloy, (c) elemental distribution of Nb in as-cast MoNb alloy and (d) overlay image of the elemental distribution indicating all the elements are homogeneously distributed with some Nb rich regions in MoNb as-cast alloy. (e) BSE micrograph of the MoNb homogenized alloy, (f) elemental distribution of Mo in homogenized MoNb alloy, (g) elemental distribution

of Nb in homogenized MoNb alloy and (h) overlay image of the elemental distribution indicating all the elements are homogeneously distributed with some Nb rich regions in MoNb homogenized alloy.

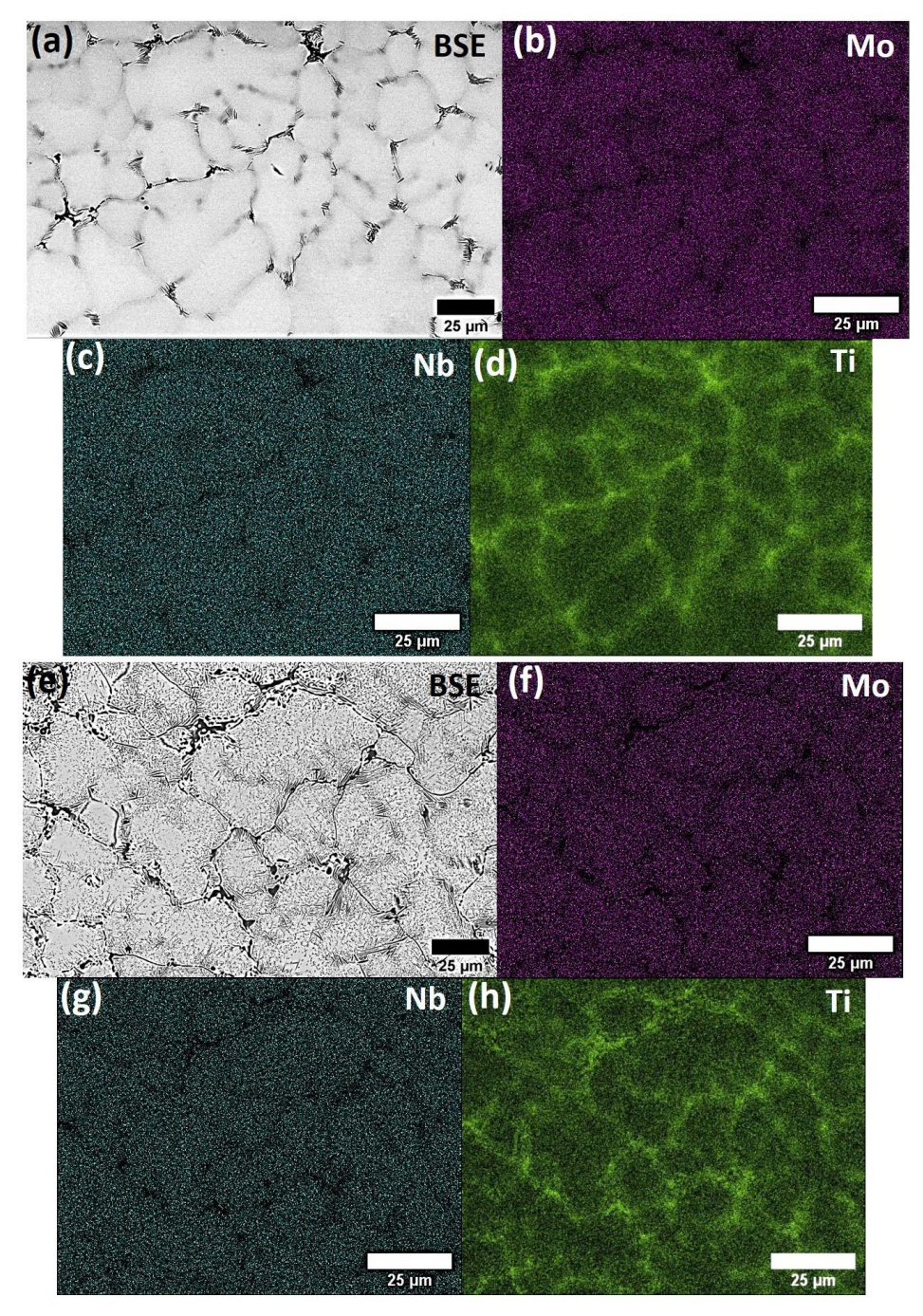


Fig. 4.20 (a) BSE micrograph of the MoNbTi as-cast alloy, (b) elemental distribution of Mo in as-cast MoNbTi alloy, (c) elemental distribution of Nb in as-cast MoNbTi alloy and (d) elemental distribution of Ti in as-cast MoNbTi alloy. (e) BSE micrograph of MoNbTi

homogenized alloy, (f) elemental distribution of Mo in homogenized MoNbTi alloy, (g) elemental distribution of Nb in homogenized MoNbTi alloy and (h) elemental distribution of Ti in homogenized MoNbTi alloy.

Fig. 4.19 and Fig. 4.20 show the BSE-FESEM microstructure and corresponding EDS maps of MoNb and MoNbTi alloys in as-cast and homogenized conditions, respectively. From Fig. 4.19 (d), it can be concluded that both Mo and Nb are homogeneously distributed throughout the ascast alloy with some minor Nb-rich regions (dark spots in the microstructures). Fig. 4.19 (h) shows that after homogenization of the MoNb alloy, both Mo and Nb are still homogeneously distributed with minor Nb-rich regions. It can thus be concluded that the homogenized microstructure is a thermodynamically stable structure for the present heat treatment conditions. Fig. 4.20 (b), (c), and (d) indicate that Mo, Nb, and Ti are also homogeneously distributed throughout the as-cast MoNbTi alloy, with some Ti segregation at the grain boundaries. After homogenization of the MoNbTi alloy, no variation was observed with respect to the chemical distribution of the elements compared to the as-cast MoNbTi alloy, which can be seen in Fig. 4.20 (f), (g), and (h). Summary of the average chemical composition obtained from EDS area maps for all the samples is shown in Table 4.6. Good agreement can be observed between the EDS data and the nominal composition in all cases.

Table 4.6 Summary of chemical composition obtained from EDS area mapping

Alloy (condition)	Mo (at. %)	Nb (at. %)	Ti (at. %)
MoNb (As-cast)	52.1	47.9	
MoNb (Heat treated)	51.9	48.1	
MoNbTi (As-cast)	33.6	35.2	31.2
MoNbTi (Heat treated)	34.8	33.4	31.8

To determine the grain size and morphology of both the alloys in as-cast and homogenized conditions, EBSD studies are performed. Fig. 4.21 (a) shows the inverse pole figure (IPF) map of the as-cast MoNb alloy with an average grain size of 115 μ m. Ti addition to the MoNb alloy results in significant grain refinement with an average grain size of 34 μ m as shown in Fig. 4.21 (b). For the MoNb homogenized alloy shown in Fig. 4.21 (c), the average grain size is 117 μ m, and for the MoNbTi homogenized alloy shown in Fig. 4.21 (d), the average grain size is

41 µm. Further, it is clear that as-cast microstructures of both the alloys (Fig. 4.21 (a-b)) show equiaxed grains, whereas post homogenization (Fig. 4.21 (c-d)), the grain morphology is elongated probably due to the competing effects resulting from inter-diffusion of the participating elements at high temperature.

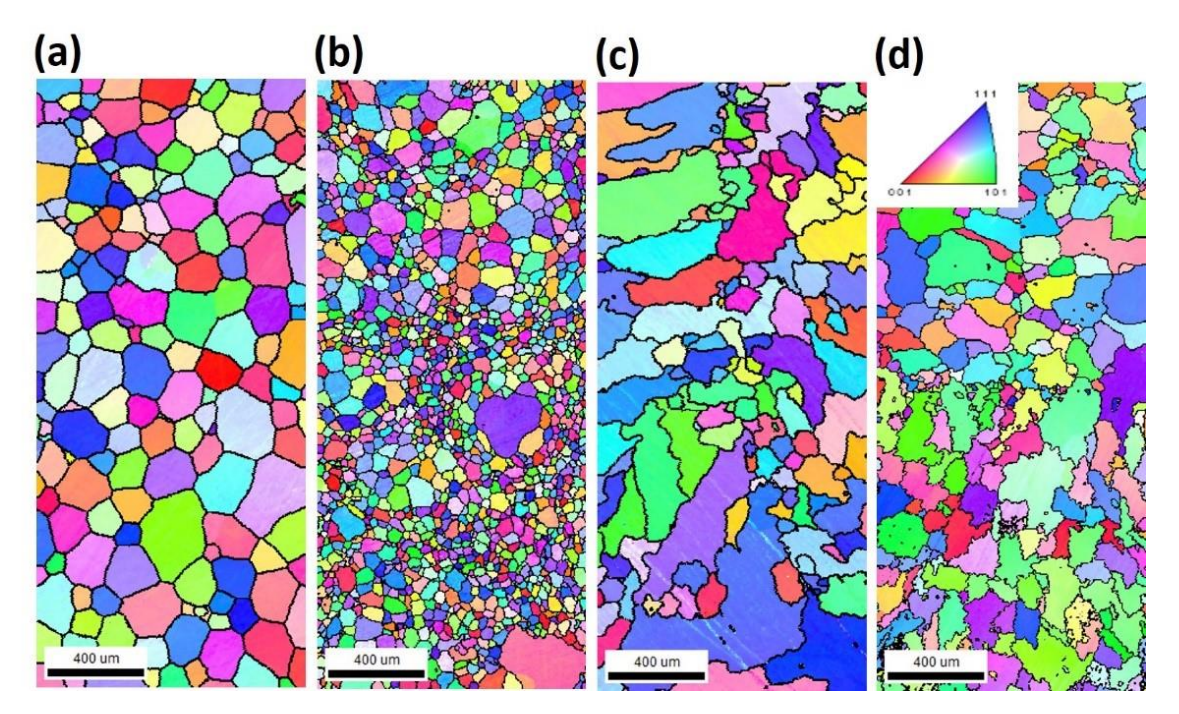


Fig. 4.21 Inverse pole figure maps of the (a) as-cast MoNb alloy, (b) as-cast MoNbTi alloy, (c) homogenized MoNb alloy and (d) homogenized MoNbTi alloy. as-cast condition shows an equiaxed grain morphology, whereas homogenization results in elongated grains in these alloys.

Hardness

The effect of grain refinement due to Ti addition on the hardness is explored using the macro Vickers hardness measurements. Macro hardness values at different loads on these alloys is shown in Fig. 4.22 (a). While the hardness is different for the different alloys and heat treatment states, it does not show much variation with load. Macro hardness testing is performed to cover many grains (finer to coarser), which results in an appropriate representative hardness value. It may be noted that the Vickers hardness is converted to GPa by a multiplying factor of 9.807×10^{-3} to enable comparison with flow stress. At the highest load of 10000 gf the hardness is: as-cast MoNb: 4.27 ± 0.02 GPa, as-cast MoNbTi: 4.22 ± 0.01 GPa, homogenized MoNb: 4.06 ± 0.01 GPa and homogenized MoNbTi: 4.10 ± 0.01 GPa. This is a very striking result as Ti accounts for 33% of the alloy and yet does not have a significant effect on the overall hardness, despite it being softer than the rest of the elements. Fig. 4.22 (b & c) shows the BSE

microstructure (homogenized MoNb and MoNbTi alloys) of the macro Vickers indents at 10000 gf load. The indent residual impressions cover multiple grains. It is interesting to note that an indentation crack, albeit short, is observed in the case of MoNb and not in MoNbTi.

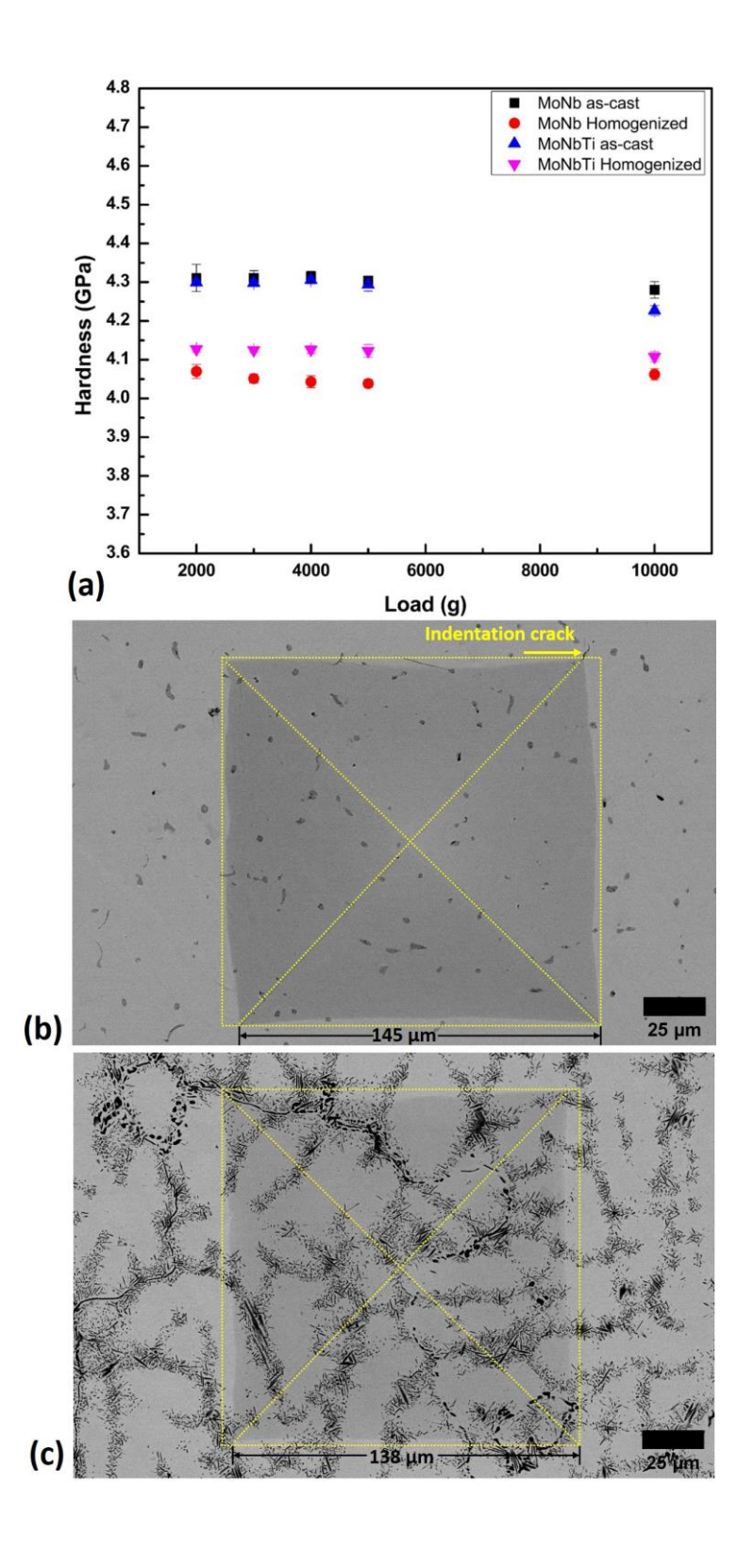


Fig. 4.22 (a) Hardness measurements at various loads (2000-10000 gf) on MoNb (as-cast and homogenized) and MoNbTi (as-cast and homogenized). BSE micrograph with indent residual impression at 10000 gf load on (b) homogenized MoNb alloy and (c) homogenized MoNbTi alloy.

In addition to the absolute hardness, "density-normalized" hardness, which is the ratio of hardness to density, is an important metric for light weighting applications. Fig. 4.23 shows the "density-normalized" hardness for different refractory MPEAs reported in the literature along with the present MoNb and MoNbTi homogenized alloys. The plot clearly shows that in this particular class of alloys (MoNbTaW family), MoNbTi alloy presented in this work has an exceptionally high "density-normalized" hardness. This observation will be reconciled by a combination of microstructural observations and various strengthening mechanisms-based arguments in the subsequent sections.

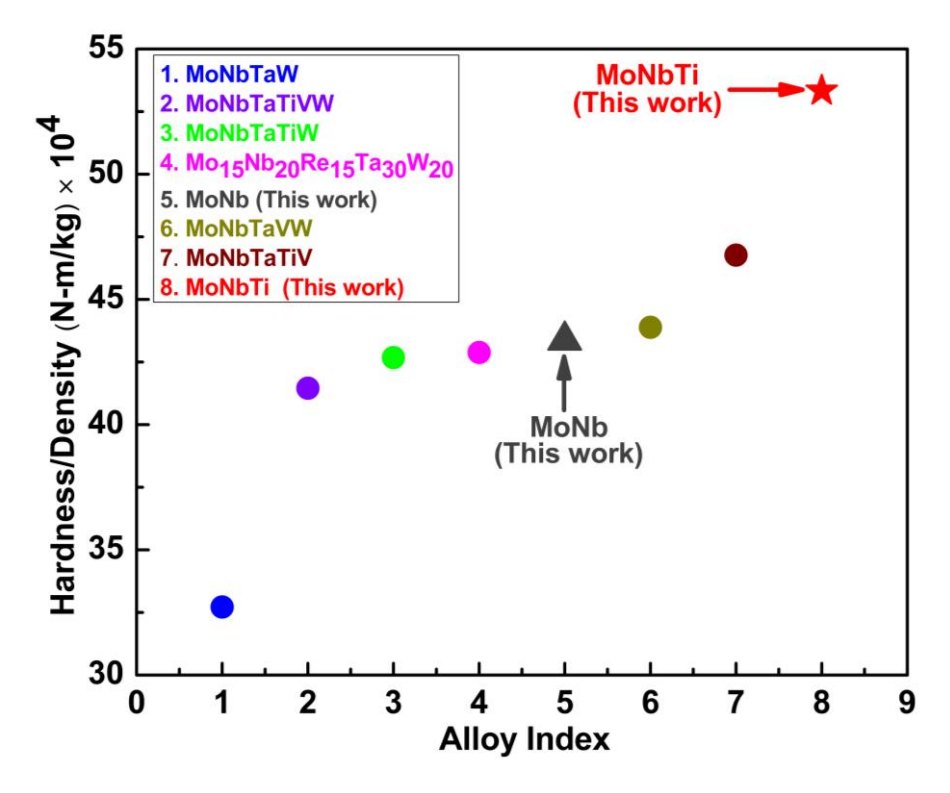


Fig. 4.23 "Density-normalized" hardness of MoNbTaW family [20–23] of alloys from the literature including the homogenized MoNb and MoNbTi alloys from the present work (indicated with an arrow).

4.4.4. Discussion

Microstructural evolution

Fig. 4.17 and Fig. 4.18 show that a single-phase BCC structure is thermodynamically stable based on both experimental outcomes and CALPHAD calculations for both MoNb and MoNbTi alloys. The homogenization temperature of 1673 K corresponds to homologous temperatures of 0.58, 0.61 and 0.86 for Mo, Nb and Ti, respectively. At this temperature, it is reasonable to expect interdiffusion of these elements within these alloys. However, even after homogenization for 24 h, it is evident that the crystal structures (Fig. 4.18) and microstructures (Fig. 4.19 and Fig. 4.20) are not altered. However, it is to be noted that minor Nb rich regions seen in Fig. 4.19 account for 1.65% (area wise) and increase to 1.97% after homogenization. Similarly, the Ti segregation, which is 1.47% in the as-cast condition increases to 2.19% after homogenization in MoNbTi alloy. As these fractions are low, they are not observed in the XRD patterns shown in Fig. 4.18. Even though the presence of minor quantities of alloying elements (Nb or Ti as is the case) is detected in the SEM investigations, practically these can be considered to offer single phase microstructures which are thermodynamically stable. The decoration of grain boundaries by Ti in MoNbTi alloy decreases the grain boundary energy and plays a key role in the significant grain refinement as shown in Fig. 4.21 (b), which can in turn help retain high hardness.

Flow stress

The hardness values for the alloys in the present work at 10000 gf load is about 4.10 GPa, which is comparable to that reported for several alloys of the MoNbTaW family [4,20,22]. A high load was applied to perform the hardness measurements with no evidence of any significant indentation cracking as shown in Fig. 4.22 (c), indicating that enough plasticity is available in the alloy. A striking feature of this investigation is that such a high hardness is achieved with either two (MoNb) or three (MoNbTi) elements in equiatomic proportion. This raises an important question regarding the need for 5 or more elements to derive high hardness or strength, especially for achieving high "density-normalized" strength. To explore this aspect in greater detail, the strengthening contributions from various sources is assessed for the alloys in the present work along with other theoretical combinations consisting of Mo, Nb, Ta, W, and Ti. Despite the refinement in grain size in the MoNbTi alloy, it is still in the micrometer scale. Previous reports [7] indicate that solid solution strengthening is the dominant strengthening mechanism in these systems. Using the previously reported analysis, in the case

of MoNbTi it is found that solid solution strengthening ($\Delta \sigma_{SS}$) and frictional stress (σ_o) contribute 95 % to the overall flow stress. Hence, we focus on these contributions to calculate the flow stress (σ_f) as

$$\sigma_f = \sigma_0 + \Delta \sigma_{SS}$$
....(4.9)

Flow stress is calculated using Eq. (4.9) for the 26 different theoretically possible equiatomic alloys (binary, ternary, quaternary and quinary) consisting of Mo, Nb, Ta, W and Ti. "Densitynormalized" flow stress (σ_f/ρ) is then calculated from Eq. (4.9) and the theoretical density for the corresponding composition. Details of the calculations for frictional stress and solid solution strengthening are available elsewhere [7,24,25]. Fig. 4.24 (a) shows the "densitynormalized" flow stress as a function of the number of elements in the alloy for the 26 different combinations of equiatomic alloys (binary to quinary) in this system (Mo, Nb, Ta, W and Ti). The values for individual elements, which do not have solid solution strengthening are also shown for comparison. The plot clearly shows the diminishing returns beyond 3 elements. It may be noted that several alloy compositions shown in the plot may not be practically feasible or yield stable single phase material. For instance, binary alloys MoTi and WTi as shown in the plot have high "density-normalized" flow stress. However, they are not miscible over the complete range of temperature (room temperature to melting temperature) [26]. The plot also shows that MoWTi and MoNbTi are the preferred compositions for the ternary alloys. However, the theoretical density of MoWTi is 11 g/cc which is significantly higher than MoNbTi (7.6 g/cc). In the case of quaternary alloy MoNbWTi has the highest normalized strength, However, even in this case the density is high (10.4 g/cc) compared to MoNbTi. This simple analysis clearly demonstrates that by a judicious choice of fewer elements that give a combination of large solid solution strengthening and lower density, high "density-normalized" flow stress can be achieved such as in the case of MoNbTi shown in the present study. The key features of MoNbTi system are the good miscibility of MoNb [26,27], and the addition of Ti that significantly reduces the density without compromising the strength. The retention of strength in MoNbTi can be attributed to the difference in the atomic radius and shear modulus between the constituent elements that naturally enhances solid solution strengthening. To specifically demonstrate the role of Ti in these alloys, "density-normalized" flow stress with and without Ti addition is shown in Fig. 4.24 (b). The plot clearly shows that Ti addition leads to an overall increase in "density-normalized" flow stress in many cases, making a strong case for Ti addition in these alloy systems. In summary, if the advantage from solid solution strengthening is exhausted with three elements, the addition of more elements in equiatomic

proportion may not be beneficial. Hence, the alloying strategy for equiatomic alloys may be accordingly framed by employing just two or three elements. Although the resultant BCC structure of the current material systems offers high strength, it may not offer good ductility. Therefore, judicial selection and optimal additions of alloying elements which could induce sufficient levels of ductility is the right approach for materials development for next generation high temperature materials.

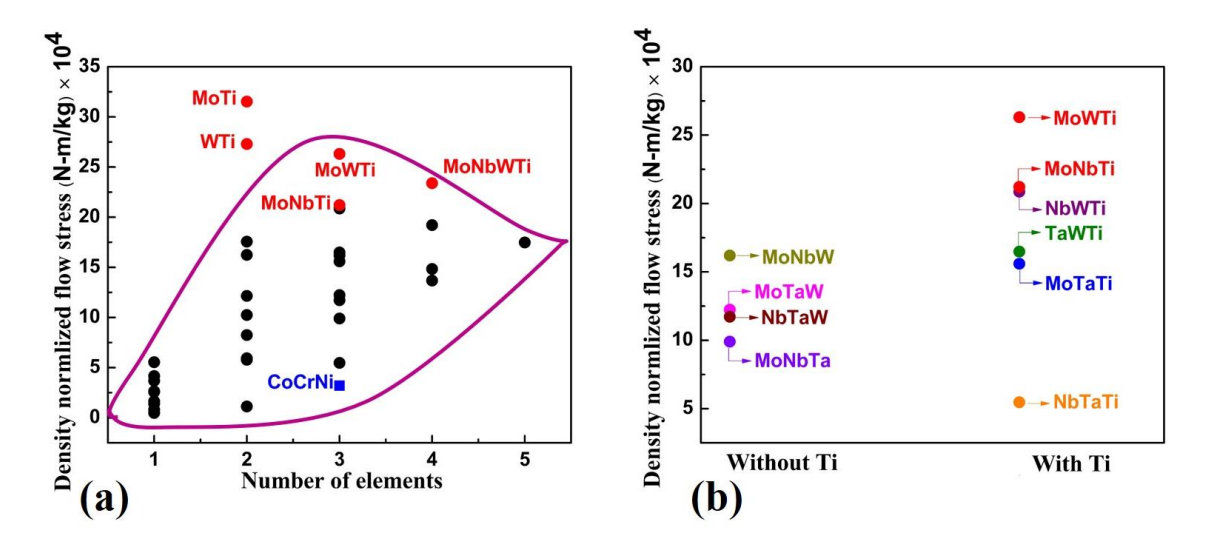


Fig. 4.24 "Density-normalized" flow stress of binary, ternary, quaternary and quinary refractory multi-principal element alloys consisting of Mo, Nb, Ta, W and Ti as a function of (a) number of elements; red color data points show the maximum value that can be obtained in these refractory multi-principal element alloys, blue color data point is for CoCrNi multi-principal element alloy, included for comparison purposes and (b) influence of Ti on refractory multi-principal element alloys. It suggests that addition of more number of alloying elements, beyond three in equiatomic proportion, may not offer major advantage in deriving high hardness (strength) in single phase multi-principal element alloys.

4.4.5. Summary

Equiatomic MoNb and MoNbTi alloys were developed by melting and casting route. Homogenization of the cast samples was carried out at 1673 K for 24 h. A single phase BCC structure which was obtained after casting was found to be stable even after homogenization. Equilibrium phase diagrams and phase fraction plots drawn for MoNb and MoNbTi alloys also showed a single BCC phase at a complete range of temperatures from room temperature to melting points. Equiaxed grains were observed in the as-cast condition, whereas elongated

grains were observed after homogenization. Titanium addition leads to overall density reduction and significant grain refinement. Titanium was found to segregate to the grain boundary regions in addition to its presence in the lattice positions in the complex MoNbTi alloy. This potentially pins the grain boundaries, thus decreasing the overall grain boundary energy. Both the alloys (MoNb and MoNbTi) exhibit comparable hardness within the MoNbTaW family of alloys. Further, the striking feature of this study is the exceptionally high "density-normalized" hardness of these alloys (MoNb and MoNbTi) that surpasses all the alloys of the MoNbTaW family reported in the literature so far. Solid solution strengthening is the dominant strengthening mechanism in these alloys. Furthermore, it was found that addition of more than three elements in equiatomic proportions may not be necessary to obtain high "density-normalized" flow stress. Instead, equiatomic binary and ternary alloys can offer more scientific/technological advantages coupled with cost reduction.

References

- [1] O.N. Senkov, J. Gild, T.M. Butler, Microstructure, mechanical properties and oxidation behavior of NbTaTi and NbTaZr refractory alloys, J. Alloys Compd. 862 (2021) 158003. https://doi.org/10.1016/j.jallcom.2020.158003.
- [2] Q.J. Li, H. Sheng, E. Ma, Strengthening in multi-principal element alloys with local-chemical-order roughened dislocation pathways, Nat. Commun. 10 (2019) 1–11. https://doi.org/10.1038/s41467-019-11464-7.
- [3] F.G. Coury, G. Zepon, C. Bolfarini, Multi-principal element alloys from the CrCoNi family: outlook and perspectives, J. Mater. Res. Technol. 15 (2021) 3461–3480. https://doi.org/10.1016/j.jmrt.2021.09.095.
- [4] Anjali Kanchi, Koteswararao V. Rajulapati, B. Srinivasa Rao, D. Sivaprahasam, and Ravi C. Gundakaram, Influence of Thermomechanical Processing on Microstructure and Mechanical Properties of MoNbTaW Refractory High-Entropy Alloy, J. of Materi Eng and Perform, 264 (2022) 48–51.
- [5] R.S. Ganji, P. Sai Karthik, K. Bhanu Sankara Rao, K. V. Rajulapati, Strengthening mechanisms in equiatomic ultrafine grained AlCoCrCuFeNi high-entropy alloy studied by micro- and nanoindentation methods, Acta Mater. 125 (2017) 58–68. https://doi.org/10.1016/j.actamat.2016.11.046.
- [6] S. Xu, Y. Su, W.R. Jian, I.J. Beyerlein, Local slip resistances in equal-molar MoNbTi multi-principal element alloy, Acta Mater. 202 (2021) 68–79.

- https://doi.org/10.1016/j.actamat.2020.10.042.
- [7] D.G. Kalali, S. Antharam, M. Hasan, P.S. Karthik, P.S. Phani, K. Bhanu Sankara Rao, K. V. Rajulapati, On the origins of ultra-high hardness and strain gradient plasticity in multi-phase nanocrystalline MoNbTaTiW based refractory high-entropy alloy, Mater. Sci. Eng. A. 812 (2021) 141098. https://doi.org/10.1016/j.msea.2021.141098.
- [8] D.G. Kalali, P.S. Karthik, K.B. Sankara, K. V Rajulapati, Ultra-hard, multi-phase nanocrystalline MoTa and MoTaTi based concentrated refractory alloys, Mater. Lett. 324 (2022) 132768. https://doi.org/10.1016/j.matlet.2022.132768.
- [9] B. Gludovatz, A. Hohenwarter, K.V.S. Thurston, H. Bei, Z. Wu, E.P. George, R.O. Ritchie, Exceptional damage-tolerance of a medium-entropy alloy CrCoNi at cryogenic temperatures, Nat. Commun. 7 (2016) 1–8. https://doi.org/10.1038/ncomms10602.
- [10] M. Kang, K.R. Lim, J.W. Won, K.S. Lee, Y.S. Na, Al-Ti-containing lightweight highentropy alloys for intermediate temperature applications, Entropy. 20 (2018). https://doi.org/10.3390/e20050355.
- [11] D. Li, Y. Dong, Z. Zhang, Q. Zhang, S. Chen, N. Jia, H. Wang, B. Wang, K. Jin, Y. Xue, Y. Dou, X. He, W. Yang, L. Wang, H. Cai, An as-cast Ti-V-Cr-Al light-weight medium entropy alloy with outstanding tensile properties, J. Alloys Compd. 877 (2021). https://doi.org/10.1016/j.jallcom.2021.160199.
- [12] S.S. Sohn, A. Kwiatkowski, Y. Ikeda, F. Körmann, W. Lu, Ultrastrong Medium-Entropy Single-Phase Alloys Designed via Severe Lattice Distortion, 1807142 (2018) 1–8. https://doi.org/10.1002/adma.201807142.
- [13] A. Roy, P. Sreeramagiri, T. Babuska, B. Krick, P.K. Ray, G. Balasubramanian, Lattice distortion as an estimator of solid solution strengthening in high-entropy alloys, Mater. Charact. 172 (2021) 110877. https://doi.org/10.1016/j.matchar.2021.110877.
- [14] B. Cantor, I.T.H. Chang, P. Knight, A.J.B. Vincent, Microstructural development in equiatomic multicomponent alloys, Mater. Sci. Eng. A. 375–377 (2004) 213–218. https://doi.org/10.1016/j.msea.2003.10.257.
- [15] O.N. Senkov, S.I. Rao, T.M. Butler, K.J. Chaput, Ductile Nb alloys with reduced density and cost, J. Alloys Compd. 808 (2019) 151685. https://doi.org/10.1016/j.jallcom.2019.151685.
- [16] L. Qi, D.C. Chrzan, Tuning Ideal Tensile Strengths and Intrinsic Ductility of bcc Refractory Alloys, 115503 (2014) 1–5. https://doi.org/10.1103/PhysRevLett.112.115503.
- [17] E.A. Holm, S.M. Foiles, How grain growth stops: A mechanism for grain-growth

stagnation in pure materials, Science (80-.). 328 (2010) 1138–1141. https://doi.org/10.1126/science.1187833.

- [18] A.R. Stokes, A.J.C. Wilson, The diffraction of x rays by distorted crystal aggregates I, Proc. Phys. Soc. 56 (1944) 174–181. https://doi.org/10.1088/0959-5309/56/3/303.
- [19] D.G. Kalali, H. Seekala, P.S. Phani, K. Bhanu Sankara Rao, K. V. Rajulapati, High speed nanoindentation aided correlative study between local mechanical properties and chemical segregation in equiatomic MoNb and MoNbTi alloys, J. Mater. Res. (2023) 28–30. https://doi.org/10.1557/s43578-023-01007-8.
- [20] O.N. Senkov, G.B. Wilks, J.M. Scott, D.B. Miracle, Mechanical properties of Nb25Mo25Ta 25W25 and V20Nb20Mo 20Ta20W20 refractory high entropy alloys, Intermetallics. 19 (2011) 698–706. https://doi.org/10.1016/j.intermet.2011.01.004.
- [21] U. Bhandari, C. Zhang, C. Zeng, S. Guo, S. Yang, Computational and experimental investigation of refractory high entropy alloy mo15nb20re15ta30w20, J. Mater. Res. Technol. 9 (2020) 8929–8936. https://doi.org/10.1016/j.jmrt.2020.06.036.
- [22] Z.D. Han, N. Chen, S.F. Zhao, L.W. Fan, G.N. Yang, Y. Shao, K.F. Yao, Effect of Ti additions on mechanical properties of NbMoTaW and VNbMoTaW refractory high entropy alloys, Intermetallics. 84 (2017) 153–157. https://doi.org/10.1016/j.intermet.2017.01.007.
- [23] H.W. Yao, J.W. Qiao, J.A. Hawk, H.F. Zhou, M.W. Chen, M.C. Gao, Mechanical properties of refractory high-entropy alloys: Experiments and modeling, J. Alloys Compd. 696 (2017) 1139–1150. https://doi.org/10.1016/j.jallcom.2016.11.188.
- [24] Z.C. Cordero, B.E. Knight, C.A. Schuh, Six decades of the Hall–Petch effect a survey of grain-size strengthening studies on pure metals, Int. Mater. Rev. 61 (2016) 495–512. https://doi.org/10.1080/09506608.2016.1191808.
- [25] R. Labusch, A Statistical Theory of Solid Solution Hardening, Phys. Status Solidi. 41 (1970) 659–669. https://doi.org/10.1002/pssb.19700410221.
- [26] J.J. English, Binary and Ternary Phase Diagrams of Columbium, Molybdenum, Tantalum, and Tungsten", Defense Metals Information Center Report, Battelle Memorial Institute, Columbus, OH. Rep. No. 53 (1961) 152.
- [27] P. Franke, D. Neuschutz, Mo-Nb, in: P. Franke, D. Neuschutz (Eds.), Binary Systems. Part 4: Binary Systems from Mn-Mo to Y-Zr: Phase Diagrams, Phase Transition Data, Integral and Partial Quantities of Alloys, Springer Berlin Heidelberg, Berlin, Heidelberg, 2006. pp. 1–4.

4.5. Length scale effects in the MoNb and MoNbTi multi-principal element alloys: Understanding their local chemical and mechanical behaviour

4.5.1. Introduction

Complex concentrated alloys (CCAs) are one of the emerging structural materials ever since they were proposed in 2004 [1–3]. The tremendous interest shown by the scientific community on this radical alloying concept is due to its reported unprecedented mechanical properties at room temperature [1,4,5] and high temperatures [6,7]. In addition, multiple characteristic length scales of these microstructures add a new dimension to the materials development scheme [4,5]. Similar to the processing of nanocrystalline materials, it is possible to develop these alloys with mechanical alloying (MA) and subsequent spark plasma sintering (SPS), after which a homogeneous microstructure is often observed [8–12]. Alternatively, these alloys can be developed with micrometer range grain size using the melting and casting route, wherein a heterogeneous microstructure is expected [4,5,7]. Generally, cast alloys are more ductile and hence more desirable than alloys developed using the MA+SPS route due to sufficient mobility of dislocations in the coarse-grained microstructure. The heterogeneous microstructure (morphology wise or chemistry wise) in the as-cast CCAs is due to the presence of elements in highly concentrated proportions with different melting points, densities, and varying miscibility characteristics [13,14]. Hence, understanding the chemical segregation behavior in the CCAs is essential, as it plays a vital role in tailoring the microstructure and mechanical properties.

Recent developments in high speed nanoindentation mapping [15–18] with reduced indent spacing [19,20] have demonstrated the ability to reliably measure hardness at the micrometer length scale. This capability has opened the doors for establishing structure-property correlations at that scale, as evidenced by the recent reports [21–24]. Most of the recent works have focused on establishing the link between microstructure (phase, crystal orientation, etc.,) and local mechanical properties [25–27]. A few recent works have also demonstrated the ability to link the chemical composition to mechanical properties [23,28–30]. However, such correlations in CCAs have not been explored yet. Given the multiple elements with different melting points and varying miscibility characteristics, chemical segregation is expected in such alloys, which makes a strong case for coupling the local chemical composition obtained by techniques such as Energy dispersive spectroscopy (EDS) with nanoindentation mapping, and this forms the basis for the present work. The aim of this paper is to assess the correlation

between hardness and chemical composition at the micrometer lengths scale. To this end, high speed nanoindentation maps and EDS maps in a given region with comparable resolutions, are analysed to establish possible correlation. The high speed nanoindentation mapping technique used in this work is, in principle, similar to the quasi-static testing, except for the duration of the test, which is less than 1 second per indent. In addition to the ability to map the hardness at a micrometer length scale, recent works [24,31,32] have also demonstrated the ability to quantify the mechanical properties of the constituents through various statistical techniques. Leveraging of these hardware and analysis capabilities, in this work we present EDS and corresponding nanoindentation maps in MoNb and MoNbTi alloys to quantitatively assess the correlation between the local chemistry and hardness & elastic modulus. Segregation of Nb and Ti at the grain boundaries is observed in these alloys and the ability of the nanoindentation mapping technique to capture the corresponding local variations in mechanical properties is presented. A comparison of the results in the as-cast and heat-treated conditions is also presented to systematically study the effect of local rearrangement in chemistry with heat treatment. Collectively, these results enable an understanding of the effect of chemical segregation on the local mechanical properties of CCAs, which can be gainfully used to tailor the microstructure and properties of these alloys.

4.5.2. Results

Crystal structure

Fig. 4.25 shows the X-ray diffractograms obtained for as-cast and heat treated conditions of both the MoNb and MoNbTi alloys. In MoNb alloy, the as-cast condition confirms a single BCC phase with a lattice parameter of 3.22 Å, and the corresponding homogenized condition also shows a single BCC phase with a lattice parameter of 3.21 Å. Similarly in MoNbTi alloy, the as-cast and homogenized conditions exhibit a single BCC phase with an identical lattice parameter of 3.23 Å. It is clear that single phase BCC structure is the most stable structure in these two alloy systems. Interestingly, Ti addition is not found to alter the crystal structure. Also, homogenization at 1673 K for 24 h does not cause any phase transformation, indicating that these CCAs are thermally stable even at 1673 K.

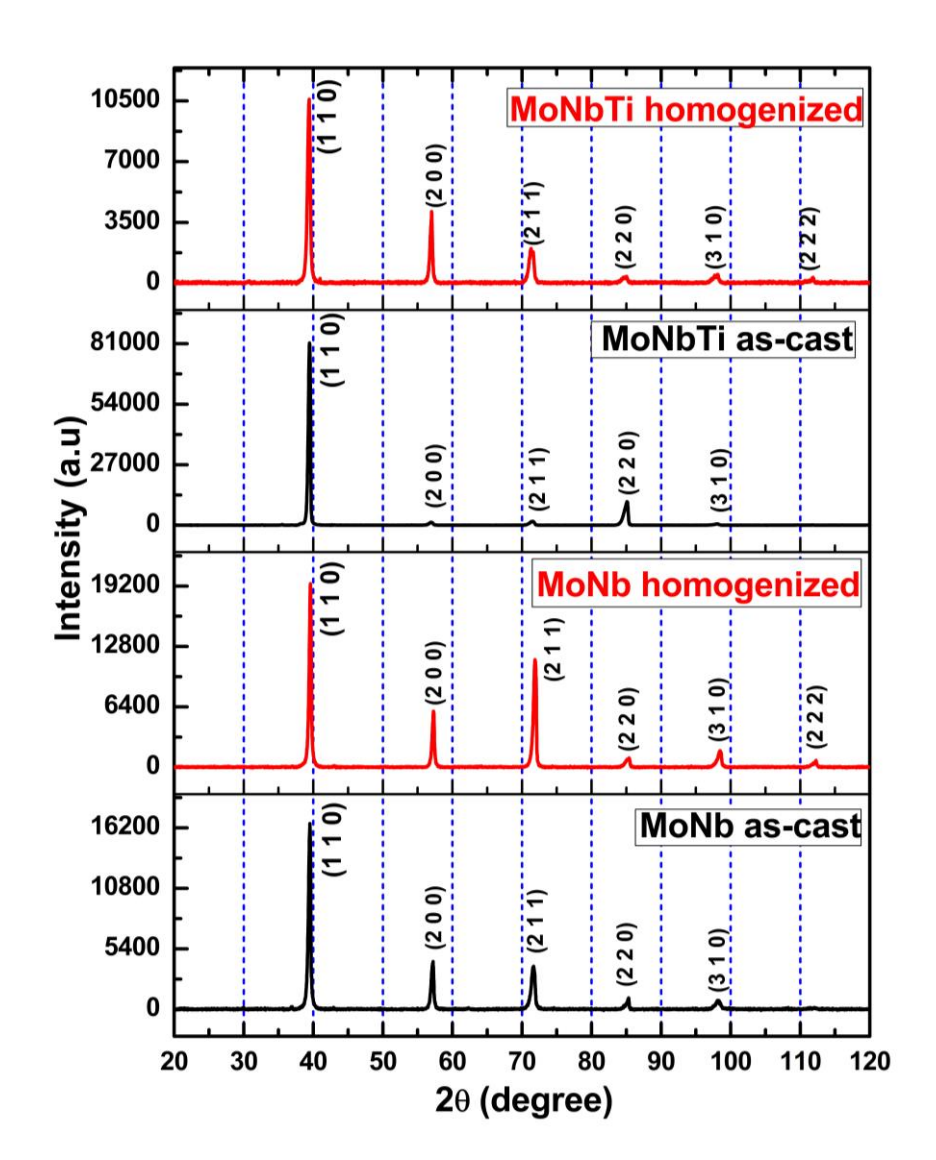


Fig. 4.25 X-ray diffractograms of equiatomic MoNb and MoNbTi CCAs in as-cast and homogenized conditions (from bottom to top). In all the cases, a single BCC phase was observed.

Microstructure and chemical analysis

Fig. 4.26 shows the FE-SEM BSE micrographs of the mapped regions in MoNb and MoNbTi alloys in as-cast and heat-treated conditions. In all the cases, clear contrast can be observed, indicating the local variations in atomic number or chemical segregation. Fig. 4.26 (a) shows the micrograph of MoNb in the as-cast condition. The dark regions in the micrograph correspond to the segregation of the lower atomic number element (Nb), as will be later shown from EDS results. Although Mo and Nb have good miscibility [33], the difference in melting points (~ 150 K) can result in some segregation, which is still relatively small (< 3 %).

Interestingly, XRD data on these alloys shown in Fig. 4.25, indicates a single BCC phase. This implies that the dark regions in the micrographs are either below the detection threshold of standard XRD measurement or have similar crystal structure, making it difficult to distinguish. Upon heat treatment, the fraction of the Nb rich regions decreases further (< 0.6 %), as shown in Fig. 4.26 (b). The micrograph also shows that the microstructure is retained even after heat treatment at 1673 K.

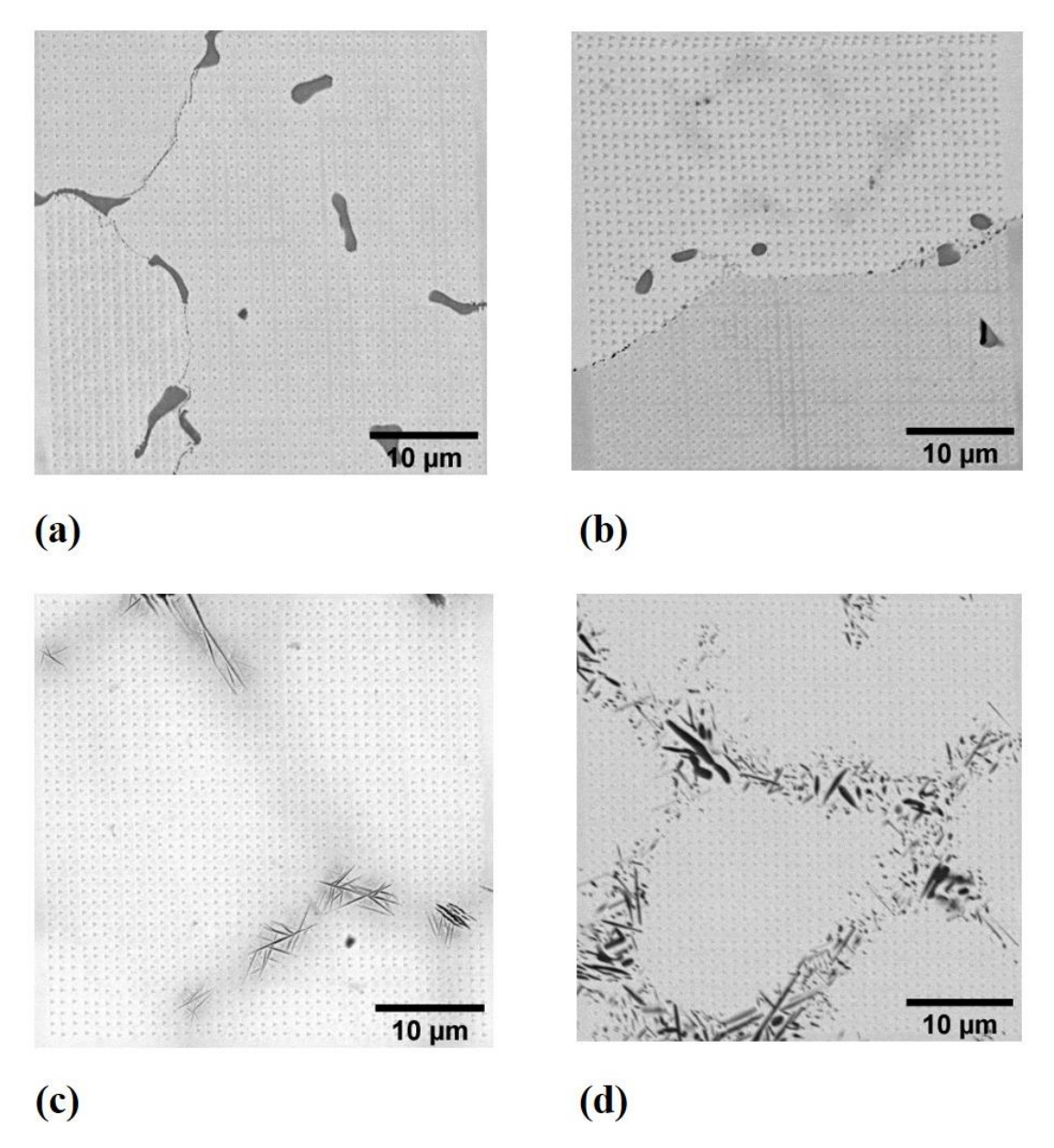


Fig. 4.26 FE-SEM, BSE micrograph with the indent overlay for (a) MoNb in as-cast condition, (b) MoNb in heat treated condition, (c) MoNbTi in as-cast condition and (d) MoNbTi in heat treated condition.

Similar to the MoNb alloy shown in Fig. 4.26 (a-b), addition of Ti also results in certain amount of chemical segregation as may be observed from the dark regions in Fig. 4.26 (c-d). However, there are clear differences in the nature of segregation. In Fig. 4.26 (c-d), the dark regions correspond to Ti enrichment and its morphology is acicular and is also of smaller length scale compared to the Nb rich regions in Fig. 4.26 (a-b). Segregation of Ti is due to the melting point difference compared to Mo and Nb and the miscibility gap of Ti with Mo and Nb [33–35]. Upon heat treatment of MoNbTi alloy, the contrast of the dark region is further enhanced due to probable diffusion of Ti, as shown in Fig. 4.26 (d).

In order to probe the local chemical composition in the microstructure shown in Fig. 4.26, EDS maps corresponding to the BSE micrographs of all the samples are presented in Fig. 4.27. The EDS maps are obtained by normalizing the counts for a given element with the total counts recorded for a given pixel, as detailed in materials and methods section. In the case of MoNb alloy (Fig. 4.27 (a-b)), the maps show the fraction of Nb. The red regions in the maps are Nb rich and a comparison with the corresponding BSE micrograph in Fig. 4.26 indicates that they correspond to the dark regions. Fig. 4.27 (a) also shows that Nb enrichment occurs at the boundaries or interfaces. Upon heat treatment as shown in Fig. 4.27 (b), the extent of segregation is reduced. In the case of MoNbTi shown in Fig. 4.27 (c-d), the EDS maps show the Ti fraction. Similar to the case of MoNb, Ti enrichment at the interfaces can be clearly observed. However, in contrast to MoNb, upon heat treatment (Fig. 4.27 (d)), the Ti fraction is further enhanced at the boundaries, which was also observed from the enhanced contrast of the BSE micrograph shown in Fig. 4.26 (d).

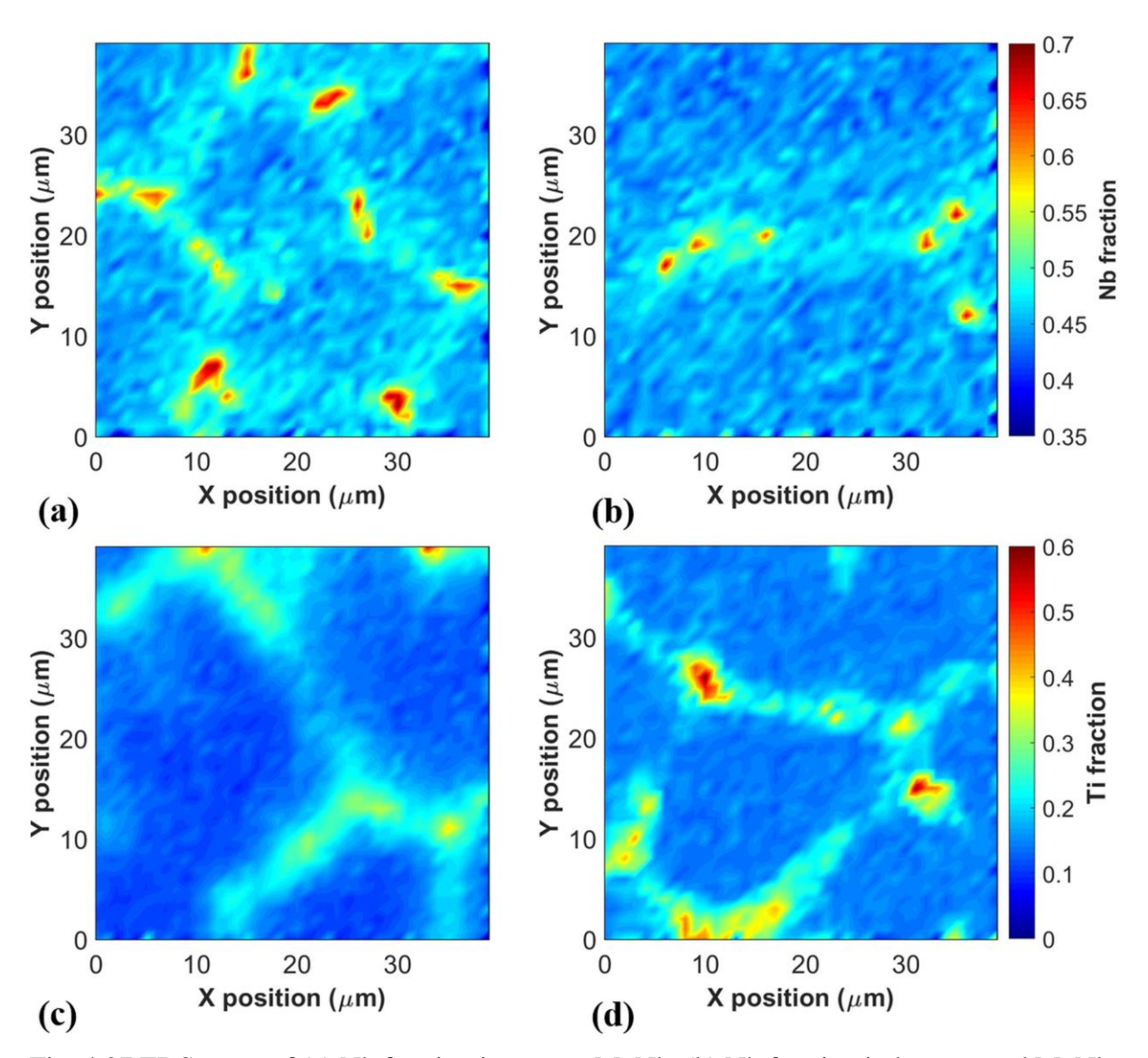


Fig. 4.27 EDS maps of (a) Nb fraction in as-cast MoNb, (b) Nb fraction in heat treated MoNb, (c) Ti fraction in as-cast MoNbTi and (d) Ti fraction in heat treated MoNbTi.

Nanoindentation

The microstructural analysis presented in the previous section shows a clear evidence of chemical segregation at the micrometer length scale, which is below the typical length scale accessed by micro hardness testing. Hence, after EDS mapping, nanoindentation mapping with an indent spacing of 1 µm was carried out in the regions shown in Fig. 4.26. Fig. 4.28 (a) shows the hardness map of the MoNb alloy in the as-cast condition. Local variation in hardness can be clearly observed from the map, wherein the higher hardness regions correspond to the Nb rich regions in the EDS map shown in Fig. 4.27 (a). The map also demonstrates the ability of the nanoindentation mapping technique to capture the local variation in mechanical properties in the vicinity of the boundary, which can be gainfully used for studying the effect of chemical

segregation on mechanical properties at the micrometer length scale. Upon heat treatment of MoNb alloy, although the higher hardness regions are significantly reduced in area fraction as shown in Fig. 4.28 (b), they still correspond to the Nb rich region shown in Fig. 4.27 (b). Also, the overall hardness of the specimen shows a slight reduction with heat treatment. In the case of the MoNbTi alloys shown in Fig. 4.28 (c-d), the spatial variation in hardness is very clear, with the regions close to the boundaries which are also Ti rich, show higher hardness. In the as-cast condition shown in Fig. 4.28 (c), the higher hardness regions are relatively thick (~ 5 μm) and also mostly continuous. This trend agrees well with the EDS map of Ti fraction shown in Fig. 4.27 (c). In contrast, upon heat treatment, the higher hardness regions are not continuous along the boundaries as shown in Fig. 4.28 (d), and also show a marginal increase in hardness possibly due to further enrichment of Ti. Again, this trend agrees well with the corresponding EDS map of Ti fraction shown in Fig. 4.27 (d). Furthermore, the hardness in the interior regions of the grain does not change much upon heat treatment, indicating the thermal stability of the alloy. A comparison of the hardness maps in the as-cast condition of MoNb (Fig. 4.28 (a)) and MoNbTi (Fig. 4.28 (c)), shows that the hardness decreases with Ti addition, which will be quantified and discussed in detail in the next section. In addition to hardness, elastic modulus was also measured, which shows similar trend as hardness, although with slight differences. This aspect will also be discussed in the next section.

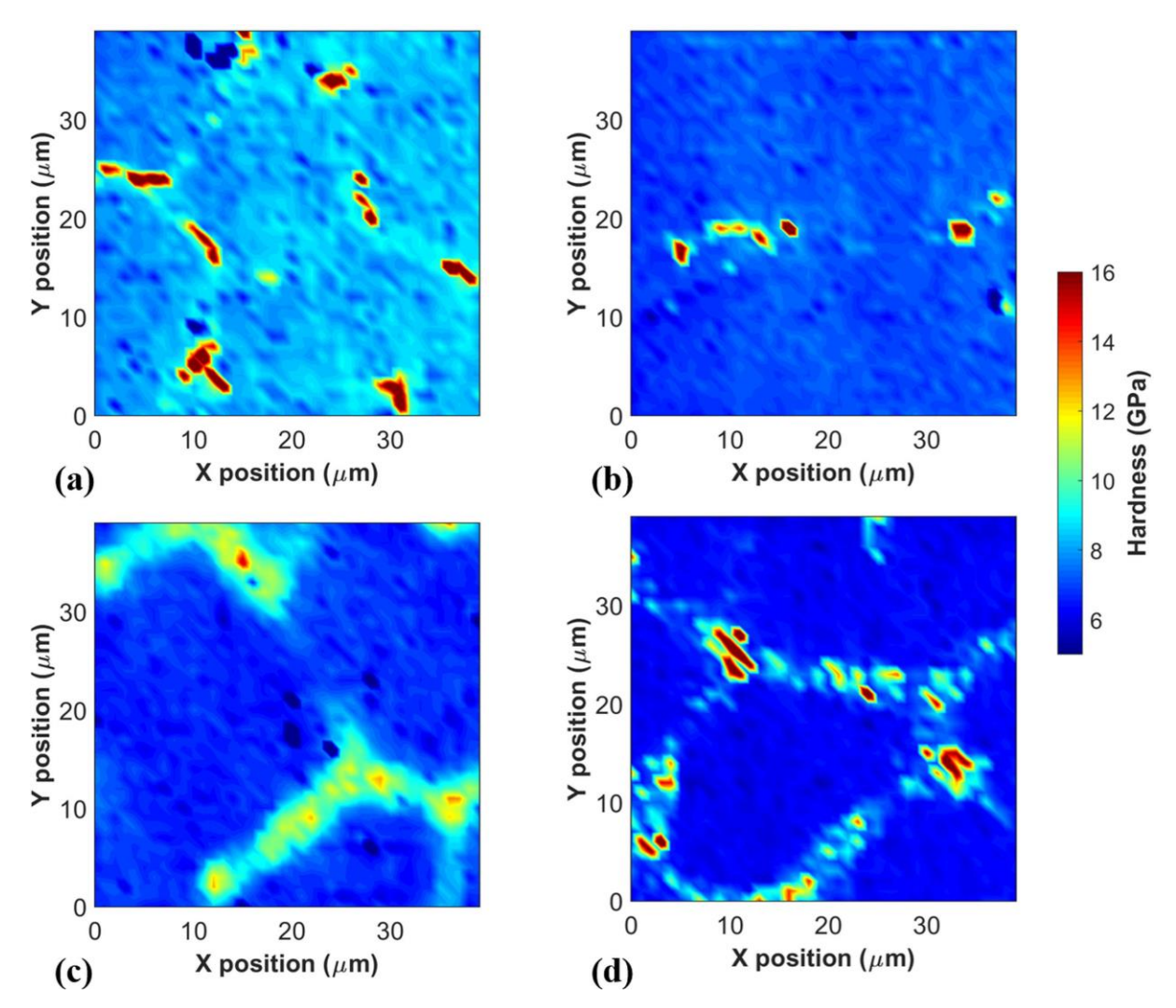


Fig. 4.28 Hardness maps from high-speed nanoindentation for (a) MoNb as-cast alloy, (b) MoNb heat-treated alloy, (c) MoNbTi as-cast alloy and (d) MoNbTi heat-treated alloy.

4.5.3. Discussion

Correlation between local chemistry and mechanical properties

The hardness maps presented in the previous section show spatial variation, especially with proximity to the boundary, which also corresponds to Nb or Ti enrichment. To explore this aspect further, in this section a quantitative correlation between the local chemistry and mechanical properties is presented by coupling the EDS and nanoindentation maps. In order to demonstrate the EDS-nanoindentation coupling, MoNbTi in as-cast condition is taken as a reference. Fig. 4.29 shows a montage of the SEM micrograph, EDS map, hardness map and deconvoluted hardness map of a 40 X40 µm² region in as-cast MoNbTi. The correlation between the EDS and hardness maps is extremely good, which also correlates well with the SEM micrographs. The map shows that the boundaries are enriched with Ti, which results in

higher hardness in the vicinity of the boundary. In order to quantify the composition and hardness of these distinct regions, the hardness map is deconvoluted into two regions, viz., grain interiors and vicinity of boundary, using the procedure described in 4.4.5. The resultant deconvoluted map is also shown in the Fig. 4.29 (d), wherein the red coloured regions correspond to the regions in the vicinity of the boundary and the blue regions correspond to the grain interiors. Subsequent to deconvoluting the data into two distinct regions, the corresponding average hardness or elastic modulus and composition in the respective regions is calculated from a simple arithmetic mean. It may be noted that the values (hardness, elastic modulus or composition) corresponding to the regions close to the boundary are not representative of the grain boundary strength or composition, but a larger region around the boundary. Given the 1 μ m resolution of the nanoindentation map, accurately measuring the strength or hardness of the grain boundary (~ nm) alone is not feasible.

Fig. 4.30 (a) shows the average hardness as a function of Nb fraction in the grain interiors and in the vicinity of the boundary obtained by deconvolution in the as cast and heat-treated conditions. The plot clearly establishes that higher Nb fractions occur at the boundaries and also corresponds to higher hardness. The Nb fraction in the grain interiors remains unaltered upon heat treatment, while the hardness slightly decreases. On the contrary, in the vicinity of the boundary, the Nb fraction and hardness decreases upon heat treatment, moving towards a more homogeneous microstructure.

The corresponding correlation between the local chemical composition and hardness in the case of the MoNbTi alloy is shown in Fig. 4.30 (b). Similar to the case of MoNb alloy, clear correlation between the Ti fraction and hardness can be observed, with the hardness increasing with increasing Ti fraction. In the grain interiors, heat treatment results in slight increase in Ti fraction without any appreciable change in hardness. On the contrary, the Ti fraction in the vicinity of the boundary increases upon heat treatment and the hardness also shows a corresponding increase. This can also be qualitatively observed from the BSE micrograph shown in Fig. 4.26 (d), wherein the contrast at the boundary is enhanced with heat treatment, indicating greater segregation.

In addition to hardness measurements, elastic modulus is also measured during nanoindentation mapping. Fig. 4.30 (c) shows the variation in elastic modulus obtained by deconvolution in the as cast and heat-treated conditions. While the general trend is identical to that of the hardness shown in Fig. 4.30 (a), appreciable differences in the elastic modulus with proximity to the boundary or Nb fraction is not observed. This indicates that the overall crystal structure is not

significantly altered, which was also confirmed by the XRD measurements. With the addition of Ti, the elastic modulus shows a slight decrease as shown in Fig. 4.30 (d) for the MoNbTi alloys. Again, the general trend in modulus is similar to that of the hardness for MoNbTi alloys shown in Fig. 4.30 (b). However, unlike the modulus of MoNb alloys, a slight increase in modulus with heat treatment is observed, indicating that the crystal structure / phase is altered in the vicinity of the boundary. Further investigation with Transmission Electron Microscopy is required to reconcile this observation. From the hardness and elastic modulus results it may also be observed that despite the local variations, hardness decrease with Ti addition is less than that of the elastic modulus, thereby resulting in improved ductility with Ti addition. An interesting and surprising outcome of these results is the significant increase in hardness in

the Nb rich regions in MoNb alloys and in the vicinity of the boundary in MoNbTi alloys. Hardness close to 15 GPa is observed in Ti rich regions close to the boundary in these alloys. Such a high local hardness is usually possible by the presence of a secondary phase, ideally an intermetallic compound comprising of two or more elements of Mo, Nb and Ti in this case. The thermodynamic data for this system also indicates the possibility of secondary phases. However, the XRD results do not show any evidence of a secondary phase, which could be either due to the small length scale of the region ($\sim 5 \mu m$) or due to absence of a distinct crystal structure. Micro-focus XRD and EBSD measurements were also attempted to probe the local crystal structure, both of which, despite experimental challenges, did not indicate the presence of a second phase. This leaves an open question on the possible strengthening mechanism to account for the high hardness observed near grain boundary. In this regard, it may be noted that classical strengthening calculations considering frictional stress, solid solution strengthening, Taylor hardnening, Hall-Petch strengthening [8] for this alloy composition yields a hardness close to 6 GPa, which agrees well with the data points realized in the interior of the grain. However, the near doubling of hardness close to the boundary naturally implies the role of other strengthening mechanisms like precipitation strengthening. Given the micrometer length scale (~ 5 µm) of this strengthening effect, it is arguably different from the classical grain boundary segregation and the associated strengthening that occurs at the nanometer length scale. Hence, the reasons for the significant hardness increase in the vicinity of the boundary are unclear at this time.

In summary, a clear correlation between the local chemistry and hardness is observed in both the alloys in the as-cast and heat-treated conditions. The Ti or Nb rich regions are observed in the vicinity of the boundaries which also correspond to higher hardness. Local rearrangement

in Nb or Ti fraction is observed with heat treatment, which is also clearly reflected in the hardness and to a lesser extent in elastic modulus. Addition of Ti also results in improving the ratio of elastic modulus to hardness, thereby improving the ductility.

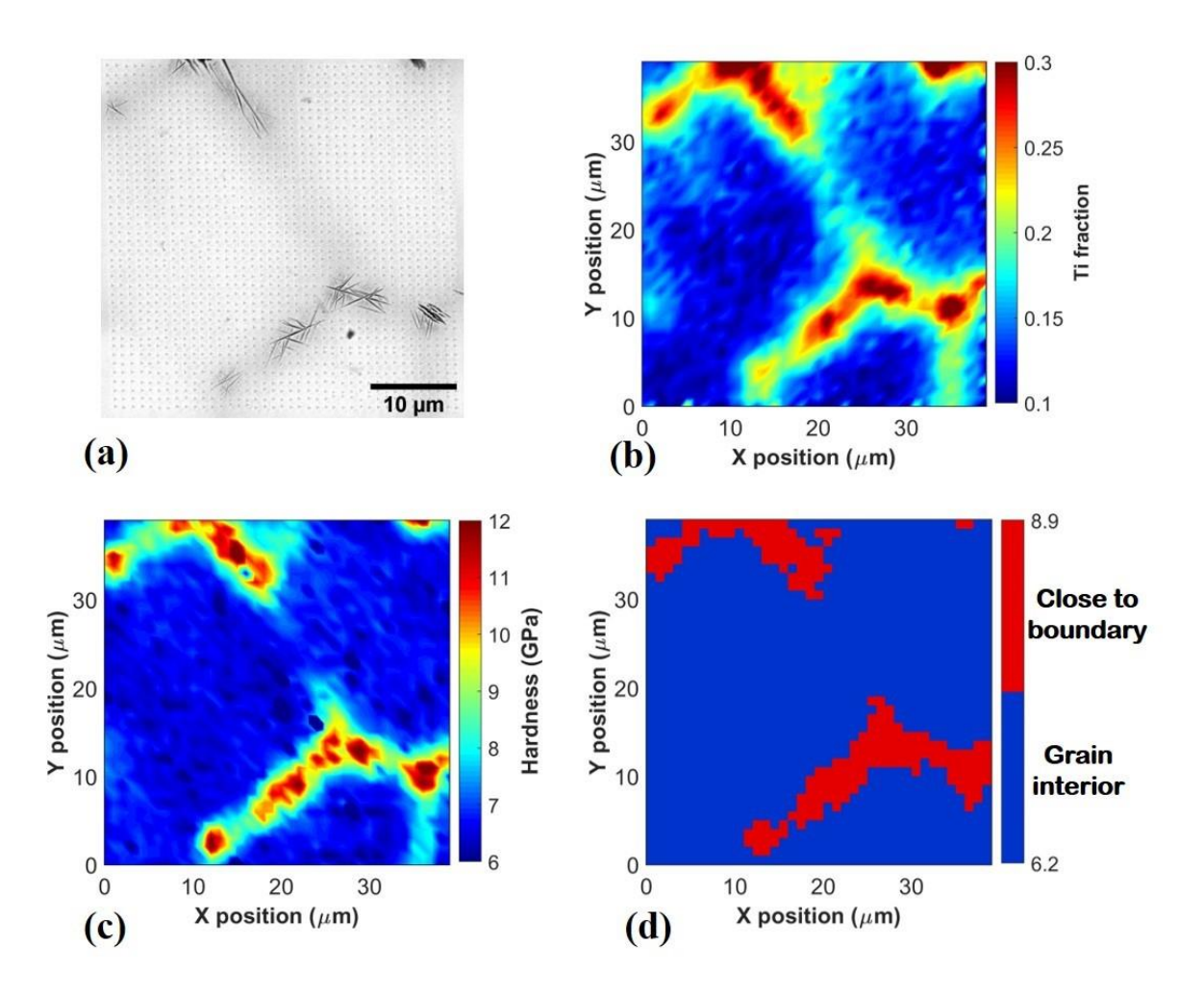


Fig. 4.29 (a) FE-SEM BSE micrograph (b) EDS map (c) hardness map and (d) deconvoluted hardness map of as-cast MoNbTi alloy.

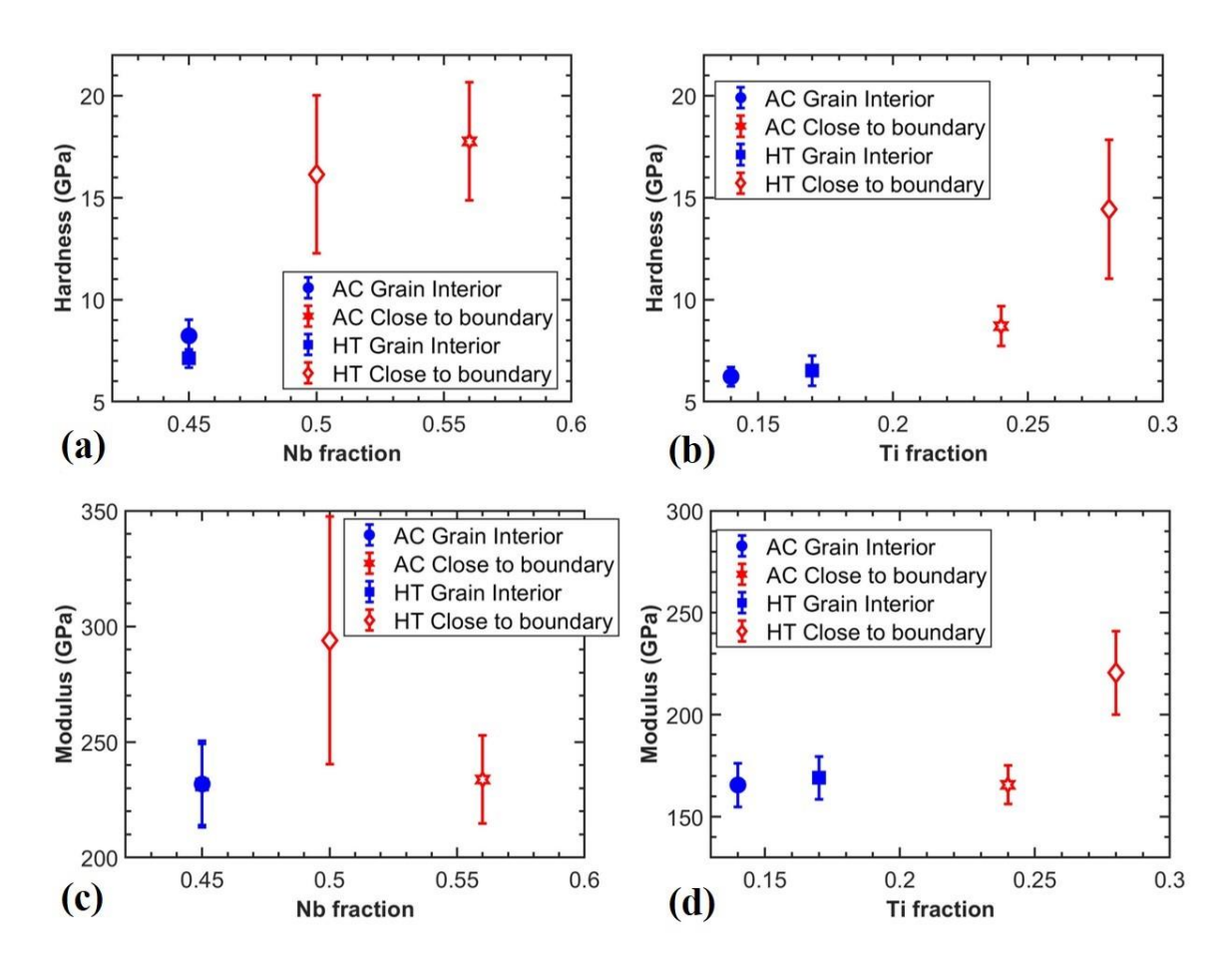


Fig. 4.30 (a) hardness and (c) elastic modulus variation with Nb fraction in MoNb alloys; (b) hardness and (d) elastic modulus variation with Ti fraction in MoNbTi alloys, showing the correlation between Nb or Ti fraction and the local hardness and elastic modulus in the as-cast and heat-treated conditions.

4.5.4. Summary

In this work, the effect of local chemical heterogeneity on the mechanical properties of equiatomic MoNb and MoNbTi alloys at the micrometer length scale are reported by coupling EDS and nanoindentation mapping and the following observations and conclusions are drawn. Excellent correlation between the local chemistry and hardness was observed for all the samples. Local variations in the Nb and Ti content were observed, wherein Nb or Ti enrichment is found in the vicinity of the boundaries. The corresponding hardness maps showed a similar local variation in hardness, wherein higher hardness was observed in the vicinity of the boundary. In the case of the MoNb alloy, the hardness in the Nb rich regions near the boundary is in the 12-20 GPa range, whereas it is in 7-8 GPa in the interior of the grains. Similarly, in the case of MoNbTi alloys, the Ti rich regions exhibit hardness in the range of 8-15 GPa,

whereas it is around 6 GPa in the interior of the grain. Despite the significant chemical and mechanical heterogeneity in the vicinity of grain boundaries, the XRD measurements show a single BCC phase. While solid solution strengthening explains the hardness in the interior of the grain, the reasons for the significant enhancement of the hardness in the vicinity of the boundary are unclear at this time. This work thus demonstrates the ability to quantitatively couple EDS and nanoindentation data to study the effect of chemical segregation on mechanical properties at the micrometer length scale, which opens new opportunities for structure-property correlations at the micrometer length scale.

4.5.5. Experimental procedure

Materials

Mo, Nb, and Ti elemental powders with purity greater than 99.5 % were procured from Alfa Aesar. The powders with appropriate composition were melted using Vacuum Arc Melting (VAM) in argon atmosphere after attaining a 10^{-6} mbar vacuum to cast MoNb and MoNbTi alloys. The alloys were flipped continuously during melting and remelted for at least 5 times to improve chemical homogeneity. Subsequently, the alloys were heat treated at 1673 K for 24 h, with a heating rate of 4.6 K/s followed by furnace cooling, to homogenize the microstructure. X-ray diffraction (XRD) measurements was performed using BRUKER D8 ADVANCE equipment with Cu K α radiation (λ =1.5419 Å) in the scan range (2 Θ) between 20 0 to 120 0 with a scan time 1sec/step and a step size of 0.02 0 , to determine the crystal structure and/or phase stability of the corresponding alloys. The microstructure was also observed using a field emission scanning electron microscope (FESEM, FEI Nova NanoSEM 450) at 20 keV accelerating voltage with 10 mm working distance.

Nanoindentation testing

iMicro® nanoindenter from Nanomechanics Inc. (now KLA, Oak Ridge, TN, USA) was used for nanoindentation testing. Prior to nanoindentation testing, samples were carefully polished starting from SiC abrasive paper of 1200 grit to 2000 grit, followed by alumina suspension with particle size of 0.3 μm and 0.05 μm. Finally, vibratory polishing in a 0.04 μm colloidal silica suspension was performed using an automatic vibratory polishing machine (SAPHIR VIBRO – ATM) for 18 hours. A diamond Berkovich tip was used for all the indentation tests. The area function and load frame stiffness calibration were performed as per the procedure detailed elsewhere [36]. A high-speed nanoindentation technique (Nanoblitz3D®), wherein

each indent takes less than one second to perform [31], was used to obtain hardness and elastic modulus maps typically over a $40x40~\mu\text{m}^2$ area, at a load of 1.8 mN and an indentation spacing of 1 μ m. These parameters were chosen based on a recent work [19] to ensure minimal influence of neighboring indents. The hardness and elastic modulus are calculated based on the procedure described by Oliver & Pharr [37]. The high speed nanoindentation mapping technique used in this work is, in principle, similar to the quasi-static testing [38], except for the duration of the test, which is less than 1 second per indent. It comprises of different test segments routinely used in quasi-static testing, such as, approaching the surface, contact detection, loading to prescribed load, unloading and moving to the next location. The ability of the mapping technique to perform indentation test in less than 1 second along with new optimal indent spacing, not only enables higher resolution (1 μ m) hardness maps, which can be used to capture hardness variations at the microstructural length scale, but also generation of large data sets (1000's indents) for subsequent data deconvolution with statistical techniques.

Elemental analysis

Elemental mapping was performed on all four alloys using an EDS detector (Octane – EDAX) in an FE-SEM (FEI NOVA NANO FESEM 450) operated at an accelerating voltage of 20 keV and 10 mm working distance. Elemental maps were obtained at a resolution of 512×492 , with 64 frames and 28 μ m field width at a magnification of 3000X. The counts recorded for individual elements were normalized by the total counts to obtain 2D maps of the elemental composition.

EDS-Nanoindentation coupling and data deconvolution

Nanoindentation and EDS elemental maps generated as described earlier, are typically obtained at different resolutions due to the inherent differences in the characterization techniques. For instance, the resolution of the nanoindentation map is determined by the indent spacing, which is 1 μ m in the present study, whereas the EDS maps have much higher resolution. In order to couple the EDS and nanoindentation data, the effective resolution of the EDS data is reduced to match that of the nanoindentation data by averaging the counts within an area of 1 μ m². Once the resolution of the EDS data is matched with that of the nanoindentation map, direct correlation between the local chemistry and indentation data can be obtained by plotting the chemical composition and hardness or modulus at every pixel. It may be noted that prior to matching the resolution of the EDS maps with that of the nanoindentation, proper care has to be taken to match the corresponding mapped areas.

The local variation in the mechanical properties and chemistry obtained by nanoindentation and EDS mapping, respectively, can be quantified to estimate the property values of chemically or mechanically distinct regions. While there are several algorithms to deconvolute the data [28], the k-means clustering algorithm is chosen in the present study [27,31]. Due to the relatively better signal-to-noise ratio in the hardness data, deconvolution was carried out using the hardness maps and the corresponding composition was calculated from the EDS maps. It may be noted that deconvolution is ideally performed based on the various phases observed in the microstructure. However, in the present study, in spite of the chemical and mechanical heterogeneity, multiple phases were not detected and hence deconvolution based on phase or crystal structure was not possible.

References

- [1] B. Cantor, I.T.H. Chang, P. Knight, A.J.B. Vincent, Microstructural development in equiatomic multicomponent alloys, Mater. Sci. Eng. A. 375–377 (2004) 213–218. https://doi.org/10.1016/j.msea.2003.10.257.
- [2] J.W. Yeh, S.K. Chen, S.J. Lin, J.Y. Gan, T.S. Chin, T.T. Shun, C.H. Tsau, S.Y. Chang, Nanostructured high-entropy alloys with multiple principal elements: Novel alloy design concepts and outcomes, Adv. Eng. Mater. 6 (2004) 299–303. https://doi.org/10.1002/adem.200300567.
- [3] B.S. Murty, J.W. Yeh, S. Ranganathan, P.P. Bhattacharjee, High-Entropy Alloys, second ed., Elsevier, United States, 2019.
- [4] M.H. Tsai, J.W. Yeh, High-entropy alloys: A critical review, Mater. Res. Lett. 2 (2014) 107–123. https://doi.org/10.1080/21663831.2014.912690.
- [5] E.P. George, D. Raabe, R.O. Ritchie, High-entropy alloys, Nat. Rev. Mater. 4 (2019) 515–534. https://doi.org/10.1038/s41578-019-0121-4.
- [6] O.N. Senkov, G.B. Wilks, J.M. Scott, D.B. Miracle, Mechanical properties of Nb25Mo25Ta 25W25 and V20Nb20Mo 20Ta20W20 refractory high entropy alloys, Intermetallics. 19 (2011) 698–706. https://doi.org/10.1016/j.intermet.2011.01.004.
- [7] D.B. Miracle, O.N. Senkov, A critical review of high entropy alloys and related concepts, Acta Mater. 122 (2017) 448–511. https://doi.org/10.1016/j.actamat.2016.08.081.
- [8] D.G. Kalali, S. Antharam, M. Hasan, P.S. Karthik, P.S. Phani, K. Bhanu Sankara Rao,K. V. Rajulapati, On the origins of ultra-high hardness and strain gradient plasticity in

multi-phase nanocrystalline MoNbTaTiW based refractory high-entropy alloy, Mater. Sci. Eng. A. 812 (2021) 141098. https://doi.org/10.1016/j.msea.2021.141098.

- [9] A. Kumar, A. Singh, A. Suhane, Mechanically alloyed high entropy alloys: existing challenges and opportunities, J. Mater. Res. Technol. 17 (2022) 2431–2456. https://doi.org/10.1016/j.jmrt.2022.01.141.
- [10] M. Vaidya, G.M. Muralikrishna, B.S. Murty, High-entropy alloys by mechanical alloying: A review, J. Mater. Res. 34 (2019) 664–686. https://doi.org/10.1557/jmr.2019.37.
- [11] R.S. Ganji, P. Sai Karthik, K. Bhanu Sankara Rao, K. V. Rajulapati, Strengthening mechanisms in equiatomic ultrafine grained AlCoCrCuFeNi high-entropy alloy studied by micro- and nanoindentation methods, Acta Mater. 125 (2017) 58–68. https://doi.org/10.1016/j.actamat.2016.11.046.
- [12] D.G. Kalali, P.S. Karthik, K.B. Sankara, K. V Rajulapati, Ultra-hard, multi-phase nanocrystalline MoTa and MoTaTi based concentrated refractory alloys, Mater. Lett. 324 (2022) 132768. https://doi.org/10.1016/j.matlet.2022.132768.
- [13] B. Gorr, M. Azim, H.J. Christ, H. Chen, D.V. Szabo, A. Kauffmann, M. Heilmaier, Microstructure Evolution in a New Refractory High-Entropy Alloy W-Mo-Cr-Ti-Al, Metall. Mater. Trans. A Phys. Metall. Mater. Sci. 47 (2016) 961–970. https://doi.org/10.1007/s11661-015-3246-0.
- [14] S. Sohn, Y. Liu, J. Liu, P. Gong, S. Prades-Rodel, A. Blatter, B.E. Scanley, C.C. Broadbridge, J. Schroers, Noble metal high entropy alloys, Scr. Mater. 126 (2017) 29–32. https://doi.org/10.1016/j.scriptamat.2016.08.017.
- [15] K.M. Schmalbach, A.C. Lin, D.C. Bufford, C. Wang, C.C. Sun, N.A. Mara, Nanomechanical mapping and strain rate sensitivity of microcrystalline cellulose, J. Mater. Res. 36 (2021) 2251–2265. https://doi.org/10.1557/s43578-021-00138-0.
- [16] Chenmin Yao, Zhengzhi Wang, Jian Yu, Pan Liu, Yake Wang, Mohammed H. Ahmed, Bart Van Meerbeek, Nanoindentation Mapping and Bond Strength Study of Adhesive-Dentin Interfaces, Adv. Mater. Interfaces. 9 (2022) 2101327. https://doi.org/10.1002/admi.202101327.
- [17] E.D. Hintsala, U. Hangen, D.D. Stauffer, High-Throughput Nanoindentation for Statistical and Spatial Property Determination, Jom. 70 (2018) 494–503. https://doi.org/10.1007/s11837-018-2752-0.
- [18] A. Orozco-Caballero, C. Gutierrez, B. Gan, J.M. Molina-Aldareguia, High-throughput nanoindentation mapping of cast IN718 nickel-based superalloys: influence of the Nb

concentration, J. Mater. Res. 36 (2021) 2213–2222. https://doi.org/10.1557/s43578-021-00133-5.

- [19] P. Sudharshan Phani, W.C. Oliver, A critical assessment of the effect of indentation spacing on the measurement of hardness and modulus using instrumented indentation testing, Mater. Des. 164 (2019) 107563. https://doi.org/10.1016/j.matdes.2018.107563.
- [20] H. Besharatloo, J.M. Wheeler, Influence of indentation size and spacing on statistical phase analysis via high-speed nanoindentation mapping of metal alloys, J. Mater. Res. 36 (2021) 2198–2212. https://doi.org/10.1557/s43578-021-00214-5.
- [21] Z. Liu, J. Zhang, B. He, Y. Zou, High-speed nanoindentation mapping of a near-alpha titanium alloy made by additive manufacturing, J. Mater. Res. 36 (2021) 2223–2234. https://doi.org/10.1557/s43578-021-00204-7.
- [22] M. Sebastiani, R. Moscatelli, F. Ridi, P. Baglioni, F. Carassiti, High-resolution high-speed nanoindentation mapping of cement pastes: Unravelling the effect of microstructure on the mechanical properties of hydrated phases, Mater. Des. 97 (2016) 372–380. https://doi.org/10.1016/j.matdes.2016.02.087.
- [23] C.M. Magazzeni, H.M. Gardner, I. Howe, P. Gopon, J.C. Waite, D. Rugg, D.E.J. Armstrong, A.J. Wilkinson, Nanoindentation in multi-modal map combinations: a correlative approach to local mechanical property assessment, J. Mater. Res. 36 (2021) 2235–2250. https://doi.org/10.1557/s43578-020-00035-y.
- [24] H. Besharatloo, M. Carpio, J.M. Cabrera, A.M. Mateo, G. Fargas, J.M. Wheeler, J.J. Roa, L. Llanes, Novel mechanical characterization of austenite and ferrite phases within duplex stainless steel, Metals (Basel). 10 (2020) 1–15. https://doi.org/10.3390/met10101352.
- [25] J.J. Roa, P. Sudharshan Phani, W.C. Oliver, L. Llanes, Mapping of mechanical properties at microstructural length scale in WC-Co cemented carbides: Assessment of hardness and elastic modulus by means of high speed massive nanoindentation and statistical analysis, Int. J. Refract. Met. Hard Mater. 75 (2018) 211–217. https://doi.org/10.1016/j.ijrmhm.2018.04.019.
- [26] S. Janakiram, P.S. Phani, G. Ummethala, S.K. Malladi, J. Gautam, L.A.I. Kestens, New insights on recovery and early recrystallization of ferrite-pearlite banded cold rolled high strength steels by high speed nanoindentation mapping, Scr. Mater. 194 (2021) 113676. https://doi.org/10.1016/j.scriptamat.2020.113676.
- [27] E.P. Koumoulos, K. Paraskevoudis, C.A. Charitidis, Constituents phase reconstruction through applied machine learning in nanoindentation mapping data of mortar surface, J.

- Compos. Sci. 3 (2019). https://doi.org/10.3390/jcs3030063.
- [28] J.M. Wheeler, Mechanical phase mapping of the Taza meteorite using correlated high-speed nanoindentation and EDX, J. Mater. Res. 36 (2021) 94–104. https://doi.org/10.1557/s43578-020-00056-7.
- [29] J.M. Wheeler, B. Gan, R. Spolenak, Combinatorial Investigation of the Ni–Ta System via Correlated High-Speed Nanoindentation and EDX Mapping, Small Methods. 6 (2022). https://doi.org/10.1002/smtd.202101084.
- [30] M.A. Wagner, J. Engel, A. Hadian, F. Clemens, M. Rodriguez-Arbaizar, E. Carreño-Morelli, J.M. Wheeler, R. Spolenak, Filament extrusion-based additive manufacturing of 316L stainless steel: Effects of sintering conditions on the microstructure and mechanical properties, Addit. Manuf. 59 (2022) 103147. https://doi.org/10.1016/j.addma.2022.103147.
- [31] B. Vignesh, W.C. Oliver, G.S. Kumar, P.S. Phani, Critical assessment of high speed nanoindentation mapping technique and data deconvolution on thermal barrier coatings, Mater. Des. 181 (2019) 108084. https://doi.org/10.1016/j.matdes.2019.108084.
- [32] N.X. Randall, M. Vandamme, F.J. Ulm, Nanoindentation analysis as a two-dimensional tool for mapping the mechanical properties of complex surfaces, J. Mater. Res. 24 (2009) 679–690. https://doi.org/10.1557/jmr.2009.0149.
- [33] D.N. P. Franke, Mo-Nb, in: P. Franke, D. Neuschutz (Eds.), Binary Systems. Part 4: Binary Systems from Mn-Mo to Y-Zr: Phase Diagrams, Phase Transition Data, Integral and Partial Quantities of Alloys, Springer Berlin Heidelberg, Berlin, Heidelberg, 2006. pp. 1–4.
- [34] B. Predel, Nb-Ti (Niobium-Titanium) in: O. Madelung (Ed.), Springer Berlin Heidelberg, Berlin, Heidelberg, 1997. pp 1-3, Li-Mg-Nd-Zr.
- [35] B. Predel, Mo-Ti (Molybdenum-Titanium) in: O. Madelung (Ed.), Springer Berlin Heidelberg, Berlin, Heidelberg, 1997. pp 1-3, Li-Mg-Nd-Zr.
- [36] P. Sudharshan Phani, W.C. Oliver, G.M. Pharr, Measurement of hardness and elastic modulus by load and depth sensing indentation: Improvements to the technique based on continuous stiffness measurement, J. Mater. Res. 36 (2021) 2137–2153. https://doi.org/10.1557/s43578-021-00131-7.
- [37] W.C. Oliver, G.M. Pharr, An improved technique for determining hardness and elastic modulus using load and displacement sensing indentation experiments, J.Mater. Res. 7 (1992) 1564–1583, https://doi.org/10.1557/JMR.1992.1564.
- [38] Oliver, W.C., and Pharr, G.M. Measurement of hardness and elastic modulus by

instrumented indentation: Advances in understanding and refinements to methodology. $J. Mater. Res.\ 19\ (2004)\ 3-20.\ https://doi.org/10.1557/jmr.2004.19.1.3.$

Chapter 5

Conclusions and Future Scope

5.1. Conclusions

Multi-principal element approach, a novel methodology, is used to manufacture the highstrength materials in this work for the aerospace gas turbine engine applications. The alloys developed using this approach are called multi-principal element alloys (MPEAs). The significant outputs of the work include:

- Novel alloy design, manufacturing of various refractory multi-principal element alloys with high "density-normalized" hardness.
- Strain gradient plasticity and indentation size effect studies on these novel refractory MPEAs using the classic models.
- Understanding the length scale effects on the microstructure and mechanical properties.
- Correlative studies on the local chemical segregation and local mechanical properties.
- Estimation of "density-normalized" flow stress of various RMPEAs.

Chapter 4.1

- Fully dense multi-phase nanocrystalline MoNbTaTiW complex concentrated alloy was prepared using ball milling followed by SPS.
- Single phase BCC structure obtained after milling for 30 h has transformed to a new BCC and two FCC (FCC1, FCC2) phases with different lattice constants.
- Some amount of Fe has also entered the alloy from the milling media. It appears that very fine nanocrystalline structure coupled with the presence of relatively low melting elements such as Ti and Fe aids the phase decomposition during SPS.
- Exceptionally high hardness in the range 18.87-13.89 GPa was observed in this multiphase alloy which is the highest reported till now in the family of alloys based on MoNbTaW composition.
- "Density-normalized" hardness is also remarkably high for this alloy making as an attractive candidate material for structural applications.
- Detailed analysis on probable strengthening mechanisms suggest that solid solution strengthening and Hall-Petch strengthening are the major strengthening mechanisms in this alloy.

- The hardness data of this alloy was observed to follow the Meyer hardening power law with an index of 1.82 suggesting the presence of indentation size effect.
- The strain gradient plasticity of this multi-phase RHEA was explained based on the considerations of GNDs that exists owing to the multi-phase structure with different crystal structures (BCC, FCC1, FCC2), by using the Nix-Gao model.
- The plastic incompatibility is expected to arise from the different slip characteristics of BCC and FCC phases at room temperature at smaller indentation loads, leading to the generation of back stress at interphase (BCC/FCC) boundaries.
- The depth-independent hardness of 11.8 GPa and the characteristic length scale of 1.07 µm were obtained in the analysis.

Chapter 4.2

- Single phase BCC structures were observed after ball milling of MoTa and MoTaTi alloys. Fe has entered the systems from milling media.
- Spark plasma sintering resulted in formation of three phase structure in MoTa (Fe), two phase structure in MoTaTi (Fe) alloys respectively.
- Presence of Ti and Fe in these alloys triggers the phase transformations leading to the multi-phase structures.
- Extremely high hardness values are observed in both the alloy systems with a very clear ISE. Hardness at 500 g load for the alloys is mentioned below:

MoTa: 10.34 ± 0.18 GPa

MoTaTi: 11.31 ± 0.19 GPa

- The indentation size effect observed in the MoTa and MoTaTi alloys is explained using the classic Nix-Gao model and validated using the Meyer power law. Depth-independent hardness is evaluated from the Nix-Gao plot for MoTa alloy is 9.32 GPa with a characteristic length scale of 1.03 µm. For MoTaTi alloy, depth-independent hardness is 9.92 GPa with a characteristic length scale of 1.20 µm.
- These extraordinarily high hardness values could be originating from the high frictional stress, nanocrystallinity, multi-phase structure, solid solution strengthening etc.
- A very significant "density-normalized" hardness was attained by these two alloys highlighting the potential advantages for future high strength, high temperature applications.

Chapter 4.3

- MoNb and MoNbTi, in equiatomic proportions, resulted in single-phase BCC after 30 h of milling. Fe, an unintentional guest entered the system from the milling media.
- A three-phase structure in MoNb (Fe) and a two-phase structure in MoNbTi (Fe) alloy were observed after SPS. The high homologous temperatures of Ti and Fe contributed to the phase transformations after sintering compared to the as-milled condition.
- MoNbTi (Fe) alloy can be considered as one of the lowest density alloys (7.67 g/cc) compared to the various commercially available Nb-based alloys like C-103 (8.85 g/cc),
 C-129Y (9.5 g/cc), C3009 (10.1 g/cc), Cb-752 (9.03 g/cc), and FS-85 (10.61 g/cc).
- Extremely high hardness was observed in both the MoNb (Fe) and MoNbTi (Fe) alloys. Hardness at 500 g load for the alloys is mentioned below:

MoNb: 11.08 ± 0.23 GPa

MoNbTi: 11.13 ± 0.23 GPa

- A high "density-normalized" hardness observed in this work indicates that MoNbTi (Fe) is a good candidate for low-density aerospace applications.
- The cost of the MoNbTi (Fe) alloy will be significantly less when compared to commercially available Nb-based alloys due to the absence of Hf.

Chapter 4.4

- Equiatomic MoNb and MoNbTi alloys were developed by melting and casting route.
- Homogenization of the cast samples was carried out at 1673 K for 24 h. A single phase BCC structure which was obtained after casting was found to be stable even after homogenization.
- Equilibrium phase diagrams and phase fraction plots drawn for MoNb and MoNbTi alloys also showed a single BCC phase at a complete range of temperatures from room temperature to melting points.
- Titanium addition leads to overall density reduction and significant grain refinement.
 Titanium was found to segregate to the grain boundary regions in addition to its presence in the lattice positions in the complex MoNbTi alloy.
- Both the alloys (MoNb and MoNbTi) exhibit comparable hardness within the MoNbTaW family of alloys. Further, the striking feature of this study is the exceptionally high "density-normalized" hardness of these alloys (MoNb and MoNbTi) that surpasses all the alloys of the MoNbTaW family reported in the literature so far.

Solid solution strengthening is the dominant strengthening mechanism in these alloys.
 Furthermore, it was found that addition of more than three elements in equiatomic proportions may not be necessary to obtain high "density-normalized" flow stress.
 Instead, equiatomic binary and ternary alloys can offer more scientific/technological advantages coupled with cost reduction.

Chapter 4.5

- Excellent correlation between the local chemistry and hardness was observed for all the alloys in this chapter.
- Local variations in the Nb and Ti content were observed, wherein Nb or Ti enrichment is found in the vicinity of the boundaries.
- The corresponding hardness maps showed a similar local variation in hardness, wherein higher hardness was observed in the vicinity of the boundary.
- In the case of the MoNb alloy, the hardness in the Nb rich regions near the boundary is in the 12-20 GPa range, whereas it is in 7-8 GPa in the interior of the grains.
- Similarly, in the case of MoNbTi alloys, the Ti rich regions exhibit hardness in the range of 8-15 GPa, whereas it is around 6 GPa in the interior of the grain.
- Despite the significant chemical and mechanical heterogeneity in the vicinity of grain boundaries, the XRD measurements show a single BCC phase.
- While solid solution strengthening explains the hardness in the interior of the grain, the reasons for the significant enhancement of the hardness in the vicinity of the boundary are unclear at this time.
- This work thus demonstrates the ability to quantitatively couple EDS and nanoindentation data to study the effect of chemical segregation on mechanical properties at the micrometer length scale, which opens new opportunities for structureproperty correlations at the micrometer length scale.

Thus, the current investigation helped in the manufacturing of alloys with high "density-normalized" hardness. Therefore, the alloys discussed in this work are potential candidates for high-temperature gas turbine engine applications.

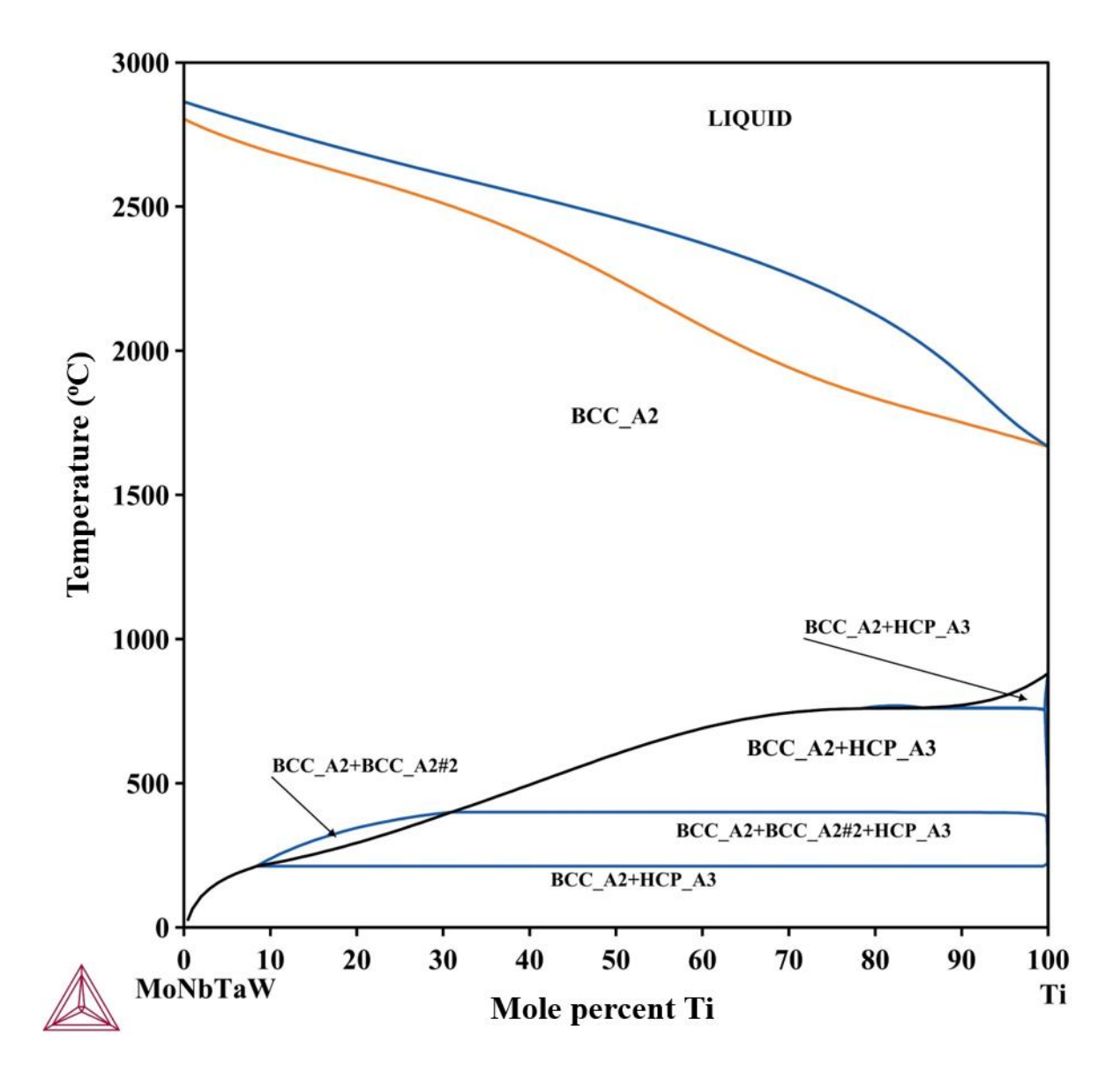
5.2. Scope of future work

In the present work, novel high-strength refractory alloys are designed and manufactured. Current work mainly evaluates mechanical properties like microhardness, nanohardness, and structural characterizations using XRD and FESEM. As these are aimed for high-temperature structural applications, further studies mentioned below are necessary to claim for high-temperature applications.

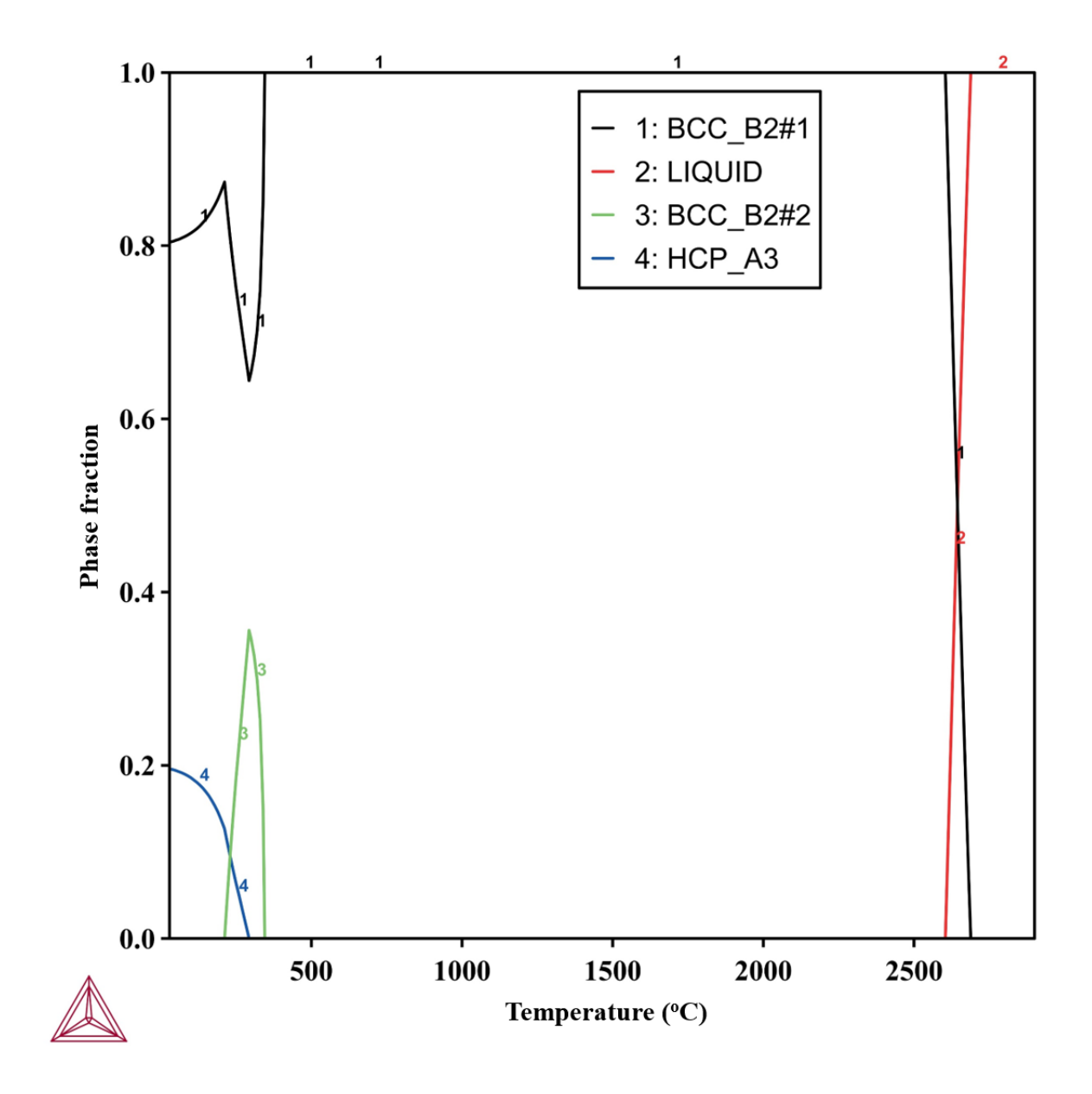
- High-temperature compression and tensile tests are to be performed to understand the yield strength and ultimate strength of all the alloys manufactured in this work which are necessary for the alloys aimed for high-temperature applications.
- High-temperature oxidation studies are necessary for these alloys to understand possible oxidation behaviour before using them for real-time high-temperature applications.
- Intentional Fe addition studies on the alloys manufactured in this work are necessary to understand the role of Fe in strengthening the alloys.

Appendix

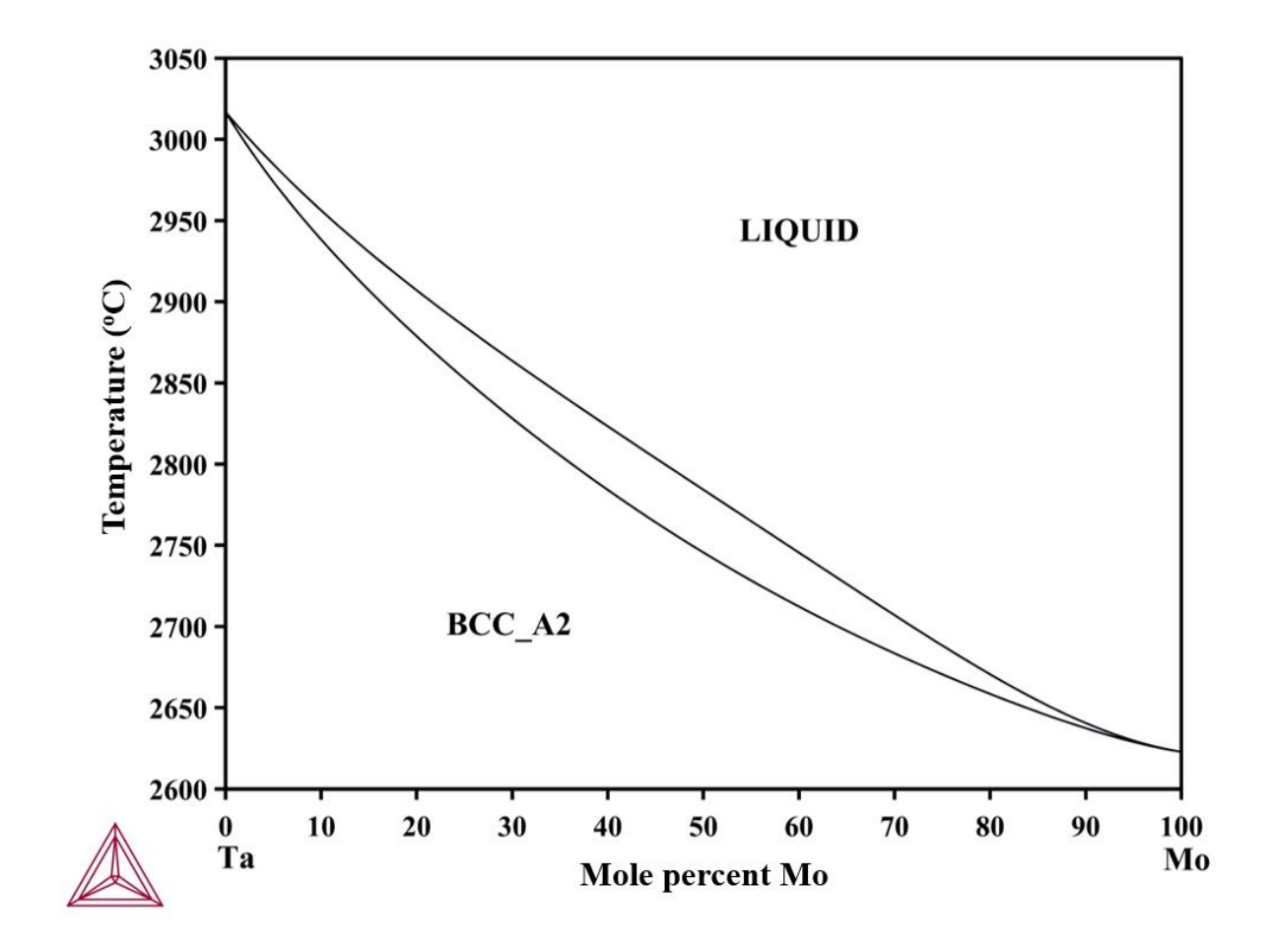
This section shows the Vertical sections of phase diagrams and phase fraction plots drawn using the ThermoCalc TCHEA6 database with respect to various alloys manufactured in this work.



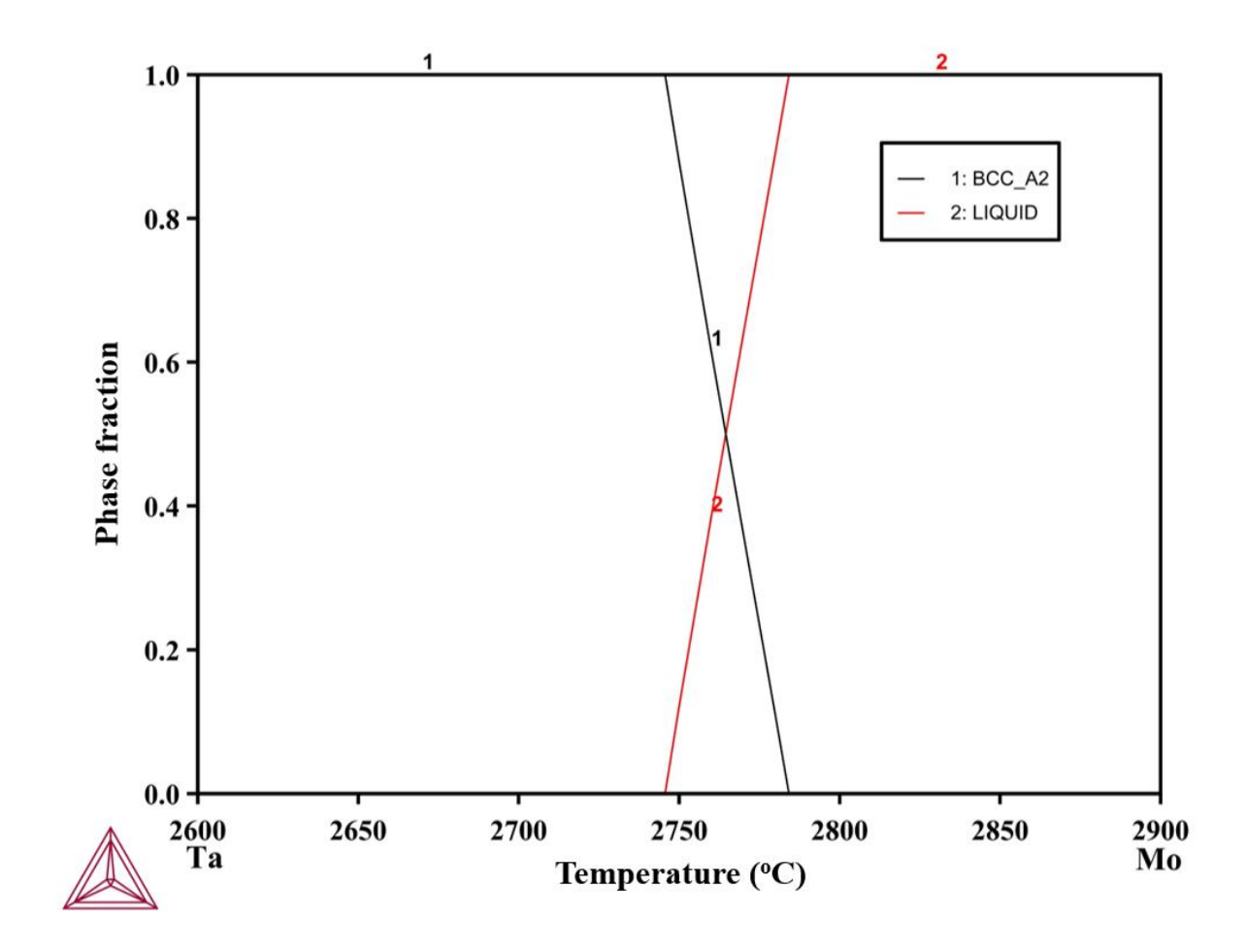
Vertical section of (MoNbTaW)_{1-x}Ti_x phase diagram



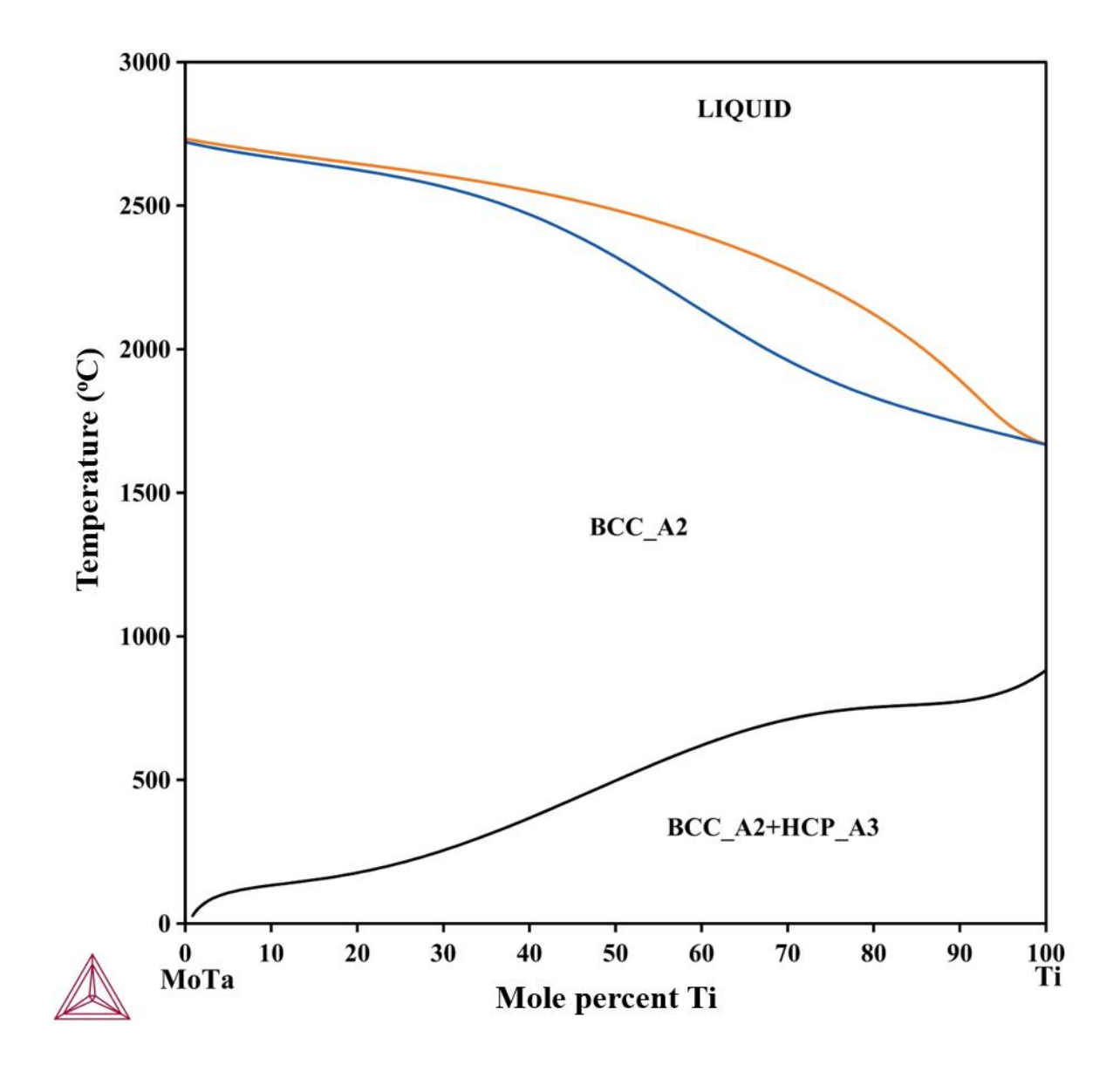
Phase fraction plot of MoNbTaTiW alloy



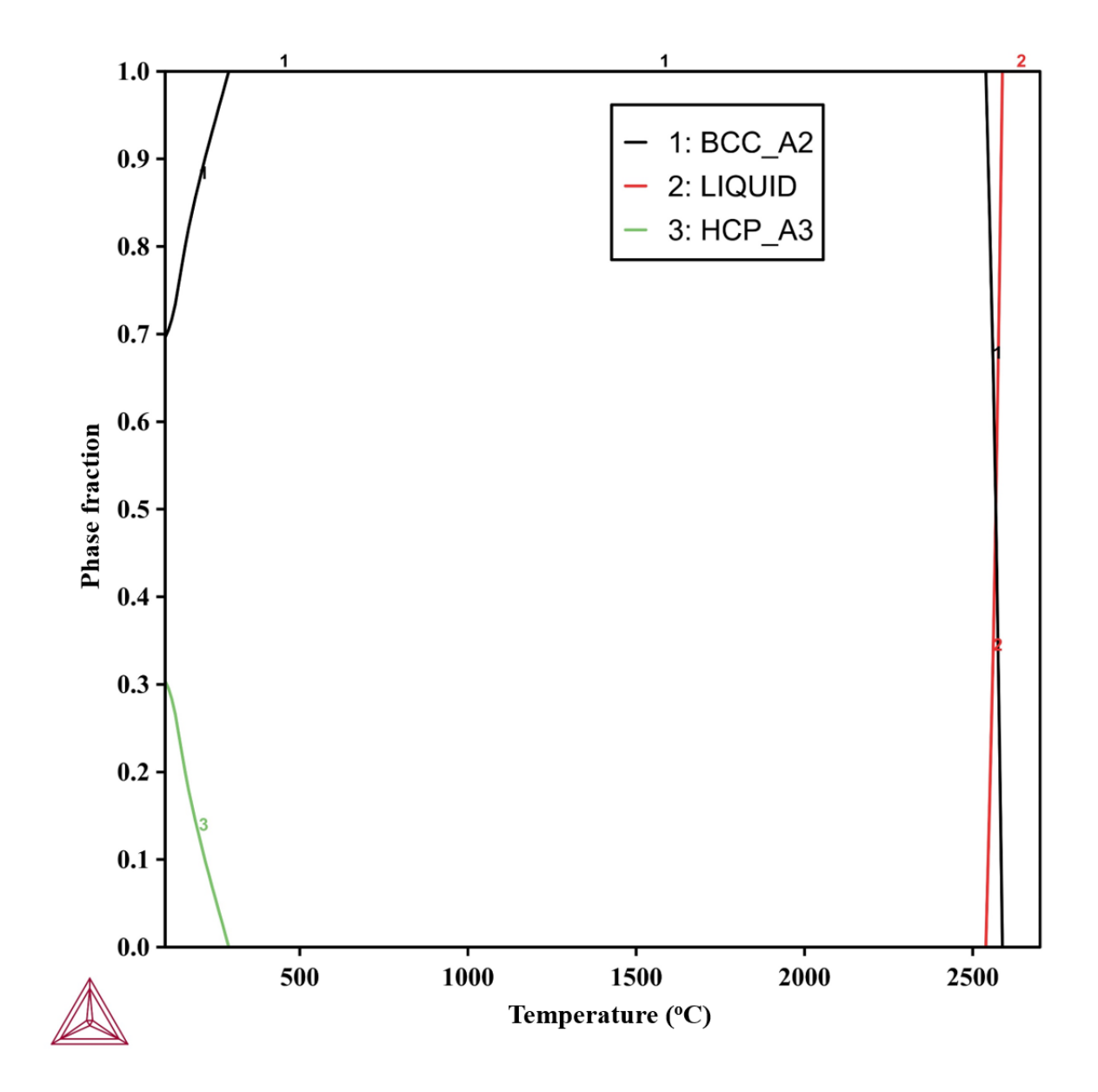
Phase diagram of MoTa alloy



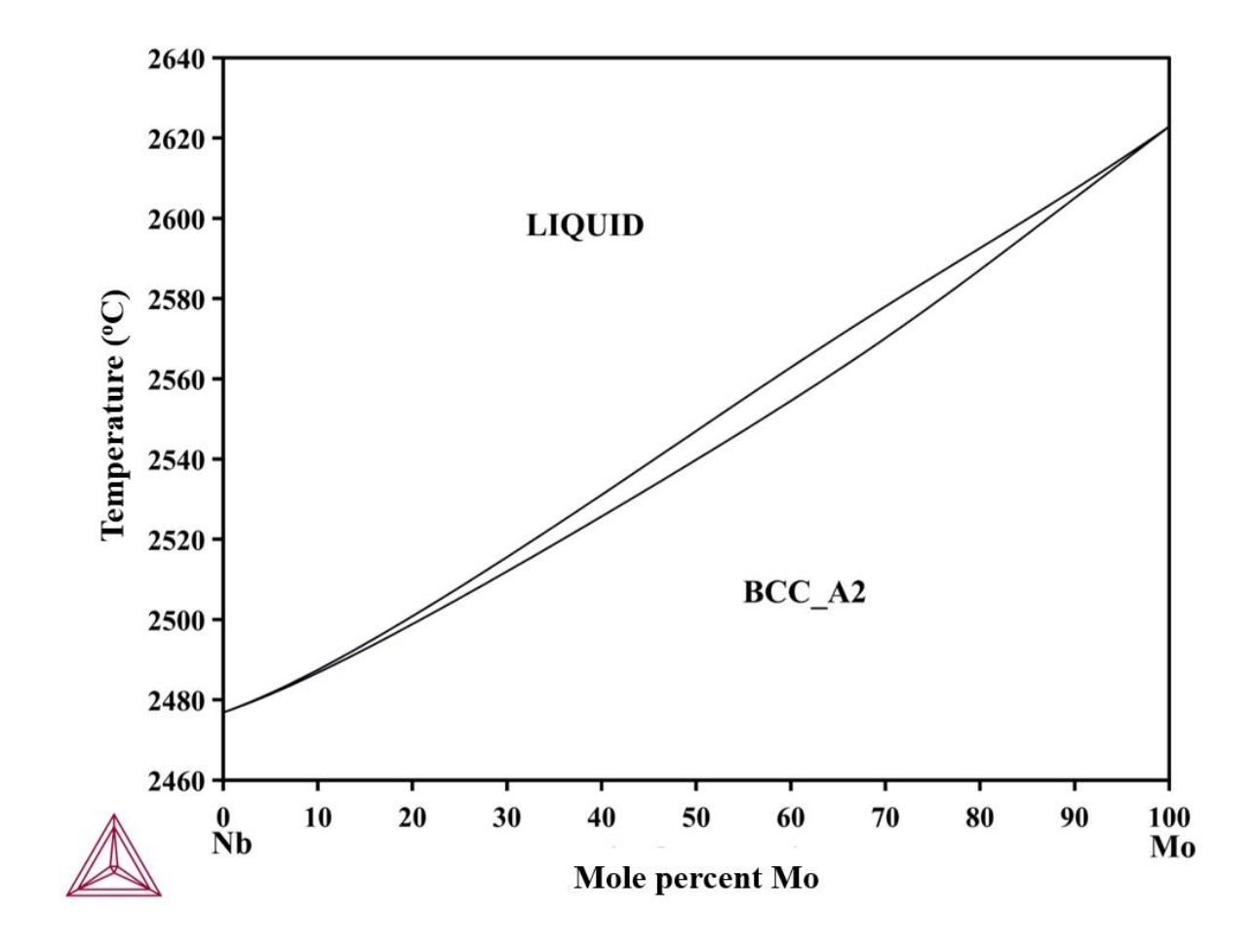
Phase fraction plot of MoTa alloy



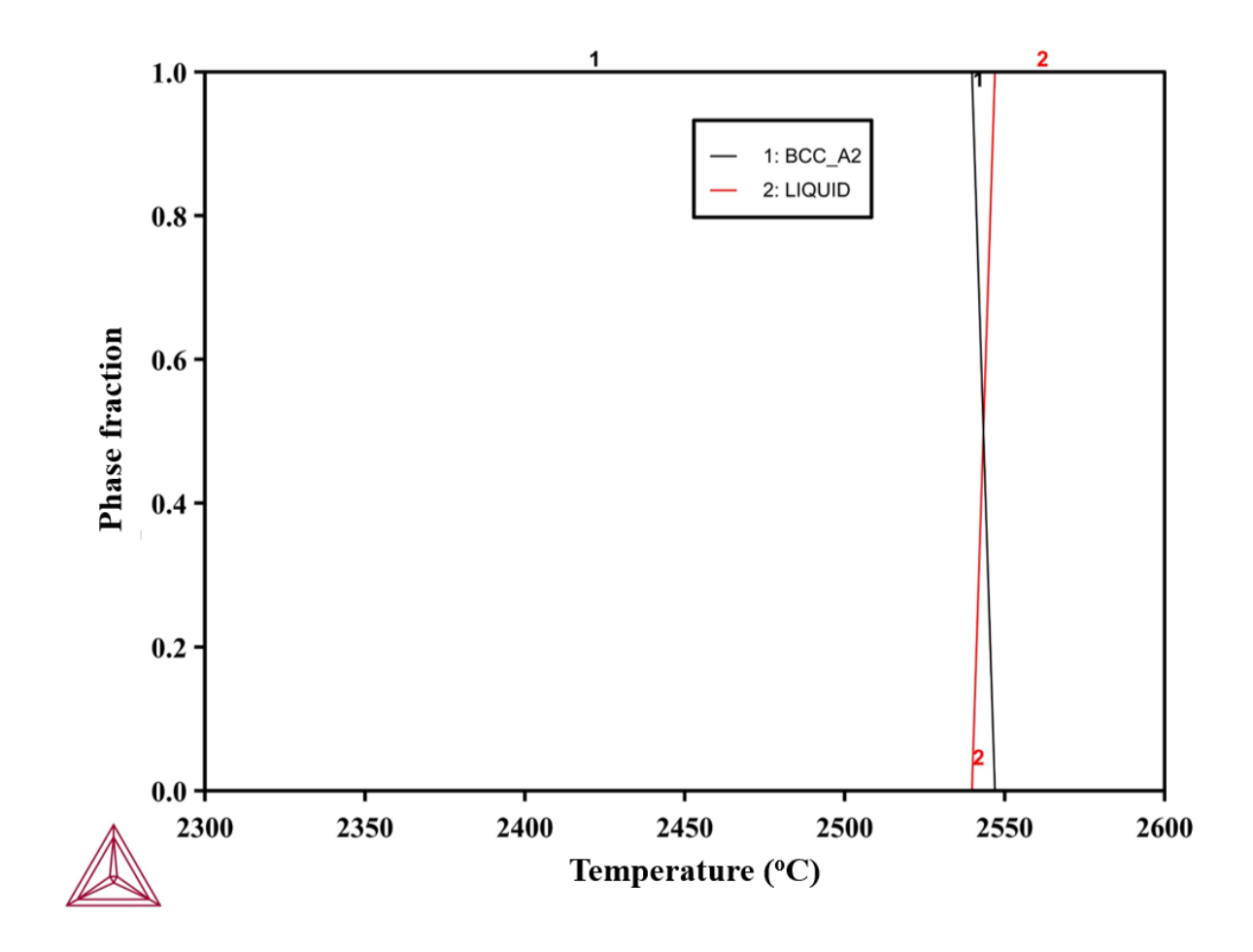
Vertical section of $(MoTa)_{I-x}Ti_x$ phase diagram



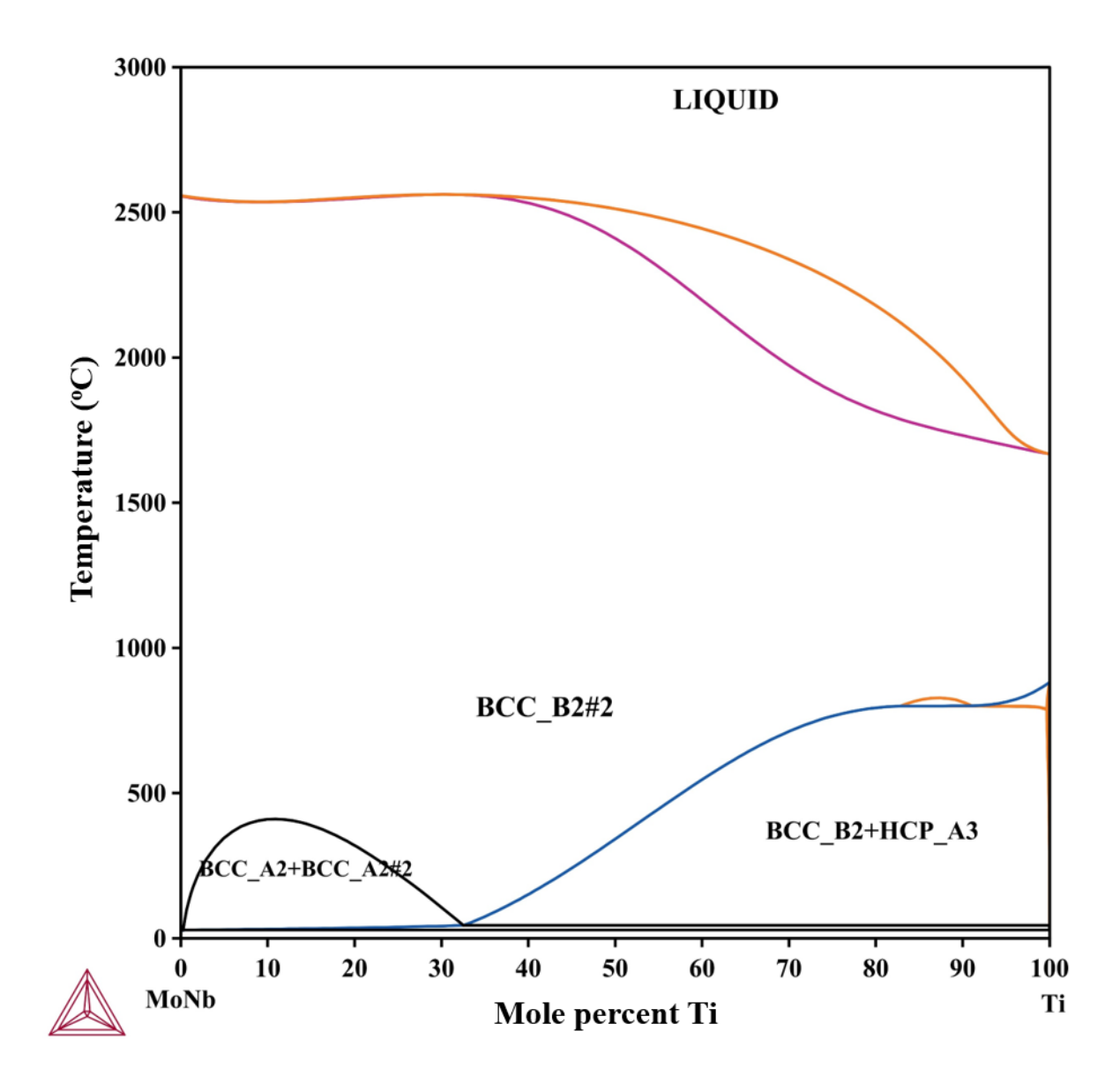
Phase fraction plot of MoTaTi alloy



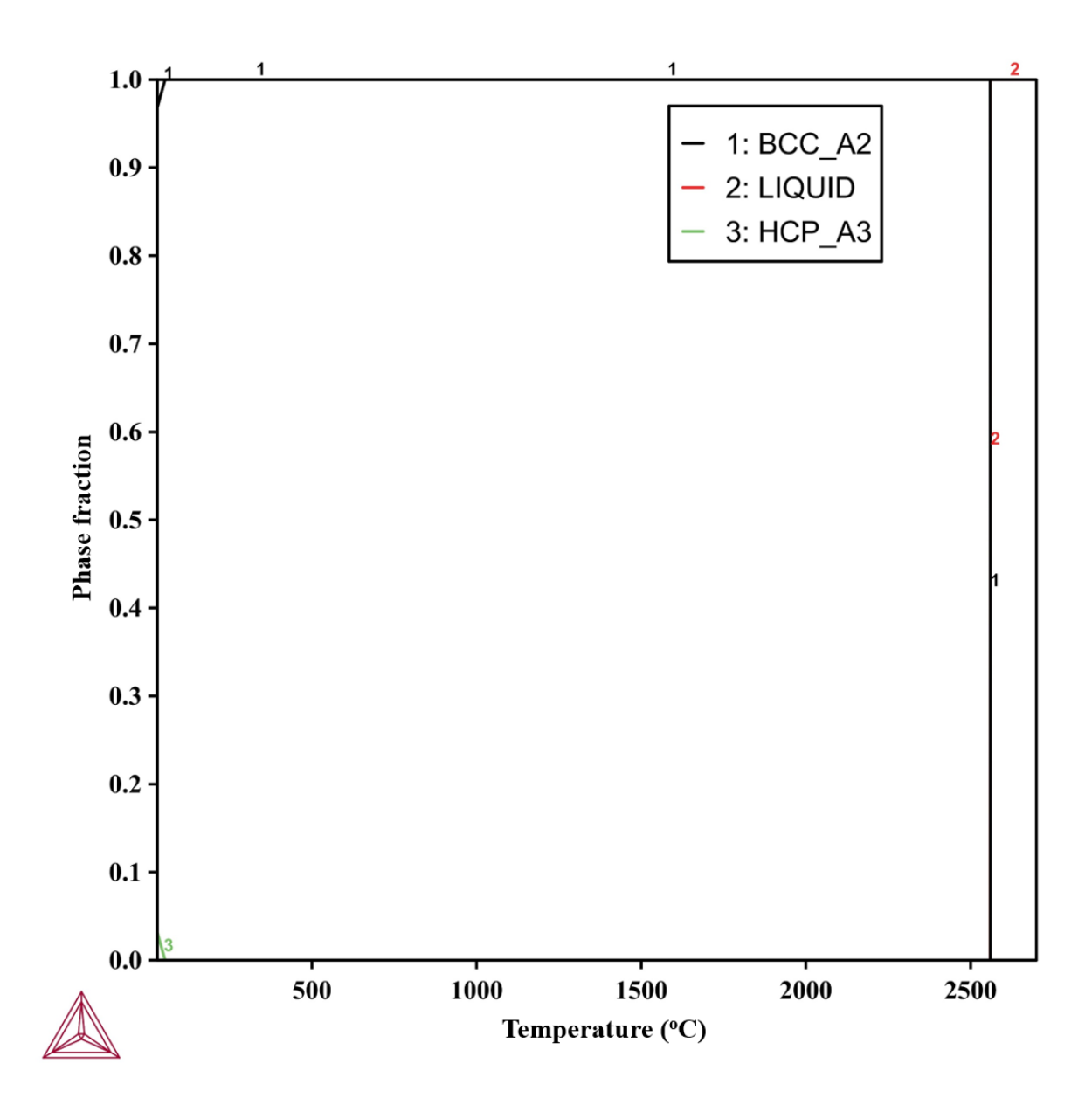
Phase diagram of MoNb alloy



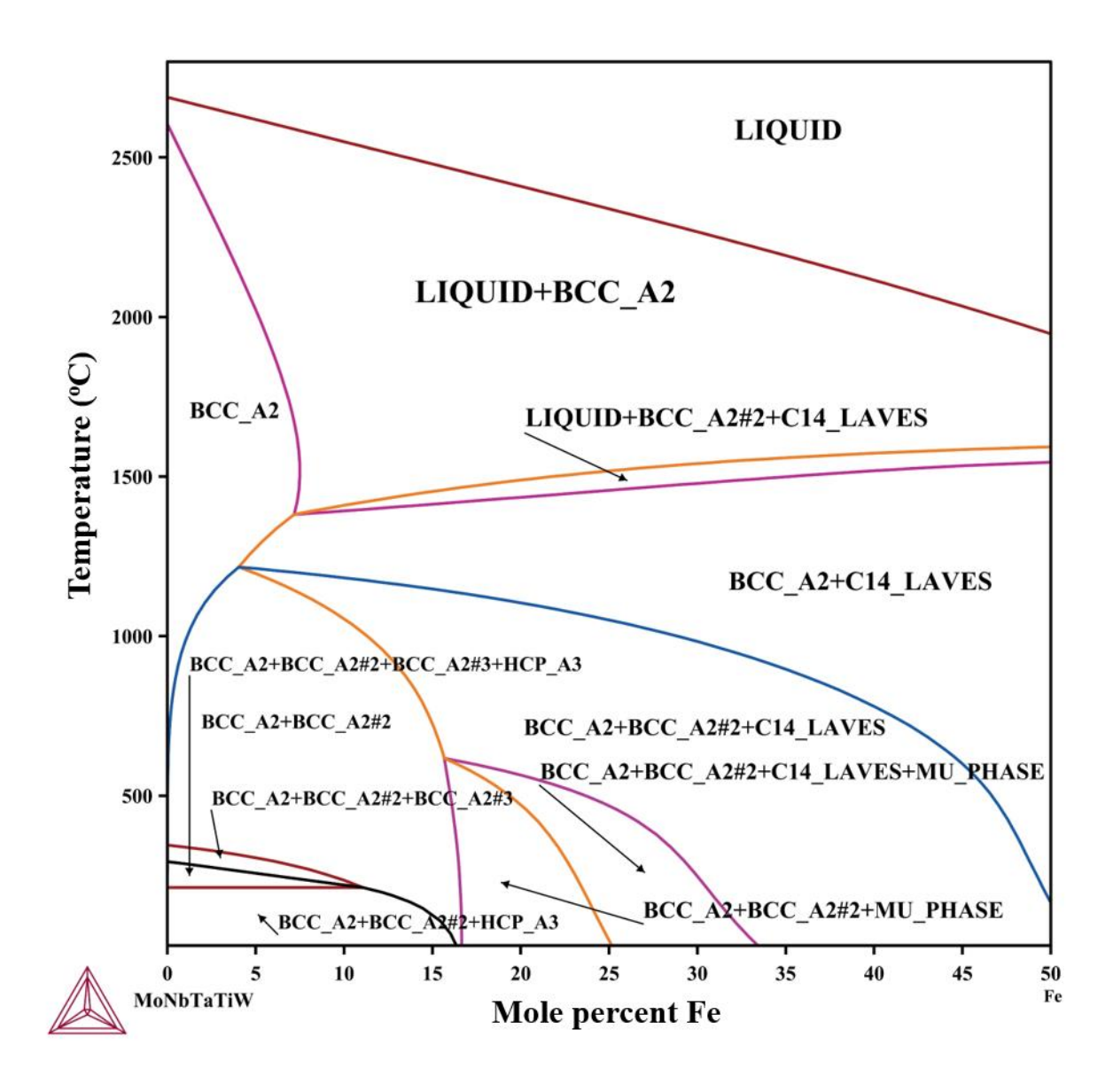
Phase fraction plot of MoNb alloy



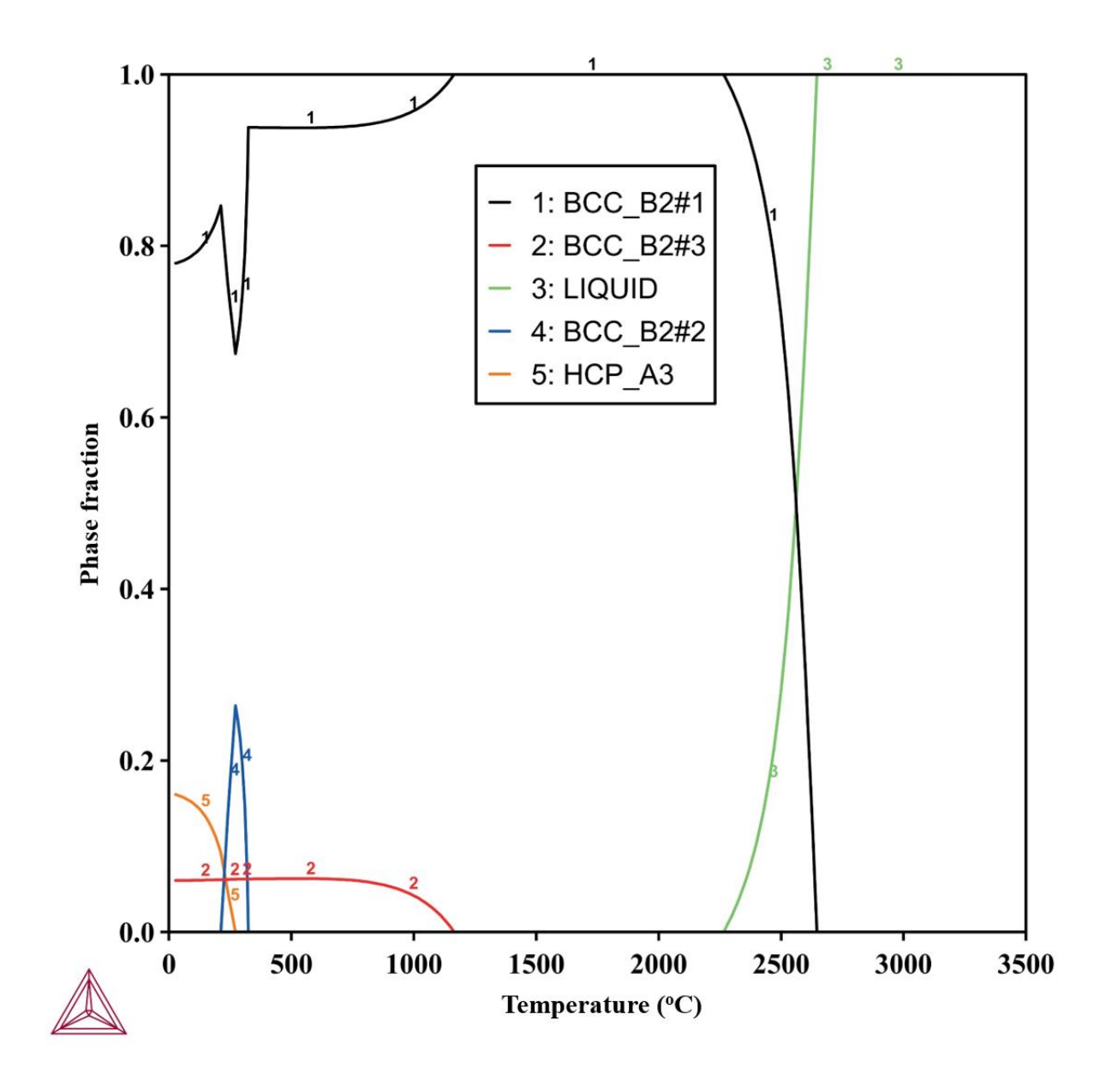
Vertical section of $(MoNb)_{I-x}Ti_x$ phase diagram



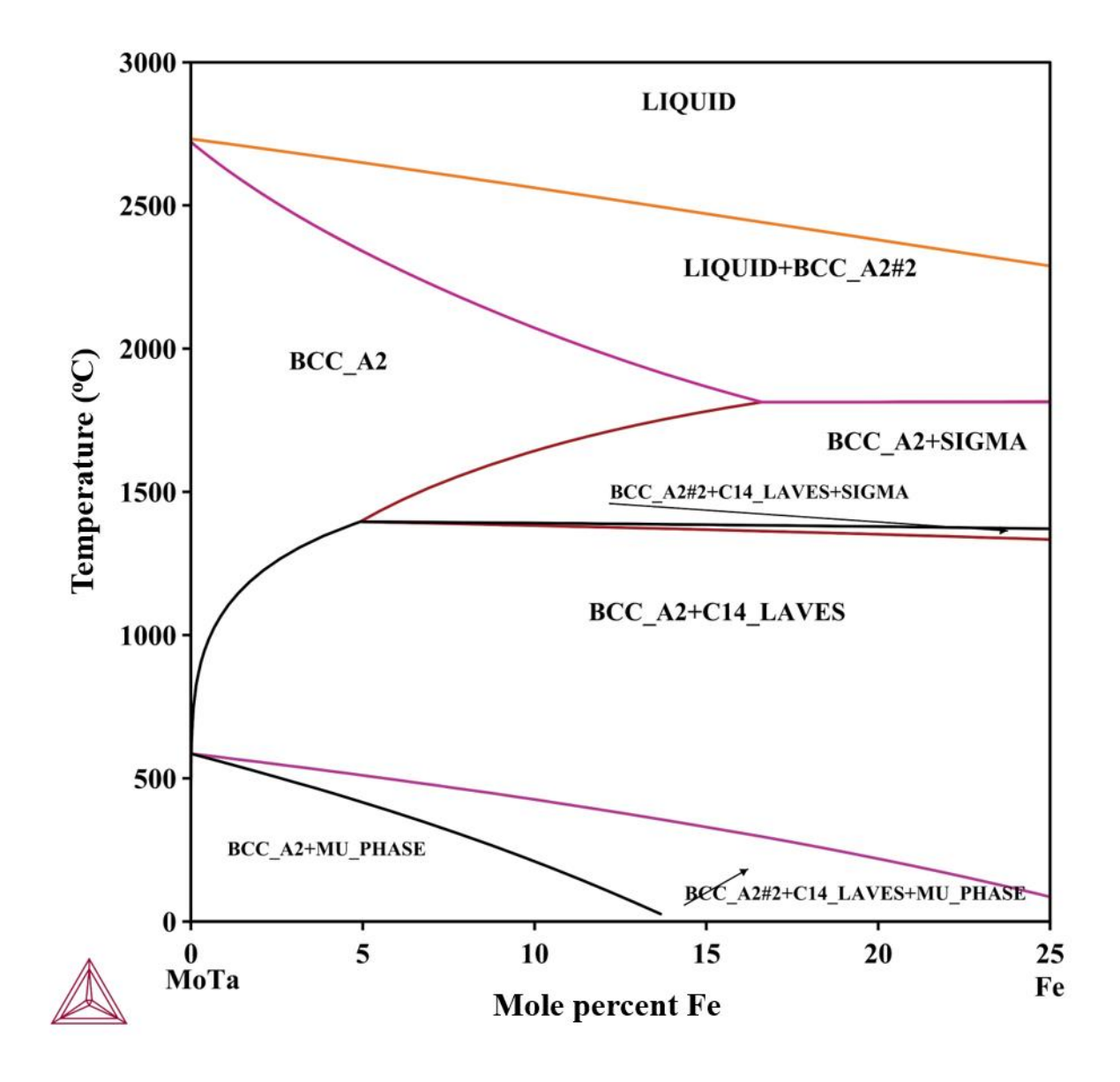
Phase fraction plot of MoNbTi alloy



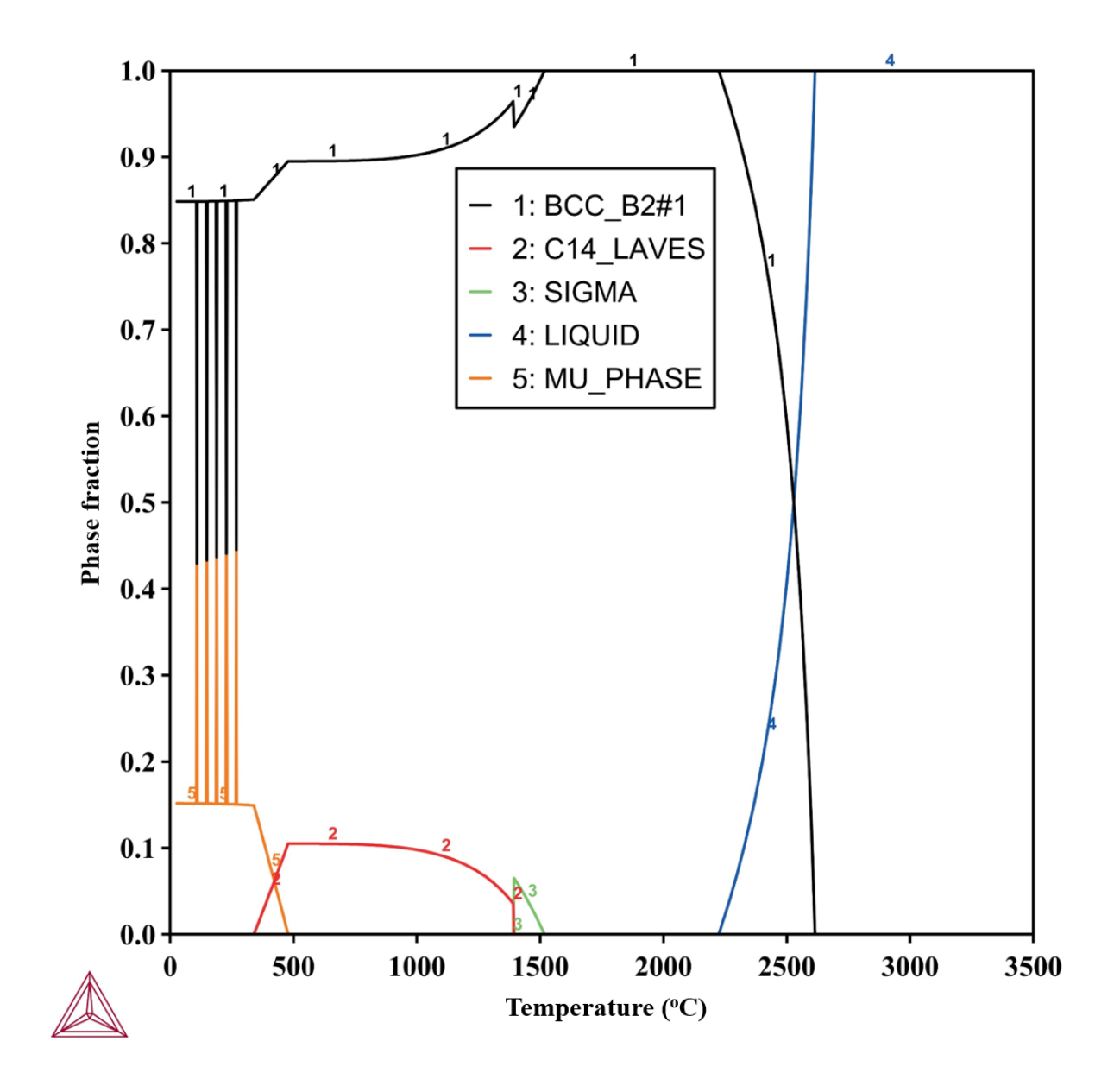
Vertical section of (MoNbTaTiW)_{1-x}Fe_x phase diagram



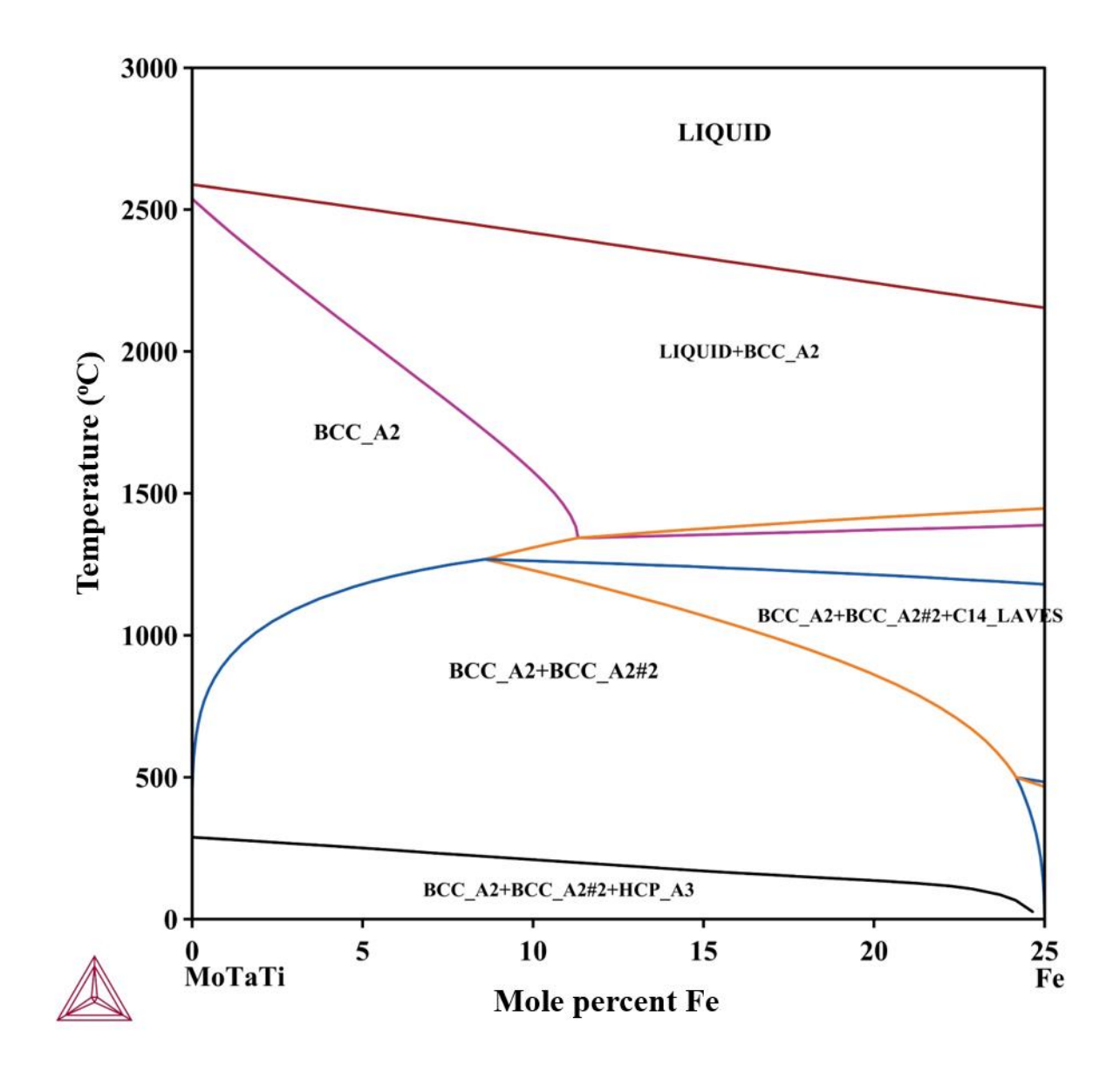
Phase fraction plot of MoNbTaTiWFe alloy, (Fe: 3 at. %)



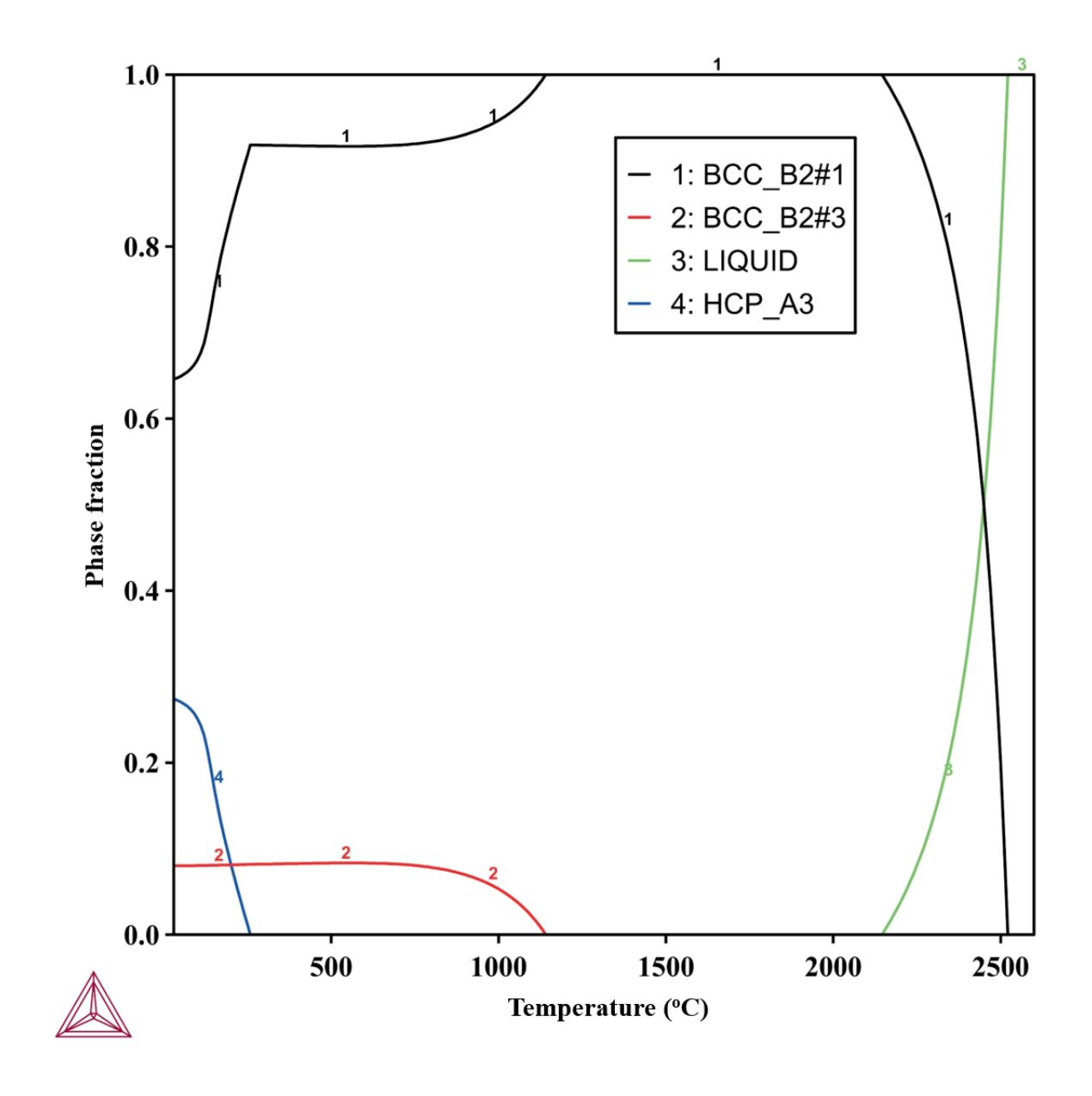
Vertical section of (MoTa)_{1-x}Fe_x phase diagram



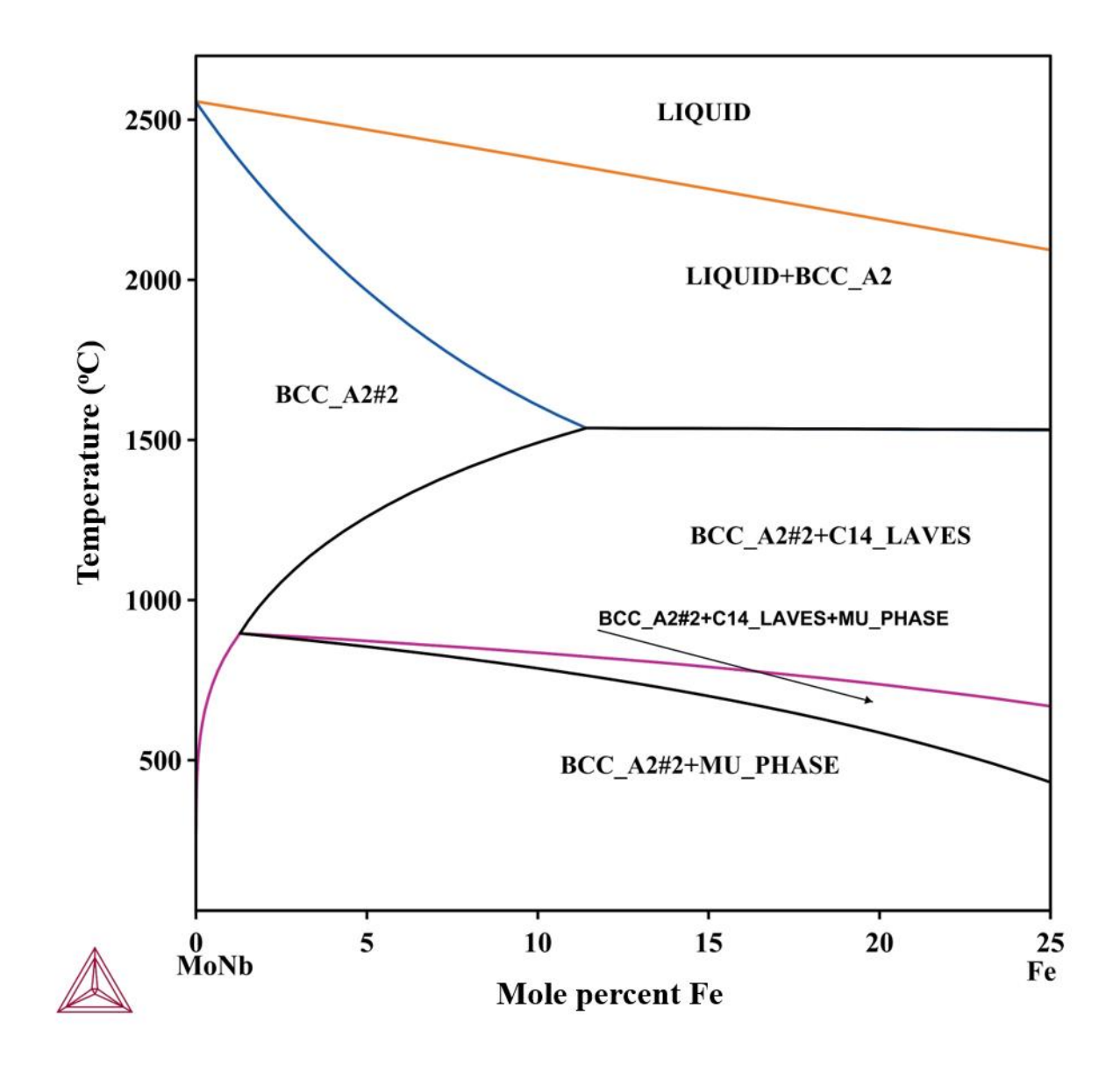
Phase fraction plot of MoTaFe alloy, (Fe: 7 at. %)



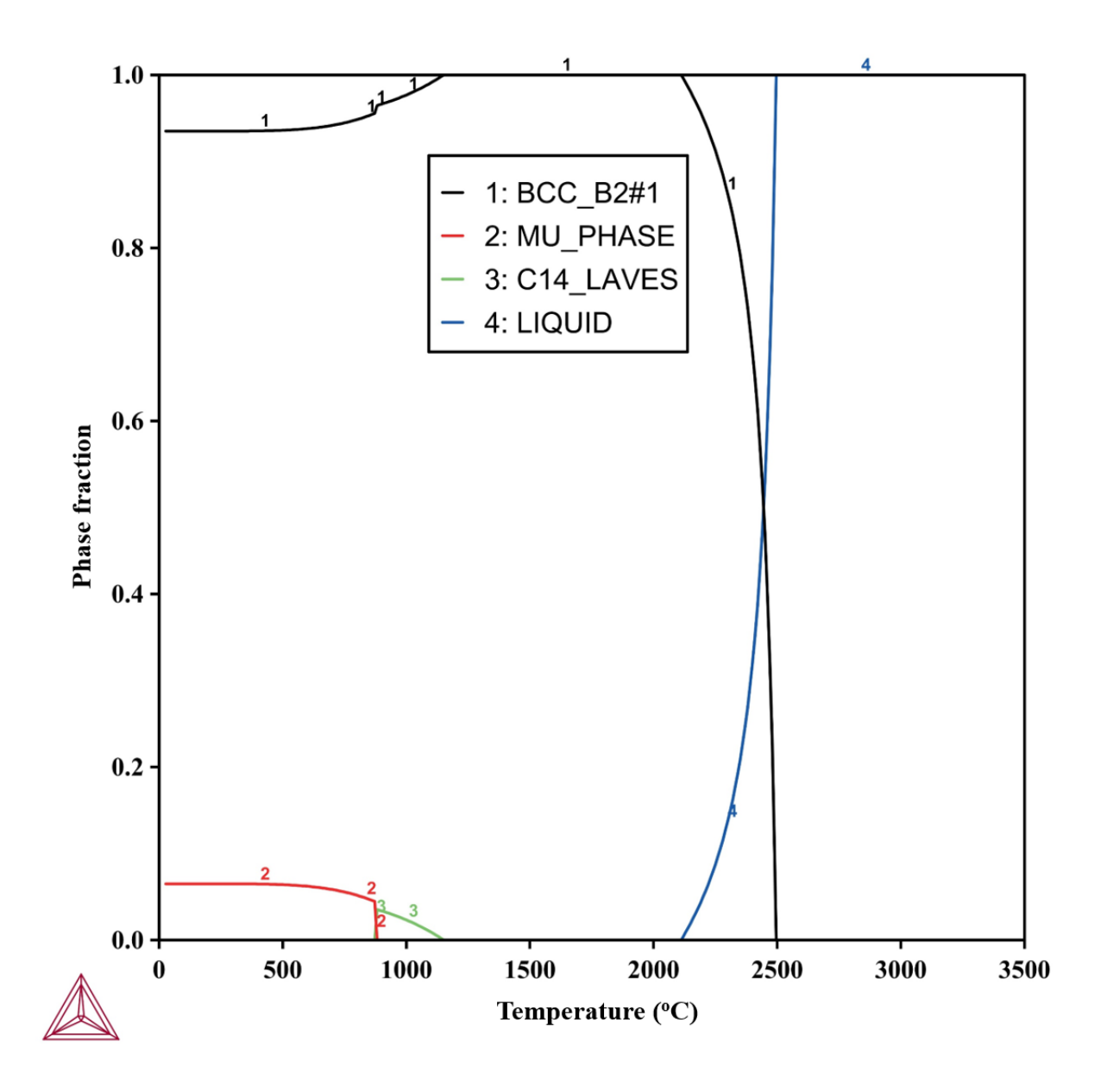
Vertical section of $(MoTaTi)_{I-x}Fe_x$ phase diagram



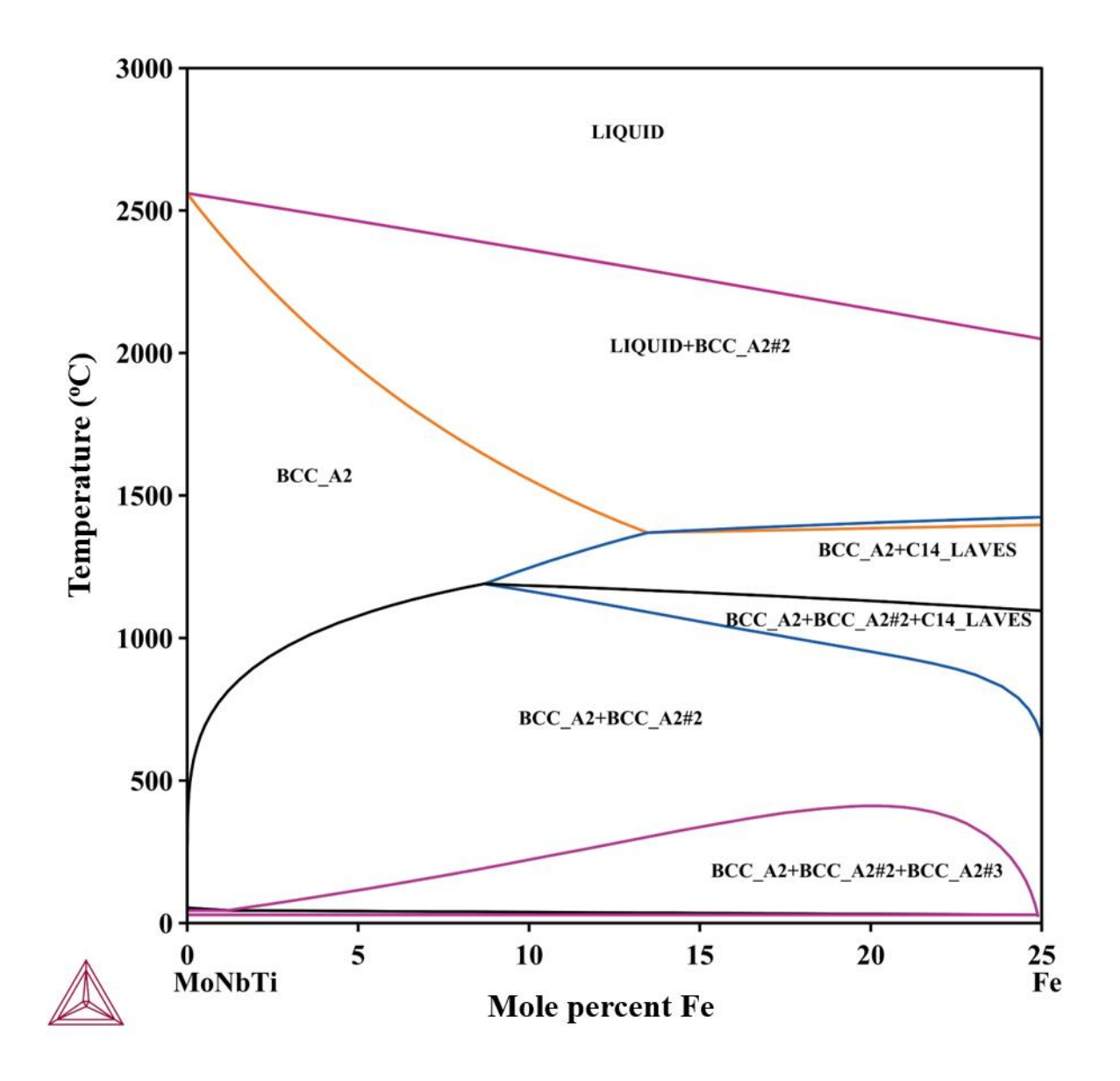
Phase fraction plot of MoTaTiFe alloy, (Fe: 4 at. %)



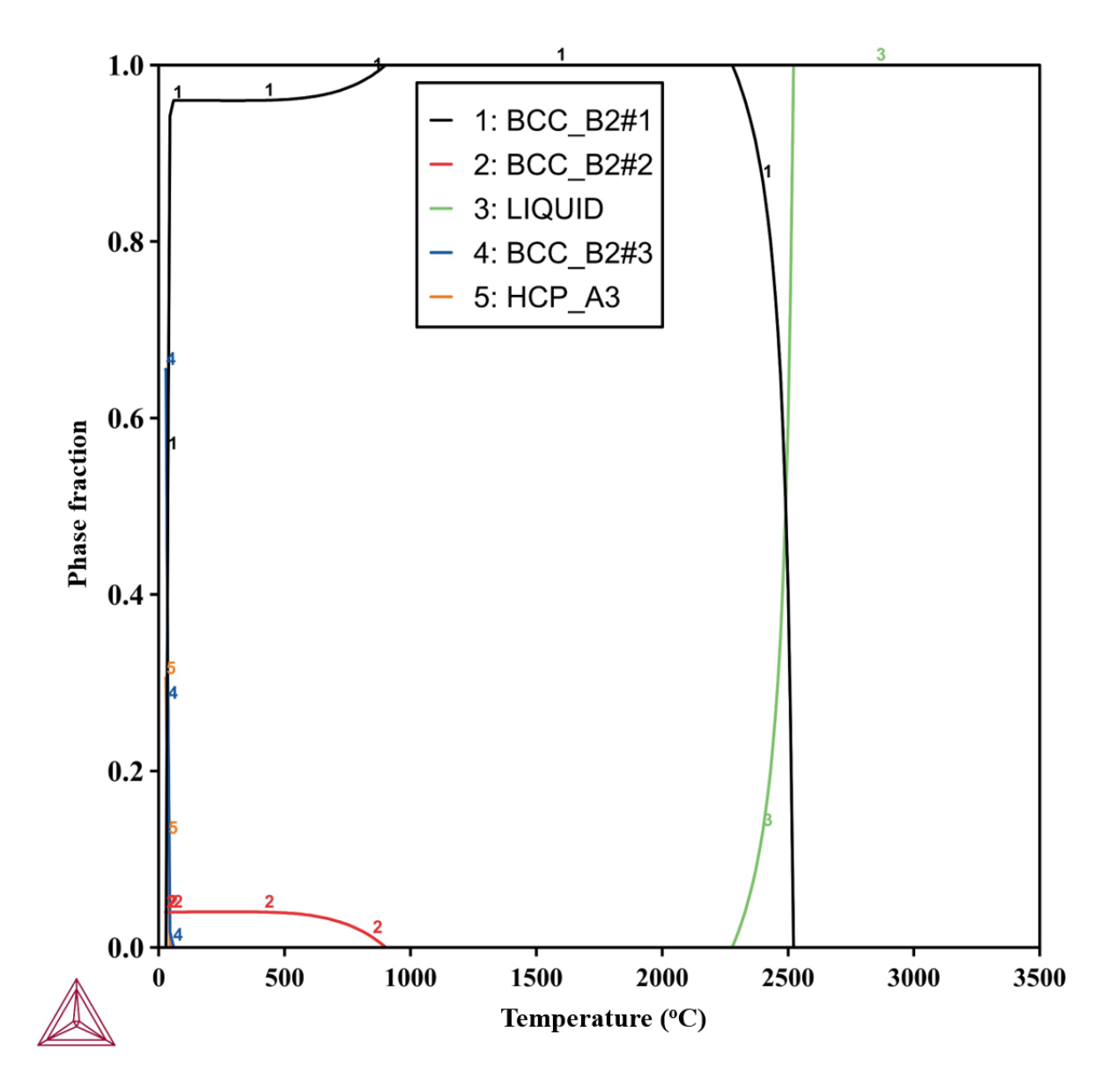
Vertical section of $(MoNb)_{I-x}Fe_x$ phase diagram



Phase fraction plot of MoNbFe alloy, (Fe: 3.5 at. %)



Vertical section of $(MoNbTi)_{I-x}Fe_x$ phase diagram



Phase fraction plot of MoNbTiFe alloy, (Fe: 2 at. %)



Professor Koteswararao V. Rajulapati

School of Engineering Sciences and Technology University of Hyderabad (An Institution of Eminence) Prof. C.R. Rao Road, P.O. Central University Gachibowli, Hyderabad 500046, INDIA.

E-mail: kvrse@uohyd.ac.in; Web: www.kvrajulapati.in

Date: 29th December 2023

To The Controller of Examination (CE), University of Hyderabad.

Dear Sir,

Subject - Clarification on similarity index in the Ph.D. thesis of K. Deekshith Goud (Reg.

No. 19ENPH01) reg.

Please find the enclosed Ph.D. thesis titled "Manufacturing of Refractory Multi-Principal Element Alloys and Understanding their Micro- and Nanomechanical Behaviour" by K. Deekshith Goud (Reg. No. 19ENPH01). This thesis has been checked for plagiarism in the central library of University of Hyderabad and the report shows a similarity index of 57%, out of which 53% is from our own published journal papers. Therefore, an effective similarity index is only 4% (57% - 53%). This is for your attention and necessary action.

Please let me know if you need any other details in this regard.

Thank you.

Yours Sincerely

Prof. Koteswararao V. Rajulapati

(Supervisor)

WARARAO V. RAJULAPATI

Professor

School of Engineering Sciences and Technology, University of Hyderabad, Prof. C. R. Rao Road, Gachibowli, Hyderabad - 500 046, INDIA.

Dean-SES

Prof. Jaj Prakash डोन IDEAN एस.ई.एस.टी / School of Engineering Sciences & Technology

हेदराबाद विश्वविद्यालय UNIVERISTY OF HYDERABAD दुराबाद / Hyderabad - 500046

Manufacturing of Refractory Multi-Principal Element Alloys and Understanding their Microand Nanomechanical Behaviour

by Deekshith Goud K

Submission date: 29-Dec-2023 11:29AM (UTC+0530)

Submission ID: 2265430925 **File name:** Deekshith.pdf (6.65M)

Word count: 29355 Character count: 153941

Librarian

Indira Gandhi Memorial Library
UNIVERSITY OF HYDERABAD
Central University P.O.

HYDERABAD-500 046.

Manufacturing of Refractory Multi-Principal Element Alloys and Understanding their Micro- and Nanomechanical Behaviour

ORIGINALITY REPORT

57%

19%

5/

3%

SIMILARITY INDEX

INTERNET SOURCES

PUBLICATIONS

STUDENT PAPERS

PRIMARY SOURCES

Deekshith G. Kalali, Sairam Antharam, Mohsin Hasan, P. Sai Karthik et al. "On the origins of ultra-high hardness and strain gradient plasticity in multi-phase nanocrystalline MoNbTaTiW based refractory high-entropy alloy", Materials Science and Engineering: A, 2021

20%

Publication

link.springer.com

Internet Source

13%

Deekshith G. Kalali, Anjali Kanchi, P.
Sudharshan Phani, K. Bhanu Sankara Rao et al. "Role of Ti on the microstructure and mechanical properties of MoNbTi mediumentropy alloy", International Journal of Refractory Metals and Hard Materials, 2023

9%

4

Deekshith G. Kalali, P. Sai Karthik, K Bhanu Sankara Rao, Koteswararao V. Rajulapati.

6%

There are from of

JAMAS V. RAJULAPAT

School of Engineering Sciences and Technology, University of Hyderabad, Prof. C. R. Rao Road, Gachibowli, Hyderabad - 500 046, INDIA.

	"Ultra-hard, multi-phase nanocrystalline MoTa and MoTaTi based concentrated refractory alloys", Materials Letters, 2022 Publication	
5	Deekshith G. Kalali, Anjali Kanchi, P. Sudharshan Phani, K. Bhanu Sankara Rao et al. "Role of Ti on the microstructure and mechanical properties of MoNbTi mediumentropy alloy", International Journal of Refractory Metals and Hard Materials, 2024 Publication	
6	Deekshith G. Kalali, Harita Seekala, P. Sudharshan Phani, K. Bhanu Sankara Rao, Koteswararao V. Rajulapati. "High speed nanoindentation aided correlative study between local mechanical properties and chemical segregation in equiatomic MoNb and MoNbTi alloys", Journal of Materials Research, 2023 Publication There are the School of Engineering Sciences and Perfectsor School of Engineer	ULAF chnoloan Ro
7	Submitted to National Institute of Technology, Rourkela Student Paper	NDIA.
8	Submitted to University of Birmingham Student Paper <1 %	
9	High-Entropy Alloys, 2016. Publication < 1 %	

10	"Spark Plasma Sintering of Materials", Springer Science and Business Media LLC, 2019 Publication	<1%
11	www.kvrajulapati.in Internet Source	<1%
12	Yapeng Sang, Dong Li, Weilun Deng. "Electron beam weldability of TiZrNbTa refractory high- entropy alloy and TC4 titanium alloy", Materials Today Communications, 2023 Publication	<1%
13	University of Tennessee, Knoxville Publication	<1%
14	Yu-sheng TIAN, Wen-zhe ZHOU, Qing-biao TAN, Ming-xu WU, Shen QIAO, Guo-liang ZHU, An-ping DONG, Da SHU, Bao-de SUN. "A review of refractory high-entropy alloys", Transactions of Nonferrous Metals Society of China, 2022 Publication	<1%
15	Submitted to University of Hyderabad, Hyderabad Student Paper	<1%
16	Ping Zhang, Ziwei Li, Haomin Liu, Yuanbin Zhang, Huaixue Li, Chuanwei Shi, Peng Liu, Dongfang Yan. "Recent progress on the microstructure and properties of high entropy	<1%

alloy coatings prepared by laser processing technology: A review", Journal of Manufacturing Processes, 2022

Publication

17	sig3.ecanews.org Internet Source	<1%
18	Jia-li Zhou, Yan-hai Cheng, Yong-xiong Chen, Xiu-bing Liang. "Composition design and preparation process of refractory high- entropy alloys: A review", International Journal of Refractory Metals and Hard Materials, 2022 Publication	<1%
19	Vivek Kumar Pandey, Vikas Shivam, B Nageswara Sarma, N K Mukhopadhyay. "Phase evolution and thermal stability of mechanically alloyed CoCrCuFeNi high entropy alloy", Materials Research Express, 2020 Publication	<1%
20	Submitted to Koc University Student Paper	<1%
21	vtechworks.lib.vt.edu Internet Source	<1%
22	Karsten Glowka, Maciej Zubko, Paweł Świec, Krystian Prusik et al. "Microstructure and	<1%

Mechanical Properties of Co-Cr-Mo-Si-Y-Zr High Entropy Alloy", Metals, 2020

Publication

Stepanov, N.D., D.G. Shaysultanov, G.A. <1% 23 Salishchev, and M.A. Tikhonovsky. "Structure and mechanical properties of a light-weight AlNbTiV high entropy alloy", Materials Letters, 2015. Publication Ramya Sree Ganji, Koteswararao V. <1% 24 Rajulapati, K. Bhanu Sankara Rao. "Development of a Multi-phase AlCuTaVW High-Entropy Alloy Using Powder Metallurgy Route and its Mechanical Properties", Transactions of the Indian Institute of Metals, 2020 **Publication** ethesis.nitrkl.ac.in <1% Internet Source worldwidescience.org 26 Internet Source www.researchgate.net Internet Source "Laser Cladding of Metals", Springer Science 28 and Business Media LLC, 2021

inis.iaea.org

Publication

29	Internet Source	<1%
30	pure-oai.bham.ac.uk Internet Source	<1%
31	www.arci.res.in Internet Source	<1%
32	www.frontiersin.org Internet Source	<1%
33	Ana C. Feltrin, Qiuwei Xing, Akeem Damilola Akinwekomi, Owais Ahmed Waseem, Farid Akhtar. "Review of Novel High-Entropy Protective Materials: Wear, Irradiation, and Erosion Resistance Properties", Entropy, 2022	<1%
34	Hahn, Eric N., and Marc A. Meyers. "Grainsize dependent mechanical behavior of nanocrystalline metals", Materials Science and Engineering A, 2015. Publication	<1%
35	Qiannan Wang, Hongwang Yang, Xiaojiao Zuo, Yinxiao Wang, Jiahao Yao. "High- Throughput Preparation and Characterization of ZrMoTaW Refractory Multi-Principal Element Alloy Film", Materials, 2022 Publication	<1%
36	Submitted to University of Leicester Student Paper	<1%

